Morfología y propiedades estructurales de óxidos metálicos complejos: Un enfoque teórico y experimental

Memoria presentada por Marisa Carvalho de Oliveira para optar al grado de doctora en régimen de cotutela por la Universitat Jaume I y por la Universidade Federal de São Carlos.

UNIVERSITAT
JAUME•I

Universidade Federal de São Carlos

Programa de Doctorado en Ciencias

Escuela de Doctorado de la Universitat Jaume I

Programa de Pós-Graduação em Química

Centro de Ciências Exatas e de Tecnologia

Dirigida por:

Prof. Dr. Juan Manuel Andrés Bort

Dr. Lourdes Gracia Edo

Prof. Dr. Elson Longo da Silva

Castellón de la Plana, Julio 2018

Juan Manuel Andrés Bort, Catedrático del Departament de Química Física i Analítica de la Universitat Jaume I de Castellón, Lourdes Gracia Edo, Ayudante Doctor del Departament de Química Física de la Universitat de València y Elson Longo da Silva, Catedrático del Departament de Química de la Universidade Federal de São Carlos de Brasil.

CERTIFICAN:

Que el trabajo con título "Morfología y propiedades estructurales de óxidos metálicos complejos: Un enfoque teórico y experimental" ha sido realizado por Marisa Carvalho de Oliveira bajo nuestra dirección para optar al grado de Doctora en Química.

Y para que conste a los efectos oportunos, firmamos el presente certificado en Castellón de la Plana a Julio de 2018.

Dr. Juan Manuel Andrés Bort **Dr. Lourdes Gracia Edo**

Dr. Elson Longo da Silva

UNIVERSITAT JAUME·I

SERVEI DE GESTIÓ DE LA DOCÈNCIA I ESTUDIANTS
DOCTORAT

TRIBUNAL DE TESI DOCTORAL

Acta de lectura de tesi doctoral
Acta de lectura de tesis doctoral
Primera sessió/Primera sesión
Doc 1

Membres del tribunal designat per la Comissió d'Investigació i Doctorat de la Universitat Jaume I:
Miembros del tribunal designado por la Comisión de Investigación y Doctorado de la Universitat Jaume I:

President/a / *Presidente/a* Dr./Dra.: Mónica Calatayud i Antonino
Vocal Dr./Dra.: Paula Fabiana dos Santos Pereira Lima
Secretari/ària / *Secretario/a* Dr./Dra.: Rosa Llusar Barelles

Nom i cognoms de l'/la autor/a de la tesi doctoral / *Nombre y apellidos del/de la autor/a de la tesis doctoral:* Marisa Carvalho de Oliveira

Títol de la tesi / *Título de la tesis:* Morfología y propiedades estructurales de óxidos metálicos complejos: Un enfoque teórico y experimental

Òrgan responsable / *Órgano responsable:* Escuela Doctorado

Facultat-Escola / *Facultad-Escuela:* ESTCE

Direcció de la tesi / *Dirección de la tesis:*

Dr./Dra.: Juan Manuel Andrés Bort
Dr./Dra.: Lourdes Gracia Edo
Dr./Dra.: Elson Longo

Primera sessió/Primera sesión

Qualificació Global / *Calificación Global:* [1] Excel·lent

El/La president/a / *El/La presidente/a*	Vocal	El/La secretari/ària / *El/La secretario/a*
Mónica Ci Antonin	PaulaFabianadosSantosPereiraLima	

Castelló de la Plana, 18 de Juliol de 2018

---

[1] "No Apte", "Aprovat", "Notable", "Excel·lent"/ "No Apto", "Aprobado", "Notable", "Sobresaliente"

Agradecimientos

Agradecer siempre es grato, para el que agradece y para el agradecido. Además, esta tesis doctoral no hubiera sido posible sin el apoyo, la implicación y confianza de todas las personas que durante este tiempo me han apoyado en el desarrollo de esta tesis, que tengo a manifestar mis más sinceros agradecimientos.

En primer lugar, agradezco a la Generalitat Valenciana por la financiación recibida a través del Programa Santiago Grisolía (2015-2018) y a la Universitat Jaume I por la oportunidad que me ha brindado para realizar y defender la presente Tesis Doctoral y a su Servei d'Informatica en cuyos ordenadores de cálculo científico he realizado la mayor parte de los cálculos que constituyen los trabajos que presentaré. Asimismo, me gustaría agradecer al proyecto ref. UJI-B2016-25, por la ayuda con los gastos ocasionados en la participación en congresos y cursos relacionados con mi formación como investigadora. También doy las gracias a la Universidade Federal de São Carlos y al Prof. Dr. Elson Longo del Centro de Desenvolvimento de Materiais Funcionais (CDMF-UFSCar/Brasil) que me ha permitido realizar la presente Tesis Doctoral en régimen de cotutela entre la UJI y la UFSCar.

En segundo lugar, quiero dar las gracias a mis directores de Tesis, Prof. Dr. Juan Andrés y Dr. Lourdes Gracia, por sus dedicaciones, sus buenas ideas, por los conocimientos y cooperaciones que me han transmitido durante estos años en la realización de este trabajo de investigación.

A mis padres y hermanos quiero agradecer hoy y siempre por el constante apoyo moral que me han dado en todo momento.

A Renan Ribeiro por su ternura serena, su amistad y colaboración, por todos los momentos compartidos, por los ánimos y cariño que siempre estará en mi corazón.

A los profesores que he tenido en las distintas universidades y principalmente a los profesores de la Universitat Jaume I del departamento de

Química Física i Analítica: Sixte Safont, Rosa Llusar, Armando Beltrán, Sergio Martí, Vicente Moliner y Mónica Oliva, por su gran nivel docente. Debo destacar el profesor Armando Beltrán por su amplio conocimiento y su ayuda en la resolución de dudas planteadas así como las discusiones altamente enriquecedoras en la elaboración de la tesis.

Agradezco también a la secretaria del departamento, Merche, por toda la ayuda que me ha ofrecido en los trámites administrativos.

Además, me gustaría extender mi agradecimiento a todos aquellos que también me han ayudado durante estos años como estudiante de doctorado, tanto en el ámbito de trabajo como en el personal: Silvia, Maite, Thiago, Isabel, Amanda, Érica, Javier, Kemel, Miquel, Daria, Natalia.

A mis padres João y Maria Cárita

A mis hermanos João Filho y Marília

A mi abuela Maria

Resumen

El diseño, el control y la caracterización directa de las propiedades de las superficies son requisitos previos para todas las aplicaciones prácticas de (nano) materiales. Dentro de este contexto, la presente tesis doctoral constituye un trabajo experimental y teórico sobre la morfología, estructura, propiedades electrónicas y ópticas de los materiales basados en óxidos metálicos complejos: $BaWO_4$, $BaMoO_4$, solución solida $BaW_{1-x}Mo_xO_4$ (x=0, 0.25, 0.50, 0.75 y 1), $CaMoO_4$, $ZnMoO_4$, $ZnMoO_4:Eu^{3+}$, $CaZrO_3$ y $CaZrO_3:Eu^{3+}$, que constituyen los sistemas estudiados en la presente Tesis Doctoral.

En el Capítulo 1 de introducción se empieza resaltando la importancia de combinar teoría, simulación y experimento en el estudio de materiales, a continuación se presenta una visión general sobre el concepto de morfología en particular como obtenerla teóricamente usando la construcción de Wulff.

En el Capítulo 2 se presentan los métodos teóricos y las simulaciones computacionales, explicando cómo caracterizamos los estados electrónicos excitados y calculamos las propiedades estructurales, electrónicas y ópticas. Las motivaciones y objetivos del presente trabajo se enumeran en el Capítulo 3. En el Capítulo 4 se presentan, analizan y se discuten los resultados obtenidos, que se llevaron a cabo en colaboración con el Centro de Desenvolvimento de Materiais Funcionais (CDMF) en la Universidade Federal de São Carlos (UFSCar) y el Laboratório de Síntese Química de Materiais (LSQM) del Departamento de Materiais de la Universidade Federal do Rio Grande do Norte (UFRN), mientras las conclusiones generales se resumen en el Capítulo 5, junto con los temas que podrían ser la continuación del presente trabajo.

A continuación se presenta un resumen, escrito en portugués, con el fin de cumplir las normativas del convenio de cotutela.

Abstract

Design, control and direct characterization of the properties of the surfaces are prerequisites for all practical applications of (nano) materials. Within this context, the present doctoral thesis is an experimental and theoretical work on the morphology, structure, electronic and optical properties of materials based on complex metal oxides: $BaWO_4$, $BaMoO_4$, solid solution $BaW_{1-x}Mo_xO_4$ (x= 0, 0.25, 0.50, 0.75 and 1), $CaMoO_4$, $ZnMoO_4$, $ZnMoO_4$:Eu^{3+}, $CaZrO_3$ and $CaZrO_3$:Eu^{3+}, which constitute the systems studied in this Doctoral Thesis.

In Chapter 1 of the introduction, we begin by highlighting the importance of combining theory, simulation and experiment in the study of materials, then we present a general view on the concept of morphology in particular, how to obtain it theoretically using Wulff's construction.

Chapter 2 presents the theoretical methods and computational simulations, explaining how we characterize the excited electronic states and calculate the structural, electronic and optical properties. The motivations and objectives of this work are listed in Chapter 3. Chapter 4 presents, analyzes and discusses the obtained results, which were carried out in collaboration with the Center de Desenvolvimento de Materiais Funcionais (CDMF), at the Federal University of São Carlos (UFSCar) and in collaboration with the Laboratório de Síntese Química de Materiais (LSQM), in the Department of Matters of the Federal University of Rio Grande do Norte (UFRN), while The general conclusions are summarized in Chapter 5, along with the topics that could be the continuation of this work. Below is a summary, written in Portuguese, in order to comply with the regulations of the “co-tutela” agreement.

Índice

1. Introducción

Los cristales de materiales inorgánicos complejos que presentan una simetría y superficies bien definidas presentan características específicas que dan lugar a diferentes propiedades físicas y químicas, siendo la energía de la superficie [1-4], y su isotropía espacial las que permiten construir estructuras en que las diferentes superficies controlan su arquitectura final [5, 6]. Sus morfologías, propiedades y aplicaciones tecnológicas han generado un gran interés científico [7-10]. Asi por ejemplo, la obtención de (nano)cristales con morfología especificas son la base de muchas tecnologías modernas, incluida la catálisis selectiva [11-14], dispositivos electrónicos [15], almacenamiento de energía [16], y medicamentos [17, 18].

Los estudios de este tipo de (nano)materiales inorgánicos no solo son útiles para encontrar estructuras cristalográficas novedosas, sino también para ofrecer una nueva oportunidad para el diseño y obtención de materiales multifuncionales con propiedades innovadoras. Por lo tanto, la modulación de la morfología y de las superficies expuestas de materiales funcionales es una línea de investigación muy activa [19-29] para aplicaciones tecnológicas avanzadas. Para ajustar con precisión la morfología de un cristal es imprescindible una compresión profunda del mecanismo de formación, y es necesario disponer de buenas imágenes de la morfología que se obtienen de la utilización de diferentes tipos de microscopias electrónicas, para poder dirigir el estudio teórico del crecimiento general de la morfología y la cinética de los pasos que forman los patrones de superficie (cubos, octaedros, hexágonos, etc.) Para ello, los métodos y las técnicas de modelización y simulación computacional junto con estudios experimentales sobre su síntesis y caracterización son una herramienta bien establecida para el desarrollo de estrategias de investigación innovadoras que permite la predicción y diseño de materiales con propiedades y aplicaciones tecnológicas.

1.1. Teoría, simulación y experimento

Hoy en día las técnicas experimentales proporcionan un amplio abanico de resultados que podemos interpretar a nivel atómico y molecular con la ayuda de estudios mecano-cuánticos. En el campo de la ciencia de materiales, la teoría y la simulación, usadas en combinación con las técnicas experimentales, permiten dar un paso más ya que posibilitan predecir las condiciones óptimas para la síntesis de nuevos materiales. Se puede conseguir así una guía para el diseño racional de materiales con propiedades definidas, o para la modificación dirigida de los existentes, desde la escala “nano” hasta la macroscópica. Todo ello requiere las leyes de la mecánica cuántica, que describe el comportamiento de toda la materia de una manera exacta. De hecho, casi 90 años después de la famosa promesa de Dirac de que todas las leyes que gobiernan la química son completamente conocidas [30], se ha logrado un progreso notable aplicando la mecánica cuántica a química, ciencia de la materia, y nanotecnología.

Esta discusión sirve para motivar el tema central de la presente Tesis Doctoral, que consiste en entrar en un diálogo autocrítico entre la teoría y la experimentación en lugar de hacer una teoría o experimental de forma aislada y confiar incondicionalmente en los resultados de tales estudios por separado. De hecho, la teoría puede tener una precisión insuficiente debido a las aproximaciones que son necesarias utilizar en lo cálculos cánticos; así, las fuentes de error pueden conducir a estructuras o propiedades electrónicas incorrectas. Por otra parte, el experimento puede dar lugar a resultados demasiado complicados para ser interpretados o que se basan en suposiciones simplistas, y no puede aplicarse a sistemas tan complejos como los materiales que estudiaremos.

Para que haya una verdadera sinergia entre teoría y experimento se hace necesario utilizar las propiedades observables del sistema. En nuestro caso, el observable es la morfología, cuya imagen se obtiene de los microscopios electrónicos, la geometría, que se obtiene de la difracción de rayos-X con refinamiento Rietveld, estructura electrónica, y de las frecuencias vibracionales que se pueden conseguir con la espectroscopia Raman, cuando estén disponibles. Esto constituye como veremos un campo de intersección muy fructífero donde confluyen la teoría y el experimento en ciencia de los materiales y nanotecnología, como se demostrará en este Tesis Doctoral. Los métodos y técnicas de la química teórica y computacional junto con las investigaciones experimentales constituyen una herramienta fundamental para el estudio de materiales desde la escala “macro” hasta la escala “nano”.

De hecho, la nanotecnología ha experimentado un enorme crecimiento en los últimos años, como consecuencia de los nuevos fenómenos exhibidos por materiales confinados en dimensiones menores que unos pocos centenares de nanómetros, es decir, (nano)materiales. Sus propiedades dependen de la composición, el tamaño y la morfología, y son las responsables de que puedan ser utilizados en aplicaciones tecnológicas nuevas y innovadoras [31, 32], y han dado lugar a numerosas aplicaciones en diferentes áreas como por ejemplo baterías [33, 34] y electrónica [35].

En los últimos años, se ha convertido en una prioridad el desarrollo de tecnologías sostenibles para abordar necesidades sociales fundamentales que constituyen los grandes desafíos a los que nos enfrentamos actualmente, como la limpieza del aire/agua o el suministro de energía limpia, la desalinización de agua [36] y interacciones drogas/gen.[37]. En estos campos de investigación se están desarrollando una gama de técnicas de simulación que se aplica a problemas relacionados con materiales para la generación, el almacenamiento y la conversión de energía, incluyendo celdas solares, reactores nucleares, baterías, pilas de combustible y sistemas catalíticos [38].

La modelización y simulación de las propiedades de los materiales y de los procesos en que participan, a partir de cálculos de primeros principios, han conseguido cada vez más precisión para facilitar el diseño y la obtención de nuevos materiales "in silico" [39-41]. También es importante señalar que las dificultades encontradas por los experimentos para separar los diferentes factores os no están presentes cuando se emplean modelos teóricos en los que uno puede representar diferentes morfologías para una composición o variar la composición para un determinado morfología.

A este respecto, cabe resaltar que en un número reciente de la revista Nature Materials la editorial se centra en reconocer e impulsar la simulación de materiales [42], destacando que las simulaciones de materiales se han convertido en una herramienta fundamental en este campo de investigación. Asimismo, se han publicado varias revisiones de los métodos actuales de la mecánica cuántica para la modelización de materiales, en las que se ponen de manifiesto sus ventajas y también sus inconvenientes, así como sus perspectivas de futuro [38, 43-48]. Por tanto, es necesario un diálogo entre teoría, simulación y experimento en lugar de usarlos por separado y confiar de forma incondicional en los resultados de tales estudios por separado.

La estructura singular y las propiedades electrónicas y ópticas de las familias de los wolframatos, molibdatos, y perovskitas, que son óxidos ternarios complejos, hacen que sean unos candidatos ideales para su uso en una gran variedad de aplicaciones tecnológicas. Nuestro grupo de investigación tiene una larga y contrastada experiencia en estudios donde se combina la teoría y el experimento para caracterizar sus geometrías, estructuras electrónicas y propiedades tales como fotoluminiscencia, fotocatalisis, magnetismos, agentes microbianos y otros [49-61]. Por otra parte, los materiales de perovskita están presentes en numerosas aplicaciones tecnológicas asociadas a propiedades funcionales como la ferroelectricidad, piezoelectricidad, (anti) ferromagnetismo, multiferroismo, superconductividad, emisiones fotoluminiscentes, fotocatalísis [62-67].

En resumen, esta bien establecido que la morfología, dimensionalidad y estructura cristalina de los materiales desempeñan un papel importante en las propiedades electrónicas, ópticas y catalíticas. Comprender el papel de estas superficies y encontrar una relación con sus características físicas y químicas es de extrema importancia. Uno de los objetivos de este proyecto fue asociar los resultados experimentales y teóricos para proporcionar un major comprensión de las morfologias y las emisiones fotoluminiscentes de una serie de óxidos ternarios complejos, que pertenecen a las familia de los wolframatos, molibdatos y perovskitas, que han sido caracterizados en el centro de desenvolvimento de materiais funcionais y en laboratorio de síntesis química de materiales.

1.2. Estructuras cristalinas de AMO_4 (A= Ba, Ca y Zn; M= W o Mo) y $CaZrO_3$

Los materiales basados en molibdatos y wolframatos con fórmula química ABO_4 pertenecen tanto a la familia de las scheelitas [68-71] como a la familia de las wolframitas [72-74]. Sus características dependen de los tipos de cationes que ocupan los sitios A y/o B. Si el radio iónico del catión A es más grande que 1.0 Å, como es el caso de Ca^{2+}, Ba^{2+}, Sr^{2+}, Pb^{2+} los compuestos muestran una estructura scheelita, como por ejemplo en la familia $AMoO_4$ (A= Ca, Ba; M=W o Mo) con simetría tetragonal y grupo espacial (*I*41/*a*) presentada en la Figura 1.1

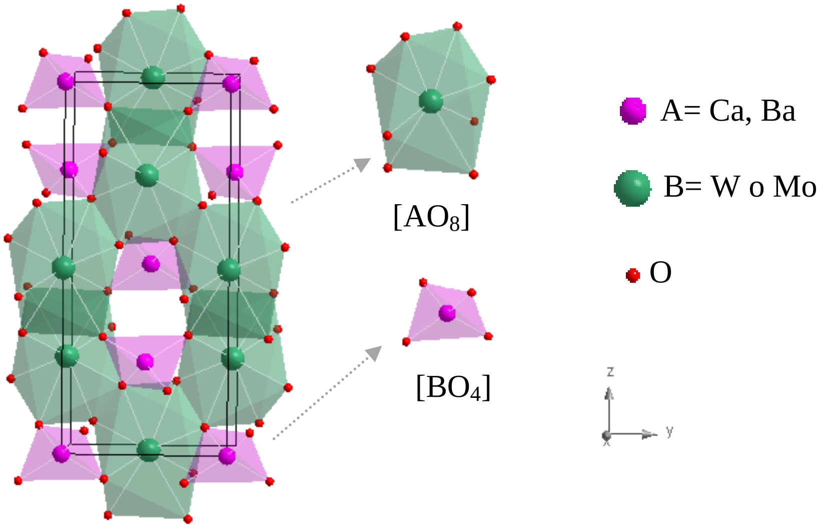

Figura 1.1. Representación esquemática de la celda unidad de las scheelitas AMO_4 (A=Ba, Ca; M=W o Mo), con clústeres tetraédricos para B y dodecaédricos para A.

Alternativamente, si el radio iónico del catión A es más pequeño que 1.0 Å, como es el caso de Fe^{2+}, Mn^{2+}, Ni^{2+}, Mg^{2+}, Zn^{2+} los compuestos adoptan la estructura de wolframita [75, 76], como la estructura de $ZnMoO_4$ con simetría triclínica y grupo espacial ($P\bar{1}$) [77-79] presentada en la Figura 1.2.

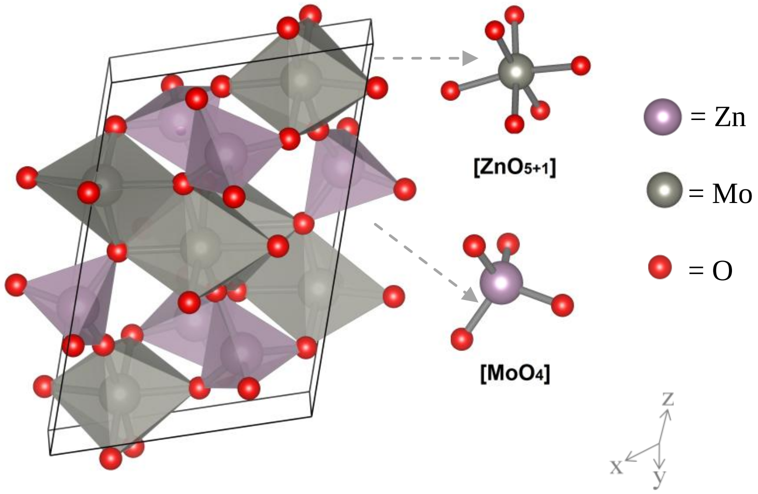

Figura 1.2. Representación esquemática de la celda unidad para la wolframita $ZnMoO_4$. Se han resaltado los clústeres, $[ZnO_{5+1}]$ y $[MoO_4]$, como unidades estructurales.

Los molibdatos y wolframatos han sido ampliamente estudiados y tienen una larga historia de aplicaciones prácticas y han sido objeto de una extensa investigación desde la década de 1960 [80]. Los wolframatos exhiben propiedades funcionales interesantes como sensores de humedad [81], fotocatalizadores [82], dispositivos electrocrómicos [83], convertidores Raman [84], centelleadores [85], materiales fotoluminiscentes [86] y láseres [87, 88].

Por otra parte, los molibdatos metálicos también han sido intensamente investigados debido sus diversas propiedades, principalmente, fotoluminiscentes [89-91]. En particular, los molibdatos y wolframatos de los metales alcalinos térreos de Ca y Ba [92-100], y el $ZnMoO_4$ [101-105]

Conjuntamente, la familia de las perovskitas presentan la formula estequiométrica del tipo ABO_3 y su estructura ideal tiene simetría cúbica y grupo espacial (Pm3m), sin embargo permite pasar de la simetría cúbica ideal a simetrías inferiores debido variaciones estructurales como se muestra en la Figura 1.3 de la estructura $CaZrO_3$ ortorrómbica distorsionada.

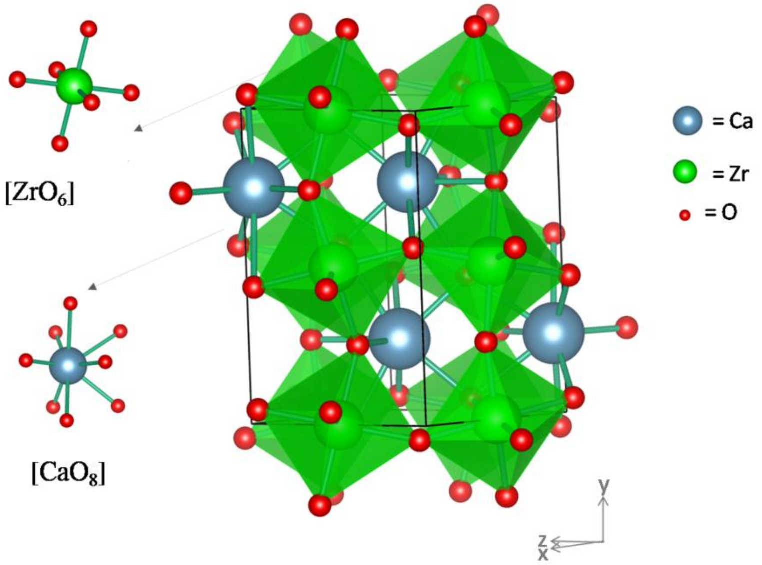

Figura 1.3. Representación esquemática de celda unidad de la perovskita $CaZrO_3$. Los clústeres que corresponden a las coordinaciones locales de los cationes Zr y Ca, $[ZrO_6]$ y $[CaO_8]$, respectivamente, están indicados.

Las propiedades y aplicaciones de estos materiales basados en perovskitas o scheelitas, son muy dependientes de los métodos de síntesis utilizados. Por este motivo, se hace necesaria encontrar las técnicas de producción que propicien un control adecuado del tamaño, forma y organización estructural. Sin embargo, la preparación de materiales por nuevas rutas puede llevar al descubrimiento de nuevas características morfológicas, tamaño de la partícula, composición, nivel de cristalinidad, que pueden ser controlada por medio de modificaciones en la temperatura, pH, concentración, entre otros [106], que es un paso esencial en la comprensión de sus propiedades físicas y químicas, además de predecir resultados que puedan llevar a diferentes aplicación tecnológicas [107, 108].

1.3. Superficies y morfología

La obtención de las superficies de una estructura cristalina consiste en seccionar el "bulk" perpendicularmente al vector de la dirección deseada, formando una estructura periódica en dos dimensiones (x,y), pero con espesor finito (dirección z). De esta forma las superficies quedan definidas por dos vectores ortogonales a la dirección [hkl] elegida. En general, las superficies más estables termodinámicamente son las que presentan bajos índices de Miller [hkl].

El estudio teórico de las superficies de materiales tiene gran importancia debido a que es la clave para entender sus posibles aplicaciones en catálisis y formación de filmes finos, por ejemplo. De esta forma, el control de la morfología del cristal es uno de los retos actuales en el campo de la nanotecnología y ciencia de materiales, porque pequeños cambios en el ambiente de crecimiento pueden afectar a morfología de los materiales [109-111] y las superficies expuestas, que son factores importantes que influyen en su aplicación [112, 113]. Por lo tanto, el control de la morfología afecta directamente el diseño de las propiedades, es decir, diferentes planos de cristal exhiben diferentes respuestas anisotrópicas a diversas actividades mecánicas, físicas y químicas como: dureza, piezoelectricidad y reactividad [114, 115].

Como hemos comentado anteriormente la combinación de estudios teóricos y técnicas experimentales se han convertido en una herramienta fundamental para la compresión de la morfología de los cristales y sus mecanismos de modulación a nivel atómico. En la Figura 1.4 se presenta de forma esquemática las posibles morfologías, simetrías y estructuras que pueden presentar los materiales tanto a nivel "nano" como macro. [116].

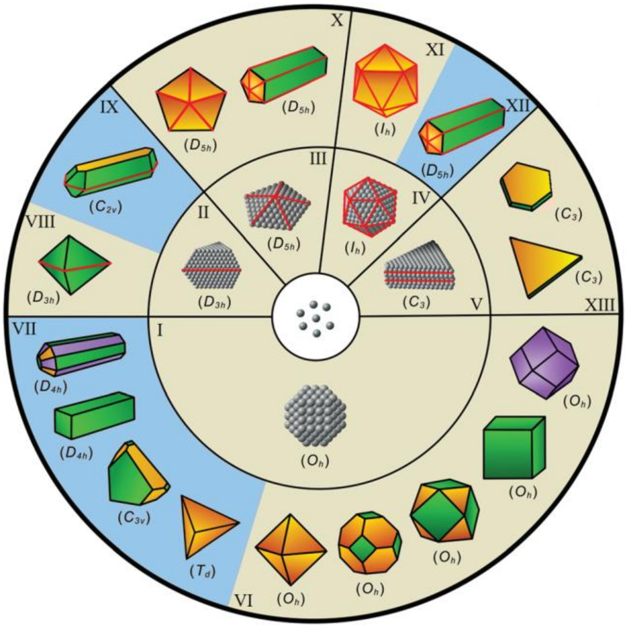

Figura 1.4. Posibles morfologías, simetrías y estructuras. Reproducido a partir de [117] con permiso del The Royal Society of Chemistry.

Aristóteles fue el primero que intento correlacionar el conjunto natural de reglas que impulsa a toda materia a adoptar una forma y una apariencia[118] (Figura 1.5).

Hýlé (matéria) $\xrightarrow[\text{(propósito)}]{\text{telos}}$ morphé (forma) + eidos (aparencia)
Causal y final

Figura 1.5. Correlación de Aristóteles.

Goethe fue el precursor de la morfología en 1795, el cual escribió que “la morfología puede verse como una teoría en sí misma” y “se puede decir que la morfología incluye los principios de la forma estructurada y la formación y transformación de cuerpos orgánicos”. Este concepto va mucho más lejos del simple control de la pureza, la composición y el orden de traslación de largo alcance de las disciplinas más tradicionales y es, por su propia esencia, moderno. Es bien sabido que desde los primeros días en la cristalografía que la forma era el tema central. Steno en 1669 al observar cristales de cuarzo, descubrió que el ángulo entre caras diferentes era constante e independiente del tamaño. Más adelante, en 1784 Haüy propuso la ley de ángulos interfaciales constantes. Los primeros estudios en este campo se basaron en la medición de los ángulos entre las caras y las relaciones de simetría en los cristales. Por consiguiente, la estructura se obtuvo a partir de la forma del cristal y se describieron muchas formas poliédricas como cubos, octaedros, tetraedros y otros, por lo que la morfología junto con la geometría se convirtieron en conceptos fundamentales para describir los cristales.

A principios del siglo XX, Georg Wulff [119] desarrolló un modelo sistemático para caracterizar las formas y hábitos cristalinos encontrados en minerales, revolucionando los campos de la cristalografía y geología. Sin embargo, a finales del siglo XX ese método fue redescubierto en el campo de la ciencia de materiales para caracterizar la morfología de las (nano)partículas [120]. Actualmente, las simulaciones computacionales basadas en el cálculo de la energía de superficie se emplean en conjunto con la construcción propuesta por Wulff para explicar y predecir las morfologías experimentales. Se han realizado muchos esfuerzos durante los años para desarrollar las nuevas herramientas y técnicas dedicadas al diseño y la fabricación de superficies y morfologías específicas. La síntesis controlada para obtener una morfología determinada de materiales inorgánicos en la escala nano/micrómetro ha progresado considerablemente en la última década [121]. Muchas propiedades dependientes de determinadas superficies han sido descubiertas debido a la exitosa síntesis de (nano)cristales con una serie de morfologías bien definidas. El control de la morfología de los (nano)cristales es importante en diversas aplicaciones, como la catálisis heterogénea [122, 123], celdas solares [124], diodos para emisión de luz [125, 126], y marcadores biológicos [127, 128].

La modulación de los planos cristalográficos de materiales funcionales para la obtención de morfologías deseables es tan significativa como el tamaño, la composición, fase y cristalinidad en la determinación de las propiedades químicas y físicas de los sólidos cristalinos. Es imprescindible una mejor comprensión del control de las superficies expuestas, lo cual generaría una nueva capacidad para diseñar las estructuras necesarias para aplicaciones reales, a la vez que ofrecería una nueva oportunidad para la construcción de materiales multifuncionales con potencial único y propiedades asombrosas [129].

Además las superficies de alta energía, que contienen abundantes átomos de coordinación insaturados que muestran alta reactividad, [3, 130-

136] han sido diseñados para diferentes aplicaciones, en las que las superficies cristalográficas bien definidas juegan un papel clave [137-139] como catalizador mejorado [140, 141], óptico [142], magnético [143] y propiedades electroquímicas[113, 144]. En este contexto, la síntesis de (nano)cristales inorgánicos con morfologías controladas y superficies reactivas, han despertado gran interés en la última década, debido a las propiedades fascinantes de su formato[145-147], así como gran importancia en estudios fundamentales y aplicaciones tecnológicas [112, 148, 149].

1.3.1. Construcción de Wulff: Morfología de los (nano)materiales.

El formalismo desarrollado por Wulff se basó en el concepto de minimización de la energía propuesto por Gibbs en 1874, al cual un (nano)cristal presenta una determinada morfología de equilibrio cuando su energía total es mínima. Su energía total es la suma de las energías del "bulk" y de sus superficies (γ). Por lo tanto, para un volumen fijo, la energía total encuentra un mínimo global cuando la energía de superficie (γ) es minimizada [150].

En un sólido, la energía superficial depende de la orientación de los planos cristalográficos debido a la anisotropía intrínseca asociada a los diferentes ordenamientos atómicos de los planos. De esta forma, Georg Wulff [119] propuso que la morfología de un (nano)cristal sea representada por un grupo de planos con diferentes índices de Miller [hkl], siendo sus respectivas energías ($\gamma_{[hkl]}$) proporcionales a la distancia de dicho plano ($d_{[hkl]}$) en relación al origen al centro de la superficie (c), conforme a la ecuación:

$$\frac{\boldsymbol{\gamma}_{[\mathbf{hkl}]}}{\mathbf{d}_{[\mathbf{hkl}]}} = \mathbf{c} \qquad (1)$$

Asimismo, la construcción de Wulff combina distintos valores de la energía superficial en función de la orientación, donde el tamaño del vector ($d_{[hkl]}$) que conecta el origen al centro de la superficie es proporcional a γ. La combinación de todos los vectores representados en el plano bidimensional permite la obtención de un poliedro que contiene los diferentes planos cristalográficos, como se muestra en la Figura 1.6.

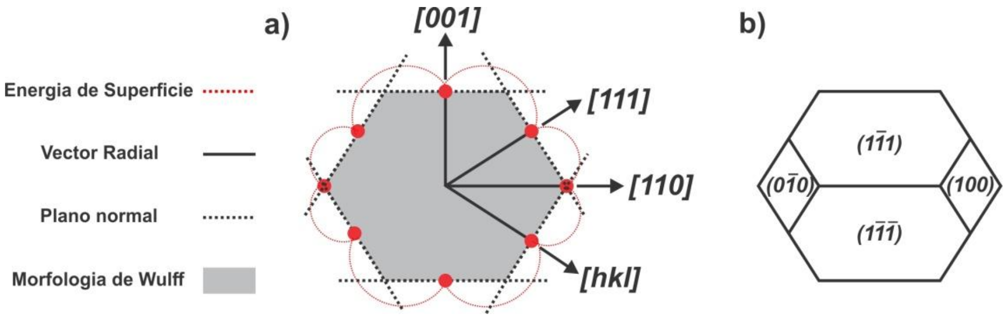

Figura 1.6. Combinación entre los diferentes planos cristalográficos (a) que originan el poliedro que representa la morfología de equilibrio para un determinado (nano)cristal (b).

Para poder obtener la morfología utilizando la construcción de Wulff es necesario el cálculo de las energías de superficie (γ) de un determinado material. γ se puede representar como E_{surf}, y también denominarse energía superficial. Se puede calcular a partir del corte en un plano cristalográfico del cristal [151], y corresponde a la energía de corte “cleavage”. Estos planos cristalográficos dependen del grupo puntual de simetría del material y las superficies se obtienen al cortar el cristal por una sección perpendicular del “bulk” en relación a los vectores de la dirección deseada, y así se obtiene una estructura periódica en dos dimensiones (“slab”), pero con espesor finito (eje z) [152]. De esta forma la energía superficial o de “cleavage” (γ) se define como la energía por unidad de área requerido para formar la superficie 2-D relativa al “bulk” y se calcula mediante la siguiente expresión a T=0ºK:

$$\boldsymbol{\gamma = \frac{E_{slab} - N \cdot E_{bulk}}{2A}} \tag{2}$$

donde E_{slab} es la energía total del “slab” 2D, E_{bulk} es la energía total del “bulk”, respectivamente, mientras que N y A representan el número de unidades de fórmula mínima y el área de la, respectivamente. El factor 2 en el denominador proviene de la existencia de las superficies superior e inferior del “slab”, que presenta una composición simétrica.

Después del proceso de optimización correspondiente y de comprobar que el valor de γ ha convergido, es decir, que ha alcanzado un valor constante y no depende del espesor del “slab”, se obtiene el valor de γ.

Otros autores [153, 154] prefieren expresar la ecuación (2) del siguiente modo:

$$\boldsymbol{\gamma = \lim_{n\to\infty} E_s(N) = \lim_{n\to\infty} E_{slab}(N) - N \cdot E_{bulk}/2A} \tag{3}$$

donde E_{slab} (N) y E_{bulk} son la energía de un “slab” de N capas y del “bulk”, respectivamente; A es el área de la celda de la unidad primitiva de la superficie; el factor 2 en el denominador representa las superficies superior e inferior del “slab”. E_s (N) es, por lo tanto, la energía (por unidad de área) requerida para la formación de la superficie a partir del volumen. Cuando n → ∞, E_s (N) convergerá a la energía de la superficie por unidad de área (γ). El número de capas dhkl a considerar en cada “slab”, N, se obtiene cuando la diferencia relativa entre E_s (N) y E_s (N - 1) es menor que 1%, para asegurar una convergencia satisfactoria en la energía de la superficie.

Cabe indicar que nuestros valores de energía superficial, γ, no se corrigieron por error de superposición de conjunto base (BSSE) [154], ya que solo estamos interesados en determinar la morfología de equilibrio y las accesibles de los materiales estudiados, que no depende de los valores absolutos de las energías superficiales de las superficies, pero sí de sus valores relativos, además se ha demostrado que para otros materiales, la corrección BSSE [155, 156] reduce todos los valores de energía superficial de un porcentaje similar, dejando así la morfología sin variar.

Es importante señalar que al realizar el corte directo del cristal a lo largo de una superficie se generan estructuras inestables debido a la tensión de los enlaces que se rompen, por lo que es necesario llevar a cabo una optimización de la geometría, lo que permite el cálculo de los valores de γ, que posteriormente se utilizan en la construcción de Wulff [120, 157] para representar la morfología. Este método se ha implementado, mejorado y utilizado por nuestro grupo de investigación en varios estudios de “bulk” y superficies y propiedades estructurales y electrónicas de perovskitas [158, 159], molibdatos [160-162], wolframatos [163-166], Ag_2CrO_4 [167], $LaVO_4$ [168], y óxidos metálicos [169, 170].

Una característica específica de nuestro grupo de investigación en el campo de la investigación de materiales es combinar los trabajos experimentales y teóricos. Estas dos líneas de investigación, cuando se aplican juntas, provocan una sinergia favorable, siendo una poderosa herramienta para estudiar y explicar las propiedades estructurales y electrónicas de los materiales, responsables de las aplicaciones tecnológicas posteriores. Por lo tanto, hay dos frentes de investigación: (1) la línea experimental en la que el objetivo es el desarrollo de nueva metodología de síntesis para encontrar un material con propiedades deseables y (2) la línea teórica en la que los cálculos de los primeros principios complementan los resultados experimentales, siendo una guía fundamental para un diseño racional de materiales innovadores.

La ingeniería asociada a la morfología de un cristal es crucial para la síntesis exitosa de semiconductores inorgánicos con aplicaciones funcionales. Para el desarrollo de materiales funcionales es importante controlar su morfología y estructura, y el objetivo principal es comprender la química de las superficies, ya muchos procesos físicos y químicos tienen lugar en las superficies. La morfología es una propiedad clave de los materiales.

La Figura 1.7 ilustra una representación esquemática del procedimiento que utilizaremos en la presente Tesis Doctoral, donde se comparan los resultados teóricos y experimentales. Según los métodos de síntesis seguidas, los materiales pueden presentar tamaño en la escala micro o nano, y una morfología bien definida. A partir de los parámetros estructurales obtenidos por los resultados experimentales, de difracción de rayos-X con refinamiento Rietveld, es posible construir el modelo teórico adecuado y mediante cálculos de primeros principios se puede determinar la geometría 3-D, sus frecuencias vibraciones, propiedades electrónicas y ópticas, como el "band gap", y mediante la caracterización de los estados electrónicos excitados se puede interpretar las emisiones fotoluminescentes. Por otra parte con el cálculo de las energías superficiales y la utilización de la construcción de Wulff, se puede determinar las morfologías accesibles de un determinado material, y comparar con las imágenes que se obtienen experimentalmente por microscopia electrónica *(*"field emsission scanning electron miscroscopy", FE-SEM), y así predecir el camino seguido durante la síntesis y qué superficies se deben estabilizar/desestabilizar para alcanzar una determinada morfología.

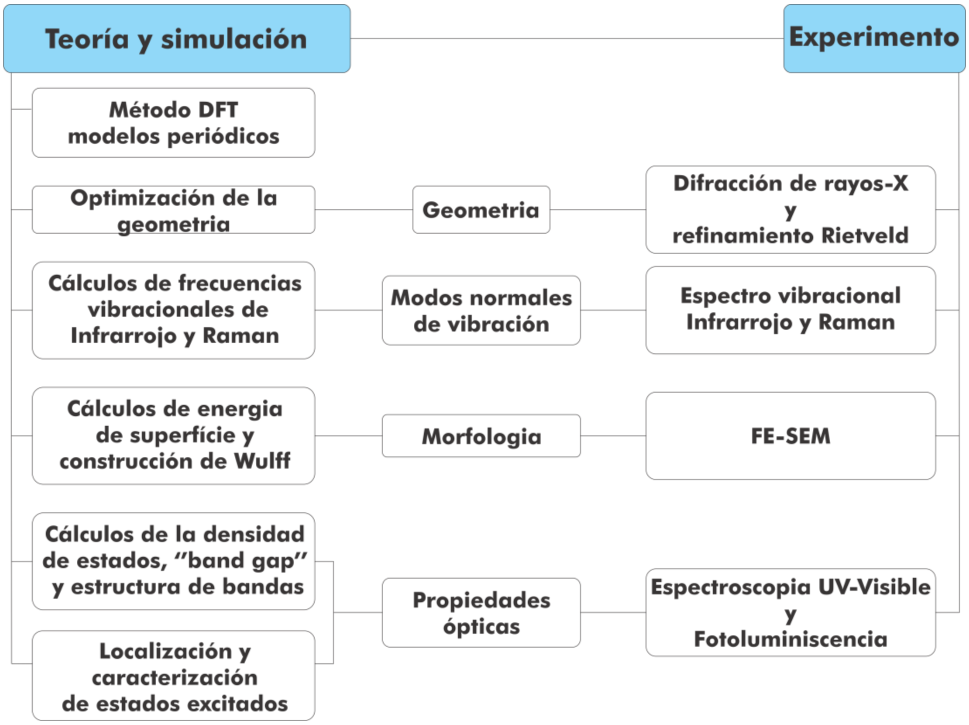

Figura 1.7. Representación esquemática de las propiedades que se pueden comparar a partir de los resultados teóricos y experimentales.

El objetivo de esta Tesis Doctoral ha sido alcanzar una investigación interdisciplinaria, tanto fundamental como aplicada, en óxidos ternarios complejo. Para obtener los resultados se utilizó un enfoque teórico y experimental para caracterizar y discutir mejor las estructuras y propiedades de los materiales; en particular la morfología, propiedades electrónicas y ópticas ("band gap" y emisiones de fotoluminiscencia) y se ha demostrado cómo los métodos y técnicas de la química teórica y computacional se pueden utilizar para comprender las propiedades físicas y químicas de estos materiales para buscar un diseño racional de los mismos.

2. Métodos teóricos y simulaciones computacionales

2.1. Métodos teóricos

La interacción entre electrones determina una gran parte de la estructura y propiedades de la materia, desde los átomos a los sistemas sólidos. En este contexto, la principal herramienta para tal descripción consiste en simulaciones computacionales basadas en la mecánica cuántica, más precisamente en la resolución de la ecuación de Schrödinger que permite el cálculo de las propiedades electrónicas del sistema en cuestión a partir de la obtención de la respectiva función de onda (Ψ).

$$\widehat{\mathbf{H}}\ \boldsymbol{\Psi} = \mathbf{E}\boldsymbol{\Psi} \tag{4}$$

donde Ψ representa la función de onda total del sistema, $\widehat{H}$ el operador Hamiltoniano y E la energía total del sistema.

2.1.1 Metodología DFT

Los métodos mecano-cuánticos más utilizados en el campo del estado sólido se basan en la teoría del funcional de la densidad (DFT). En los últimos 20 años los estudios que involucran el diseño de materiales se han concebido, principalmente debido al tratamiento más preciso de los efectos de intercambio y correlación, recursos computacionales más poderosos, algoritmos numéricos más eficientes y la introducción de numerosos paquetes libres y comerciales para el desarrollo de tales simulaciones [38, 171].

El foco central de la DFT es la densidad electrónica (ρ) que permite escribir la Ecuación de Schrödinger a través de una ecuación dependiente de ρ. La densidad electrónica total referente a los *N* electrones del sistema es definida como la suma de los cuadrados de las funciones de onda mono-electrónicas sobre todo el espacio:

$$\boldsymbol{\rho}(\mathbf{r}) = \mathbf{N} \int \dots \int |\boldsymbol{\Psi}(\mathbf{r_1}, \mathbf{r_2}, \dots, \mathbf{r_N})|^2 \mathbf{ds_1 dr_2} \dots, \mathbf{dr_N} \tag{5}$$

Esta densidad electrónica no es la base sólo para el desarrollo de la DFT, sino de todo un conjunto de métodos que estudian átomos y moléculas pudiendo ser medidos a través de análisis experimentales como difracción de electrones o de rayos X, en lugar de la función de onda utilizada en el método Hartree-Fock (HF). Además de ser un observable experimental, la densidad electrónica depende únicamente de 3 variables que definen la posición espacial y el volumen donde la densidad electrónica está concentrada, simplificando el complejo problema de la resolución de la ecuación de Schrödinger para múltiples cuerpos (N) basada, hasta entonces, en funciones de onda dependiente de 4N variables que dependen de las 3 coordenadas espaciales y de la coordenada de espín de cada electrón [38, 172-175] Así, el método DFT puede ser resumido como:

$$\boldsymbol{\rho}(\mathbf{r}) \rightarrow \boldsymbol{\Psi}(\mathbf{r_1}, \mathbf{r_2}, \dots, \mathbf{r_N}) \rightarrow \textbf{observables} \tag{6}$$

Las raíces de esta metodología están relacionadas con la Teoría desarrollada por Thomas-Fermi-Dirac para el gas de electrones libres y perfeccionada por Slater en los años 50. Sin embargo, la forma actual del método DFT fue fundamentada en 1964 por Pierre Hohenberg y Walter Kohn [171] mediante dos teoremas. Primeramente, ellos establecieran que para una determinada densidad electrónica del estado fundamental $\rho(r)$ es posible calcular la correspondiente función de onda para ese estado $\Psi_0(r_1,r_2,...,r_N)$. Esto significa que para un determinado sistema y su densidad electrónica del estado fundamental tenemos un único potencial externo (V_{ext}) probando que Ψ_0 es una función única de ρ, es decir, $\Psi_0[\rho]$ y, en consecuencia, todos los demás observables de estado fundamental (O) también son funcionales de ρ: [172-174, 176-180].

$$\langle \mathbf{O} \rangle[\boldsymbol{\rho}] = \langle \boldsymbol{\Psi_0}[\boldsymbol{\rho}] | \hat{\mathbf{O}} | \boldsymbol{\Psi_0}[\boldsymbol{\rho}] \rangle \tag{7}$$

En el segundo teorema, Hohenberg y Kohn muestran que la energía del estado fundamental puede ser obtenida a través del método variacional una vez que la energía total del estado fundamental (E_0) es minimizada solo para la correspondiente densidad electrónica del estado fundamental (ρ_0). Según el teorema variacional, tenemos que para una densidad electrónica de prueba ($\tilde{\rho}$) la energía total obtenida tiene que ser igual o superior a la energía del estado fundamental[172-174, 176-179]:

$$\langle \widetilde{\boldsymbol{\Psi}} | \widehat{\mathbf{H}} | \widetilde{\boldsymbol{\Psi}} \rangle = \mathbf{E}[\widetilde{\boldsymbol{\rho}}] \geq \mathbf{E}[\boldsymbol{\rho_0}] = \langle \boldsymbol{\Psi_0} | \widehat{\mathbf{H}} | \boldsymbol{\Psi_0} \rangle \tag{8}$$

Así pues, para obtener la densidad exacta del estado fundamental, tendremos que encontrar la densidad que minimiza la energía:

$$\left[\frac{\boldsymbol{\delta}\mathbf{E}[\boldsymbol{\rho}]}{\boldsymbol{\delta\rho}}\right] = \mathbf{0} \tag{9}$$

En 1965 Kohn-Sham [181] presentaron una propuesta innovadora que consistía en utilizar un sistema de ecuaciones monoelectrónicas y el método variacional para obtener la energía del estado fundamental de forma autoconsistente (Self Consistent Field, SCF). Ese método consiste en sistema de referencia con N electrones que no interaccionan entre ellos moviéndose bajo un potencial externo que genera una función de onda que tiene la misma densidad del sistema real. Para este sistema ideal, el método Hartree-Fock es exacto dado que no hay interacciones electrón-electrón y el operador de Fock (F_{HF}) contiene todas las informaciones para las energías cinéticas (T) de los electrones con la aproximación de Born-Openheimer y también las interacciones coulombicas con los núcleos (V). El problema es que F_{HK} no tiene relación directa con la densidad y los términos no-clásicos que restan del operador son añadidos como un término adicional. También, tenemos que las interacciones electrón-electrón pueden ser divididos en termos clásicos y non-clásicos. El término clásico se conoce como repulsión coulómbica entre las cargas de los electrones que disminuye con el cuadrado de la distancia entre ellos. De esta forma, la energía total del sistema puede ser descrita como una suma entre los componentes clásicos (energías cinética (T) y potencial (V)), repulsión electrónica (j) y un término no clásico que describe los términos de intercambio y correlación para la interacción electrónica (XC) así como la parte residual de T [172-174, 176-179].

$$\mathbf{E_{DFT} = E_T + E_V + E_j + E_{XC}} \tag{10}$$

Donde:

$$\begin{bmatrix} \mathbf{E_T = \sum_{i-1}^{n} \frac{-\nabla_i^2}{2}; E_V = \sum_i^n \sum_A^N \frac{-Z_A}{r_{iA}};} \\ \mathbf{E_j = \sum_i^n \sum_j^n \frac{1}{r_{ij}}; E_{XC} = \Delta\!< T_\rho > \; + \Delta\!< V_\rho^{ij} >} \end{bmatrix} \tag{11}$$

La inclusión del término de intercambio y correlación en la energía calculada por el método DFT convierte las ecuaciones de Kohn-Sham en exactas, una vez que se incluyen todos los componentes necesarios para la descripción del estado fundamental. Aunque los teoremas dicen que hay un funcional de intercambio y correlación para la densidad electrónica, éste es completamente desconocido de forma exacta, siendo necesario el uso de diferentes aproximaciones.

Por lo tanto, el método DFT se basa en la resolución de la Ecuación de Schrödinger utilizando los orbitales de Kohn-Shan y el operador H_{KS} que contiene todas las componentes de energía del sistema:

$$\mathbf{\hat{H}_{KS}\Psi_{KS} = E_{KS}\Psi_{KS}} \tag{12}$$

La resolución analítica utiliza el método KS-SCF (Kohn-Shan *Self Consistent Field*) donde la densidad electrónica determina los orbitales KS y por lo tanto la función de onda del estado fundamental que permite obtener las diferentes propiedades [172, 173, 176].

2.1.1.1. Funcionales de la densidad electrónica

El primer y más simple funcional propuesto se basa en la teoría del gas de electrones homogéneo para derivar funcionales de intercambio y correlación aproximados, denominado aproximación de la densidad de spin local (LDA/LSDA). En este caso, un sistema no homogéneo con densidad electrónica ρ(r) es tratado por la aproximación de $E_{XC}[\rho]$ por el valor correspondiente al gas de electrones homogéneo con densidad electrónica igual a ρ(r). En esta suposición se tiene que la densidad electrónica varía suavemente en las proximidades del punto r, como proponía Slater. A pesar de la no homogeneidad de la densidad electrónica, en átomos o moléculas las aproximaciones LSDA/LDA obtuvieron gran éxito en la descripción de estructuras en complejos de metales de transición y estado sólido [172, 173, 176].

Sin embargo, el funcional LSDA/LDA presenta serios problemas cuando se aplican a sistemas reales donde la densidad electrónica no es homogénea. La principal forma de corregir esta deficiencia se introduce a partir de las correcciones no locales basadas en el gradiente de la densidad electrónica (GGA). Esta aproximación es importante, principalmente para la previsión energética de reacciones químicas, siendo los funcionales PBE, PBESOL, Becke, PWGGA los más utilizados [155, 182-187].

La principal desventaja del uso de las funciones locales y semi-locales (LDA, LSDA, GGA) consiste en un error intrínseco denominado de auto-interacción. En líneas generales, este error se refiere a la posibilidad de interacción de los electrones con ellos mismos para los citados funcionales. Para representar tal efecto podemos utilizar un sistema monoelectrónico. En ese caso el término de intercambio y correlación de la DFT debe cancelar la repulsión Coulombiana, pero el trato de las aproximaciones locales y semi-locales generalmente es insuficiente para producir esa cancelación y, consecuentemente, hay un error en la representación de ese sistema. Este efecto también puede ser expandido a sistemas multielectrónicos donde puede causar errores significativos para la correcta representación de la densidad electrónica [174, 188, 189]. La única forma de corregir los funcionales semi locales y locales en relación con la no-localidad de Exc para el sistema con electrones no interactuantes es sustituir parte del término de intercambio de los funcionales semi locales por el término exacto proveniente del método HF [174, 175, 190]. Esta técnica se conoce como hibridación y da origen a los llamados funcionales híbridos. La existencia de estos funcionales es permitida por la conexión adiabática, método que permite la conexión de un sistema con electrones no interactuantes al sistema de N electrones que interactúan entre sí, de forma que la densidad electrónica permanezca igual a la densidad electrónica exacta.

La aproximación más simple para E_{XC} basada en la conexión adiabática fue propuesta por Becke en 1993, a partir de la interpolación linear entre las regiones interactuantes y no interactuantes, originando el denominado Funcional Híbrido *Half-Half* [191].

$$\mathbf{E_{xc} = \frac{1}{2}E_X^{HF} + \frac{1}{2}E_{XC}^{LSDA}} \tag{13}$$

En el mismo año, Becke propuso un nuevo funcional híbrido basado en la corrección de gradiente de la densidad electrónica para los términos de intercambio y correlación. Este funcional se denominó B3PW91, siendo su representación general:

$$\mathbf{E_{XC}^{B3PW91} = E_{XC}^{LSDA} + a\left(E_X^{exato} - E_X^{LSDA}\right) + b\Delta E_X^{B88} + c\Delta E_C^{PW91}} \tag{14}$$

En esta ecuación a, b y c representan coeficientes semiempíricos que pueden determinarse a partir de una minimización en relación a datos experimentales, siendo E_X^{exato} la energía exacta de cambio del sistema (HF), ΔE_X^{B88} la corrección de gradiente para la energía de cambio propuesta por Becke (1988) y ΔE_C^{PW91} la corrección de gradiente para la energía de correlación desarrollada por Perdew y Wang (1992). El segundo término de este funcional sustituye parte del término de intercambio obtenido del gas de electrones por el término exacto procedente del método HF. De esta forma, el coeficiente a refleja la importancia del sistema de electrones no interactuantes para la composición del término E_{XC}. El tercer y el cuarto término permiten una mezcla entre las correcciones de gradiente para los términos de intercambio y correlación. Este funcional fue aplicado a diferentes átomos y moléculas de la base de datos G1 de Pople [192] y a partir de la minimización de la E_{XC} en relación a las energías de atomización, afinidades protónicas y electrónicas, así como potenciales de ionización los coeficientes semiempíricos se determinaron como a= 0.2, b= 0.72 y c= 0.81, respectivamente [175, 193].

Frisch y colaboradores (1994) propusieron la sustitución del gradiente de correlación definido por Perdew y Wang (PW91) del funcional B3PW91 por el funcional desarrollado por Lee, Yang y Parr (LYP) en 1988 [194].

$$\mathbf{E_{XC}^{B3LYP}} = (\mathbf{1} - \mathbf{a})\mathbf{E_{X}^{LSDA}} + \mathbf{aE_{X}^{HF}} + \mathbf{b\Delta E_{X}^{B88}} + \mathbf{c\Delta E_{C}^{LYP}} + (\mathbf{1} - \mathbf{c})\mathbf{E_{C}^{VWN}} \quad (15)$$

Los coeficientes semiempíricos poseen los mismos valores que en el funcional B3PW91. La principal diferencia está en los dos últimos términos que implican la corrección de gradiente para el término de correlación. Como el funcional de LYP no tiene un componente local separable fácilmente, el funcional local para la correlación desarrollado por Vosko, Wilk y Nusair (VWN) fue utilizado para proporcionar diferentes contribuciones de los términos locales y corregidos por el gradiente. Este funcional se conoce como B3LYP y en los últimos años se ha convertido en uno de los más utilizados para el estudio de materiales, principalmente en estado sólido. La principal restricción a este funcional está en la representación de metales donde el límite de gas de electrones uniforme no se reproduce correctamente. Este error se produce porque el término local para la correlación utilizada en B3LYP reproduce superficialmente el lento decaimiento de la densidad electrónica en el límite del sistema no interactuante [175, 195-197].

Estos aspectos fueron corregidos por el funcional PBE0 propuesto por Perdew, Burke y Ernzherhof (PBE) y desarrollado por Adamo y Barone (1999). Este funcional se basa en el aumento del porcentaje del término de intercambio exacto al 25% asociado al término de intercambio y correlación PBE. En el término de intercambio y correlación corregido por el gradiente de Perdew, Burke y Ernzherhof el término referente al gradiente de la correlación se basa en el funcional de Perdew y Wang (PW91), así como para el B3PW91, posibilitando al funcional PBE0 la correcta predicción del límite de gas de electrones uniforme [175, 190, 198].

Aunque este funcional es muy aplicado a sólidos, el costo computacional en su tratamiento es elevado, principalmente debido al lento decaimiento de la parte correspondiente a las interacciones a largo alcance del término de intercambio y correlación. Para corregir esta limitación Janesko y los colaboradores propusieron un funcional, denominado HSE, en el que sólo las interacciones a corto alcance se tratan a nivel HF. En los últimos años este funcional ha ganado elevada aceptación en la comunidad científica [174].

A pesar de la aparición de un gran número de funcionales híbridos, el funcional B3LYP sigue siendo uno de los más utilizados debido a su capacidad de ser aplicado tanto a sistemas sólidos tanto en "bulk" como a superficies. Este hecho se debe a la excelente relación entre el coste computacional y la precisión en el cálculo de geometrías y propiedades electrónicas, "band gap" y densidad de estados, entre otros. [182, 184, 199-202].

2.2. Simulaciones computacionales

2.2.1. Densidad de estados y estructura de bandas

La periodicidad confiere a los sistemas cristalinos una estructura electrónica peculiar. Mientras en los átomos aparecen niveles discretos de energía, en las moléculas hay una combinación de estos. Sin embargo, en sistemas infinitos la separación entre niveles se puede despreciar y se obtiene una estructura de bandas, todas ellas resultantes de la interacción periódica de los electrones con los núcleos cargados del cristal.

Una vez se conoce la estructura de bandas del sólido, es necesario conocer la ocupación de cada una de ellas, es decir, cómo se acomodan los electrones en los niveles de energía. Como el cristal es finito y los niveles de energía son discretos, cada banda de energía podrá acomodar un número limitado de electrones. Conocido el número de electrones, cada una de las bandas podrá estar llena, vacía o parcialmente ocupada. Si consideramos únicamente las bandas que provienen de niveles de energía más externos o de valencia, banda de valencia (BV), el sólido se comportará como un *aislante* si el número de electrones es tal que las bandas de energía permitidas están llenas y el salto de energía entre bandas es grande. En este caso, ningún electrón puede moverse en presencia de un campo eléctrico. El sólido actuará como un *conductor metálico* si una o más bandas están parcialmente ocupadas. En un *semiconductor intrínseco* la diferencia de energía entre bandas es pequeña (~1-3 eV) como aparece representado en la Figura 2.1, de modo que un aumento de temperatura puede promocionar algunos electrones a la banda de conducción (BC). Asimismo, la presencia de átomos de impurezas en el material semiconductor intrínseco, genera un cristal extrínseco que puede ser del tipo n o p. Cuando en un cristal de Si puro se adiciona átomos pentavalentes (como As, Ge o Sb), los cuatro electrones de valencia de estos átomos forman enlaces covalentes con átomos de silicio vecinos, de forma que el quinto electrón se convierte en un electrón libre y el material pasa a ser un dador de electrones, caracterizando al material como un semiconductor del tipo n. En cambio, cuando en un cristal de Si puro se adiciona átomos trivalentes (como B, Ga o In), los tres electrones de valencia son incapaces de formar los cuatro enlaces, y pasando a ser un aceptor de electrones, caracterizando al material como semiconductor del tipo p.

En general, las diferentes propiedades de óxidos semiconductores pueden ser explicadas por un mecanismo que involucra la absorción de luz que resulta en la excitación de electrones localizados en la BV hacia la BC, originando un par electrón-hueco (e-h), seguido por un decaimiento electrónico espontáneo que permite la emisión de fotones [203].

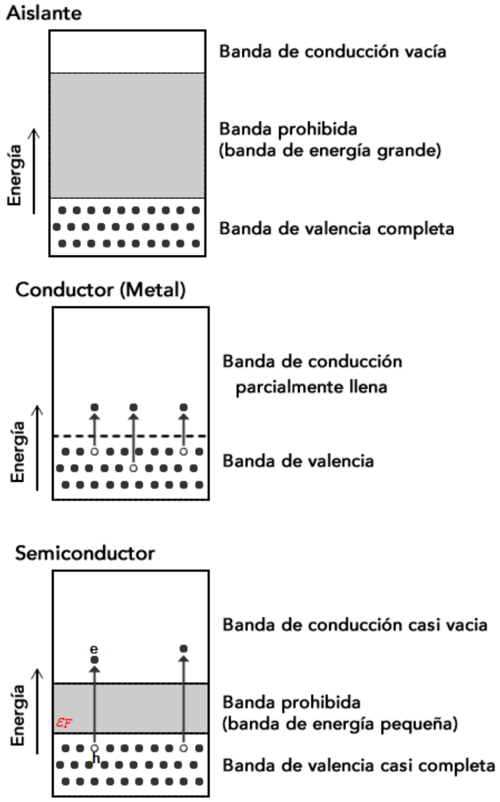

Figura 2.1. Estructura de bandas de un sólido (metal y semiconductor) y distribución de los electrones en los niveles de energía de la banda de valencia y de conducción.

Además de conocer la energía de los niveles, debemos conocer su población, lo que se consigue mediante el cálculo de la densidad de estados (DOS). El DOS representa el número de niveles permitidos por unidad de volumen del sólido, en un rango de energía ε y $\varepsilon+d\varepsilon$, y puede proyectarse sobre unos determinados átomos y/o orbitales, de manera que se puede analizar la contribución de los diferentes átomos y orbitales a cada banda.

Para una capa cerrada, cada banda está ocupada por $2N$ electrones, siendo N el número de celdas. Si cada celda tiene n electrones, las $n/2$ bandas de menor energía estarán ocupadas y separadas de las de mayor energía por un “gap”. Si el sistema es de capa abierta o si hay cruzamiento entre las bandas, más de $n/2$ bandas estarán parcialmente ocupadas. La *energía de Fermi*, ε_F, es aquella en la que el número de niveles con una energía inferior a ε_F es igual a la mitad del número de electrones. De esta forma, en los conductores, el nivel de Fermi se situará dentro de la banda de conducción, estando ocupados todos los niveles por debajo del nivel de Fermi y no habiendo electrones con energía superiores a ε_F. En los semiconductores, el nivel de Fermi estará forzosamente en la banda prohibida entre la de conducción y la de valencia.

Basándonos en lo anterior, se puede decir que las propiedades electrónicas de los sólidos dependerán de las energías de las bandas, de su amplitud y de las regiones prohibidas entre ellas.

2.2.2. Estados electrónicos excitados

Los fenómenos ópticos asociados con la interacción radiación-materia involucran necesariamente la participación de los estados excitados que son poblados debido a la absorción de uno o más fotones por un sistema (cristal) en estado fundamental hacia un nivel de energía superior que corresponde al estado excitado. De esta forma, la estructura y la distribución electrónica de los diferentes estados tanto del fundamental como de los excitados es de fundamental importancia para entender las propiedades ópticas, como la fotoluminiscencia. Sin embargo, las emisiones fotoluminiscentes son de corta duración y los estados electrónicos excitados son altamente inestables y reactivos, haciendo que su caracterización y manipulación sean extremadamente complicadas desde un punto de vista experimental.

Una herramienta alternativa para superar las dificultades encontradas en los experimentos consiste en emplear métodos teóricos y modelos computacionales, basados en la mecánica cuántica, para localizar y describir estos estados excitados, con el objetivo de determinar su geometría y la estructura electrónica y, por lo tanto, proponer un mecanismo que permita explicar las emisiones comportamiento fotoluminiscentes.

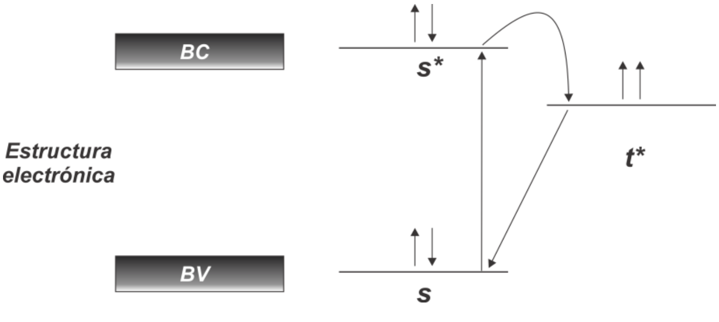

Figura 2.2. Representación de la estructura electrónica de un semiconductor, utilizando los conceptos de BV y BC (izquierda), y los estados electrónicos fundamental, s y excitados singlete, s*, y triplete, t*(derecha).

Desde el punto de vista teórico, la modelización y caracterización de los estados electrónicos excitados y sus propiedades un reto para los métodos basados en la DFT, pues esta metodología corresponde a una teoría de estado fundamental. La combinación entre el método DFT convencional y restricciones adicionales sobre la densidad de carga, permite la obtención de un funcional de densidad adecuado para sistemas que requieren configuraciones electrónicas específicas. Así, se puede calcular la estructura electrónica de materiales en diferentes estados fundamental, normalmente singlete, y excitados (singlete y triplete), facilitando el estudio de las excitaciones electrónicas de óxidos semiconductores [204, 205].

El desarrollo de estas simulaciones requiere una ruptura de la simetría entre las ocupaciones electrónicas de los spin-orbitales, permitiendo la existencia de estados spin-polariza dos. En el caso de un estado singlete excitado, esta perturbación elimina la degeneración de los spin-orbitales a los niveles ocupados de mayor energía sin alterar la multiplicidad del modelo. Un estado electrónico excitado triplete requiere una redistribución electrónica que resulta en diferentes ocupaciones de los spin-orbitales ($n_\alpha \neq n_\beta$). Este tratamiento permite que la naturaleza de los estados electrónicos excitados y sus respectivas geometrías puedan ser caracterizadas y analizadas, haciendo posible la descripción de los mecanismos de transferencia de carga entre los clústeres que constituyen la estructura cristalina del estado fundamental y de los estados excitados así como su relación con los efectos de orden-desorden, tanto estructurales como electrónicos, como se muestra en la Figura 2.2.

La evaluación de la estructura electrónica mediante los análisis de DOS y estructura de bandas permite que la excitación electrónica pueda ser descrita por etapas. Así, la transferencia electrónica puede ser comprendida a partir de la localización de electrones y huecos en clústeres, que corresponden a las coordinaciones locales de los diferentes metales A y B, que constituyen la red 3-D. El análisis estructural y electrónico de los diferentes clústeres y sus modos de vibración, tanto del estado electrónicos fundamental como excitados, permiten describir las distorsiones estructurales que se originan de las transiciones electrónicas entre orbitales enlazantes y no enlazantes.

Estudios anteriores, basados en ese tratamiento teórico, permitieron racionalizar el comportamiento fotoluminiscente del $SrTiO_3$, evidenciando que la estabilización de los estados electrónicos excitados (singlete excitado y triplete) es acompañada por una distorsión tetragonal en clústeres de titanio,

$[TiO_6]$ a $[TiO_5.V_O]$, caracterizando una transición orden-desorden .[206]. Posteriormente, esta metodología fue aplicada para estudiar las propiedades luminiscentes del sistema $CaWO_4$, comprobando que los estados excitados que resultan en la emisión fotoluminiscente se obtienen a partir de una distorsión en los clústeres $[CaO_8]$ y $[WO_4]$ [207]. Recientemente, este método ha sido ampliamente aplicado para la racionalización de comportamientos fotoluminiscentes en diferentes clases de materiales, como $SrTiO_3$:Sm, $BaZr_{1-x}Hf_xO_3$, $BaZrO_3$, como se muestra en la Figura 2.3, presentando un excelente acuerdo con resultados experimentales [208-211].

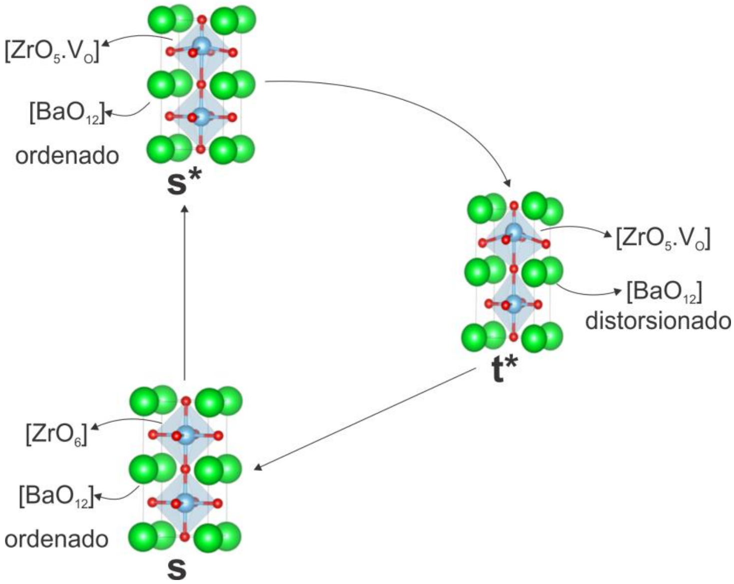

Figura 2.3. Celda unidad para estructuras s, s* y t* del sistema $BaZrO_3$.

2.2.3. Cálculos de las propiedades estructurales y electrónicas

Para el cálculo y la optimización de las geometrías y estructuras 3-D de los materiales que estudiamos, partimos de la geometría obtenida por la difracción de Rayos X y refinamiento Rietveld, cuya posición de los diferentes átomos constituyentes en la red cristalina se conoce. Para el cálculo de la estructura 3-D más estable es necesario minimizar la energía total, por medio de la optimización de los parámetros de red y coordenadas de los átomos. Los criterios de convergencia utilizados fueron de 10^{-8} Hartree y se utilizó un mallado de puntos k adaptado a las dimensiones de cada sistema [212].

En nuestros trabajos se describen los centros atómicos utilizando los conjuntos de bases pseudopotenciales para los átomos de Mo y Eu [213, 214] en $BaMoO_4$, $CaMoO_4$, $ZnMoO_4$, $ZnMoO_4$:Eu^{3+} y $CaZrO_3$:Eu^{3+}, respectivamente. Además conjuntos de base pseudopotencial derivado de Hay y Wadt y modificado por Cora *et al.* [215] se usan para la descripción del átomo W en $BaWO_4$. Mientras que átomos de Ba [216], átomos de O [217], átomos de Ca [218], átomos de Zn [219] y átomos de Zr [220] se describen mediante conjuntos de bases 6-31G*, respectivamente.

Los modelos computacionales se han construido usando una celda convencional 1x1x1, como unidad repetitiva para representar las estructuras 3-D del "bulk" de los sistemas puros $BaWO_4$ y $BaMoO_4$ y solución solida $BaW_{1-x}MoxO_4$ (x =0.25, 0.50 y 0.75). Los modelos de superficies resultantes en $BaWO_4$ y $BaMoO_4$ consistieron en 4 unidades moleculares que contienen 24 átomos. Sin embargo, los modelos de superficie en la solución solida $BaW_{1-x}MoxO_4$ (x =0.25, 0.50 y 0.75) consistieron en 4, 4, 4, 8, 4 y 4 unidades moleculares para las superficies (001), (101), (110), (100), (111) y (112), respectivamente, simétricas y estequiométricas. Además, con el fin de investigar la distribución energética de los cationes de W^{6+} por Mo^{6+} en la solución sólida, se exploraron varias posiciones de sustitución en la celda convencional 1x1x1 para cada porcentaje estudiado, analizando las más estables.

Para el cálculo del "bulk" y de las superficies del $CaMoO_4$ con la estructura scheelita y simetría tetragonal se siguió el mismo procedimiento. El $ZnMoO_4$ presenta una estructura tipo wolframita con simetría triclínica como ya se ha descrito en la figura 1.2. Este estudio surge de una colaboración experimental en la que se ha dopado este material con tierras raras (TR) en los porcentajes de $ZnMoO_4$:TR^{3+} (TR^{+3}= 1% Tb, 1% Tm, x%Eu (x=1, 1.5, 2, 2.5 y 3%) en mol. Como el porcentaje de dopaje de TR es muy pequeño, es necesario utilizar tamaños de celdas muy grandes para simular estos sistemas, lo que hace que su cálculo sea muy costoso desde el punto de vista computacional. Por esta razón, solo hemos podido alcanzar un dopaje de 12.5% para $ZnMoO_4$:Eu^{3+}. La sustitución de los cationes Eu^{3+} por cationes Zn^{2+} genera un desequilibrio en las cargas dentro de la estructura cristalina de $ZnMoO_4$, debido a que los estados de oxidación de los cationes son diferentes. Para mantener la neutralidad del sistema, se reemplazan 2 cationes de Eu^{3+} por 2 cationes de Zn^{2+}, con la creación de una vacante de Zn^{2+}. De este modo, se ha modelizado una supercelda triclínica 1×2×2 con 144 y 143 átomos en los materiales $ZnMoO_4$ y $ZnMoO_4$:Eu^{3+}, respectivamente. El mismo número de átomos se ha utilizado para el estudio de las superficies (120), (011), (001), (201), (220), (100), (111) y (112) en ambos sistemas. Se exploraron varias posiciones de sustitución en el “bulk” como en las superficies, analizando las más estables.

Caracterizar la estructura y la distribución electrónica de los estados fundamental como de los excitados es clave para entender las propiedades ópticas, como la fotoluminiscencia que presenta el $CaZrO_3$. El $CaZrO_3$ presenta una estructura ortorrómbica, y se ha modelizado la transformación del estado fundamental s a al estado excitado s* mediante un desplazamiento de 0.2 Å a lo largo de la dirección (001) en un 25% de los átomos de zirconio. Sin embargo, la transformación del estado fundamental s a un estado excitado triplete t* se obtiene realizando el mismo desplazamiento pero produciéndose otras distorsiones en la estructura debido a cambios en la multiplicidad de spin. Las superficies generadas para el estado fundamental contienen 8 unidades moleculares (en estado singlete) y 4 unidades moleculares (en estado de triplete) para (121), (100), (010), (101), (001), (111) y (011) superficies, respectivamente.

Para el dopaje del $CaZrO_3$ con Eu^{3+}, se hace necesaria la construcción de un modelo de supercelda convencional 2x1x2 para simular el dopaje a la concentración de 12.5%. Para mantener la neutralidad del sistema, se reemplazan 2 cationes de Eu^{3+} por 2 cationes de Ca^{2+}, con la creación de una vacante de Ca^{2+}. El modelo de supercelda corresponde a 79 átomos tanto para el “bulk” como para las superficies (001), (121), (100), (011), y (111).

Para confirmar la geometría de los estados electrónicos fundamental y excitados singlete y triplete de todos los sistemas estudiados, se comprobó que cumplen la condición de mínimo en las diferentes superficies de energía potencial, a la vez que se aseguró que las frecuencias vibracionales, asociadas a los modos normales de vibración, presentaban valores positivos.

El estudio de las propiedades electrónicas del “bulk” y de las superficies en los trabajos descritos en el apartado anterior, se realizó a través del análisis de las estructuras de bandas y DOS proyectado en átomos y orbitales atómicos. En el análisis de las estructuras de bandas de energía se consideraron las 10 últimas bandas en la BC y las 10 primeras bandas en la BV, de acuerdo con los puntos k correspondientes para cada sistema en la primera zona de *Brillouin* como se presenta en la Figura 2.4. Asimismo, la diferencia de energía generada entre las bandas BV y BC, la llamada energía de “gap” (“band gap”), se calculó para el “bulk” y superficies.

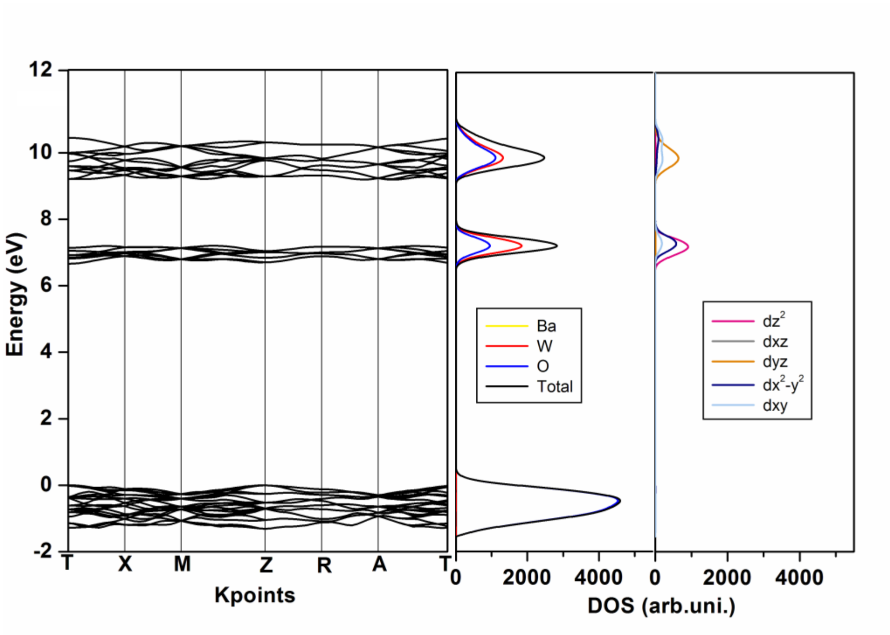

Figura 2.4. (a) Estructura de bandas y (b) DOS, proyectado en átomos y orbitales atómicos. Se han considerado las 10 últimas bandas en la BC y las 10 primeras bandas en la BV.

2.2.4. Cálculo de las propiedades ópticas: fotoluminiscencia

La evaluación de las propiedades ópticas se llevó a cabo utilizando los conceptos de la teoría de estados excitados descritos en el apartado 2.2.2 de esta tesis doctoral, como una forma de investigar las propiedades fotoluminescentes de los materiales $CaZrO_3$ y $CaZrO_3:Eu^{3+}$.

Para estos estudios se utilizaron las geometrías ordenada y desordenada como describimos en el apartado 2.4.1.4, y posteriormente se procede al cálculo de los estados excitados singlete y triplete. El estado singlete excitado se calculó usando la geometría optimizada desordenada con un sistema de capa abierta y a continuación para el cálculo de triplete excitado fue necesaria una supercelda optimizada en un sistema de capa abierta y diferencia de espín α-β igual a 2. Adicionalmente, se utilizaron mapas de densidad de espín para evaluar y localizar los electrones desapareados.

Conjuntamente, el análisis vibracional de los modos Raman.a nos permite establecer un mecanismo que permite explicar el paso del estado electrónico fundamental a los excitados excitados singlete y triplete.

2.2.5. Programas de cálculo y visualización.

En esta Tesis Doctoral se ha utilizado el paquete de programa de cálculo CRYSTAL versión 2014 [221], que permite realizar cálculos periódicos desde 0, 1, 2 ("slabs" bi-dimensionales), y a 3 dimensiones (cristales). Para describir los átomos, los orbitales cristalinos se expresan como combinación lineal de productos de funciones gaussianas con diferentes exponentes, que dependen del número y tipo de átomos que contiene la celda unidad. El conjunto de bases puede englobar todos los electrones o puede representarse mediante pseudopotenciales, donde parte de los electrones quedan englobados en el "*core*" del átomo y no se tratan como electrones de valencia[222]. Los archivos de salida CRYSTAL14, contienen las coordenadas fraccionarias optimizadas y los parámetros de celda 2D optimizados para las diferentes surperficies de los sistemas que estudiamos. Todas estos "slabs" poseen carga neutral y retienen el centro de inversión o el plano del paralelo a la supeficie (hkl), para asegurar que el momento dipolar del "slab" es cero. [153, 154].

Las figuras utilizadas en la creación de los mapas morfológicos, se construyeron de acuerdo con el teorema de Wulff con la ayuda del programa Visualization for Electronic and Structural Analysis (VESTA) [223], que se implementó una forma de crear morfología de nano(cristales) por medio de las distancias de los planos hasta el centro del cristal. Esta distancia es directamente proporcional a la modulación de energía.

Mediante el uso del programa JICE [224] se permite la visualización y clasificación los modos normales de vibración .

Los mapas de densidad de spin para evaluar y localizar los electrones desapareados en $CaZrO_3$ y $CaZrO_3:Eu^{3+}$ se han dibujado utilizando el programa X-Window Crystalline Structures and Densities (XCrySDen) [225]. Las figuras correspondientes al DOS y estructura de bandas de han obtenido con el programa ORIGINLab.

Un esquema representativo de los cálculos periódicos utilizando el programa CRYSTAL y los programas de visualizaciones se muestra en la Figura 2.5.

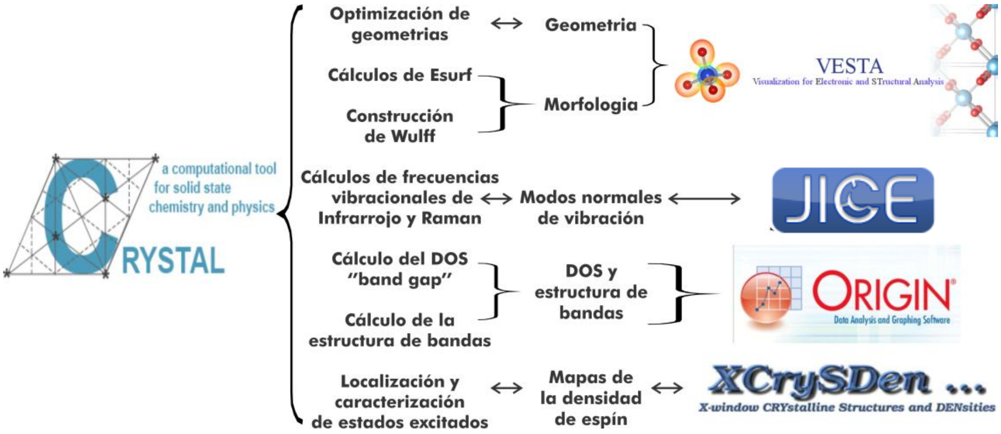

Figura 2.5. Esquema de los programas de cálculo y visualización utilizados, con indicación de las propiedades calculadas con el programa CRYSTAL y visualizadas en los diferentes programas VESTA, JICE, ORIGINLab y XCrySDen.

3. Objetivos

Los objetivos de la presente Tesis Doctoral se pueden dividir en generales y específicos:

Generales

- Proporcionar una guía científica para el control morfológico de la síntesis de (nano)materiales.
- Desarrollar un modelo termodinámico universal para predecir la morfología accesible de un material dado (nano). La modulación morfológica de cristales tridimensionales se ha demostrado utilizando la teoría del funcional de densidad para realizar a cabo los cálculos de primeros principios.
- Obtener mediante el uso del modelo y mediante el cambio de los valores relativos de las energías superficiales, tanto la morfología deseada como del camino que une la morfología ideal (más estable) a la morfología que se encuentra experimentalmente, que depende del método y las condiciones de la síntesis. Esta estrategia nos permite el control de las morfologías cristalinas, así como racionalizar los diferentes canales que parten de la morfología ideal.
- Este análisis combinado da lugar a un mapa completo de las morfologías accesibles en una amplia gama de (nano) materiales, y puede servir como una guía para que los investigadores, al analizar las imágenes de microscopía electrónica, obtengan una mayor comprensión de cómo controlar la forma del cristal sintéticamente ajustando la química de la superficie y controlando los valores relativos de las energías superficiales.
- Utilizar los métodos teóricos y modelos computacionales basados en la mecánica cuántica, para localizar y describir estados excitados, con el objetivo de determinar su geometría y la estructura electrónica y, por lo tanto, predecir y explicar las emisiones fotoluminiscentes de los (nano)materiales.

Específicos

Las morfologías de algunos materiales scheelitas, wolframitas y perovskitas se manifiestan bajo diversas condiciones de preparación, como son el molibdato de bario ($BaMoO_4$), wolframato de bario ($BaWoO_4$), soluciones sólidas $BaW_{1-x}Mo_xO_4$ (x= 0.25, 0.5, 0.75), molibdato de calcio ($CaMoO_4$), molibdato de zinc ($ZnMoO_4$), y zirconato de calcio ($CaZrO_3$). Estos son los materiales que investigaremos en la presente Tesis Doctoral en la que los siguientes objetivos específicos se pueden resumir del siguiente modo:

- Estudiar la influencia de la sustitución de los cationes de W^{6+} por Mo^{6+} en la solución solida completa $BaW_{1-x}Mo_xO_4$ (x= 0, 0.25, 0.5, 0.75 y 1) en función de las propiedades estructurales, electrónicas, ópticas, frecuencias vibracionales y morfologías calculadas. Comparar todo ello con la parte experimental realizada a través de la microscopía electrónica.
- Analizar la estructura y propiedades electrónicas de $CaMoO_4$, la estabilidad de las correspondientes superficies y sus transformaciones morfológicas.
- Investigar la influencia del dopante Eu^{3+} en la matriz de $ZnMoO_4$, tanto en la geometría, estructura electrónica como en la morfología en función del análisis comparativo de los cálculos teóricos con la microscopía electrónica.
- Comprender los espectros de fotoluminiscencia basados en la localización y caracterización de los estados electrónicos fundamental (singlete, s) y excitados (singlete, s* y triplete, t*), utilizando estructuras ideales y distorsionadas de $CaZrO_3$ puro y dopado con Eu^{3+}. Además, correlacionar sus correspondientes geometrías, morfologías, estructuras electrónicas y frecuencias vibracionales.

4. Resultados y discusiones

La presente Tesis Doctoral ha sido el resultado de diferentes colaboraciones entre el Laboratorio de Química Teórica y Computacional (LQTC) y el Centro de Desenvolvimento de Materiais Funcionais (CDMF), en la Universidade Federal de São Carlos (UFSCar) y el Laboratório de Síntese Química de Materiais (LSQM) del Departamento de Materiais de la Universidade Federal do Rio Grande do Norte (UFRN). Ha dado lugar a las siguientes publicaciones en las que se indica mi contribución así como del resto de coautores:

I. Título: Synthesis and morphological transformation of $BaWO_4$ crystals: Experimental and theoretical insights
Autores: Marisa Carvalho Oliveira, Lourdes Gracia, Içamira Costa Nogueira, Maria Fernanda do Carmo Gurgel, Jose Manuel Rivas Mercury, Elson Longo, Juan Andrés.
Revista: *Ceramics International* **2016**, 42, 10913-10921. (Material Science, Ceramics, Q1)

II. Título: On the morphology of $BaMoO_4$ crystals: A theoretical and experimental approach.
Autores: Marisa Carvalho Oliveira, Lourdes Gracia, Içamira Costa Nogueira, Maria Fernanda do Carmo Gurgel, Jose Manuel Rivas Mercury, Elson Longo, Juan Andrés.
Revista: *Crystal Research and Technology* **2016**, 51, 634-644. (Crystallography, Q4)

III. Título: Geometry, electronic structure, morphology and photoluminescence emissions of $BaW_{1-x}Mo_xO_4$ (x=0, 0.25, 0.50, 0.75, and 1) solid solutions: theory and experiment in concert.
Autores: Marisa Carvalho Oliveira, Juan Andrés, Lourdes Gracia, Michelle Suzane M. P. de Oliveira, Jose Manuel R. Mercury, Elson Longo, Içamira Costa Nogueira.
Revista: Enviado para su publicación a la revista *Applied Surface Science*. (Materials Science, Coatings & Films, Q1).

IV. Título: Crystal Growth: Concepts, Mechanisms and Applications: Analysis for the Morphology Prediction of Materials from First Principles Calculations
Autores: Marisa Carvalho Oliveira, Thiago Martins Duarte, Lourdes Gracia, Elson Longo, Juan Andrés.

Livro*: Nova Science Publishers* (**2017**).ISBN**:** 978-1-53612-226-8.

Las síntesis y caracterizaciones experimentales descritas en estos cuatro trabajos se realizaron en el CDMF por la Dra. I. C. Nogueira y supervisión del Prof. E. Longo. El Dr. J. M. Rivas Mercury del Instituto Federal do Maranhão ayudo en la presentación y discusión de los resultados experimentales de los artículos I, II, y III. La Dra. M. F. C. Gurgel de la Universidad Federal de Goiás ayudo en la presentación y discusión de los resultados experimentales de los artículos I y II. El estudiante de doctorado T.M. Duarte, que realizo una estancia predoctoral de un año en el LQTC, participó en el capítulo del libro (contribución IV), en particular en el estudio del sistema $BaSnO_3$. El Prof. Dr. J. Andrés y la Dra. Lourdes Gracia propusieron, planificarón y ayudaron en la realización de los cálculos, y junto con el Prof. Dr. Elson Longo en la redacción final de estos cuatro trabajos. Mi participación se ha centrado en la realización de los cálculos en el LQTC, análisis y discusión de los resultados teóricos, preparación de las figuras y tablas, la revisión bibliográfica y la redacción de los cuatro manuscritos.

V. Título: Experimental and theoretical study to explain the morphology of $CaMoO_4$ crystal.
Autores: Fernanda Karine Fonseca de Oliveira, Marisa Carvalho Oliveira, Lourdes Gracia, Ricardo Luis Tranquilin, Carlos Alberto Paskocimas, Fabiana Villela da Motta, Elson Longo, Juan Andrés, Mauricio Roberto Bomio Delmonte.
Revista: *Journal of Physics and Chemistry of Solids* **2018**, 114, 141-152. (Chemistry, Multidisciplinary, Q2).

VI. Título: Structure, morphology and photoluminescence emissions of $ZnMoO_4$: RE^{3+}= Tb^{3+} - Tm^{3+} - x Eu^{3+} (x = 1, 1.5, 2, 2.5 and 3 mol %) particles obtained by the sonochemical method.
Autores: Laura Ximena Lovisa, Marisa Carvalho Oliveira, Juan Andrés, Lourdes Gracia, Maximo Siu Li, Elson Longo, Ricardo Luis Tranquilin, Carlos Alberto Paskocimas, Fabiana Villela da Motta, Mauricio Roberto Bomio Delmonte.
Revista: *Journal of Alloys and Compounds.* **2018**, 750, 55-70. (Materials Science, Multidisciplinary, Q1)

Las síntesis y caracterizaciones experimentales descritas en estos trabajos se realizaron en el Laboratório de Síntese Química de Materiais, por la estudiante de grado F.K.F Oliveira en $CaMoO_4$ y por la estudiante de doctorado. L. X. Lovisa en $ZnMoO_4$: RE^{3+}= Tb^{3+} - Tm^{3+} - xEu^{3+} (x = 1, 1.5, 2, 2.5 and 3) y supervisión de los Dr. M.R. Bomio, Dr. F.V. Motta, Dr. C.A. Paskocimas de la Universidad Federal del Rio Grande del Norte en los artículos V y VI. El Prof. Dr. M. S. Li de la Universidad de São Paulo en Sao Carlos realizó las medidas de espectroscopia de fotoluminiscencia en el artículo VI. El Dr. R. L. Tranquilin de la Universidad Federal de São Carlos obtuvo las imágenes de la microscopía electrónica de barrido de emisión de campo en el artículo V y VI. El Prof. Dr. J. Andrés y la Dra. Lourdes Gracia propusieron, planificarón y ayudaron en la realización de los cálculos, y junto con el Prof. Dr. Elson Longo en la redacción final de estos dos trabajos. Mi participación se ha centrado en la realización de los cálculos en el LQTC, análisis y discusión de los resultados teóricos, preparación de las figuras y tablas, la revisión bibliográfica, y la redacción de los dos manuscritos.

VII. Título: Mechanism of photoluminescence in intrinsically disordered $CaZrO_3$ crystals: First principles modeling of the excited electronic states.

Autores: Marisa Carvalho Oliveira, Lourdes Gracia, Marcelo Assis, Ieda Lúcia Viana Rosa, Maria Fernanda do Carmo Gurgel, Elson Longo, Juan Andrés.

Revista: *Journal of Alloys and Compounds* **2017**, 722, 981-995. (Materials Science, Multidisciplinary, Q1)

VIII. Título: Study of the energetic, morphological and photoluminescent properties of $CaZrO_3$:Eu^{3+}. An experimental and theoretical insight.

Autores: Marisa Carvalho Oliveira, Lourdes Gracia, Marcelo Assis, Ieda Lúcia Viana Rosa, Maria Fernanda do Carmo Gurgel, Elson Longo, Juan Andres.

Revista: Preparado para enviar a publicación.

Las síntesis y caracterizaciones experimentales descritas en estos trabajos se realizaron en el CDMF por el estudiante de doctorado M. Assis y supervisión del Prof. Dr. E. Longo. La Dra. I. L. V. Rosa de la Universidad Federal de São Carlos y la Dra. M. F. C. Gurgel de la Universidad Federal de Goiás ayudo en la presentación y discusión de los resultados experimentales de los artículos VII y VIII. El Prof. Dr. J. Andrés y la Dra. Lourdes Gracia propusieron, planificarón y ayudaron en la realización de los cálculos, y junto con el Prof. Dr. Elson Longo en la redacción final de estos cuatro trabajos. Mi participación se ha centrado en la realización de los cálculos en el LQTC, análisis y discusión de los resultados teóricos, preparación de las figuras y tablas, la revisión bibliográfica y la redacción de los dos manuscritos.

En este capítulo presentaremos y discutiremos de forma resumida los resultados más relevantes que serán divididos en cuatro apartados, de acuerdo con los trabajos derivados de la presente Tesis Doctoral.

4.1. Artículos I, II, III y IV.

Tanto el $BaWO_4$, $BaMoO_4$ y las soluciones sólidas $BaW_{1-x}Mo_xO_4$ (x=0, 0.25, 0.50, 0.75, 1) presentan la estructura tetraédrica con grupo espacial I41/a. Esto nos permite realizar el resumen considerando los resultados de la solución sólida. El análisis de los valores de los parámetros de red (*a* y *c*), que se obtienen tanto por refinamento Rietveld como de los cálculos teóricos, señalaron la existencia de distorsiones electrónicas y estructurales en los clústeres [WO_4], [MoO_4] [BaO_8] así como cambios en el parámetro de red y reducción de volumen de la celda unidad, debido el efecto de la sustitución de cationes de W^{6+} por Mo^{6+}.

La celda unidad convencional scheelita $BaMO_4$ (M= W o Mo) contiene 24 átomos que se muestra en las Figuras 4.1(a-e). Hay cuatro cationes W en la estructura generada a partir de la posición 4a Wyckoff por simetría, con el fin de investigar la energía de la distribución del catión Mo^{6+}. Con el objetivo de encontrar la posición en la que la sustitución de W^{6+} por Mo^{6+}, se exploraron las diferentes posibilidades y se encontró que la disposición más estable en $BaW_{1-x}Mo_xO_4$ (x = 0.25, 0.50, 0.75) presentado en las Figuras (4.1b-d).

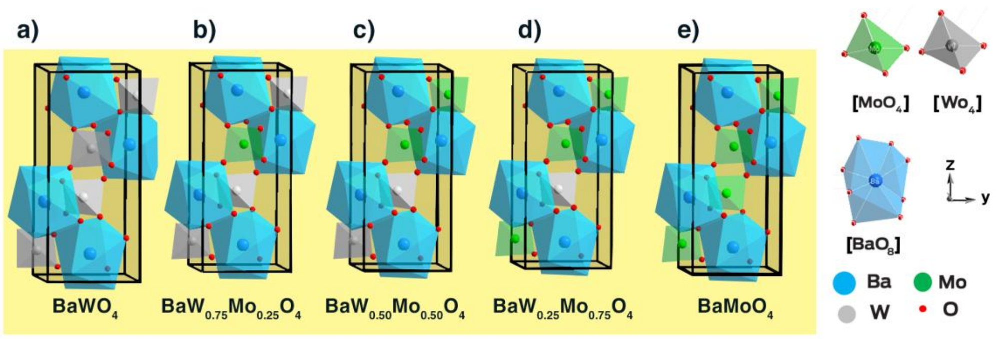

Figura 4.1. Representación de celdas unidad de cristales $BaW_{1-x}Mo_xO_4$: (a) x=0, (b) x=0.25, (c) x =0.50, (d) x =0.75 y (e) x =1.

Adicionalmente, las superficies se modelaron mediante la estructura del “bulk” y utilizando las descripciones del apartado 2.2.3. Los planos cristalográficos de las soluciones solidas de cristales $BaW_{1-x}Mo_xO_4$ (x=0, 0.25, 0.50, 0.75, 1) se representan en la Figura 4.2.

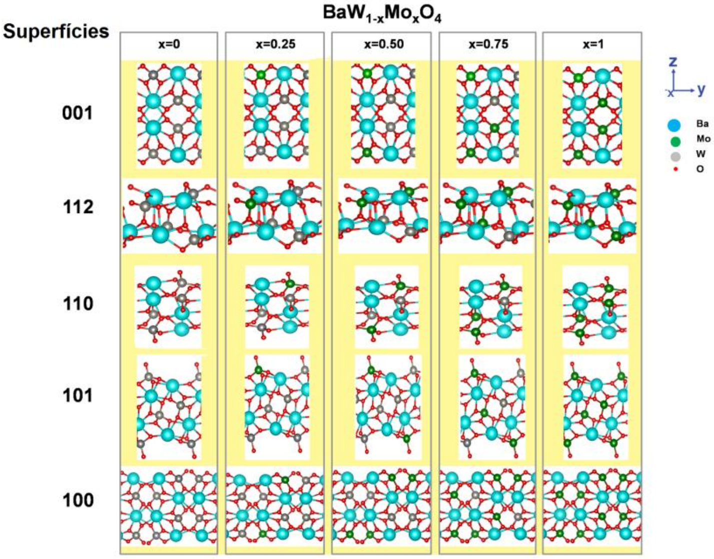

Figura 4.2. Representaciones esquemáticas de las diferentes superficies de soluciones sólidas $BaW_{1-x}Mo_xO_4$ (x = 0, 0.25, 0.50, 0.75 y 1).

Los espectros Raman se han interpretado mediante el análisis de los modos de vibración activos, en particular los asociados a los tetraedros $[MO_4]^{2-}$ (M = M o W) presentes a altas frecuencias (927cm^{-1} en $BaWO_4$ y 894 cm^{-1} en $BaMoO_4$), que se muestran en las Figuras 4.3(a-b).

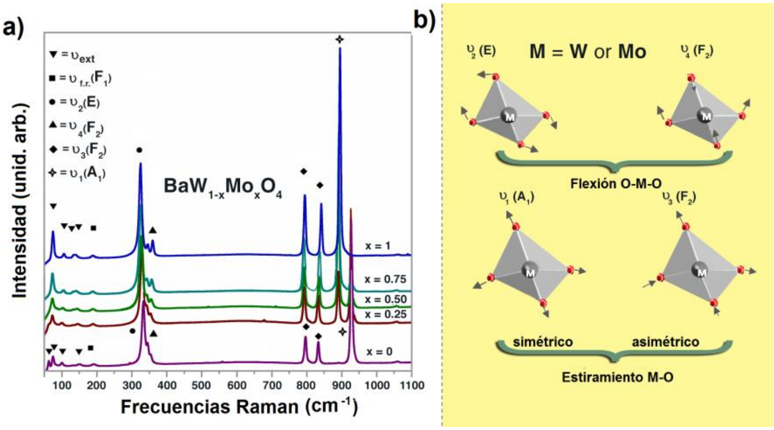

Figura 4.3. (a) Espectro Raman experimental y (b) representación de los modos normales Raman de las soluciones sólidas $BaW_{1-x}Mo_xO_4$ (x = 0, 0.25, 0.50, 0.75 y 1).

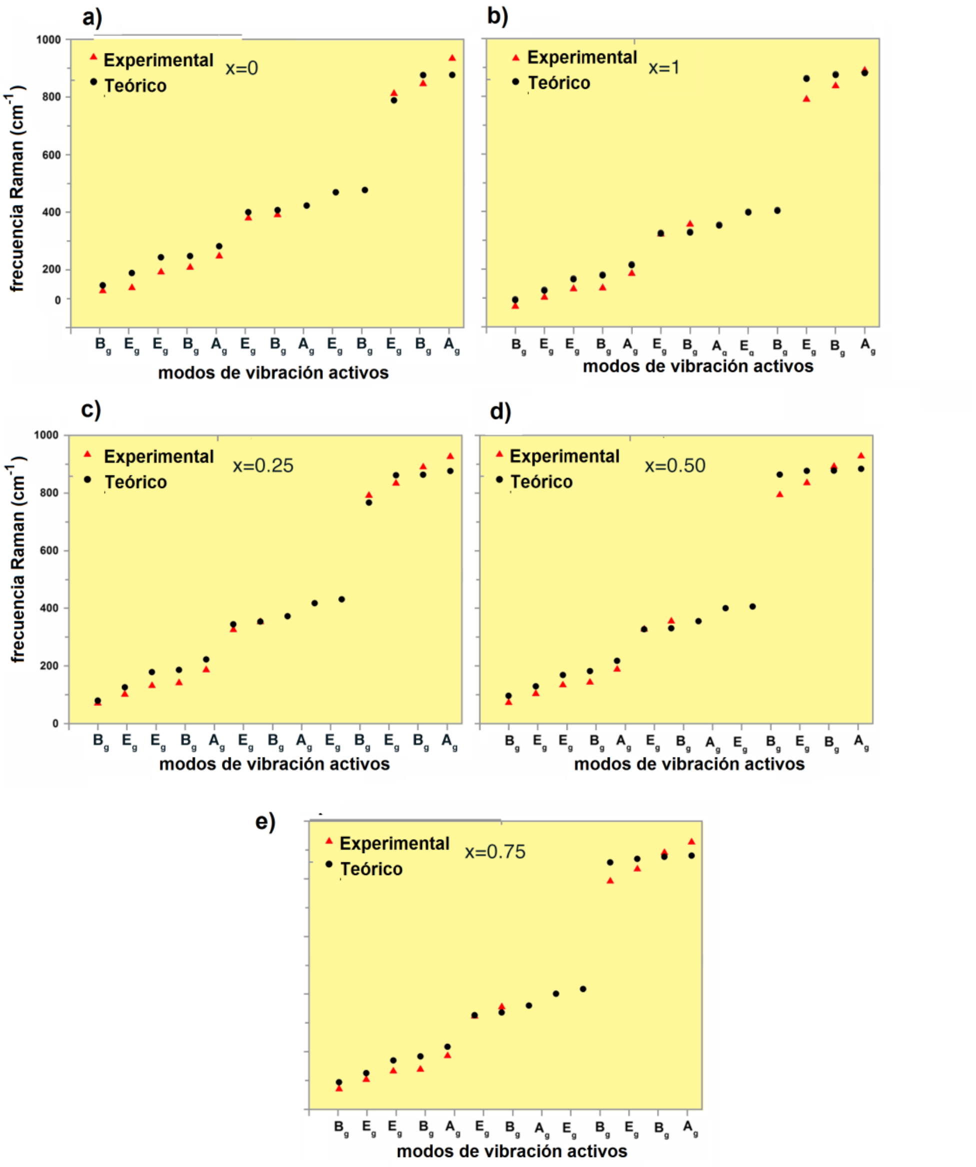

Figura 4.4. Representación de los valores de los modos normales Raman calculado de las soluciones sólidas (a) x=0, (b) x=1, (c) x=0.25, (d) x=0.50 y (e) x=0.75.

En la Figura 4.3a-b se muestra el espectro Raman experimental que indicó la existencia de una fuerte interacción entre los iones, que surgen de las vibraciones de estiramiento y flexión de los enlaces de metal-oxígeno [226]. Por otra parte, en las Figuras 4.4(a-e) se comparan los valores de los resultados experimentales y de los cálculos de los modos activos Raman para las soluciones sólidas $BaW_{1-x}Mo_xO_4$ (x=0, 0.25, 0.50, 0.75, 1). Un análisis de los resultados indican la presencia de tres modos (A_g, E_g y B_g, aproximadamente en el rango 452-375 cm^{-1}) no observados experimentalmente. Una explicación plausible para este resultado puede ser que estos modos tienen una intensidad muy baja y no son fácilmente detectables mediante técnicas experimentales. Los cálculos DFT en el método tienden a sobreestimar los valores de las frecuencias vibracionales; por lo tanto, se utilizó un factor de escala de 0.96 [227].

Las propiedades electrónicas de las soluciones solidas se analizaron mediante la estructura de bandas y la proyección del DOS sobre orbitales atómicos y átomos. El “bulk” y las superficies (001) y (112) que son las más relevantes en la morfología ideal, se muestran en las Figuras 4.5 (a-c) para el sistema a x=0.50 ($BaW_{0.5}Mo_{0.5}O_4$), las demás composiciones se presentan en la Tabla 1, con los valores de la energía de “band gap” y de la energía superficial.

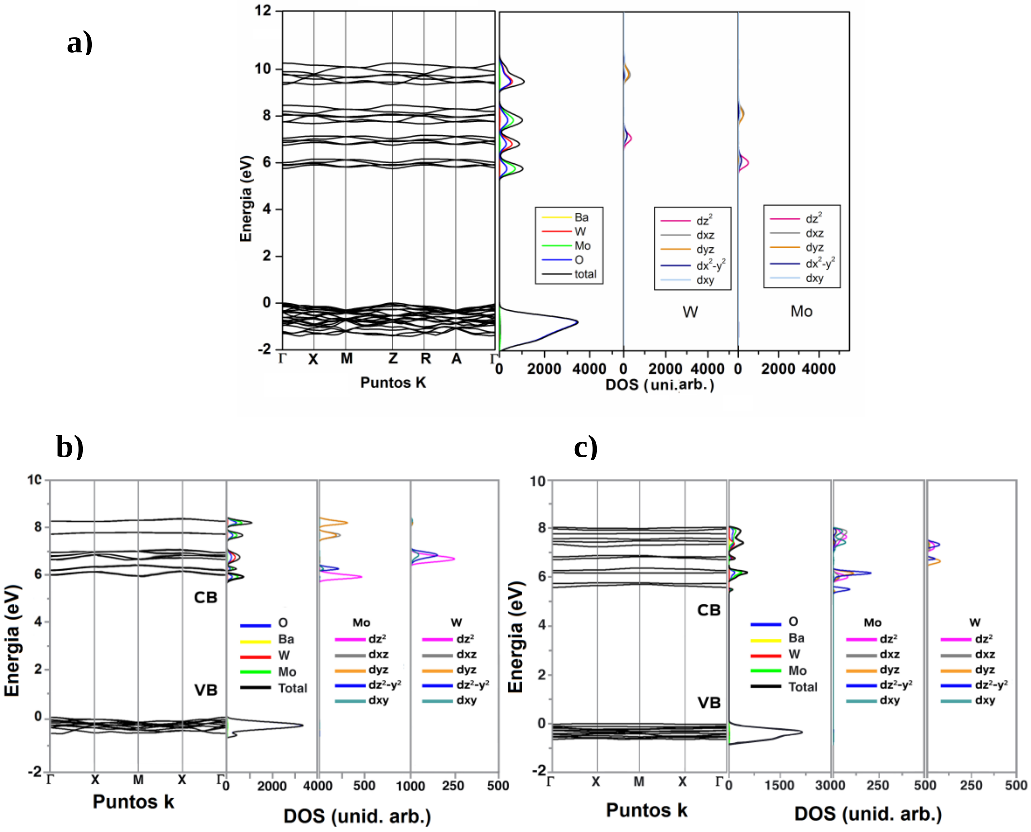

Figura 4.5. Estructura de banda y densidad de los estados proyectados en átomos y orbitales para (a) “bulk”, (b) superficie (001), (c) superficie (112) para el $BaW_{0.5}Mo_{0.5}O_4$.

Tabla 1: Valores calculados de la energía superficial y “band gap” para cada superficie en las soluciones sólidas $BaW_{1-x}Mo_xO_4$ para x = 0, 0.25, 0.5, 0.75 y 1.

Superficies	**Mo(%)**	**E_{suf} (J/m^2)**	**E_{gap} (eV)**
(001)	0%	0.92	6.52
	25%	0.55	5.92
	50%	0.54	5.97
	75%	0.54	5.69
	100%	0.99	5.69
(112)	0%	0.92	6.60
	25%	0.65	6.14
	50%	0.64	5.57
	75%	0.63	5.54
	100%	1.02	5.81
(100)	0%	1.22	6.47
	25%	1.09	5.49
	50%	1.09	5.48
	75%	1.08	5.33
	100%	1.17	5.38
(110)	0%	1.10	6.45
	25%	0.80	6.15
	50%	0.79	6.14
	75%	0.80	5.49
	100%	1.23	5.63
(101)	0%	1.31	6.17
	25%	0.91	6.16
	50%	0.89	6.21
	75%	0.90	5.31
	100%	1.34	5.09
(111)	0%	2.06	Conductor
	25%	1.91	
	50%	1.89	
	75%	1.90	
	100%	2.23	

A partir del análisis del DOS se verifica que los aniones oxígeno son los que presentan una mayor contribución a lo largo de la BV, con orbitales 2p; mientras que los cationes de Mo y W contribuyen más significativamente en la BC con los orbitales 4d y 5d, respectivamente. En la estructura de bandas se muestra el camino seguido de puntos k de alta simetría Γ(0,0,0); X(0,0,1); M(1,1,0); X(0,1,0); Γ(0,0,0) de la zona de *Brillouin*.

Utilizando los valores de las energías superficiales calculadas y mediante la aplicación de la construcción Wulff ha sido posible obtener la morfología de los sistemas puros $BaWO_4$ y $BaMoO_4$ Figuras 4.6(a-b) y sus correspondientes soluciones solidas $BaW_{1-x}Mo_xO_4$ para x= 0.25, 0.50 y 0.75 que se presentan en las Figuras 4.7.

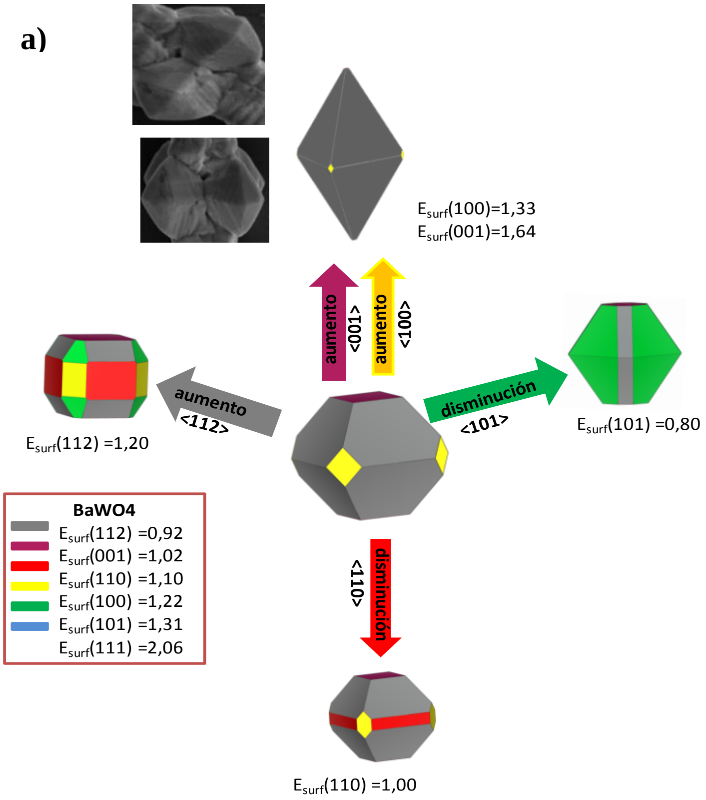

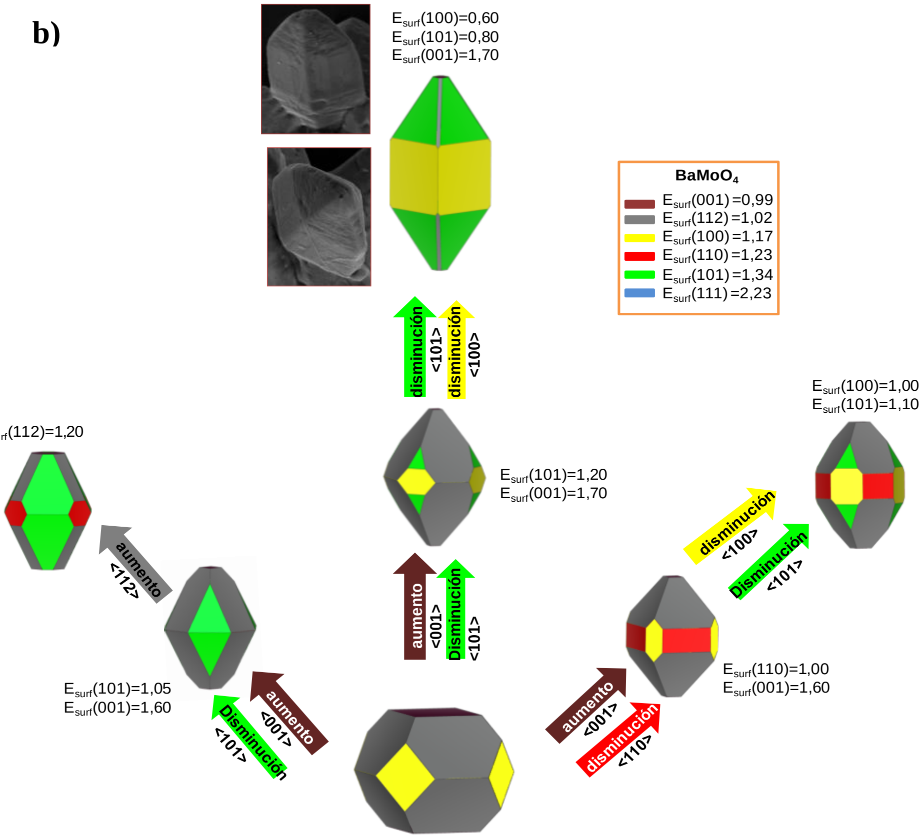

Figura 4.6. Mapa de morfología para los sistemas puros (a) $BaWO_4$ y (b) $BaMoO_4$. Las energías de superficie están en J/m^2. Las imágenes FE-SEM experimentales se incluyen para su comparación.

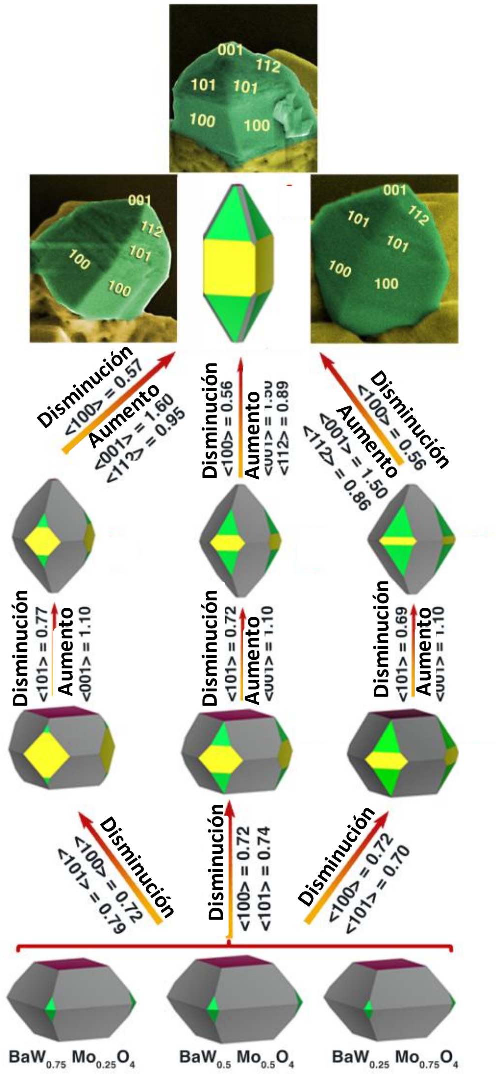

Figura 4.7. Mapa de morfología para la solución solida $BaW_{1-x}Mo_xO_4$ (x= 0.25, 0.50 y 0.75) y energías de superficie en J/m^2. La forma cristalina de equilibrio predicha por las construcciones Wulff ajustando los valores de las energías de las diferentes superficies. Las imágenes FE-SEM experimentales se incluyen para su comparación.

En este estudio, el efecto provocado por la sustitución de cationes de W^{6+} por Mo^{6+} en la solución sólida $BaW_{1-x}Mo_xO_4$ se presenta principalmente por la alteración del orden de estabilidad entre (001) y (112) superficies, así como para las superficies (100) y (110). Aunque, ajustando los valores de energía superficial desde la morfología ideal fue posible obtener la morfología experimental que se muestra en la parte superior de la Figura 4.7.

4.2. Artículo V

La representación esquemática de la estructura tetragonal (grupo espacial I41/a) de la celda unidad del $CaMoO_4$ con las coordinaciones locales de los átomos de Ca y Mo se presenta en la Figura 1.1. Las coordinaciones atómicas en las superficies se muestran en las Figuras 4.8(a-f).

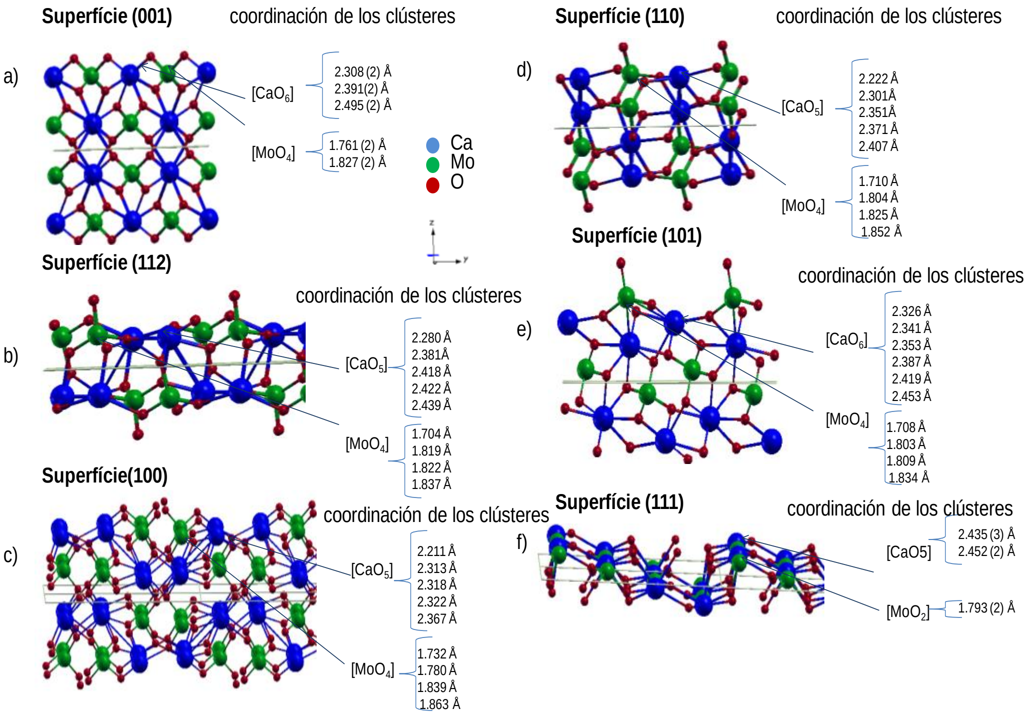

Figura 4.8. Las superficies y las distancias de enlaces de los átomos Ca-O y Mo-O: (a) (001), (b) (112), (c) (100), (d) (110), (e) (101) y (f) (111).

Además, se calcularon las energías de las diferentes superficies, asumiendo la contribución de los vacantes de O presente en los clústeres Mo y Ca. Estos valores obtenidos se usaron para representar las diversas morfologías disponibles para $CaMoO_4$, que se ilustra en la Figura 4.9.

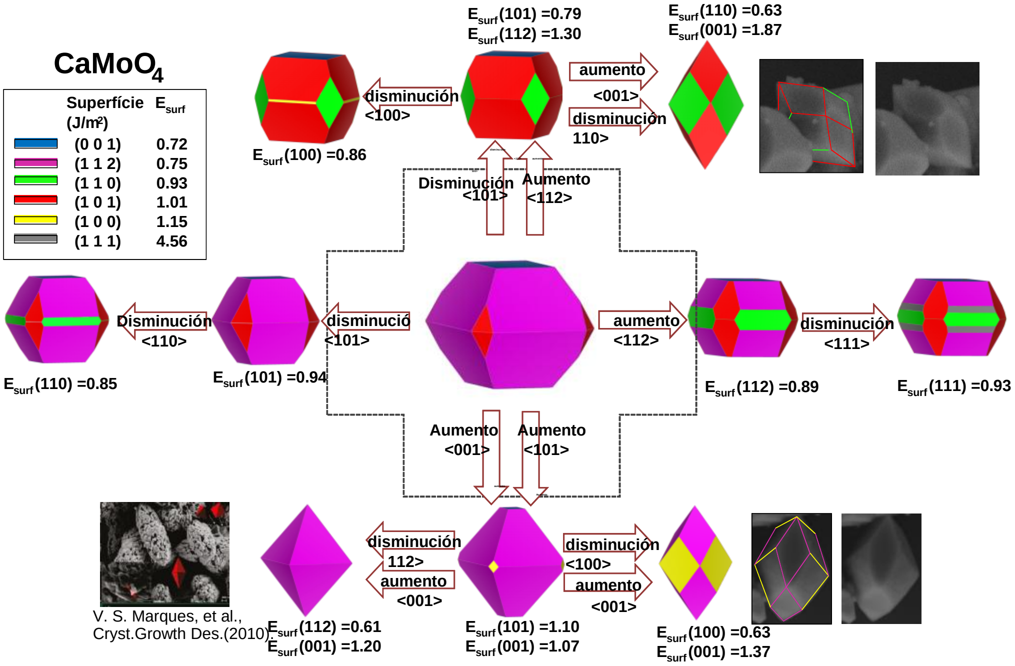

Figura 4.9. Mapa de morfologías de CaMoO$_4$ con planos cristalinos (001), (112), (110), (101), (100) y (111). Para su comparación se muestran las morfologías experimentales, así como los reportados en la literatura.

El análisis del DOS muestra contribuciones similares de los orbitales 2p de los aniones oxígeno en la parte superior de la BV, mientras que la parte inferior de la BC se compone principalmente de los orbitales 4d de Mo como se muestra en la Figura 4.5. Además, el "band gap" es directo y con valor de 4.92 eV en los puntos k de Γ a Γ.

4.3. Artículo VI

El ZnMoO$_4$ presenta una estructura triclínica (grupo espacial P$\bar{1}$). En la Figura 1.2 se muestran las coordinaciones locales de los cationes Zn y Mo. La estructura de ZnMoO$_4$:Eu^{3+} se representa en la Figura 4.10.

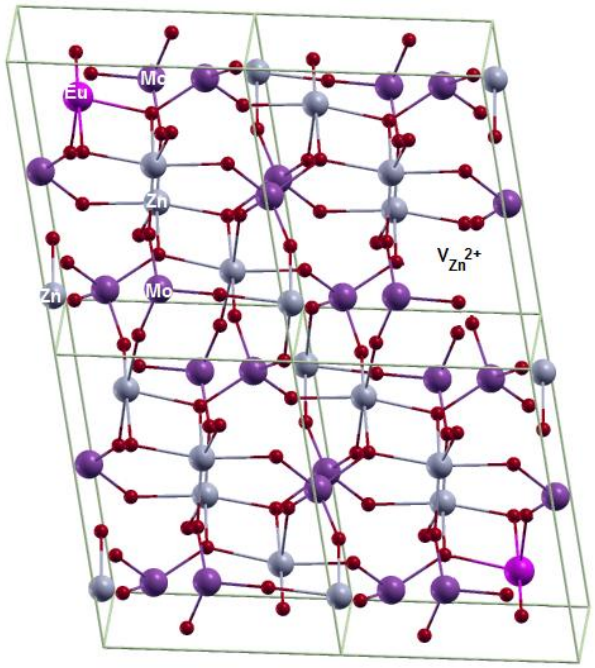

Figura 4.10. Representación esquemática de la supercelda 1x2x2 triclínica correspondiente a $ZnMoO_4$: Eu^{3+} (12.5%).

Se realizaron los cálculos de la supercelda del “bulk” y de las superficies (120), (011), (001), (201), (220), (100), (111) y (112) correspondiente a 143 átomos, que se muestra en la Figura 4.11.

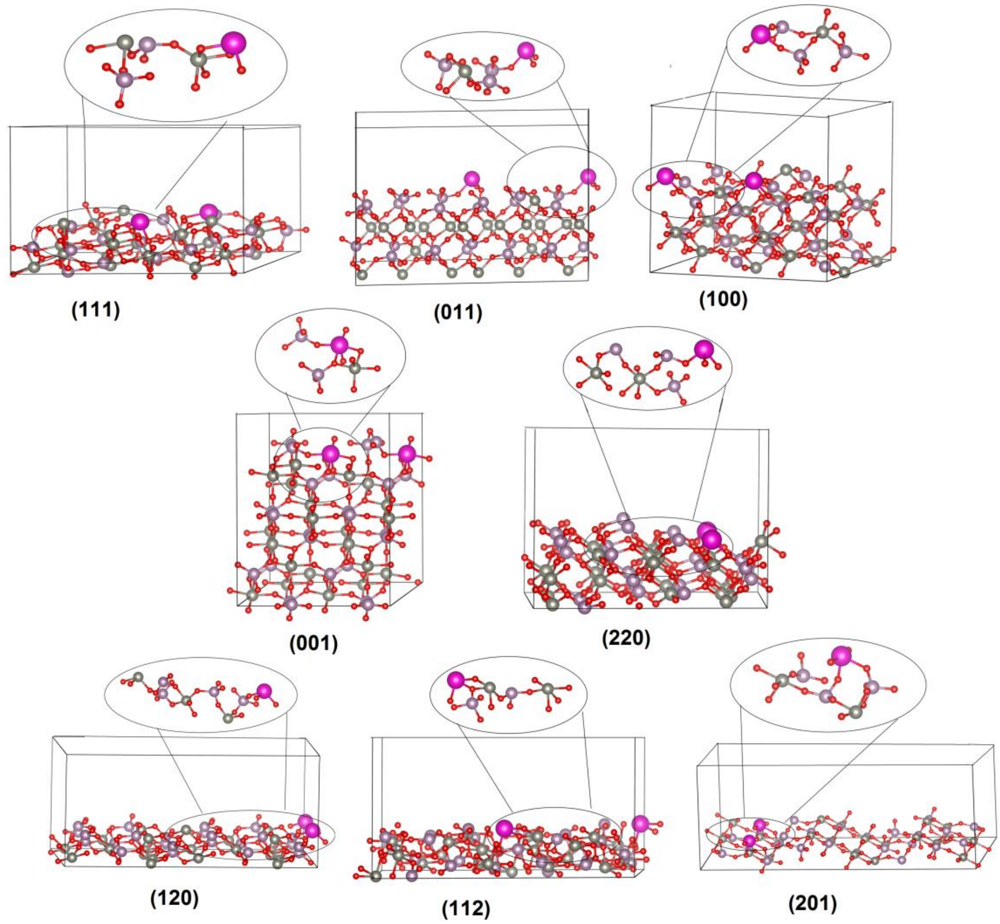

Figura 4.11. Representación teórica des superficies (111), (011), (100), (001), (220), (120), (112) y (201), correspondiente a $ZnMoO_4$: Eu^{3+} (12.5%).

Cuando se incorpora en la matriz de $ZnMoO_4$ cationes Eu^{3+} hay un exceso de cargas positivas y es necesario crear vacantes de Zn^{2+} para mantener la neutralidad de los sistemas. La presencia de estos defectos promueve la aparición de niveles electrónicos intermedios en las bandas, que contribuye para la disminución de los valores de energía del “band gap”. El análisis de las transiciones electrónicas experimentales indican un valor en el rango de 3.55- 4.25 eV, mientras que los cálculos predicen un valor para el “band gap” de 5.28 y 2.67 eV (Figuras 4.12a-b) para los sistemas $ZnMoO_4$ y $ZnMoO_4$:Eu^{3+} (12.5%), respectivamente.

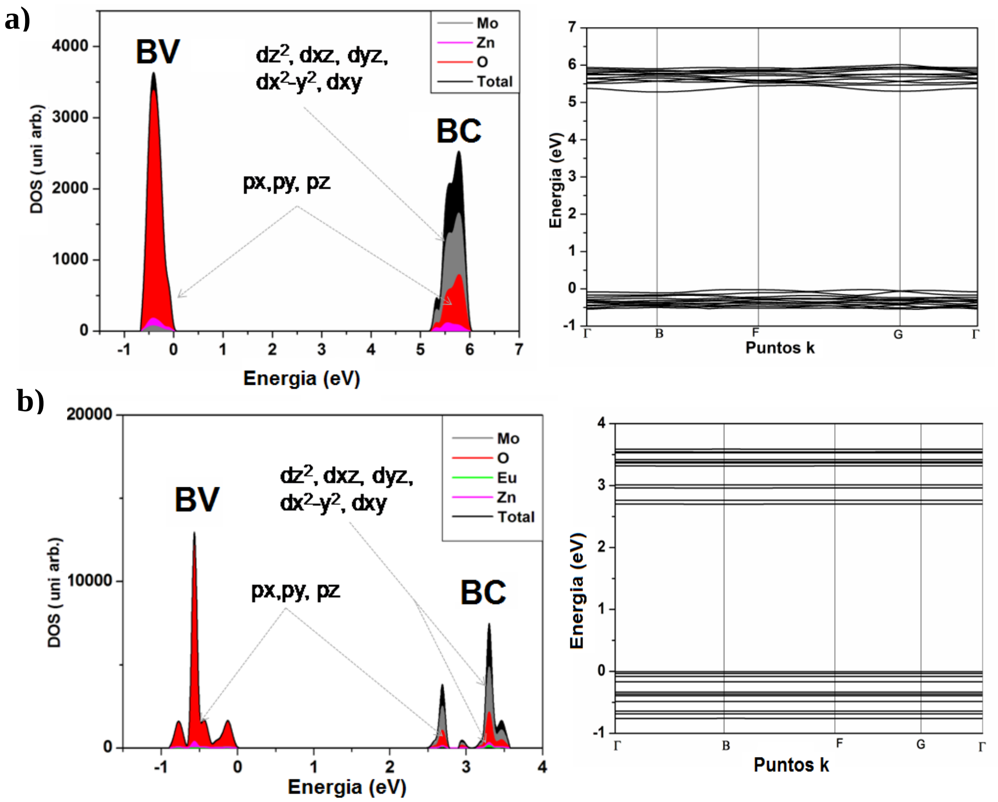

Figura 4.12. DOS y estructura de bandas proyectados de (a) $ZnMoO_4$ y (b) $ZnMoO_4$: Eu^{3+}.

Los DOS que se muestran en las Figuras 4.12a-b, están compuestos principalmente por orbitales de oxígeno (p_x, p_y y p_z) en la BV, mientas que en la BC están formados principalmente por orbitales de Eu y de Mo (d_{z^2}, $d_{x^2-y^2}$, d_{xy}, d_{xz}, d_{yz}). El "band gap" es indirecto ya que se produce a lo largo de los puntos k: F→G (010 a 001) desde la parte superior de la BV hasta la parte inferior de la BC, aunque la estructura de bandas para el sistema dopado es muy plana.

Los morfologías de los cristales $ZnMoO_4$ y $ZnMoO_4$:Eu^{3+} se calcularon utilizando la construcción de Wulff, lo que nos permitió obtener el mapa de morfología para estos dos cristales, que se muestran en las Figuras 4.13a-b, en el que aparecen las morfologías accesibles de estos materiales.

a)

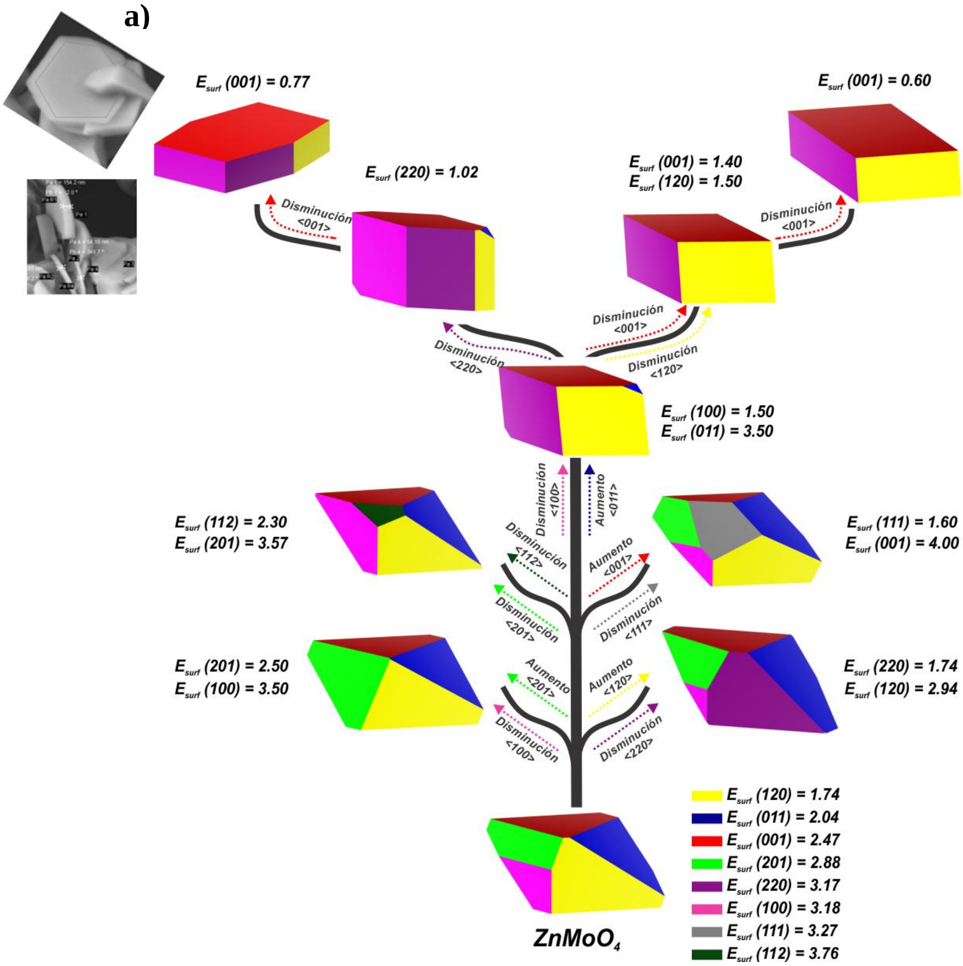
E_{surf} (001) = 0.77
E_{surf} (220) = 1.02
E_{surf} (001) = 1.40
E_{surf} (120) = 1.50
E_{surf} (001) = 0.60
Disminución <001>
Disminución <001>
Disminución <001>
Disminución <220>
Disminución <120>
E_{surf} (100) = 1.50
E_{surf} (011) = 3.50
Disminución <100>
Aumento <011>
E_{surf} (112) = 2.30
E_{surf} (201) = 3.57
E_{surf} (111) = 1.60
E_{surf} (001) = 4.00
Disminución <112>
Aumento <001>
Disminución <201>
Disminución <111>
E_{surf} (201) = 2.50
E_{surf} (100) = 3.50
E_{surf} (220) = 1.74
E_{surf} (120) = 2.94
Aumento <201>
Aumento <120>
Disminución <100>
Disminución <220>
E_{surf} (120) = 1.74
E_{surf} (011) = 2.04
E_{surf} (001) = 2.47
E_{surf} (201) = 2.88
E_{surf} (220) = 3.17
E_{surf} (100) = 3.18
E_{surf} (111) = 3.27
E_{surf} (112) = 3.76
$ZnMoO_4$

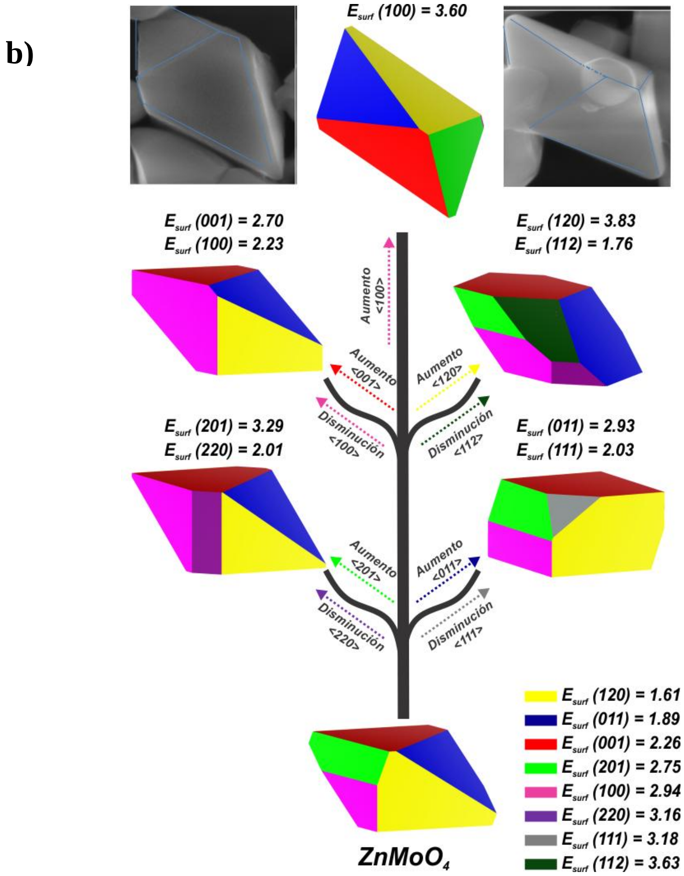

Figura 4.13. Mapa de morfología para (a) cristales de $ZnMoO_4$ y (b) $ZnMoO_4$:Eu^{3+}. Los valores de E_{surf} para (120), (011), (001), (201), (100), (220), (111) y (112) superficies están en $J.m^{-2}$.

Las superficies predominantes que componen la morfología ideal en los sistemas $ZnMoO_4$ y $ZnMoO_4$:Eu^{3+}son (120), (001), (011), (201) y (100). Se pueden obtener otras morfologías modificando los valores relativos de las energías de la superficie de cada superficie, como se muestra en las Figuras 4.13a-b. Por otra parte, en el mapa de la Figura 4.13b podemos encontrar la morfología experimental obtenida para $ZnMoO_4$:Eu^{3+}, mediante el aumento del valor de energía superficial de la superficie (100) a 3.60 $J.m^{-2}$. Las morfologías experimentales presentadas en la Figura 4.13a han sido reportadas en la literatura en los trabajos de Jia et al. y Wang et al[228, 229] y se pudieron reproducir teóricamente al variar los valores relativos de energía superficial de las diferentes superficies.

4.4. Artículos VII y VIII

Previamente, en la Figura 1.3 se ha presentado una estructura ortorrómbica perteneciente al grupo espacial Pcmn para el sistema $CaZrO_3$, así como las coordinaciones locales de los cationes Ca y Zr, correspondiente al estado electrónico fundamental. La estructura de los estados electrónicos excitados s* y t* para $CaZrO_3$ se representan en los apartados a) y b) de la Figura 4.14, respectivamente.

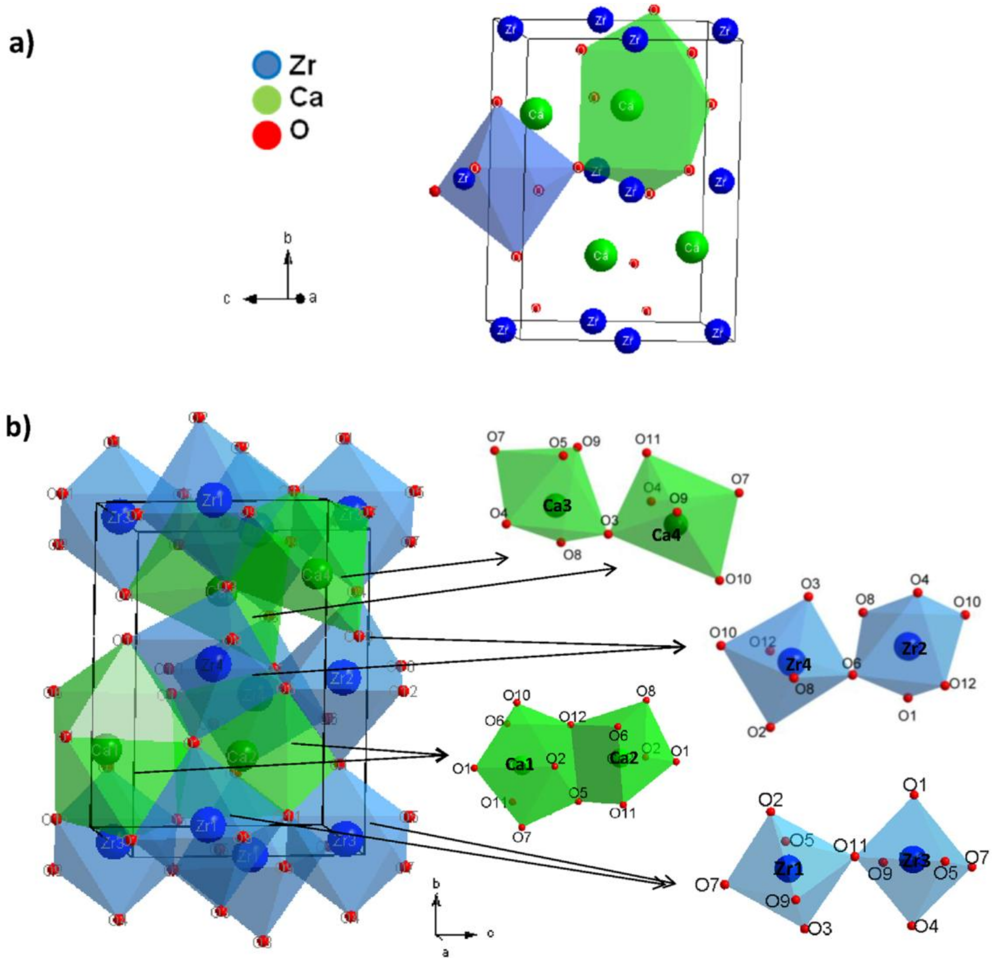

Figura 4.14. Estados electrónicos excitados de $CaZrO_3$: a) singlete, s* y b) triplete t*.

Un análisis de la figura 4.14 muestra que la transformación del estado fundamental s a s* se produce por una ligera distorsión de los clústeres $[ZrO_6]$. Para el estado t* se observa una expansión de los parámetros de celda de ~ 1.5%. En particular, el desplazamiento del átomo de Zr provoca una ligera distorsión de los clústeres Zr2 y Zr4, así como los clústeres Ca3 y Ca4, formando clústeres del tipo $[CaO_{6+2}]$.

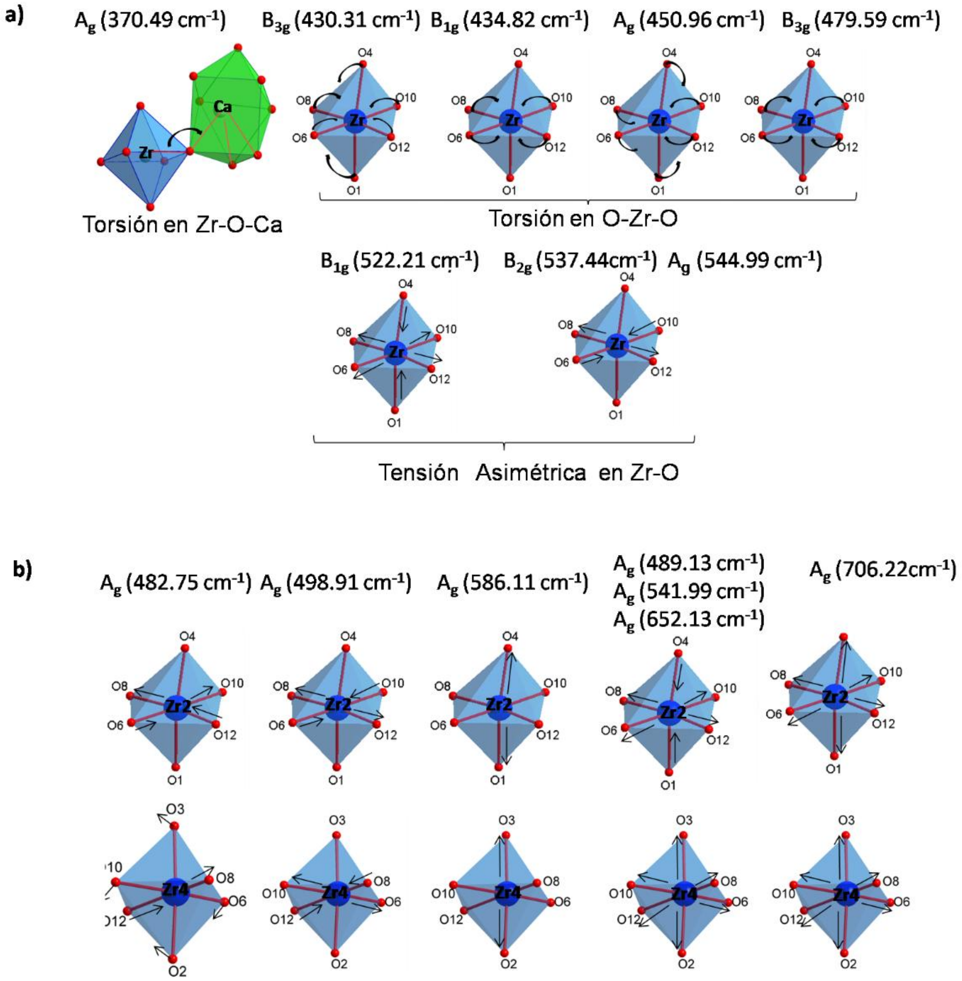

Figura 4.15. Modos Raman calculados para el sistema $CaZrO_3$, asociados principalmente al clúster octaédrico $[ZrO_6]$: a) estado fundamental singlete, s, y b) estado excitado triplete, t*.

Un análisis y comparación de las frecuencias vibracionales Raman para s, s* y t*, ha dado lugar a los siguientes resultados: La estructura ortorrómbica experimenta un cambio hacia una simetría inferior sin ruptura de enlaces, lo que implica un efecto de orden-desorden estructural que se puede asociar al modo de estiramiento asimétrico del Zr-O de 544.99 y

544.28 cm^{-1} para s y s*, respectivamente. Por otro lado, la transición de los estados electrónicos excitados s* a t* corresponde a los movimientos vibracionales de 544.28 y 541.99 cm^{-1}para s * y t *, respectivamente. Sin embargo, es importante tener en cuenta que las vías para llegar a los estados electrónicos s* y t* implican una nueva redistribución de espín que se asocia a una distorsión estructural que da como resultado nuevas configuraciones electrónicas. Los principales modos de vibración para s y t* se muestran en la Figura 4.15.

La relación de los modos normales de vibración y el orden-desorden estructural asociado al paso del estado electrónico fundamental a los excitados, ofrece la oportunidad para interpretar los estados excitados como posibles responsables del comportamiento fotoluminiscente. Durante el proceso de fotoluminiscencia, tiene lugar una ruptura de simetría a corto alcance, implicando a los dos tipos de clúster, es decir, distorsiones estructurales asociadas a una coordinación imperfecta principalmente relacionada con sitios Zr. Estos cambios estructurales son capaces de poblar los estados electrónicos excitados y por lo tanto generar nuevos modos de vibración Raman activos. El efecto de orden-desorden estructural está principalmente relacionado a la coordinación del catión Zr y los aniones O vecinos, cuyas distancias de enlace Zr-O en el estado t* se estiran y acortan a 2.294 y 1.995 Å, respectivamente,

Para llevar a cabo el análisis electrónico, se ha calculado la estructura de bandas y el DOS proyectado en átomos y orbitales para los estados electrónicos s, s* y t*, se presentan en los apartados a, b y c de la Figura 4.16, respectivamente.

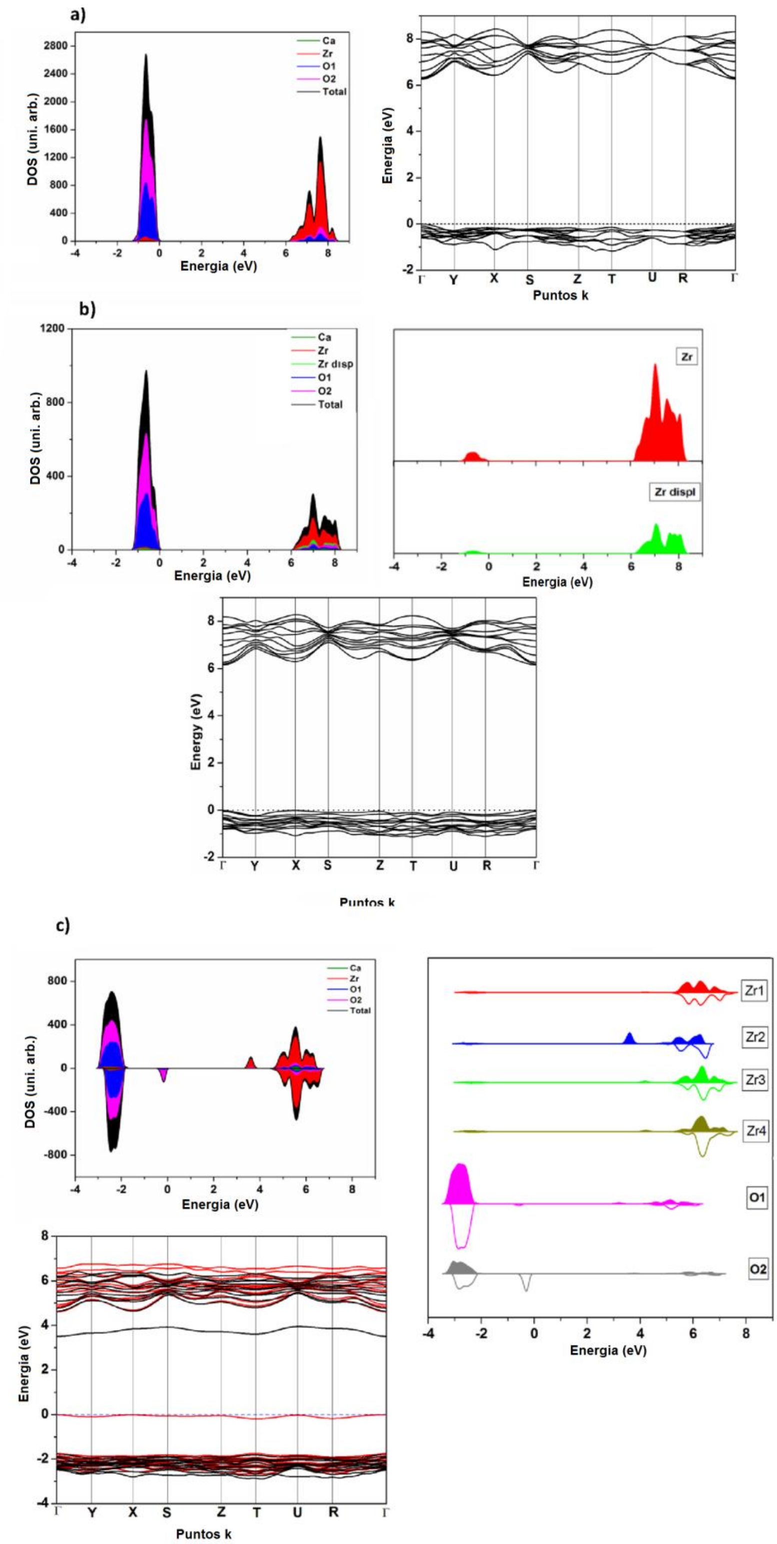

Figura 4.16. Diagramas de estructura de bandas y DOS para estados electrónicos de $CaZrO_3$: a) s, b) s * y c) t *.

A partir del análisis de las estructuras de las bandas observadas en la Figura 4.16 se obtiene un “band gap” directo con valor de 6.23 eV para s, mientras que los estados electrónicos excitados s* y t* presentan valores de 6.14 eV y 3.5 eV, respectivamente. A partir del DOS observado para los estados s, s* y t*, se muestra que la BV superior está compuesta predominantemente por los orbitales atómicos 2p (p_x, p_y, p_z) de los aniones de O y la parte inferior de la BC formado principalmente por los orbitales atómicos 4d (d_{xz}, d_{xy}, d_{yz}, d_z^2, d_x^2-$_y^2$) de los cationes de Zr. Para el estado t*, el desplazamiento del átomo de Zr causa una ligera distorsión de los enlaces Zr4-O6, Zr4-O10 y Zr2-O1, lo que lleva a la creación de estados electrónicos intermedios y una disminución en el valor de “band gap”.

La combinación de los cálculos de energía superficiales de los estados electrónicos fundamental y excitado t* asociados con la construcción de Wulff se ha utilizado para evaluar la morfología de $CaZrO_{3,}$ ya que se ha observado que las propiedades ópticas tales como fotoluminiscencia son fuertemente dependientes de las características estructurales y morfológicas del cristal (Figura 4.17 y Figura 4.18). Hemos obviado realizar el mismo cálculo para s*, ya que su geometría, y por tanto de las superficies son muy similares a la del s.

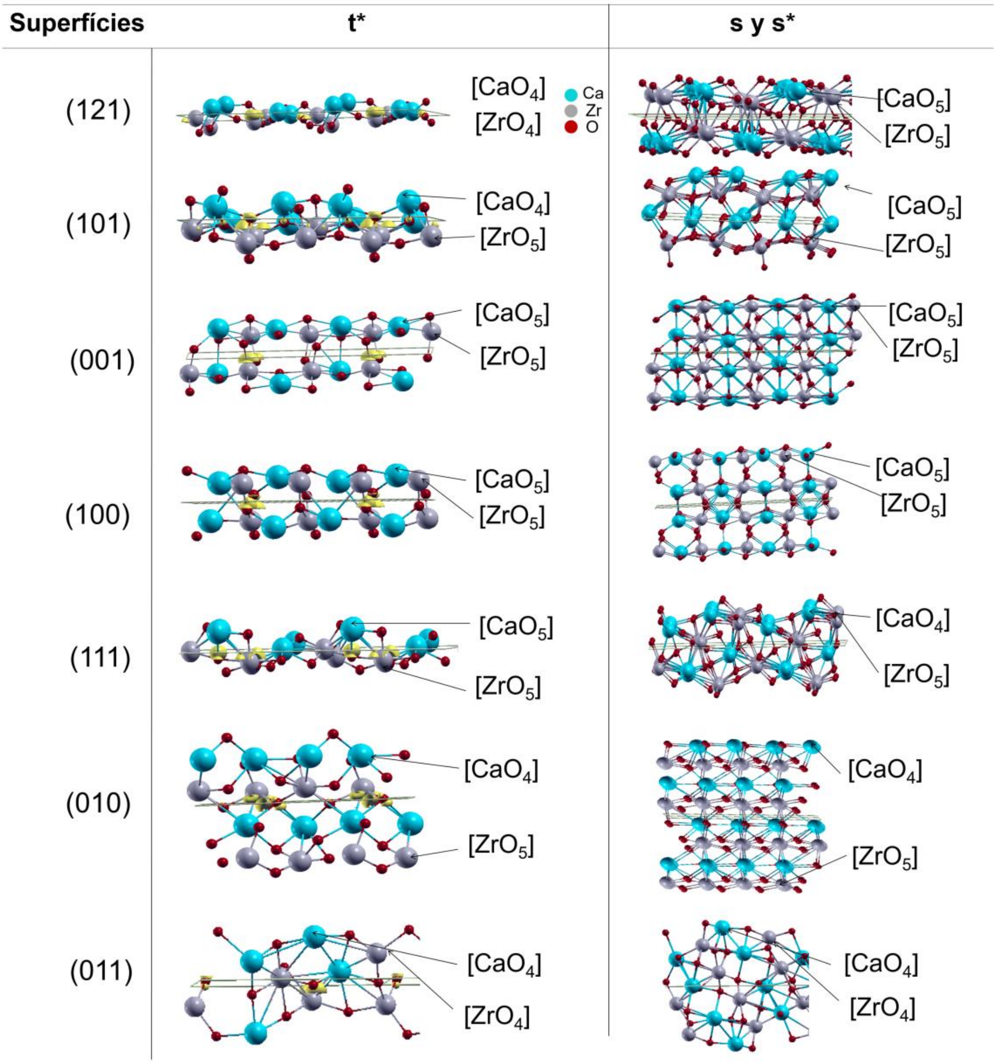

Figura 4.17. Una representación esquemática de las superficies y clústeres externos del estado s, s* y t* de $CaZrO_3$ donde se representa la densidad de espín (en amarillo).

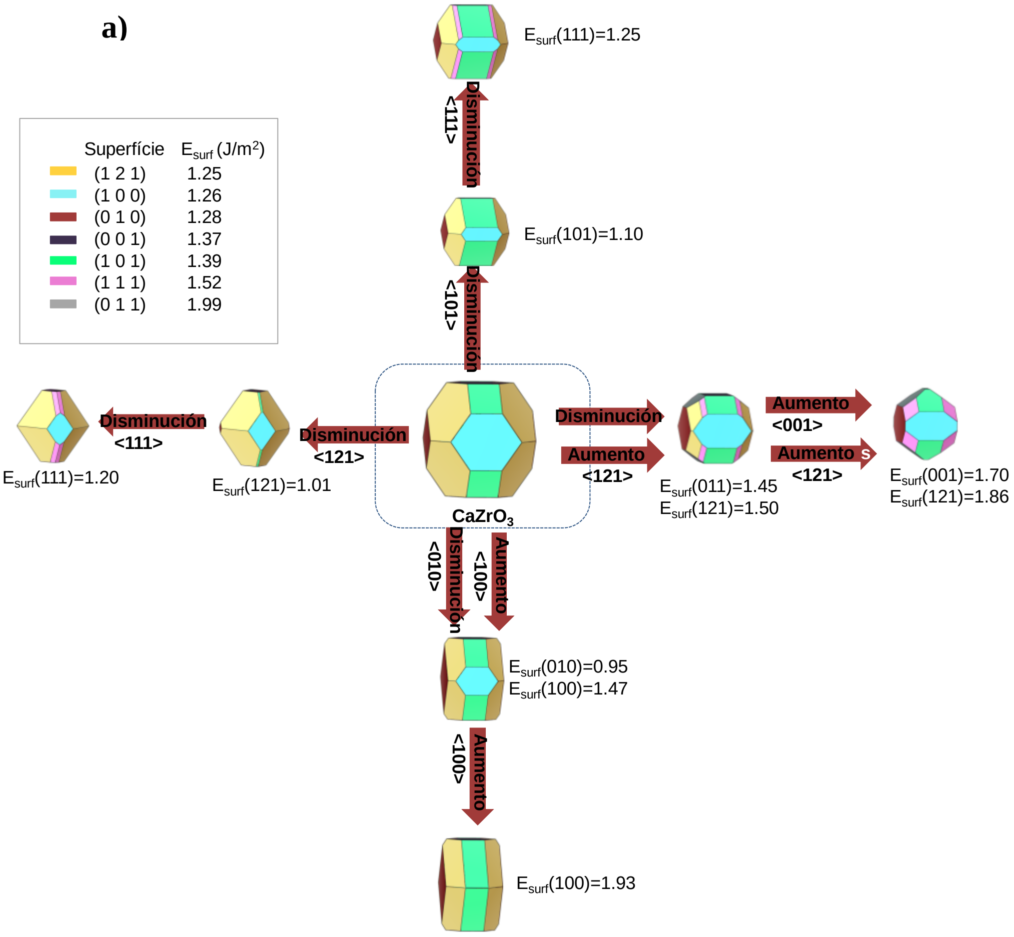
a)
Superfície
E_{surf} (J/m^2)
(1 2 1) 1.25
(1 0 0) 1.26
(0 1 0) 1.28
(0 0 1) 1.37
(1 0 1) 1.39
(1 1 1) 1.52
(0 1 1) 1.99
E_{surf}(111)=1.25
Disminución <111>
E_{surf}(101)=1.10
Disminución <101>
CaZrO_3
Disminución <111>
E_{surf}(111)=1.20
Disminución <121>
E_{surf}(121)=1.01
Disminución
Aumento <121>
E_{surf}(011)=1.45
E_{surf}(121)=1.50
Aumento <001>
Aumento s <121>
E_{surf}(001)=1.70
E_{surf}(121)=1.86
Disminución <010>
Aumento <100>
E_{surf}(010)=0.95
E_{surf}(100)=1.47
Aumento <100>
E_{surf}(100)=1.93

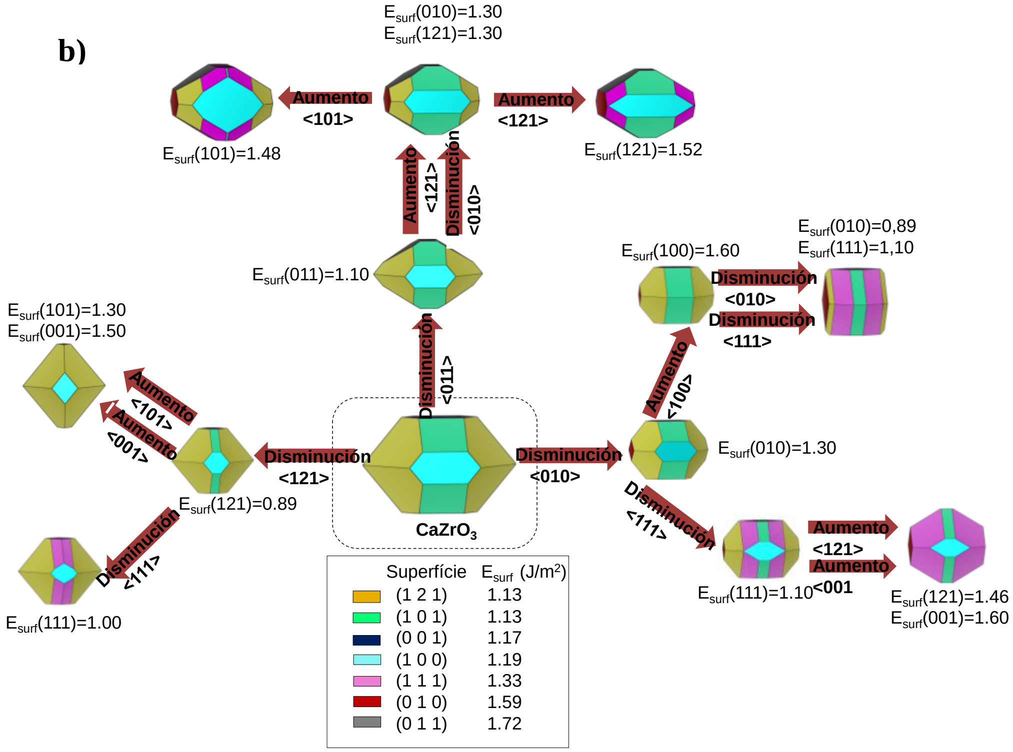

Figura 4.18. Morfologías de $CaZrO_3$ para los estados electrónicos: a) s y b) t*.

La morfología ideal de $CaZrO_3$ en estado fundamental s se describe a través de las superficies (121), (100), (101), (001) y (010), mientras que en el t* la superficie (010) no aparece en la morfología ideal ya que su valor de energía superficial es menos estable que en el estado s. Asimismo, se observa una ligera modificación en el orden de estabilidad de las superficies de los estados s y t*, que es consistente con las configuraciones atómicas y la coordinación local de los átomos para cada superficie. La modulación de la morfología mediante disminución/aumento en los valores de energía de superficie para los estados s y t* de $CaZrO_3$ se presentan en los apartados a y b de la Figura 4.18, respectivamente.

Por otra parte, cálculos teóricos para $CaZrO_3:Eu^{3+}$ (12.5%) muestran valores de "band gap" de 5.09 eV, 4.90 eV y 3.88 eV para s, s* y t*, respectivamente. La reducción de la energía de "gap" se debe a la densidad de defectos en el material dopado correlacionado con los cambios estructurales causados por la sustitución de cationes Ca^{2+} por cationes Eu^{3+} en el clúster $[CaO_8]$.

Un análisis del DOS muestra que los niveles superiores de la BV los constituyen los aniones O, mientras que la BC se compone principalmente por cationes de Zr y Eu con una pequeña contribución de átomos de Ca. Además, se observa la degeneración de las bandas tanto para la banda de valencia máxima como para banda de conducción mínima, que son sensibles al mecanismo de excitación que generan los estados electrónicos excitados (Figura 4.19).

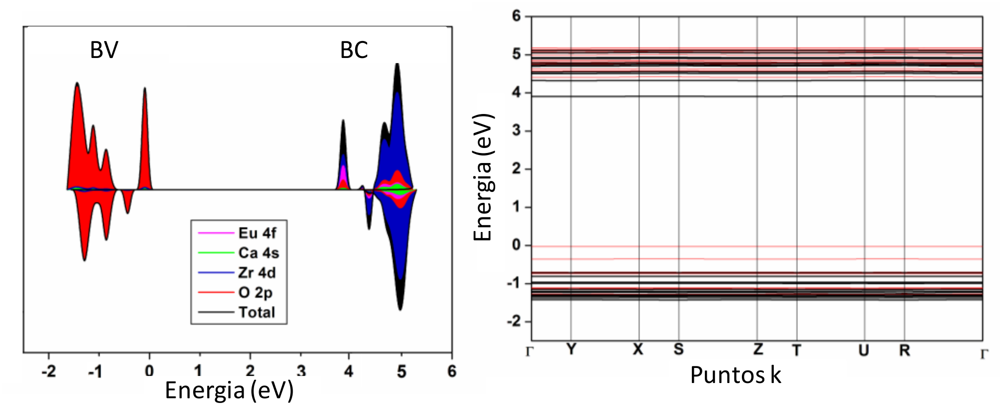

Figure 4.19. DOS y estructura de bandas para el estado excitado t *.

Asimismo, la fotoluminiscencia presentada en $CaZrO_3:Eu^{3+}$ puede estar asociada la morfología, ya que los defectos asociados con la concentración del Eu^{3+} causa defectos resultantes de la sustitución como de la generación de vacantes de Ca^{2+}. La morfología de $CaZrO_3:Eu^{3+}$ en estado t* se ha basado en los valores de energía superficial para las superficies (001), (121), (100), (011) y (111), que se presenta en la Figura 4.20.

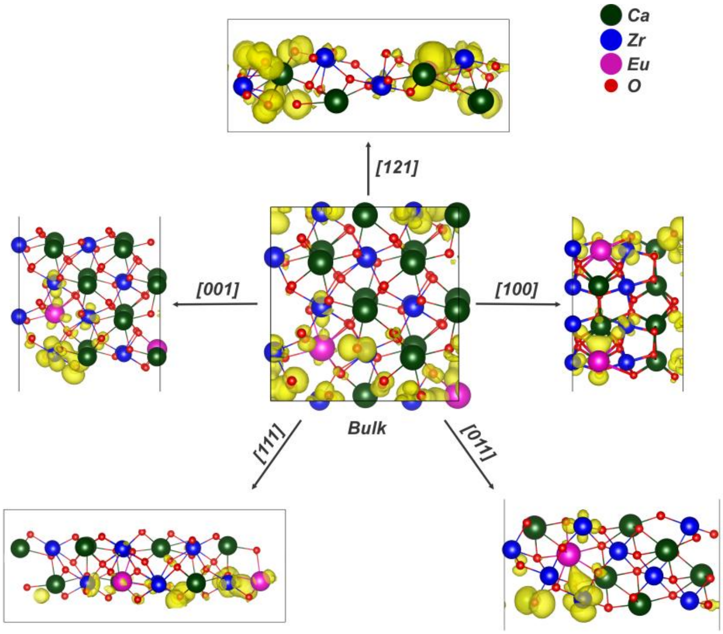

Figura 4.20. Representación esquemática de isosuperficies de densidad de espín (en amarillo) calculadas para modelos del "bulk" y de superficies de $CaZrO_3:Eu^{3+}$ (12.5%) en el estado de triplete (t *).

Los valores de energía superficial siguen el orden de estabilidad (111)> (001)> (011)> (100)> (121) en estado s y (111)> (100)> (011)> (001)> (121) en el estado electrónico t*. La morfología ideal de los estados electrónicos s y t* para $CaZrO_3:Eu^{3+}$ se presentan en las Figuras 4.21a-b. Asimismo, modificando el valor de la energía de las superficies usando el teorema de Wulff es posible obtener otras morfologías para $CaZrO_3:Eu^{3+}$.

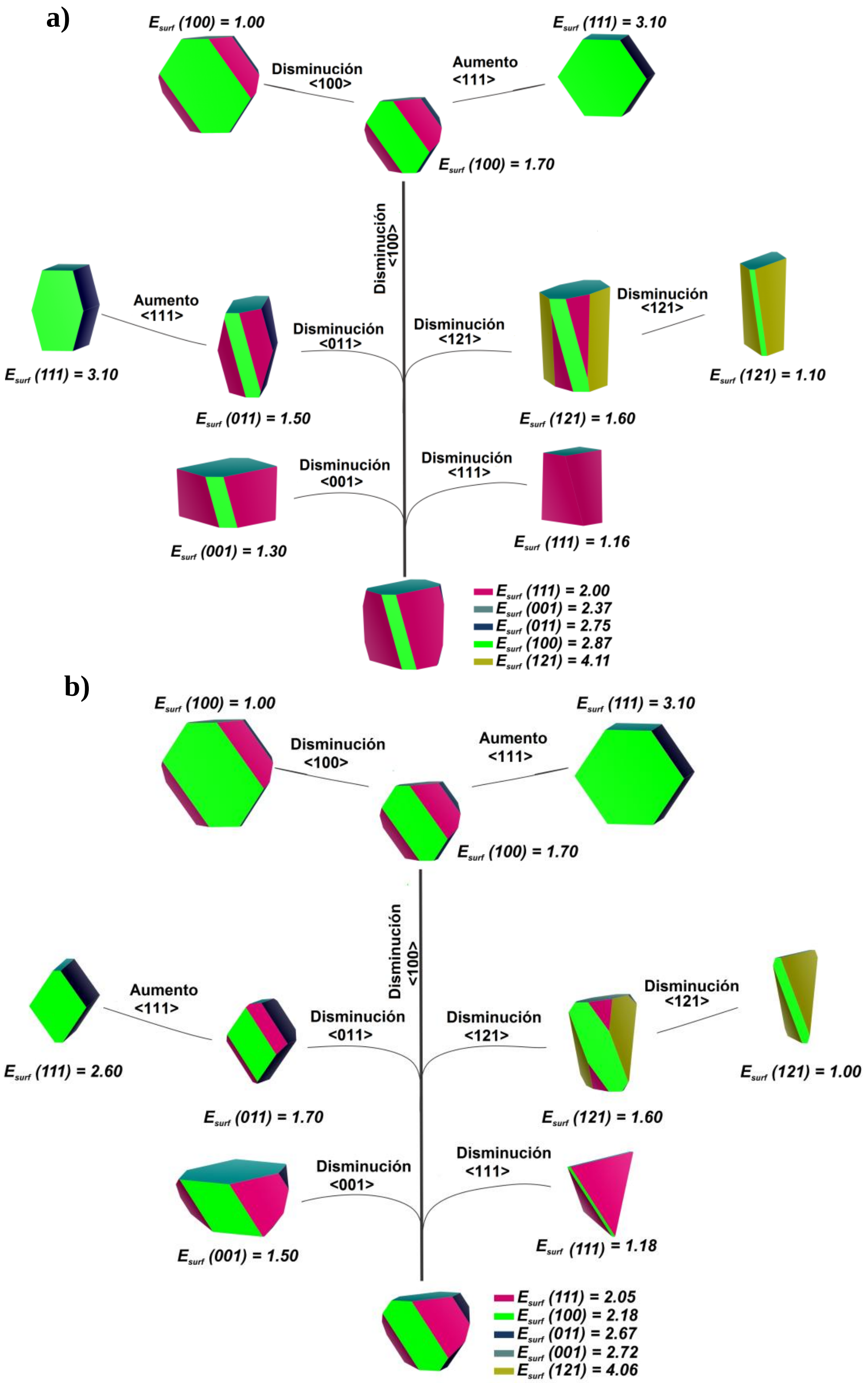

Figura 4.21. Representación esquemática de las morfologías accesibles del $CaZrO_3$: Eu^{3+} (12.5%): (a) s y (b) t*

La superficie (121) es la más inestable para el material $CaZrO_3$:Eu^{3+}, lo que evidencia una inversión del orden de estabilidad en comparación con el $CaZrO_3$ puro (Figura 4.18), donde esta superficie se presenta con menor valor de energía de superficie. Asimismo, en la difracción de rayos X (Figura 4.22) realizado para ambas muestras se observa un desplazamiento alrededor de 2θ=31.60 en la superficie (121), que sugiere el efecto de la inserción de cationes Eu^{3+} y vacantes de Ca^{2+} para la obtención de $CaZrO_3$:Eu^{3+} produciendo cambios en los parámetros de la red cristalina debido a la diferencia en el radio iónico con respecto al de los cationes Ca^{2+}, que genera trasformaciones en la estructura cristalina de $CaZrO_3$ y afecta principalmente en este plano, como se puede observar a partir de la amplificación del pico de difracción (Figura 4.22b).

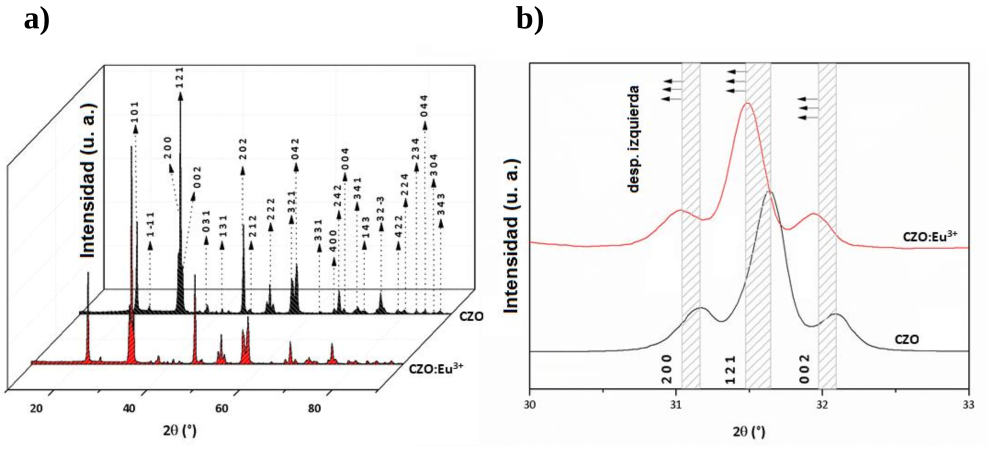

Figura 4.22. Difracción de rayos X de los cristales (a) $CaZrO_3$ puro con planos indexados y $CaZrO_3$:Eu^{3+} y (b) desplazamiento hacia la izquierda de los picos (200), (121) y (002).

5.Conclusiones

¿Puedo creer en la modelización y la simulación?' Es una pregunta frecuente tanto para los investigadores experimentales como teóricos. Responderla requiere una comprensión profunda de las fortalezas y las limitaciones de la modelización computacional y de los métodos de simulación empleados, así como las técnicas experimentales y sus rangos de aplicación. Es obligatorio realizar un diálogo autocrítico entre la teoría y experimento en lugar de hacer ambos por separado y dar confianza incondicional en los resultados de tales estudios de forma aislada. La combinación de ambos proporciona un campo fértil con oportunidades interesantes y una enorme gama de aplicaciones potenciales. Es crucial para el modelización entender los puntos de interés para experimentales, la complejidad de los sistemas químicos y cómo abordarlos de forma adecuado.

Las simulaciones basadas en la mecánica cuántica complementan los experimentos y permiten entenderlos a nivel atómico, esto es pueden probar hipótesis e interpretar y analizar datos en términos de interacciones a nivel atómico no disponibles experimentalmente. El empleo conjunto y la comparación de los resultados teóricos y experimentales también pueden sugerir experimentos y simulaciones que pueden aumentar aún más nuestro conocimiento. Por lo tanto, los resultados que se obtiene de la simulación son sinérgicos con los que surgen de los nuevos experimentos, y a veces abren el camino para resolver los problemas donde los experimentos no pueden hacerlo. La mecánica cuántica está en el centro de este esfuerzo y proporciona el marco para una descripción de nivel atómico y molecular de la estructura química y reactividad que forman la base para la interpretación de los datos experimentales y proporciona orientación y guía para realizar nuevos experimentos. Por lo tanto, hay una gran oportunidad para la verdadera sinergia entre la teoría y experimento. Sin embargo, el punto de encuentro común deben ser las propiedades observables del sistema que se pretende investigar. Los observables incluyen morfología, geometría, estructura electrónica, las frecuencias vibracionales, cuando estén disponibles, y toda esta información es muy útil que es el punto de encuentro más fructífero para la teoría y experimentar en ciencia de materiales y nanotecnología.

La morfología es una propiedad clave de los materiales y para el desarrollo de materiales funcionales es importante controlar su morfología y estructura, y el objetivo principal es comprender la química de la superficie, una vez que muchos procesos físicos y químicos toman lugar en las superficies. En la presente Tesis Doctoral se recogen un conjunto de artículos publicados en los cuales se alcanzan los resultados mediante el uso conjunto de trabajos experimentales y teóricos.

Las principales conclusiones se pueden resumir de la siguiente manera: (i) Hemos caracterizado las como las morfologías accesibles deel molibdato de bario ($BaMoO_4$), wolframato de bario ($BaWO_4$), soluciones sólidas $BaW_{1-x}Mo_xO_4$ (x= 0.25, 0.5, 0.75), molibdato de calcio ($CaMoO_4$), molibdato de zinc ($ZnMoO_4$), y zirconato de calcio ($CaZrO_3$), aplicando la construcción de Wulff y utilizando la teoría del funcional de densidad para realizar a cabo los cálculos de primeros principios, para obtener la energía superficial de las diferentes superficies de estos materiales, con el objetivo de proporcionar una guía científica para el control morfológico de la síntesis de estos (nano)materiales. (ii) Los resultados presentados aquí confirman una variedad de morfologías que se pueden conseguir ajustando las estabilidades superficiales, que dependen de los métodos de síntesis y las condiciones de reacción. Existe una correlación entre la energía de la superficie y la densidad de enlaces rotos en cada una de las diferentes superficies. Así, al analizar las imágenes de microscopía electrónica, se puede obtener una mayor comprensión de cómo controlar la forma del cristal sintéticamente ajustando la química de la superficie y controlando los valores relativos de las energías superficiales. (iii) Hemos estudiado la estructura y propiedades electrónicas de $CaMoO_4$, la estabilidad de las correspondientes superficies y sus transformaciones morfológicas. Esta estrategia permite la predicción de posibles morfologías de otros materiales inorgánicos controlando los valores relativos de las energías de las superficies, y explicar y racionalizar los resultados experimentales encontrados en la literatura. Este enfoque tiene el potencial de ser cuantitativo si se combina con medidas de morfología, por ejemplo, las obtenidas por TEM. Las morfologías experimentales se corresponden con las morfologías de crecimiento calculadas, mientras que las morfologías de equilibrio calculadas coincidieron con las observadas. (iv) Hemos investigado y realizado una comparación entre los resultados teóricos como experimentales para comprender la influencia del dopante Eu^{3+} en la matriz de $ZnMoO_4$, tanto en la geometría, estructura electrónica como en la morfología. (v) Comprender los espectros de fotoluminiscencia, basados en la localización y caracterización de los estados electrónicos fundamental (singlete, s) y excitados (singlete, s* y triplete, t*), utilizando estructuras ideales y distorsionadas de $CaZrO_3$ puro y dopado con Eu^{3+}. Además, correlacionar sus correspondientes geometrías, morfologías, estructuras electrónicas y frecuencias vibracionales.

Para finalizar debemos señalar que este trabajo, que constituye la presente Tesis Doctoral, se encuadra dentro de una línea de investigación que se viene llevando a cabo en colaboración entre el grupo de Química Teórica y Computacional de la UJI, y el CDMF de la UFSCar desde hace casi 30 años. Esta colaboración se basa en el siguiente pilar "Los avances en la modelización y simulación computacional, basados en la aplicación de los métodos y técnicas de la química teorica y computacional, se establecen como una componente fundamental en la investigación orientada y aplicada en áreas como el diseño racional de sólidos y (nano)materiales con propiedades químicas y físicas innovadoras". La continuación de los trabajos aquí presentados deberian abordar al menos los tres siguintes aspectos: (i) Discenir si las morfologías observadas experimentalemente son impulsadas por la termodinámica (morfología de equilibrio), como se ha realizado en esta Tesis Doctoral, o por la cinética (morfología de crecimiento). Se necesitarán simulaciones dinámicas para investigar el mecanismo de crecimiento. (ii) incluir y evaluar sucesivamente la influencia del agua y/o la adsorción de impurezas en las superficies de los materiales estudiados, tanto en equilibrio como durante el crecimiento de materiales durante la síntesis. De hecho, para evaluar estos efectos de adsorción en la morfología del cristal, es fundamental un análisis en profundidad de la estructura y la energética de las caras de cristal actuando como sustratos. Las estructuras de las superficies optimizadas que se han determinado en este trabajo se pueden utilizar para calcular las energías de adsorción liberadas cuando las moléculas de agua o impurezas específicas se ponen en contacto con el cristal. (iii) incluir la densidad de spin en los mapas de morfología, lo que implicaría la consideración no solo de la energía superficial sino también la magnetización de cada una de las superficies, en la que hubiera electrones desapareados, y (iv) es necesario mejorar el método de cálculo utilizado para caracterizar los estados electrónicos excitados; el funcional de la densidad dependiente del tiempo podría ser una buena opción.

Conclusions

Can I believe in modeling and simulation? It is a frequent question for both experimental and theoretical researchers. Answering it requires a deep understanding of the strengths and limitations of computational modeling and the simulation methods used, as well as the experimental techniques and their application ranges. It is mandatory to conduct a self-critical dialogue between theory and experiment instead of doing both separately and giving unconditional confidence in the results of such studies in isolation. The combination of both provides a fertile field with interesting opportunities and a huge range of potential applications. It is crucial for the modeling to understand the points of interest for experimental, the complexity of the chemical systems and how to approach them in an appropriate way.

Simulations based on quantum mechanics complement the experiments and allow them to be understood at the atomic level, that is, they can test hypotheses and interpret and analyze data in terms of interactions at the atomic level that are not experimentally available. The joint use and the comparison of the theoretical and experimental results can also suggest experiments and simulations that can further increase our knowledge. Therefore, the results obtained from the simulation are synergistic with those that arise from the new experiments, and sometimes open the way to solve problems where experiments can not do it. Quantum mechanics is at the center of this effort and provides the framework for an atomic and molecular level description of the chemical structure and reactivity that forms the basis for the interpretation of experimental data and provides guidance and guidance for conducting new experiments. Therefore, there is a great opportunity for true synergy between theory and experiment. However, the common point of convergence must be the observable properties of the system to be investigated. The observables include morphology, geometry, electronic structure, vibrational frequencies, when available, and all this information is very useful which is the most fruitful meeting point for the theory and to experiment in materials science and nanotechnology.

Morphology is a key property of materials and for the development of functional materials it is important to control their morphology and structure, and the main objective is to understand the chemistry of the surface, since many physical and chemical processes take place on surfaces. In the present Ph. D, a set of published articles are collected in which the results are achieved through the joint use of experimental and theoretical works. The main conclusions can be summarized as follows: (i) We characterized the accessible morphologies of barium molybdate ($BaMoO_4$), barium tungstate ($BaWO_4$), solid solutions $BaW_{1-x}Mo_xO_4$ (x = 0.25, 0.5, 0.75) , calcium molybdate ($CaMoO_4$), zinc molybdate ($ZnMoO_4$), and calcium zirconate ($CaZrO_3$), applying the Wulff construction and using the density functional theory to perform the first principles calculations, to obtain the energy surface of the different surfaces of these materials, with the aim of providing a scientific guide for the morphological control of the synthesis of these (nano) materials. (ii) The results presented here confirm a variety of morphologies that can be achieved by adjusting surface stabilities, which depend on the synthesis methods and the reaction conditions. There is a correlation between the energy of the surface and the density of broken links in each of the different surfaces. Thus, by analyzing electron microscopy images, a greater understanding of how to control the shape of the crystal can be obtained synthetically by adjusting the chemistry of the surface and controlling the relative values of the surface energies. (iii) We have studied the structure and electronic properties of $CaMoO_4$, the stability of the corresponding surfaces and their morphological transformations. This strategy allows the prediction of possible morphologies of other inorganic materials by controlling the relative values of the surface energies, and explaining and rationalizing the experimental results found in the literature. This approach has the potential to be quantitative if is combined with measurements of morphology, e.g., TEM. Experimental morphologies were well-reproduced by calculated growth morphologies, while calculated equilibrium morphologies matched those observed. (iv) We have investigated and made a comparison between the theoretical and experimental results to understand the influence of the Eu^{3+} dopant in the $ZnMoO_4$ matrix, both in geometry, electronic structure and in morphology. (v) Understand the photoluminescence spectra, based on the location and characterization of fundamental (singlet, s) and excited electronic states (singlet, s * and triplet, t *), using ideal and distorted structures of pure $CaZrO_3$ and doped with Eu^{3+}. In addition, correlate their corresponding geometries, morphologies, electronic structures and vibrational frequencies.

To conclude, we must point out that this work, which is the present Doctoral Thesis, is part of a line of research that has been carried out in collaboration between the Theoretical and Computational Chemistry Group of the UJI, and the CDMF of the UFSCar since almost 30 years ago. This collaboration is based on the following pillar "The advances in computer modeling and simulation, based on the application of the methods and techniques of theoretical and computational chemistry, are established as a fundamental component in oriented and applied research in areas such as rational design of solids and (nano)materials with innovative chemical and physical properties ". The continuation of the works presented here should address at least the following four aspects: (i) Discerning if the morphologies observed experimentally are driven by thermodynamics (equilibrium morphology), as has been done in this Ph. D., or by kinetics (morphology of growth). Dynamical simulations will be required to investigate the growth mechanism at the root of this phenomenon. (ii) to include and evaluate the influence of water and/or the adsorption of impurities on the surfaces of the materials studied, both in equilibrium and during the growth of materials during the synthesis. In fact, to evaluate these effects of adsorption on the crystal morphology, an in-depth analysis of the structure and energetics of the glass faces acting as substrates is fundamental. The optimized surface structures that have been determined in this work can be used to calculate the adsorption energies released when the water molecules or specific impurities come into contact with the crystal. (iii) to include the spin density in the morphology maps, which would imply the consideration not only of the surface energy but also the magnetization of each of the surfaces, in which there would be unpaired electrons, and (iv) it is necessary to improve the calculation method used to characterize the excited electronic states; the functional of the time-dependent density could be a good option.

6. Referencias

[1] J. Xu, S. Li, J. Weng, X. Wang, Z. Zhou, K. Yang, M. Liu, X. Chen, Q. Cui, M. Cao, Q. Zhang,Adv. Funct. Mater. 18 (2008) 277-284.
[2] T. Ming, W. Feng, Q. Tang, F. Wang, L. Sun, J. Wang, C. Yan,J. Am. Ceram. Soc. 131 (2009) 16350-16351.
[3] Y. Ma, Q. Kuang, Z. Jiang, Z. Xie, R. Huang, L. Zheng,Angew. Chem. Int. Ed. 47 (2008) 8901-8904.
[4] N. Tian, Z.-Y. Zhou, S.-G. Sun,J. Phys. Chem. C 112 (2008) 19801-19817.
[5] J.J. Teo, Y. Chang, H.C. Zeng,Langmuir 22 (2006) 7369-7377.
[6] N. Wang, X. Cao, L. Guo, S. Yang, Z. Wu,ACS Nano 2 (2008) 184-190.
[7] V. Sebastian, C.D. Smith, K.F. Jensen,Nanoscale 8 (2016) 7534-7543.
[8] P. Liu, R. Qin, G. Fu, N. Zheng,J. Am. Ceram. Soc. 139 (2017) 2122-2131.
[9] J.M. Rahm, P. Erhart,Nano Lett. 17 (2017) 5775-5781.
[10] L. Xu, H.-W. Liang, Y. Yang, S.-H. Yu,Chem. Rev. (2018).
[11] B. Lim, M. Jiang, P.H.C. Camargo, E.C. Cho, J. Tao, X. Lu, Y. Zhu, Y. Xia,Science 324 (2009) 1302-1305.
[12] G. Prieto, J. Zečević, H. Friedrich, K.P. de Jong, P.E. de Jongh,Nat. Mater. 12 (2012) 34.
[13] M. Kim, Y. Kim, J.W. Hong, S. Ahn, W.Y. Kim, S.W. Han,Chem. Commun. 50 (2014) 9454-9457.
[14] Z. Niu, N. Becknell, Y. Yu, D. Kim, C. Chen, N. Kornienko, G.A. Somorjai, P. Yang,Nat. Mater. 15 (2016) 1188.
[15] J.-H. Choi, H. Wang, S.J. Oh, T. Paik, P. Sung, J. Sung, X. Ye, T. Zhao, B.T. Diroll, C.B. Murray, C.R. Kagan,Science 352 (2016) 205-208.
[16] P. Jena,J. Phys. Chem. Lett. 2 (2011) 206-211.
[17] L. Liu, F. Ni, J. Zhang, X. Jiang, X. Lu, Z. Guo, R. Xu,Acta Biochi. Bioph. Sin. 43 (2011) 316-323.
[18] P.D. Howes, R. Chandrawati, M.M. Stevens,Science 346 (2014).
[19] H.G. Yang, C.H. Sun, S.Z. Qiao, J. Zou, G. Liu, S.C. Smith, H.M. Cheng, G.Q. Lu,Nature 453 (2008) 638.
[20] J.H. Zeng, B.B. Jin, Y.F. Wang,Chem. Phys. Lett. 472 (2009) 90-95.
[21] X. Xie, Y. Li, Z.-Q. Liu, M. Haruta, W. Shen,Nature 458 (2009) 746.
[22] K. Zhu, J. Hu, C. Kübel, R. Richards,Angew. Chem. Int. Ed. 45 (2006) 7277-7281.
[23] N. Zhao, W. Ma, Z. Cui, W. Song, C. Xu, M. Gao,ACS Nano 3 (2009) 1775-1780.
[24] X. Wang, H.-F. Wu, Q. Kuang, R.-B. Huang, Z.-X. Xie, L.-S. Zheng,Langmuir 26 (2010) 2774-2778.
[25] B. Geng, C. Fang, F. Zhan, N. Yu,Small 4 (2008) 1337-1343.
[26] Z. Fei, P. Lu, X. Feng, B. Sun, W. Ji,Catal. Sci. Technol. 2 (2012) 1705-1710.
[27] J. Zhang, M.R. Langille, M.L. Personick, K. Zhang, S. Li, C.A. Mirkin,J. Am. Ceram. Soc. 132 (2010) 14012-14014.

[28] J. Zhang, L. Zhang, S. Xie, Q. Kuang, X. Han, Z. Xie, L. Zheng,Chemistry – A European Journal 17 (2011) 9915-9919.
[29] M. Jin, H. Zhang, Z. Xie, Y. Xia,Angew. Chem. Int. Ed. 50 (2011) 7850-7854.
[30] P.A.M. Dirac,Proc. R. Soc. Lond. A 123 (1929) 714-733.
[31] B. Radisavljevic, A. Radenovic, J. Brivio, V. Giacometti, A. Kis,Nature Nanotechnol. 6 (2011) 147.
[32] Q.H. Wang, K. Kalantar-Zadeh, A. Kis, J.N. Coleman, M.S. Strano,Nature Nanotechnol. 7 (2012) 699.
[33] E. Busto, V. Gotor-Fernandez, V. Gotor,Chem. Soc. Rev. 39 (2010) 4504-4523.
[34] A.S. Aricò, P. Bruce, B. Scrosati, J.-M. Tarascon, W. van Schalkwijk,Nat. Mater. 4 (2005) 366.
[35] A.N. Shipway, E. Katz, I. Willner,ChemPhysChem 1 (2000) 18-52.
[36] K.P. Lee, T.C. Arnot, D. Mattia,J. Membrane Sci. 370 (2011) 1-22.
[37] D.A. Giljohann, D.S. Seferos, W.L. Daniel, M.D. Massich, P.C. Patel, C.A. Mirkin,Angew. Chem. Int. Ed. 49 (2010) 3280-3294.
[38] G. Hautier, A. Jain, S.P. Ong,J. Mate. Sci. 47 (2012) 7317-7340.
[39] A.S. Barnard,ACS Nano 8 (2014) 6520-6525.
[40] K.T. Butler, J.M. Frost, J.M. Skelton, K.L. Svane, A. Walsh,Chem. Soc. Rev. 45 (2016) 6138-6146.
[41] Q. Cui, R. Hernandez, S.E. Mason, T. Frauenheim, J.A. Pedersen, F. Geiger,J. Phys. Chem. B 120 (2016) 7297-7306.
[42] N.M. Editoral,Nat. Mater. 15 (2016) 365.
[43] E.A. Carter,Science 321 (2008) 800-803.
[44] G. Fitzgerald, G. Goldbeck, P. Kung, M. Petersen, L. Subramanian, J. Wescott,Comp. Model. Eng. Sci. 24 (2008) 169.
[45] V. Mlinar,J. Mater.Chem. 22 (2012) 1724-1732.
[46] R. Riedel,Chem. Soc. Rev. 41 (2012) 5029-5031.
[47] N. Lopez, N. Almora-Barrios, G. Carchini, P. Blonski, L. Bellarosa, R. Garcia-Muelas, G. Novell-Leruth, M. Garcia-Mota,Catal. Sci. Technol. 2 (2012) 2405-2417.
[48] M.S. Dyer, C. Collins, D. Hodgeman, P.A. Chater, A. Demont, S. Romani, R. Sayers, M.F. Thomas, J.B. Claridge, G.R. Darling, M.J. Rosseinsky,Science 340 (2013) 847-852.
[49] M. Anicete-Santos, E. Orhan, M.A.M.A. de Maurera, L.G.P. Simões, A.G. Souza, P.S. Pizani, E.R. Leite, J.A. Varela, J. Andrés, A. Beltrán, E. Longo,Phys. Rev. B 75 (2007) 165105.
[50] M.R.D. Bomio, L.S. Cavalcante, M.A.P. Almeida, R.L. Tranquilin, N.C. Batista, P.S. Pizani, M. Siu Li, J. Andres, E. Longo,Polyhedron 50 (2013) 532-545.
[51] V.M. Longo, L.S. Cavalcante, E.C. Paris, J.C. Sczancoski, P.S. Pizani, M.S. Li, J. Andrés, E. Longo, J.A. Varela,J. Phys. Chem. C 115 (2011) 5207-5219.

[52] V.M. Longo, L. Gracia, D.G. Stroppa, L.S. Cavalcante, M. Orlandi, A.J. Ramirez, E.R. Leite, J. Andrés, A. Beltrán, J.A. Varela, E. Longo,J. Phys. Chem. C 115 (2011) 20113-20119.
[53] M.A.P. Almeida, L.S. Cavalcante, C. Morilla-Santos, P.N.L. Filho, A. Beltrán, J. Andrés, L. Gracia, E. Longo,Mater. Charact. 73 (2012) 124-129.
[54] L.S. Cavalcante, E. Moraes, M.A.P. Almeida, C.J. Dalmaschio, N.C. Batista, J.A. Varela, E. Longo, M. Siu Li, J. Andrés, A. Beltrán,Polyhedron 54 (2013) 13-25.
[55] E. Longo, L.S. Cavalcante, D.P. Volanti, A.F. Gouveia, V.M. Longo, J.A. Varela, M.O. Orlandi, J. Andrés,Sci. Rep. 3 (2013) 1676.
[56] V.M. Longo, C.C. De Foggi, M.M. Ferrer, A.F. Gouveia, R.S. André, W. Avansi, C.E. Vergani, A.L. Machado, J. Andrés, L.S. Cavalcante, A.C. Hernandes, E. Longo,J. Phys. Chem. A 118 (2014) 5769-5778.
[57] Y.V.B.D. Santana, J.E.C. Gomes, L. Matos, G.H. Cruvinel, A. Perrin, C. Perrin, J. Andrès, J.A. Varela, E. Longo,Nanomater. Nanotechn. 4 (2014) 22.
[58] J. Andrés, M.M. Ferrer, L. Gracia, A. Beltran, V.M. Longo, G.H. Cruvinel, R.L. Tranquilin, E. Longo,Part. Part. Syst. Char. 32 (2015) 646-651.
[59] R.A. Roca, J.C. Sczancoski, I.C. Nogueira, M.T. Fabbro, H.C. Alves, L. Gracia, L.P.S. Santos, C.P. de Sousa, J. Andres, G.E. Luz, E. Longo, L.S. Cavalcante,Catal. Sci. Technol. 5 (2015) 4091-4107.
[60] P.S. Lemos, A. Altomare, A.F. Gouveia, I.C. Nogueira, L. Gracia, R. Llusar, J. Andres, E. Longo, L.S. Cavalcante,Dalton T. 45 (2016) 1185-1191.
[61] A. Catto, F. Tomas, É. L.S. Souza, W. Avansi Jr, J. Andres, K. Aguir, E. Longo, L. S. Cavalcante, L. Da Silva,J. Alloy. Compd. 748 (2018) 411-417.
[62] P. Zubko, S. Gariglio, M. Gabay, P. Ghosez, J.-M. Triscone,Annual Rev. Condensed. Matter. Phys. 2 (2011) 141-165.
[63] L.G. Tejuca, J.L. G.Fierro, J.M. D.Tascon, Structure and Reactivity of Perovskite-Type Oxides. In Advances in Catalysis, in: A. Press (Ed.), New York, 1989.
[64] J. Andres, V.M. Longo, L.S. Cavalcante, M.L. Moreira, J.A. Varela, E. Longo, A Fresh Look at the Structural, Ferroelectric and Photoluminescent Properties in Perovskites, 1 ed., Photoluminescence: Applications, Types and Efficacy, New York - United States, 2012.
[65] E. Grabowska,Appl. Catal. B 186 (2016) 97–126.
[66] W. Wang, M. O.Tadé, Z. Shao,Chem. Soc. Rev. 44 (2015) 5371-5408.
[67] M. Misono,Stud. Surf. Sci. Catal. 176 (2013) 67-95.
[68] G. Botelho, I. Nogueira, E. Moraes, E. Longo,Mater. Chem.Phys. 183 (2016) 110-120.
[69] F.A. Rabuffetti, S.P. Culver, L. Suescun, R.L. Brutchey,Inorg. Chem. 53 (2014) 1056-1061.
[70] S. Balamurugan, T.K. Sana Fathima, K. Veluraja,J. Alloy. Compd. 735 (2018) 1227-1231.
[71] B. Xiao, M. Schmidt,Inorg. Chem. 56 (2017) 14948-14959.

[72] E.S. Babu, B.J. Rani, G. Ravi, R. Yuvakkumar, R.K. Guduru, V. Ganesh, S. Kim,Mater. Lett. 220 (2018) 209-212.
[73] P. Yadav, S.K. Rout, E. Sinha,J. Alloy. Compd. 726 (2017) 1014-1023.
[74] V.B. Mikhailik, H. Kraus, V. Kapustyanyk, M. Panasyuk, P. Yu, V. Tsybulskyi, L. Vasylechko,J. Phys.: Condensed. Matter. 20 (2008) 365219.
[75] S.C. Abrahams,J. Chem. Phys. 46 (1967) 2052-2063.
[76] G.-K. Choi, J.-R. Kim, S.H. Yoon, K.S. Hong,J. Eur. Ceram. Soc. 27 (2007) 3063-3067.
[77] E.S. Kim, C.J. Jeon, P.G. Clem, A. Feteira,J. Am. Ceram. Soc. 95 (2012) 2934-2938.
[78] D.C. Agarwal, D.K. Avasthi, S. Varma, F. Kremer, M.C. Ridgway, D. Kabiraj,J. Appl. Phys. 115 (2014) 163506.
[79] W. Reichelt, T. Weber, T. Söhnel, S. Däbritz,Z. Allg. Chem. 626 (2000) 2020-2027.
[80] L.G. Uitert, J.J. Rubin, W.A. Bonner,J. Am. Ceram. Soc. 46 (1963) 512-512.
[81] R. Sundaram, K.S. Nagaraja,Mater. Res. Bull. 39 (2004) 581-590.
[82] S. Song, Y. Zhang, Y. Xing, C. Wang, J. Feng, W. Shi, G. Zheng, H. Zhang,Adv. Funct. Mater. 18 (2008) 2328-2334.
[83] R.D. Rauh, F. Wang, J.R. Reynolds, D.L. Meeker,Electrochim. Acta 46 (2001) 2023-2029.
[84] P. Černý, H. Jelínková, P.G. Zverev, T.T. Basiev,Prog. Quantum Electron. 28 (2004) 113-143.
[85] T. Oi, K. Takagi, T. Fukazawa,Appl.Phys. Lett. 36 (1980) 278-279.
[86] G. Benoît, J. Véronique, A. Arnaud, G. Alain,Solid State Sci. 13 (2011) 460-467.
[87] N. Faure, C. Borel, M. Couchaud, G. Basset, R. Templier, C. Wyon,Appl. Phys. B 63 (1996) 593-598.
[88] M. Bradler, P. Baum, E. Riedle,Appl. Phys. B 97 (2009) 561.
[89] M. Amberg, J.R. Günter, H. Schmalle, G. Blasse,J. Solid State Chem. 77 (1988) 162-169.
[90] A.P.A. Marques, F.V. Motta, E.R. Leite, P.S. Pizani, J.A. Varela, E. Longo, D.M.A. de Melo,J. Appl. Phys. 104 (2008) 043505.
[91] J.H. Ryu, J.-W. Yoon, C.S. Lim, W.-C. Oh, K.B. Shim,J. Alloy. Compd. 390 (2005) 245-249.
[92] L. Jiang, Z. Wang, H. Chen, Y. Chen, P. Chen, Z. Xu,J. Alloy. Compd. 734 (2018) 179-187.
[93] Y. Zhang, L. Wang, D. Chu, L. Wang, Z. Wang, Z. Wang,Nano-Struct. Nano-Objects 6 (2016) 46-51.
[94] X. Liu, L. Li, H.M. Noh, S.H. Park, J.H. Jeong, H.K. Yang, K. Jang, D.S. Shin,Opt. Mater. 43 (2015) 10-17.
[95] X. Ma, W. Zhao, J. Wu, X. Jia,Mater. Lett. 188 (2017) 248-251.

[96] L.D.S. Alencar, A. Mesquita, C.A.C. Feitosa, R. Balzer, L.F.D. Probst, D.C. Batalha, M.G. Rosmaninho, H.V. Fajardo, M.I.B. Bernardi,Ceram. Inter. 43 (2017) 4462-4469.
[97] M. Li, Y. Guan, Y. Yin, X. Cui, S. Rong, G. Jin, Y. Hao, Q. Wu,Superlattices Microst. 80 (2015) 222-228.
[98] Y. Yin, Z. Gan, Y. Sun, B. Zhou, X. Zhang, D. Zhang, P. Gao,Mater. Lett. 64 (2010) 789-792.
[99] A. Phuruangrat, T. Thongtem, S. Thongtem,Superlattices Microst. 52 (2012) 78-83.
[100] M.Y.A. Khan, M. Zahoor, A. Shaheen, N. Jamil, M.I. Arshad, S.Z. Bajwa, N.A. Shad, R. Butt, I. Ali, M.Z. Iqbal, A. Wu, G. Nabi, S. Hussain, T. Mahmood, I. Aslam, W.S. Khan,Mater. Res. Bull. 104 (2018) 38-43.
[101] V.Y. Degoda, Y.P. Kogut, I.M. Moroz, F.A. Danevich, S.G. Nasonov, E.P. Makarov, V.N. Shlegel,Mater. Res. Bull. 89 (2017) 139-149.
[102] J. Zhang, X. Mao, W. Xiao, Y. Zhuang,Chinese J. Catal. 38 (2017) 2009-2020.
[103] V.Y. Degoda, Y.P. Kogut, I.M. Moroz, F.A. Danevich,J. Lumin. 181 (2017) 269-276.
[104] J. Fei, Q. Sun, J. Li, Y. Cui, J. Huang, W. Hui, H. Hu,Mater. Lett. 198 (2017) 4-7.
[105] N. Jain, Bheeshma P. Singh, R.K. Singh, J. Singh, R.A. Singh,J. Lumin. 188 (2017) 504-513.
[106] C. Raab, M. Simkó, U. Fiedeler, M. Nentwich, A. Gazsó,NanoTrust Dossiers 6 (2011) 1-5.
[107] J. Grunes, J. Zhu, E.A. Anderson, G.A. Somorjai,J. Phys. Chem. B 106 (2002) 11463-11468.
[108] X. Yang, I.D. Williams, J. Chen, J. Wang, H. Xu, H. Konishi, Y. Pan, C. Liang, M. Wu,J. Mater.Chem. 18 (2008) 3543-3546.
[109] M.D. Hollingsworth,Science 295 (2002) 2410-2413.
[110] M. Alfredsson, F. Corà, D.P. Dobson, J. Davy, J.P. Brodholt, S.C. Parker, G.D. Price,Surf. Sci. 601 (2007) 4793-4800.
[111] A.S. Barnard, C.A. Feigl, S.P. Russo,Nanoscale 2 (2010) 2294-2301.
[112] N. Tian, Z.Y. Zhou, S.G. Sun, Y. Ding, Z.L. Wang,Science 316 (2007) 732-735.
[113] C.-S. Tan, S.-C. Hsu, W.-H. Ke, L.-J. Chen, M.H. Huang,Nano Lett. 15 (2015) 2155-2160.
[114] C. Schmidt, J. Ulrich,J. Cryst. Growth 353 (2012) 168-173.
[115] P. Dandekar, Z.B. Kuvadia, M.F. Doherty,Annual Rev. Mater. Res. 43 (2013) 359-386.
[116] W. Piskorz, J. Gryboś, F. Zasada, P. Zapała, S. Cristol, J.-F. Paul, Z. Sojka,J. Phys. Chem. C 116 (2012) 19307-19320.
[117] K.D. Gilroy, H.-C. Peng, X. Yang, A. Ruditskiy, Y. Xia,Chem. Commun. 53 (2017) 4530-4541.
[118] M. Antonietti,Small 12 (2016) 2107-2114.

[119] G. Wulff,zkri 34 (1901) 449-530.
[120] G.D. Barmparis, Z. Lodziana, N. Lopez, I.N. Remediakis,Beilstein J. Nanotech. 6 (2015) 361-368.
[121] M.H. Huang, S. Rej, S.-C. Hsu,Chem. Commun. 50 (2014) 1634.
[122] T.S. Ahmadi, Z.L. Wang, T.C. Green, A. Henglein, M.A. El-Sayed,Science 272 (1996) 1924–1926.
[123] F. Zaera,ChemSusChem 6 (2013) 1797 – 1820.
[124] W.U. Huynh, X. Peng, A.P. Alivisatos,Adv. Mater. 11 (1999) 923-927.
[125] M.C. Schlamp, X. Peng, A.P. Alivisatos,J. Appl. Phys. 82 (1997) 5837-5842.
[126] H. Mattoussi, L.H. Radzilowski, B.O. Dabbousi, E.L. Thomas, M.G. Bawendi, M.F. Rubner,J. Appl. Phys. 83 (1998) 7965-7974.
[127] M. Bruchez, M. Moronne, P. Gin, S. Weiss, A.P. Alivisatos,Science 281 (1998) 2013–2016.
[128] W.C.W. Chan, N. Shuming,Science 281 (1998) 2016-2018.
[129] S. Sun, Z. Yang,RSC Adv. 4 (2014) 3804-3822.
[130] N. Tian, Z.-Y. Zhou, S.-G. Sun,Chem. Commun. (2009) 1502-1504.
[131] T. Xu, X. Zhou, Z. Jiang, Q. Kuang, Z. Xie, L. Zheng,Cryst. Growth Des. 9 (2009) 192-196.
[132] D. Fan, P.J. Thomas, P. O'Brien,J. Am. Ceram. Soc. 130 (2008) 10892-10894.
[133] H.-G. Liao, Y.-X. Jiang, Z.-Y. Zhou, S.-P. Chen, S.-G. Sun,Angew. Chem 47 (2008) 9100–9103.
[134] M. Leng, M. Liu, Y. Zhang, Z. Wang, C. Yu, X. Yang, H. Zhang, C. Wang,J. Am. Ceram. Soc. 132 (2010) 17084-17087.
[135] H.G. Yang, G. Liu, S.Z. Qiao, C.H. Sun, Y.G. Jin, S.C. Smith, J. Zou, H.M. Cheng, G.Q. Lu,J. Am. Ceram. Soc. 131 (2009) 4078-4083.
[136] X. Xie, Y. Li, Z.-Q. Liu, M. Haruta, W. Shen,Nature 458 (2009) 746-749.
[137] K. Zhou, Y. Li,Angew. Chem. Int. Ed. 51 (2012) 602-613.
[138] B. Wu, N. Zheng,Nano Today 8 (2013) 168-197.
[139] Q. Kuang, X. Wang, Z. Jiang, Z. Xie, L. Zheng,Accounts Chem. Res. 308-318 (2014) 308-318.
[140] X. Han, M. Jin, S. Xie, Q. Kuang, Z. Jiang, Y. Jiang, Z. Xie, L. Zheng,Angew. Chem. Int. Ed. 48 (2009) 9180-9183.
[141] L. Hu, Q. Peng, Y. Li,J. Am. Chem. Soc. 130 (2008) 16136-16137.
[142] L. Wang, H. Li, S. Xu, Q. Yue, J. Liu,Mater. Chem.Phys. 147 (2014) 1134-1139.
[143] T. Luo, Q.-Q. Meng, C. Gao, X.-Y. Yu, Y. Jia, B. Sun, Z. Jin, Q.-X. Li, J.-H. Liu, X.-J. Huang,Chem. Commun. 50 (2014) 15952-15955.
[144] X.-Y. Yu, Q.-Q. Meng, T. Luo, Y. Jia, B. Sun, Q.-X. Li, J.-H. Liu, X.-J. Huang,Sci. Rep. 3 (2013) 2886.
[145] Y.-w. Jun, J.-s. Choi, J. Cheon,Angew. Chem. Int. Ed. 45 (2006) 3414-3439.

[146] C. Wang, H. Daimon, T. Onodera, T. Koda, S. Sun,Angew. Chem. Int. Ed. 47 (2008) 3588-3591.
[147] A.R. Tao, S. Habas, P. Yang,Small 4 (2008) 310-325.
[148] Z.-Y. Jiang, Q. Kuang, Z.-X. Xie, L.-S. Zheng,Adv. Funct. Mater. 20 (2010) 3634-3645.
[149] B. Liu, A. Khare, E.S. Aydil,ACS Appl. Mater. Inter. 3 (2011) 4444-4450.
[150] Y. Xia, X. Xia, H.-C. Peng,J. Am. Ceram. Soc. 137 (2015) 7947-7966.
[151] S. De Waele, K. Lejaeghere, M. Sluydts, S. Cottenier,Phys. Rev. B 94 (2016) 235418.
[152] J. Andrés, L. Gracia, A.F. Gouveia, M.M. Ferrer, E. Longo,Nanotechnol. 26 (2015) 405703.
[153] R. Dovesi, R. Orlando, B. Civalleri, C. Roetti, R. Saunders Victor, M. Zicovich-Wilson Claudio,zkri 220 (2005) 571–573.
[154] R. Dovesi, B. Civalleri, R. Orlando, C. Roetti, V.R. Saunders, In:Reviews in Computational Chemistry, in: B.K. Lipkowitz, R. Larter, T.R. Cundari (Eds.) John Wiley & Sons, New York, 2005, pp. 1-125.
[155] R. Demichelis, M. Bruno, F.R. Massaro, M. Prencipe, M.D.L. Pierre, F. Nestola,J. Comput. Chem. 36 (2015) 1439-1445.
[156] M. De La Pierre, M. Bruno, C. Manfredotti, F. Nestola, M. Prencipe, C. Manfredotti,Mol. Phys. 112 (2014) 1030-1039.
[157] F. Vines, J.R.B. Gomes, F. Illas,Chem. Soc. Rev. 43 (2014) 4922-4939.
[158] M.L. Moreira, J. Andrés, L. Gracia, A. Beltrán, L.A. Montoro, J.A. Varela, E. Longo,J. Appl. Phys. 114 (2013) 043714
[159] M.C. Oliveira, L. Gracia, M. de Assis, I.L.V. Rosa, M.F. do Carmo Gurgel, E. Longo, J. Andrés,J. Alloy. Compd. 722 (2017) 981-995.
[160] A. Beltrán, L. Gracia, E. Longo, J. Andrés,J. Phys. Chem. C 118 (2014) 3724-3732.
[161] M.T. Fabbro, C. Saliby, L.R. Rios, F.A.L. Porta, L.E. Gracia, M.S. Li, J. Andrés, L.P.S. Santos, E. Longo,Sci. Technol. Adv. Mater 16 (2015) 065002.
[162] M.C. Oliveira, L. Gracia, I.a.C. Nogueira, M.F.C. Gurgel, J.M.R. Mercury, E. Longo, J. Andrés,Cryst. Res. Technol 51 (2016) 634–644.
[163] L. Gracia, V. M. Longo, L. S. Cavalcante, A. Beltrán, W. Avansi, M. S. Li, V. R. Mastelaro, J. A. Varela, E. Longo, J. Andrés,J. Appl. Phys. 110 (2011) 043501.
[164] F.M.C. Batista, F.A.L. Porta, L. Gracia, E. Cerdeiras, L. Mestres, M.S. Li, N.C. Batista, J. Andrés, E. Longo, L.S. Cavalcante,J. Mol. Struct. 1081 (2015) 381-388.
[165] E. Longo, D.P. Volanti, V.M. Longo, L. Gracia, I.C. Nogueira, M.A.P. Almeida, A.N. Pinheiro, M.M. Ferrer, L.S. Cavalcante, J. Andrés,J. Phys. Chem. C 118 (2014) 1229-1239

[166] M.C. Oliveira, L. Gracia, I.C. Nogueira, M.F.C. Gurgel, J.M.R. Mercury, E. Longo, J. Andrés,Ceram. Inter. 42 (2016) 10913-10921.
[167] G.S. Silva, L. Gracia, M.T. Fabbro, L.P. Serejo dos Santos, H. Beltrán-Mir, E. Cordoncillo, E. Longo, J. Andrés,Inorg. Chem. 55 (2016) 8961-8970.
[168] A.F. Gouveia, M.M. Ferrer, J.R. Sambrano, J. Andrés, E. Longo,Chem. Phys. Lett. 660 (2016) 87-92.
[169] R.A.P. Ribeiro, S.R. de Lazaro, L. Gracia, E. Longo, J. Andrés,J. Magn. Magn. Mater. 453 (2018) 262-267.
[170] M.M. Ferrer, A.F. Gouveia, L. Gracia, E. Longo, J. Andrés,Model. Simul. Mater. Sci. Eng. 24 (2016) 025007.
[171] P. Hohenberg, W. Kohn,Phys. Rev. 136 (1964) B864-B871.
[172] E.G. Lewars, Computational Chemistry: Introduction to the Theory and Applications of Molecular and Quantum Mechanics, 1 ed. ed., Springer Netherlands, Dordretch, 2011.
[173] N.H. Morgon, K. Coutinho, Métodos de Química Teórica e Modelagem Molecular, 1 Ed. ed., Livraria da Física, São Paulo, 2007.
[174] B.G. Janesko, T.M. Henderson, G.E. Scuseria,Phys. Chem. Chem. Phys. 11 (2009) 443-454.
[175] A.D. Becke,J. Chem. Phys. 140 (2014) 18A301.
[176] D.M. Vianna, A. Fazzio, S. Canuto, Teoria Quântica de Moléculas e Sólidos: Simulação Computacional, 1 ed., Livraria da Física, São Paulo, 2004.
[177] J. Andrés, J. Beltran, Quimica teórica y computacional, 1 ed., Universidade Jaume I, Castello de La Plana, 2000.
[178] R.A. Evarestov, Theoretical Modeling of Inorganic Nanostructures: Symmetry and ab-initio Calculations of Nanolayers, Nanotubes and Nanowires, Springer Berlin, 2015.
[179] D. Young, Computational Chemistry: A Practical Guide for Applying Techniques to Real World Problems, 1 ed., John Wiley & Sons, New York, 2004.
[180] P. Atkins, J. De Paula, R. Friedman, Quanta, Matéria e Mudança: Uma abordagem molecular para a Físico-Química, 1 ed., LTC, São Paulo, 2011.
[181] W. Kohn, L.J. Sham,Phys. Rev. 140 (1965) A1133-A1138.
[182] Z.-y. Chen, J.-l. Yang,Front. Phys. China 1 (2006) 339-343.
[183] A. Erba, J. Maul, M.D.L. Pierre, R. Dovesi,J. Chem. Phys. 142 (2015) 204502.
[184] F. Cesare,J. Phys.: Condensed. Matter. 26 (2014) 253202.
[185] M.D.L. Pierre, R. Orlando, L. Maschio, K. Doll, P. Ugliengo, R. Dovesi,J. Comput. Chem. 32 (2011) 1775-1784.
[186] H. Jiang,Int. J. Quantum Chem. 115 (2015) 722-730.
[187] A.J. Cohen, P. Mori-Sánchez, W. Yang,Phys. Rev. B 77 (2008) 115123.
[188] J.P. Perdew, A. Zunger,Phys. Rev. B, Condensed. Matter. Mater. Phys. 23 (1981) 5048-5079.

[189] A.J. Cohen, P. Mori-Sanchez, W. Yang,Phys. Rev. B, Condensed. Matter. Mater. Phys. 77 (2008) 115123.
[190] C. Franchini,J. Phys.: Condensed. Matter. 26 (2014) 253202.
[191] A.D. Becke,J. Appl. Phys. 98 (1993) 1372-1377.
[192] J.A. Pople, M. Head-Gordon, D.J. Fox, K. Raghavachari, L.A. Curtiss,J. Chem. Phys. 90 (1989) 5622-5629.
[193] A.D. Becke,J. Comput. Chem. 98 (1993) 5648-5652.
[194] C. Lee, W. Yang, R.G. Parr,Phys. Rev. B, Condensed. Matter. Mater. Phys. 37 (1988) 785-789.
[195] P.J. Stephens, F.J. Devlin, C.F. Chabalowski, M.J. Frisch,J. Phys. Chem. 98 (1994) 11623-11627.
[196] J. Paier, M. Marsman, G. Kresse,J. Chem. Phys. 127 (2007) 024103.
[197] K. Burke,J. Chem. Phys. 136 (2012) 150901.
[198] C. Adamo, V. Barone,J. Chem. Phys. 110 (1999) 6158-6170.
[199] F. Corà, M. Alfredsson, G. Mallia, D.S. Middlemiss, W.C. Mackrodt, R. Dovesi, R. Orlando, The Performance of Hybrid Density Functionals in Solid State Chemistry, in: N. Kaltsoyannis, J.E. McGrady (Eds.), Principles and Applications of Density Functional Theory in Inorganic Chemistry II, Springer Berlin Heidelberg, Berlin, Heidelberg, 2004, pp. 171-232.
[200] S. Piskunov, E. Heifets, R.I. Eglitis, G. Borstel,Comp. Mater. Sci. 29 (2004) 165-178.
[201] S.F. Sousa, P.A. Fernandes, M.J. Ramos,J. Phys. Chem. A 111 (2007) 10439-10452.
[202] F.R. Sensato, R. Custodio, E. Longo, A. Beltrán, J. Andrés,Catal. Today 85 (2003) 145-152.
[203] B. Di Bartolo, Optical Properties of Excited States in Solids, 1 ed., Springer, London, 1992.
[204] Q. Wu, T. Van Voorhis,J. Chem. Theory Comput. 2 (2006) 765-774.
[205] X. Qin, X. Liu, W. Huang, M. Bettinelli, X. Liu,Chem. Rev. 117 (2017) 4488-4527.
[206] L. Gracia, J. Andrés, V.M. Longo, J.A. Varela, E. Longo,Chem. Phys. Lett. 493 (2010) 141-146.
[207] L. Gracia, V.M. Longo, L.S. Cavalcante, A. Beltrán, W. Avansi, M.S. Li, V.R. Mastelaro, J.A. Varela, E. Longo, J. Andrés,J. Appl. Phys. 110 (2011) 043501.
[208] L.F. da Silva, J.-C. M'Peko, J. Andrés, A. Beltrán, L. Gracia, M.I.B. Bernardi, A. Mesquita, E. Antonelli, M.L. Moreira, V.R. Mastelaro,J. Phys. Chem. C 118 (2014) 4930-4940.
[209] V.M. Longo, M. das Graca Sampaio Costa, A. Zirpole Simoes, I.L.V. Rosa, C.O.P. Santos, J. Andres, E. Longo, J.A. Varela,Phys. Chem. Chem. Phys. 12 (2010) 7566-7579.
[210] M.L. Moreira, P.G.C. Buzolin, V.M. Longo, N.H. Nicoleti, J.R. Sambrano, M.S. Li, J.A. Varela, E. Longo,J. Phys. Chem. A 115 (2011) 4482-4490.

[211] R. Uarth Fassbender, T. Strelow Lilge, S. Cava, J. Andres, L. Fernando da Silva, V. Roberto Mastelaro, E. Longo, M. Lucio Moreira,Phys. Chem. Chem. Phys. 17 (2015) 11341-11349.
[212] H.J. Monkhorst, J.D. Pack,Phys. Rev. B 13 (1976) 5188.
[213] http://Www.Crystal.Unito.It/Basis_Sets/Molibdenum.Html, Molibdenum Basis set.
[214] http://Www.Crystal.Unito.It/Basis_Sets/europium.Html.
[215] F. Cora, A. Patel, N.M. Harrison, R. Dovesi, C.R.A. Catlow,J. Am. Chem. Soc. 118 (1996) 12174-12182.
[216] http://Www.Tcm.Phy.Cam.Ac.Uk/˜Mdt26/Basis_Sets/Ba_Basis.Txt.
[217] http://Www.Crystal.Unito.It/Basis_Sets/Oxygen.Html.
[218] L. Valenzano, F.J. Torres, K. Doll, F. Pascale, C.M. Zicovich-Wilson, R. Dovesi,Z. Phys. Chem. 220 (2006) 893-912.
[219] T. Homann, U. Hotje, M. Binnewies, A. Börger, K.-D. Becker, T. Bredow,Solid State Sci. 8 (2006) 44-49.
[220] L. Valenzano, B. Civalleri, S. Chavan, S. Bordiga, M.H. Nilsen, S. Jakobsen, K.P. Lillerud, C. Lamberti,Chem. Mater. 23 (2011) 1700–1718.
[221] V.R.S. R. Dovesi, C. Roetti, R. Orlando, C. M. Zicovich-Wilson, F. Pascale, B. Civalleri, K. Doll, N.M. Harrison, I.J. Bush, Ph. D'Arco, M. Llunel, M. Caus`a, Y. No¨e, CRYSTAL14, in: U.O. Torino (Ed.) Torino-Italy, 2014.
[222] R. Dovesi, V.R. Saunders, R.O. C. Roetti, C.M. Zicovich-Wilson, B.C. F. Pascale, K. Doll, N.M. Harrison, I.J. Bush, P. D'Arco, M. Llunel, M.C. YN, http://www.crystal.unito.it/basis-sets.php. .
[223] K. Momma, F. Izumi,J. Appl. Crystallogr. 44 (2011) 1272-1276.
[224] P. Canepa, R.M. Hanson, P. Ugliengo, M. Alfredsson,J. Appl. Crystallogr. 44 (2011) 225-229.
[225] A. Kokalj,J. Mol. Graph. Model. 17 (1999) 176-179.
[226] S. Vidya, S. Solomon, J.K. Thomas,Mater. Today: Proc. 2 (2015) 904-908.
[227] J.B. Foresman, E. Frisch, Exploring Chemistry with Electronic Structure Methods, Frequency Calculations. Gaussian, Inc., Pittsburgh. P.A, 1996, pp. 61-90.
[228] R.P. Jia, C. Zhang, J.Y. Xu,Adv. Mat. Res. 624 (2012) 51-54.
[229] D. Wang, M. Huang, Y. Zhuang, H.l. Jia, J. Sun, M. Guan,Eur. J. Inorg. Chem. 16 (2017) 4939-4946.

7. Publicaciones

Ceramics International 42 (2016) 10913–10921

Contents lists available at ScienceDirect

Ceramics International

journal homepage: www.elsevier.com/locate/ceramint

Synthesis and morphological transformation of $BaWO_4$ crystals: Experimental and theoretical insights

Marisa Carvalho Oliveira [a,b], Lourdes Gracia [a], Içamira Costa Nogueira [c], Maria Fernanda do Carmo Gurgel [d], Jose Manuel Rivas Mercury [c], Elson Longo [e], Juan Andrés [a,*]

[a] Department of Analytical and Physical Chemistry, University Jaume I (UJI), Castelló E-12071, Spain
[b] CDMF-UFSCar, Universidade Federal de São Carlos, PO Box 676, 13565-905 São Carlos, SP, Brazil
[c] PPGEM-IFMA, Instituto Federal do Maranhão, CEP 65030-005 São Luís, MA, Brazil
[d] Department of Chemistry, Universidade Federal de Goiás, Regional Catalão, Av.Dr.Lamartine Pinto de Avelar, 75704-020 Catalão, GO, Brazil
[e] CDMF-UNESP, Universidade Estadual Paulista, PO Box 355, CEP 14801-907 Araraquara, SP, Brazil

ARTICLE INFO

Article history:
Received 16 February 2016
Received in revised form
18 March 2016
Accepted 29 March 2016
Available online 30 March 2016

Keywords:
$BaWO_4$ crystals
Co-precipitation method
Morphology
DFT calculations
Surface energies

ABSTRACT

$BaWO_4$ crystals have been obtained by a co-precipitation method, and their structures were characterized by X-ray diffraction and Rietveld refinement techniques, while field emission scanning electron microscopy was utilized to investigate the morphology of the as-synthesized aggregates. Geometries, bulk electronic properties, surface energies, and surface tension of the obtained $BaWO_4$ crystals were evaluated using first-principles quantum mechanical calculations. A theoretical model based on the Wulff construction was introduced to explain possible crystal morphologies by tuning their surface chemistry, which is related to the relative stability of the faceted crystals. Both the experimental and theoretical data revealed the presence of (112), (001), and (100) facets with low values of surface energy in the $BaWO_4$ crystals. The experimental morphologies of the as-synthesized samples are similar to the theoretically obtained shapes when surface energy values for the (001) and (100) surfaces are increased simultaneously.

1. Introduction

Barium tungstate ($BaWO_4$) crystals have attracted significant interest from many research groups due to their potential applications in scintillation devices, batteries, capacitors, photocatalysts, and, in particular, photoluminescent materials [1–6]. In recent years, various synthetic methods have been used to produce $BaWO_4$ crystals, such as co-precipitation (CP), sol–gel, modified Pechini, solid state reaction, solution route, Czochralski, sonochemical, and hydrothermal techniques [7–24].

$BaWO_4$ is a semiconductor that belongs to the family of scheelites with crystallized tetragonal structures having the space group $I4_1/_a$ and symmetry C_{4h}^6, in which Ba atoms are coordinated to eight O atoms, while W atoms have tetragonal coordination of O atoms; thus, the building blocks of the $BaWO_4$ crystal are deltahedral $[BaO_8]$ and tetrahedral $[WO_4]$ clusters [14,25–30]. Distortions of these clusters caused by the deformations of W–O and Ba–O bond distances as well as by tilting of O–W–O and O–Ba–O bond angles have a significant effect on their geometry, surface structure, and related properties [14]. Various theoretical studies have been published on the geometry as well as electronic and optical properties of $BaWO_4$ [19,31–33].

Surface properties of materials strongly depend on their morphology that is characterized by types and relative areas of various crystal facets, which usually can be tuned by tailoring their facets with different surface atomic arrangements and coordination. In general, the most stable surfaces control the crystal growth process, while less stable crystal facets contain large numbers of kink atoms in high-index planes [34]. Thus, studying the morphology of micro- and nanomaterials is an essential step in understanding their physical and chemical properties, while controlled synthesis of specific morphologies is critical for enhancing their performance in practical applications [35,36]. In particular, morphology-controlled syntheses of $BaWO_4$ have been performed by various research groups [37–40]. Nevertheless, these methods are far from being optimized, and their experimental aspects are still debated. In this context, experimental surface energies cannot be readily attained, and computer modeling and simulations are necessary to obtain surface characteristics of $BaWO_4$, which are powerful tools for exploring morphological mechanisms at the atomistic/molecular level.

---

* Corresponding author.
E-mail address: andres@uji.es (J. Andrés).

http://dx.doi.org/10.1016/j.ceramint.2016.03.225
0272-8842/© 2016 Elsevier Ltd and Techna Group S.r.l. All rights reserved.

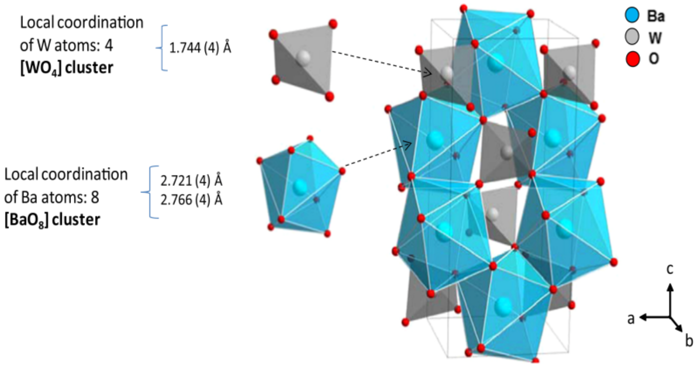

Fig. 1. A polyhedral representation of the BaWO$_4$ unit cell. The local coordination corresponding to the deltahedral [BaO$_8$] and tetrahedral [WO$_4$] clusters is depicted for both Ba and W atoms, respectively.

Using a specific methodology, which has been applied to study morphologies of various metal oxides such as SnO$_2$ [41], PbMoO$_4$ [42], and CaWO$_4$ [43], we developed a combination of experimental studies with first-principles calculations to deeper investigate electronic, structural, and energetic properties controlling the morphology and related transformation mechanisms of various metals and metal oxides such as Ag, anatase TiO$_2$, BaZrO$_3$, and α-Ag$_2$WO$_4$ [44] as well as Co$_3$O$_4$, Fe$_2$O$_3$, and In$_2$O$_3$ [45]. Based on the obtained results, we were able to explore facet-dependent photocatalytic and antibacterial properties of α-Ag$_2$WO$_4$ crystals [46] as well as the relationship between the photoluminescence and photocatalytic properties of Ag$_3$PO$_4$ microcrystals [47] and then identify and rationalize morphological, structural, and optical properties of β-Ag$_2$MoO$_4$ microcrystals [48]. These cited papers contain a description of the method of calculating surface energies, which were used to characterize the corresponding surface morphologies.

The main goal of this article is to investigate the morphology of the as-synthesized BaWO$_4$ crystals characterized by X-ray diffraction and Rietveld refinement and field emission scanning electron microscopy techniques, as well as to simulate the crystal shape possibilities using first-principles quantum mechanical calculations based on the Wulff construction.

2. Experimental

2.1. Synthesis of BaWO$_4$ crystals

BaWO$_4$ crystals were synthesized by a CP method at 353 K in aqueous solutions. A typical synthesis procedure for the BaWO$_4$ crystals can be described as follows: 1×10^{-3} mol of sodium tungstate dihydrate ($Na_2WO_4 \cdot 2H_2O$) (99.5% purity, Stream Chemical) and 1×10^{-3} mol of barium nitrate [$Ba(NO_3)_2$] (99% purity, Sigma-Aldrich) salts were dissolved in two separate beakers containing 50 mL of deionized water under constant stirring until it reaches 353 K. Next, the barium nitrate solution was added to the sodium tungstate dihydrate solution and maintained under agitation at 353 K for 20 min. As a result, a white precipitate was rapidly formed, which was washed with deionized water several times. Finally, the obtained white precipitates were collected and dried in a conventional furnace at 323 K for 8 h.

2.2. Characterization

BaWO$_4$ crystals were structurally characterized by X-ray diffraction (XRD) using a DMax/2500PC diffractometer (Rigaku, Japan) with Cu Kα radiation ($\lambda = 1.5406$ Å) in a 2θ range from 10° to 110° with an angular step of 0.02° min^{-1}. Rietveld refinement [49] of the obtained XRD patterns was performed by using a general structure analysis (GSAS) program [50]. The diffraction peak profiles were adjusted by utilizing Thompson-Cox-Hastings pseudo-Voigt (pV-TCH) and asymmetry functions as described by Finger et al. [51] Strain anisotropy broadening was corrected by applying a phenomenological model described by Stephens [52]. Morphologies of the synthesized BaWO$_4$ crystals were studied with a field-emission scanning electron microscope (FE–SEM) (model Inspect F50, FEI Company, Hillsboro, OR) operated at 15 kV.

2.3. Computational methods and modeling

First-principles calculations were conducted within the framework of the density functional theory (DFT) using the CRYSTAL14 software package [53]. The gradient-corrected correlation functional by Lee et al. [54] combined with the Becke's exchange functional (B3LYP) [55] was used for all calculations. This method has been successfully employed in various studies of bulk and surface electronic and structural properties of perovskite [56,57], tungstate [42,58,59], and molybdate-based materials [60]. Diagonalization of the Fock matrix was performed at adequate k-points grids (Pack–Monkhorst 1976) in the reciprocal space. The thresholds controlling the accuracy of the Coulomb and exchange integral calculations were set to 10^{-8} (ITOL1 to ITOL4) and 10^{-14} (ITOL5), respectively, whereas the percentage of Fock/Kohn–Sham matrices mixing was set to 30 (IPMIX=30) [61]. The W atoms were described by large-core effective core potentials derived by Hay and Wadt and modified by Cora et al. [62], while the O [63] and Ba [64] atoms were represented by the 6-31G* basis set.

The surface energy, E_{surf} [43,45], was calculated by using the equation ($E_{slab} - nE_{bulk}$)/½A, where nE_{bulk} is the number of surface molecular units multiplied by the energy of the bulk, E_{slab} is the total energy of the surface slab per molecular unit, and A is the surface area. The equilibrium shape of a crystal can be calculated by utilizing Wulff constructions that minimize the total surface free energy at a fixed volume, providing a simple relationship between the surface energy, E_{surf}, of a (hkl) plane and its distance from the center of the crystallite in the normal direction [65]. The Visualization for Electronic and Structural Analysis (VESTA) program [66] has been utilized to obtain morphologies of the BaWO$_4$ crystals. Band structures were calculated for 80 k-points along the appropriate high-symmetry paths of the adequate Brillouin zone.

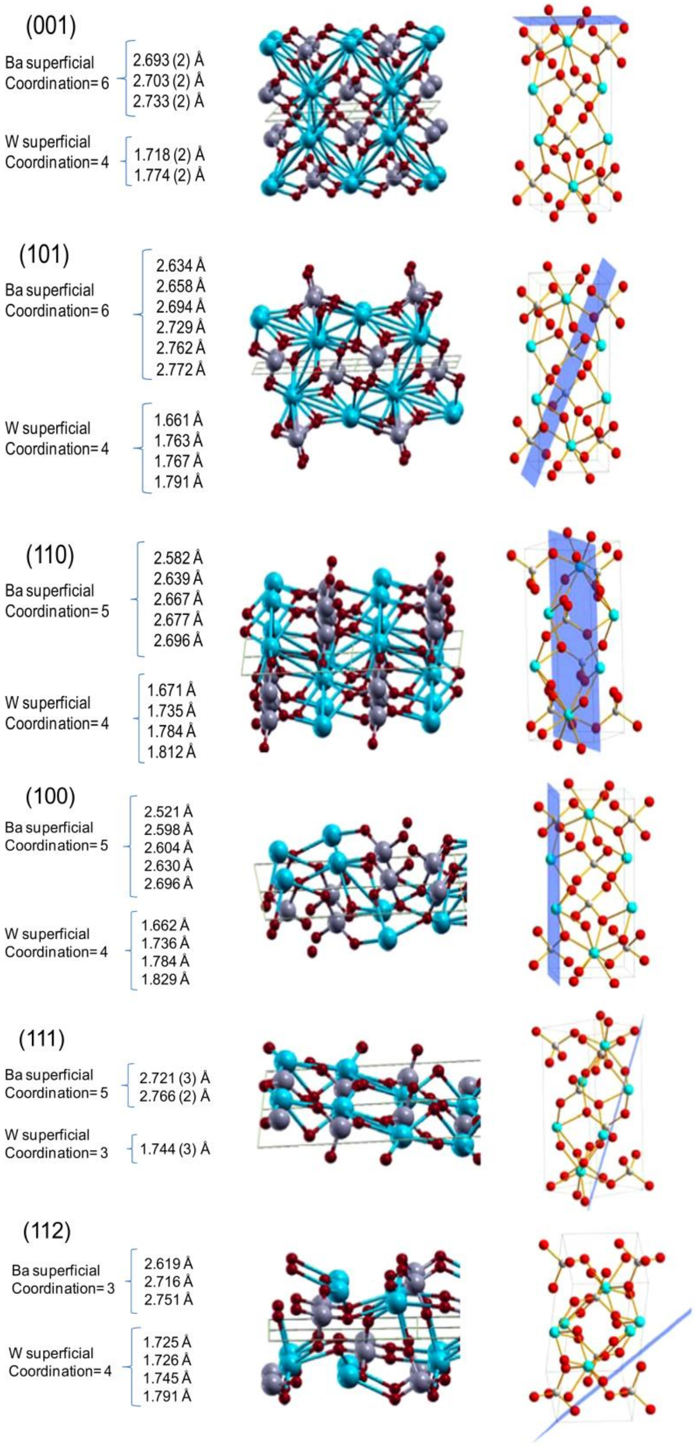

Fig. 2. Schematic representations of the (001), (101), (110), (100), (111), and (112) surfaces. The values of Ba–O and W–O bond distances are listed for the superficial Ba and W atoms, respectively.

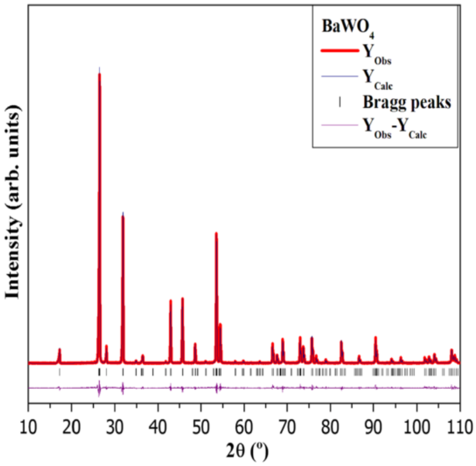

Fig. 3. Rietveld refinements for the $BaWO_4$ crystals.

Table 1
Calculated and experimental values of the lattice parameters (*a* and *c*) and atomic coordinates of the O_x, O_y, and O_z.

Data	Cell parameters		Oxygen coordinates		
	a (Å)	*c* (Å)	O_x	O_y	O_z
Theo. (this work)	5.5927	12.4055	0.2245	0.1219	0.04635
Exp. (this work)	5.6149	12.7326	0.2295	0.1294	0.05024
Exp. [5]	5.6102	12.7100	–	–	–
Exp. [2]	5.6063	12.7107	0.76731	0.14013	0.08188
Exp. [6]	5.615 (2)	12.722 (4)	0.2422 (2)	0.1403 (3)	0.0369 (9)
Exp. [10]	5.612	1 2.706	–	–	–
Exp. [14]	5.5682	12.7702	–	–	–
Exp/theo. [19]	5.611	12.6885	0.2415	0.0086	0.2126
Theo [32,33]	5.61	12.71	–	–	–
Exp. [77]	5.6034	12.6937	0.2336 (4)	0.0976 (6)	0.0499 (6)

The density of state (DOS) was obtained to analyze the corresponding electronic structures.

Based on the theoretical and experimental results, seven models were constructed using a single conventional 1 1 1 cell as a repeating unit to represent bulk and surface structures. First, structural and electronic properties were calculated for a perfect bulk $BaWO_4$ lattice (Fig. 1).

The representation of the $BaWO_4$ bulk structure is shown in Fig. 1. The W atoms are coordinated to four O atoms, producing tetrahedral [WO_4] clusters (with 4 vertices, 4 faces, and 6 edges). Correspondingly, the Ba atoms are coordinated to eight O atoms, resulting in a formation of [BaO_8] clusters (with 8 vertices, 12 faces, and 18 edges) [67].

In the second step, different surfaces were modeled by using unreconstructed (truncated bulk) [68] slab models with calculated equilibrium geometries. The (001), (101), (110), (100), (111), and (112) surfaces of $BaWO_4$ were simulated considering symmetrical slabs (with respect to the mirror plane). All surfaces were terminated with O planes; and after the corresponding optimization process and thickness convergence tests, the resulting slab models consisted of four molecular units containing 24 atoms, as shown in Fig. 2.

Note that the (101), (111), and (112) surfaces are terminated with W and O atoms, while the other listed surfaces are Ba–O terminated. The W surface atoms are coordinated to three or four O atoms, forming [WO_3] or [WO_4] clusters, respectively, while the Ba surface atoms are coordinated to three, five, or six O atoms, forming [BaO_3], [BaO_5] or [BaO_6] clusters, respectively.

Present equilibrium morphology models are derived from calculated surface energies [65,69,70] using the assumption that crystal faces with lowest surface energies control the crystal morphology [71–73]. Since surface stability depends on atomic configurations of exposed facets [74], the local coordination of both the W and Ba atoms controls the crystal morphology of $BaWO_4$ and corresponding behavior of each surface (as shown in Fig. 2).

Another important aspect that should be considered when studying solid materials is a distinction between the surface energy, E_{surf}, and the surface tension, σ. The surface tension is a “surface stress” represented by a work force per unit area in the surface layer [75,76]. The surface tension can be obtained using the thermodynamic stability model described by the equation $\sigma = \partial E_{tot}/\partial A$, where E_{tot} is the total energy with contributions from the particle bulk and surfaces. To calculate E_{tot}, uniform dilation with an area, ΔA (corresponding to a constant ratio between the in-plane lattice parameters *x*:*y*) of the structure must be performed while optimizing only the internal parameters (without optimization of the in-plane cell parameters). Thus, E_{tot} can be calculated as $½(E_{slab}\ \ nE_{bulk})$ for optimized structures and surfaces after dilation. Therefore, by applying two-dimensional dilation to a slab in the surface plane and calculating the total energy as previously described, a change in total energy (ΔE_{tot}) after dilation could be obtained for a given dilation area value.

3. Results and discussion

3.1. X-ray diffraction measurements and Rietveld refinements

The crystal structure, the lattice parameters and the atomic positions were obtained by using the Rietveld refinement method (Fig. 3). The calculated values for the $BaWO_4$ structure are collected in Table 1 and compared with experimental ones, as well as with previous theoretical and experimental results [19,32,33].

The Rietveld refinement results indicate that the obtained diffraction patterns for the $BaWO_4$ crystals match the corresponding spectra in the Inorganic Crystal Structure Database (ICSD, card N° 250487) [77], as shown in Fig. 3, which compares the observed patterns with the calculated ones. Low deviation values for the statistical parameters R_{wp}, R_p, R_{Bragg}, and χ^2 (14.73%, 9.32%, 5.45% and 1.29%, respectively) were found, which indicate good quality of the structural refinements. The lattice parameters (a, $b = 5.6149$ Å, $c = 12.7326$ Å and $\alpha = \beta = \gamma = 90°$) estimated from the refinements correspond to a tetragonal structure with space group $I4_1/_a$ (N° 88) and four molecular formula units per unit cell ($Z = 4$), which confirms the applicability of the CP method to the synthesis of $BaWO_4$ crystals.

As can be observed in Table 1, the agreement of our calculations with the experiments is reasonably good, being the unit-cell volume underestimated by 3.3% and the axial ratio c/a agrees within 2.2%. In addition, our structural data are according to previously reported theoretical and experimental results.

3.2. Band structure and density of states

The band structures and projected DOS for atoms and orbitals in the bulk $BaWO_4$ and (001), (101), (110), (100), (111), and (112) surfaces are presented in Fig. 4.

The analysis of the principal components of atomic orbitals (AOs) for selected bands shows that the $BaWO_4$ valence band (VB) mostly consists of $2p_x$, $2p_y$, and $2p_z$ orbitals of the O atoms, with the most important contribution coming from the $2p_x$ orbitals. The

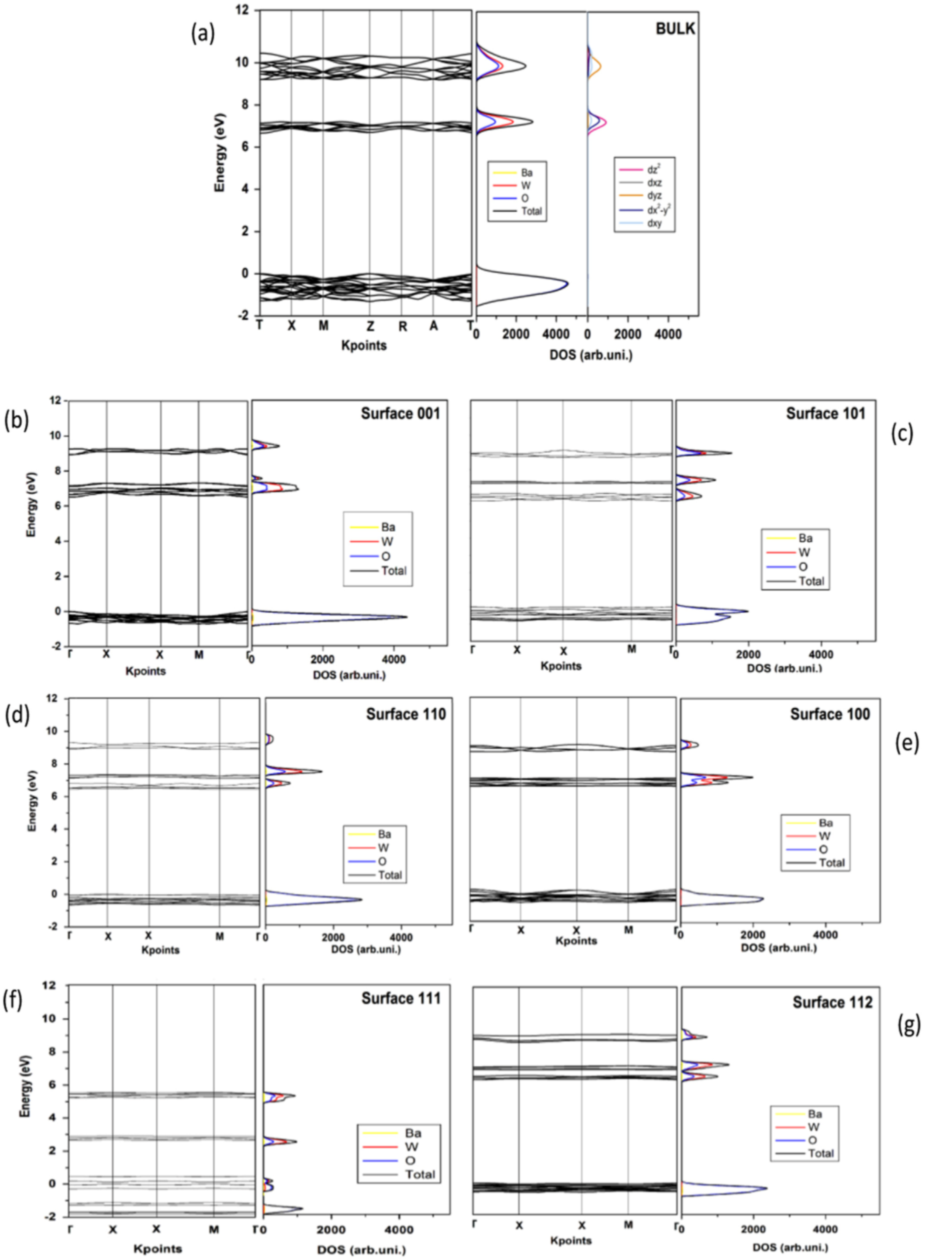

Fig. 4. Calculated band structures and DOS for the (a) bulk $BaWO_4$ and (b) (001), (c) (101), (d) (110), (e) (100), (f) (111), and (g) (112) surfaces.

lowest part of the conduction band (CB) is composed of the $5d_z{}^2$, $5d_{xz}$, $5d_{yz}$, $5d_{x2\ y2}$, and $5d_{xy}$ AOs of the W atoms, with the $5d_z{}^2$ orbitals being the most important components for the bulk $BaWO_4$.

The band structure and DOS projected for the (001), (101), (110), (100), (111), and (112) surfaces are shown in Fig. 4(b–g). The gap energy, E_{gap}, obtained for these surfaces is very similar to that for the bulk crystal (see Table 2). However, the bands contributing to the lowest part of the CB have different arrangements for each studied surface, which affect the contribution of the W 5d orbitals depending on the selected surface. It should be noted that the (111) surface exhibits conducting behavior.

Table 2
Calculated values of the surface energy, surface tension, gap energy, and change in total energy (ΔE_{tot}) for a given value of dilation area (ΔA) for each surface.

Surface	E_{suf} (J/m^2)	ΔE_{tot} (Hartree)	ΔA (Å^2)	σ (J/m^2)	E_{gap}(eV)
(112)	0.92	0.034	2.350	0.73	6.60
(001)	1.02	0.034	1.263	0.57	6.52
(110)	1.10	0.034	1.982	0.85	6.45
(100)	1.22	0.039	2.803	1.09	6.47
(101)	1.31	0.039	1.537	0.91	6.17
(111)	2.06	0.020	4.161	2.58	Conductor

3.3. FE-SEM analyses and morphologies of the BaWO$_4$ crystals

The morphologies of the BaWO$_4$ crystals obtained by FE–SEM are depicted in Fig. 5.

As shown by the obtained experimental micrographs (Fig. 5) [15], crystal morphologies can be modified by tuning surface energy values for various facets using the Wulff theorem and the related construction method [65]. Taking into account the (001), (101), (110), (100), (111), and (112) facets, various crystal morphologies for BaWO$_4$ are displayed in Fig. 6.

Fig. 2 shows the local coordination (clusters) for both the Ba and W atoms of the (001), (101), (110), (100), (111), and (112) surfaces. One of the most pronounced differences between the bulk and surface structural properties is that due to the reduced coordination of the O atoms in the top layers, the resulting vacancies produce spacing between the adjacent layers, thus providing a change in the values of the surface energy, i.e. modifying the stability of the surfaces to generate the corresponding morphology [78].

This observation can be confirmed by the detailed analysis of the results presented in Fig. 4, indicating small changes in the CB for each studied surface as compared to the bulk. The E_{gap} surface values follow the order of stability for the BaWO$_4$ surfaces obtained from the results of theoretical calculations, which is (112) > (001) > (110) > (100) > (101) > (111). Recent works of Gao et al. [78,79] revealed that the morphology of scheelite crystals present predominantly the exposed (112), (001), and (100) surfaces, being the (112) surface the most stable. This result agrees with our present data and previous results reported in the literature [80,81]. Table 2 lists the corresponding values of the surface energy and tension. The analysis of the obtained results reveals a similar trend for the given values except for the most stable

Fig. 5. FE–SEM images of the BaWO$_4$ crystals.

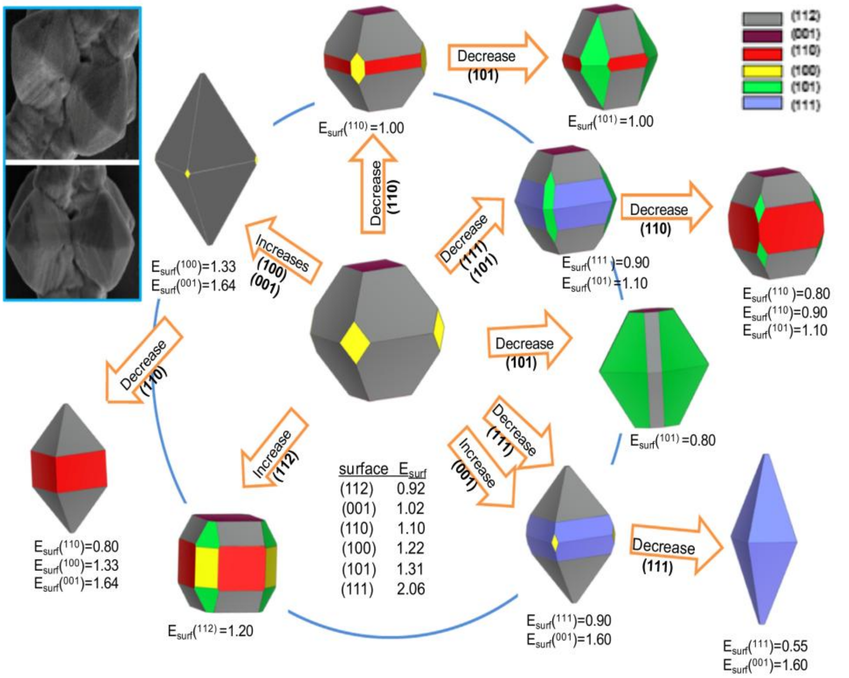

Fig. 6. Crystallographic structures and morphology map for the $BaWO_4$ crystals (the surface energy units are given in J/m^2). The experimental FE–SEM images (inset) are included for comparison.

surface, (112), which exhibits a higher value of surface tension than that for (001). This phenomenon can be explained by noticing that the (112) surface termination contains a large number of undercoordinated atoms (relative to the bulk coordination) with only three O atoms coordinated to each Ba atom. In addition, the (101) surface is characterized by a low value of surface tension, consistent with high stability due to six-coordinated Ba atoms, which is observed only for the (001) and (101) surfaces.

The analysis of the theoretical results indicates that the most stable surfaces are the (112), (001), and (100) facets [7879], which can form a truncated octahedron corresponding to the ideal morphology (shown in the central part of Fig. 6). When the relative stability of the facets changes (increases or decreases), more than one facet type appears in the resulting morphology, producing morphology variations. A truncated cube can be obtained if the surface energy of (112) is increased to 1.20 J/m^2, while a edge-truncated octahedron can be produced when the surface energy of (101) is decreased to 0.80 J/m^2 (see Fig. 6). Central part of some FE-SEM images (shown in Fig. 5) is included in the left inset of Fig. 6, which is the best well-faceted sighting to compare. A good agreement between the experimental and theoretical morphologies is obtained when the values of surface energy for the (001) and (100) facets increase simultaneously (see Fig. 6). Thus, variations in the ratio between values of surface energy affect the related morphologies and thus can be used to obtain correlations with experimental results.

4. Conclusions

Crystal morphology is an important parameter for obtaining high-quality crystals with excellent properties. $BaWO_4$ crystals have been synthesized as representative members of scheelite-based materials by using the CP method. XRD and Rietveld refinement were utilized to structurally characterize the obtained samples, while FE–SEM was used to investigate the morphologies of the as-synthesized structures. The geometry, electronic properties of the bulk, surface energies, and surface tension of the $BaWO_4$ crystals were evaluated using first-principles quantum mechanical calculations.

As a result of this work, the following conclusions were obtained: i) By using the Wulff's theorem, a simple model was proposed to determine surface energies of $BaWO_4$ crystals at atomic-level resolution. ii) The proposed computational technique was utilized to calculate equilibrium crystal morphologies. Using this model, we were able to evaluate possible morphologies and morphological transformations in $BaWO_4$ by controlling the ratio between surface energy values of each facet. iii) The stability order of the $BaWO_4$ surfaces obtained from the theoretical calculations can be expressed as $(112)>(001)>(110)>(100)>(101)>(111)$. Our work indicates that the morphology of scheelite crystals have (112), (001), and (100) as predominantly exposed surfaces, with the (112) facet being the commonly exposed surface. iv) A truncated octahedron corresponds to the ideal morphology predicted for the $BaWO_4$ crystals by theoretical calculations. However, a truncated cube or edge-truncated octahedron can be obtained due to the destabilization of the (112) surface or stabilization of the (101) surface, respectively. v) The obtained experimental and theoretical morphologies are similar when the values of surface energy for the (001) and (100) facets increase simultaneously.

Modulations of the $BaWO_4$ crystal morphologies resulting from the theoretical simulations have been applied to explain the changes observed at experimental conditions and clarify how the knowledge of surface-specific properties can be utilized to design crystal morphologies that exhibit improved performance in various applications. Using this knowledge, such modeling type can serve as a predictive tool to modify and ultimately control crystal morphologies. Therefore, computational techniques combined with experimental methods can be utilized to study morphologies of materials that can profoundly affect their physical and chemical properties as well as to improve the related performance of materials and innovate the material design.

Acknowledgments

This work was financially supported by the following Spanish research funding institutions: CTQ2012-36253-C03-02 project (Ministerio de Economia y Competitividad), PrometeoII/2014/022 and ACOMP/2014/270 projects (Generalitat Valenciana), Brazilian Research Funding Institutions: CNPq (INCTMN 573636/2008-7), FAPESP-CDMF (2013/07296-2), CAPES/PNPD 1268069, CAPES (process A104/2013 and 99999.002998/2014-09), and Programa de Cooperación Científica con Iberoamerica (Brasil) of Ministerio de Educación (PHBP14-00020). J.A. acknowledges to Ministerio de Economia y Competitividad, "Salvador Madariaga" program, PRX15/00261. L.G. acknowledges Banco Santander (Becas Iberoamérica: Jóvenes profesores e investigadores). M.C. acknowledges Generalitat Valenciana for Santiago Grisolia Program 2015/033.

References

[1] M. Kobayashi, M. Ishiib, K. Haradab, Y. Uski, H. Okuno, H. Shimizu, T. Yazawab, Scintillation and phosphorescence of $PbWO_4$ crystals, Nucl. Instrum. Methods A 373 (1996) 333–346.

[2] L.S. Cavalcante, J.C. Sczancoski, J.W.M. Espinosa, J.A. Varela, P.S. Pizani, E. Longo, Photoluminescent behavior of $BaWO_4$ powders processed in microwave-hydrotherm, J. Alloy. Compd. 474 (2009) 195–200.

[3] R. Dhilip Kumar, S. Karuppuchamy, Microwave-assisted synthesis of copper tungstate nanopowder for supercapacitor applications, Ceram. Int. 40 (2014) 12397–12402.

[4] J. Zhang, J. Pan, L. Shao, J. Shu, M. Zhou, J. Pan, Micro-sized cadmium tungstate as a high-performance anode material for lithium-ion batteries, J. Alloy. Compd. 614 (2014) 249–252.

[5] C. Anil Kumar, D. Pamu, Dielectric and electrical properties of $BaWO_4$ film capacitors deposited by RF magnetron sputtering, Ceram. Int. 41 (2015) S296–S302.

[6] C. Shivakumara, R. Saraf, S. Behera, N. Dhananjaya, H. Nagabhushana, Scheelite-type MWO_4 (M=Ca, Sr, and Ba) nanophosphors: facile synthesis, structural characterization, photoluminescence, and photocatalytic properties, Mater. Res. Bull. 61 (2015) 422–432.

[7] F.M. Pontes, M.A.M.A. Maurera, A.G. Souza, E. Longo, E.R. Leite, R. Magnani, M. A.C. Machado, P.S. Pizani, J.A. Varela, Preparation, structural and optical characterization of $BaWO_4$ and $PbWO_4$ thin films prepared by a chemical route, J. Eur. Ceram. Soc. 2 (2003) 3001–3007.

[8] D. Rangappa, T. Fujiwara, M. Yoshimura, Synthesis of highly crystallized $BaWO_4$ film by chemical reaction method at room temperature, Solid State Sci. 8 (2006) 1074–1078.

[9] M.A.P. Almeida, L.S. Cavalcante, M. Siu Li, J.A. Varela, E. Longo, Structural refinement and photoluminescence properties of $MnWO_4$ nanorods obtained by microwave-hydrothermal synthesis, J. Inorg. Organomet. Polym. Mater. 22 (2011) 264–271.

[10] Y. Shen, W. Li, T. Li, Microwave-assisted synthesis of $BaWO_4$ nanoparticles and its photoluminescence properties, Mater. Lett. 65 (2011) 2956–2958.

[11] P.F.S. Pereira, I.C. Nogueira, E. Longo, E.J. Nassar, I.L.V. Rosa, L.S. Cavalcante, Rietveld refinement and optical properties of $SrWO_4$: Eu^{3+} powders prepared by the non-hydrolytic sol–gel method, J. Rare Earth 33 (2015) 113–128.

[12] I.M. Pinatti, I.C. Nogueira, W.S. Pereira, P.F. Pereira, R.F. Goncalves, J.A. Varela, E. Longo, I.L. Rosa, Structural and photoluminescence properties of $Eu^{(3+)}$ doped alpha-Ag_2WO_4 synthesized by the green coprecipitation methodology, Dalton Trans. 44 (2015) 17673–17685.

[13] J.C. Rendón-Angeles, Z. Matamoros-Veloza, J. López-Cuevas, I.A. Gonzalez, K. L. Montoya-Cisneros, K. Yanagisawa, J. Willis-Richards, J. Diaz-Algara, Rapid synthesis of scheelite $SrWO_4$ particles using a natural $SrSO_4$ ore under alkaline hydrothermal conditions, Hydrometallurgy 157 (2015) 116–126.

[14] A. Phuruangrat, T. Thongtem, S. Thongtem, Precipitate synthesis of $BaMoO_4$ and $BaWO_4$ nanoparticles at room temperature and their photoluminescence properties, Superlattice Microstruct. 52 (2012) 78–83.

[15] M. Li, Y. Guan, Y. Yin, X. Cui, S. Rong, G. Jin, Y. Hao, Q. Wu, Controllable synthesis of 3D $BaXO_4$ (X=W, Mo) microstructures by adjusting nucleation stage and their photoluminescence properties, Superlattice Microstruct. 80 (2015) 222–228.

[16] F.J. Manjón, D. Errandonea, N. Garro, J. Pellicer-Porres, P. Rodríguez-Hernández, S. Radescu, J. López-Solano, A. Mujica, A. Muñoz, Lattice dynamics study of scheelite tungstates under high pressure I. $BaWO_4$, Phys. Rev. B 74 (2006) 144111.

[17] B. Sun, Y. Liu, W. Zhao, J. Wu, P. Chen, Hydrothermal preparation and white-light-controlled resistive switching behavior of $BaWO_4$ nanospheres, Nano-Micro Lett. 7 (2015) 80–85.

[18] L.S. Cavalcante, F.M.C. Batista, M.A.P. Almeida, A.C. Rabelo, I.C. Nogueira, N. C. Batista, J.A. Varela, M.R.M.C. Santos, E. Longo, M. Siu Li, Structural refinement, growth process, photoluminescence and photocatalytic properties of $(Ba_{1\ \ x}Pr_{2x/3})WO_4$ crystals synthesized by the coprecipitation method, RSC Adv. 2 (2012) 6438–6454.

[19] M. Tyagi, S.G. Singh, A.K. Chauhan, S.C. Gadkari, First principles calculation of optical properties of $BaWO_4$: a study by full potential method, Phys. B 405 (2010) 4530–4535.

[20] D. Ran, H. Xia, S. Sun, P. Zhao, F. Liu, Z. Ling, W. Ge, H. Zhang, J. Wang, Optical phonon modes and transmissivity in $BaWO_4$ single crystal, Cryst. Res. Technol. 41 (2006) 1189–1193.

[21] C. Kavitha, C. Narayana, B.E. Ramachandran, N. Garg, S.M. Sharma, Acoustic phonon behavior of $PbWO_4$ and $BaWO_4$ probed by low temperature Brillouin spectroscopy, Solid State Commun. 202 (2015) 78–84.

[22] H.W. Eng, P.W. Barnes, B.M. Auer, P.M. Woodward, Investigations of the electronic structure of d^0 transition metal oxides belonging to the perovskite family, J. Solid State Chem. 175 (2003) 94–109.

[23] P. Parhi, T.N. Karthik, V. Manivannan, Synthesis and characterization of metal tungstates by novel solid-state metathetic approach, J. Alloy. Compd. 465 (2008) 380–386.

[24] Y. Mi, Z. Huang, F. Hu, X. Li, Room temperature reverse-microemulsion synthesis and photoluminescence properties of uniform $BaMoO_4$ submicro-octahedra, Mater. Lett. 63 (2009) 742–744.

[25] Z. Luo, H. Li, J. Xia, W. Zhu, J. Guo, B. Zhang, Controlled synthesis of different morphologies of $BaWO_4$ crystals via a surfactant-assisted method, J. Cryst. Growth 300 (2007) 523–529.

[26] X. Wu, J. Du, H. Li, M. Zhang, B. Xi, H. Fan, Y. Zhu, Y. Qian, Aqueous mineralization process to synthesize uniform shuttle-like $BaMoO_4$ microcrystals at room temperature, J. Solid State Chem. 180 (2007) 3288–3295.

[27] J.C. Sczancoski, L.S. Cavalcante, N.L. Marana, R.O.D. Silva, R.L. Tranquilin, M. R. Joya, P.S. Pizani, J.A. Varela, J.R. Sambrano, M.S. Li, E. Longo, J. Andrés, Electronic structure and optical properties of $BaMoO_4$ powders, Curr. Appl. Phys. 10 (2010) 614–624.

[28] J.H. Ryu, J.W. Yoon, K.B. Shim, Microwave-assisted synthesis of $BaMoO_4$ nanocrystallites by a citrate complex method and their anisotropic aggregation, J. Alloy. Compd. 413 (2006) 144–149.

[29] A. Phuruangrat, T. Thongtem, S. Thongtem, Barium molybdate and barium tungstate nanocrystals synthesized by a cyclic microwave irradiation, J. Phys. Chem. Solids 70 (2009) 955–959.

[30] M. Anicete-Santos, F.C. Picon, C. Nahum Alves, P.S. Pizani, J.A. Varela, E. Longo, The role of short-range disorder in $BaWO_4$ crystals in the intense green photoluminescence, J. Phys. Chem. C 115 (2011) 12180–12186.

[31] O. Gomis, J.A. Sanz, R. Lacomba-Perales, D. Errandonea, Y. Meng, J.C. Chervin, A. Polian, Complex high-pressure polymorphism of barium tungstate, Phys. Rev. B 86 (2012) 054121.

[32] H. Zhang, T. Liu, Q. Zhang, Xi'en Wang, J. Yin, M. Song, X. Guo, First-principles study on electronic structures of $BaWO_4$ crystals containing F-type color centers, J. Phys. Chem. Solids 69 (2008) 1815–1819.

[33] H. Zhang, T. Liu, Q. Zhang, Xi'en Wang, X. Guo, M. Song, J. Yin, First-principles study on electronic structures and absorption spectra for $BaWO_4$ crystal containing barium vacancy, Nucl. Instrum. Methods B 267 (2009) 1056–1060.

[34] G. Dhanaraj, K. Byrappa, V. Prasad, M. Dudley, Provides the Reader with the Most Complete State-of-the-Art Presentation on the Basics and Realization of Crystal Growth, Springer Handbook of Crystal Growth, Springer-Verlag Berlin Heidelberg, 2010, ISBN: 978-3-540-74761-1.

[35] Q. Kuang, X. Wang, Z. Jiang, Z. Xie, L. Zheng, High-energy-surface engineered metal oxide micro- and nanocrystallites and their applications, Acc. Chem. Res. 47 (2014) 308–318.

[36] K. Huang, L. Yuan, S. Feng, Crystal facet tailoring arts in perovskite oxides, Inorg. Chem. Front. 2 (2015) 965–981.

[37] G. Zhou, M. Lü, F. Gu, S. Wang, Z. Xiu, Morphology-controlled synthesis of $BaWO_4$ nanocrystals via a surfactant-assisted method, Mater. Lett. 59 (2005) 2706–2709.

[38] L.S. Cavalcante, J.C. Sczancoski, L.F. Lima Jr., J.W.M. Espinosa, P.S. Pizani, J. A. Varela, E. Longo, Synthesis, characterization, anisotropic growth and photoluminescence of $BaWO_4$, Cryst. Growth Des. 9 (2009) 1002–1012.

[39] Y. Yin, F. Yang, Y. Yang, Z. Gan, Z. Qin, S. Gao, B. Zhou, X. Li, Controlled synthesis of $BaWO_4$ hierarchical nanostructures by exploiting oriented attachment in the solution of H_2O and C_2H_5OH, Superlattice Microstruct. 49 (2011) 599–607.

[40] C. Cui, J. Bi, D. Gao, K. Zhao, Morphology and crystal phase control in preparation of highly crystallized $BaWO_4$ film via galvanic cell method, J. Alloy. Compd. 462 (2008) L16–L19.

[41] D.G. Stroppa, L.A. Montoro, A. Campello, L. Gracia, A. Beltrán, J. Andrés, E. R. Leite, A.J. Ramirez, Prediction of dopant atom distribution on nanocrystals using thermodynamic arguments, Phys. Chem. Chem. Phys. 16 (2014) 1089–1094.

[42] M.R.D. Bomio, R.L. Tranquilin, F.V. Motta, C.A. Paskocimas, R.M. Nascimento, L. Gracia, J. Andres, E. Longo, Toward understanding the photocatalytic activity of $PbMoO_4$ powders with predominant (111), (100), (011), and (110) facets. A

combined experimental and theoretical study, J. Phys. Chem. C 117 (2013) 21382–21385.

[43] V.M. Longo, L. Gracia, D.G. Stroppa, L.S. Cavalcante, M. Orlandi, A.J. Ramirez, E. R. Leite, J. Andrés, A. Beltrán, J.A. Varela, E. Longo, A joint experimental and theoretical study on the nanomorphology of $CaWO_4$ crystals, J. Phys. Chem. C 115 (2011) (2011) 3–20119.

[44] J. Andrés, L. Gracia, L., A.F. Gouveia, M.M. Ferrer, E. Longo, Effects of surface stability on the morphological transformation of metals and metal oxides as investigated by first principles calculations, Nanotechnology 26 (2015) 405703.

[45] M.M. Ferrer, A.F. Gouveia, L. Gracia, E. Longo, J. Andrés, A 3D platform for the morphology modulation of materials: first principles calculations on the thermodynamic stability and surface structure of metal oxides: Co_3O_4, α-Fe_2O_3, and In_2O_3, Model. Simul. Mater. Sci. Eng. 24 (2016) 025007.

[46] R.A. Roca, J.C. Sczancoski, I.C. Nogueira, M.T. Fabbro, H.C. Alves, L. Gracia, L.P. S. Santos, C.P. de Sousa, J. Andrés, G.E. Luz, E. Longo, L.S. Cavalcante, Facet-dependent photocatalytic and antibacterial properties of α-Ag_2WO_4 crystals: combining experimental data and theoretical insights, Catal. Sci. Technol. 5 (2015) 4091–4107.

[47] G. Botelho, J. Andres, L. Gracia, L.S. Matos, E. Longo, Photoluminescence and photocatalytic properties of Ag_3PO_4 microcrystals: an experimental and theoretical investigation, ChemPlusChem 81 (2016) 202–212.

[48] M.T. Fabbro, C. Saliby, L.R. Rios, F.A. La Porta, L. Gracia, M.S. Li, J. Andrés, L.P. S. Santos, E. Longo, Identifying and rationalizing the morphological, structural, and optical properties of β-Ag_2MoO_4 microcrystals, and the formation process of Ag nanoparticles on their surfaces: combining experimental data and first-principles calculations, Sci. Technol. Adv. Mater. 16 (2015) 065002.

[49] H.M. Rietveld, A profile refinement method for nuclear and magnetic structures, J. Appl. Cryst. 2 (1969) 65–71.

[50] A.C. Larson, R.B.V. Dreele, General Structure Analysis System (GSAS), Los Alamos National Laboratory, New Mexico, USA, 2004, Report LAUR.

[51] L.W. Finger, D.E. Cox, A.P. Jephcoat, A correction for power diffraction peak asymmetry due to axial divergence, J. Appl. Cryst. 27 (1994) 892–900.

[52] P.W. Stephens, Phenomenological model of anisotropic peak broadening in power diffraction, J. Appl. Cryst. 32 (1999) 281–289.

[53] R. Dovesi, V.R.S., C. Roetti, R. Orlando, C.M. Zicovich-Wilson, F. Pascale, B. Civalleri, K. Doll, N.M. Harrison, I.J. Bush, P.H. D'Arco, M. Llunell, M. Causa, Y. Noël, CRYSTAL14 User's Manual, University of Torino, Torino, 2014.

[54] A.D. Becke, Perspective on density functional thermochemistry. III. The role of exact exchange, J. Chem. Phys. 98 (1993) 5648–5652.

[55] C.T. Lee, W.T. Yang, R.G. Parr, Development of the Colle–Salvetti correlation-energy formula into a functional of the electron density, Phys. Rev. B: Condens. Matter 37 (1988) 785–789.

[56] M.L. Moreira, J. Andres, L. Gracia, A. Beltrán, L.A. Montoro, J.A. Varela, E. Longo, Quantum mechanical modeling of excited electronic states and their relationship to cathodoluminescence of $BaZrO_3$, J. Appl. Phys. 114 (2013) 043714.

[57] L. Gracia, V.M. Longo, L.S. Cavalcante, A. Beltran, W. Avansi, M.S. Li, V. R. Mastelaro, J.A. Varela, E. Longo, J. Andres, Presence of excited electronic state in $CaWO_4$ crystals provoked by a tetrahedral distortion: an experimental and theoretical investigation, J. Appl. Phys. 110 (2011) 043501.

[58] E. Longo, D.P. Volanti, V.M. Longo, L. Gracia, I.C. Nogueira, M.A.P. Almeida, A. N. Pinheiro, M.M. Ferrer, L.S. Cavalcante, J. Andrés, Toward an understanding of the growth of Ag filaments on α-Ag_2WO_4 and their photoluminescent properties: a combined experimental and theoretical study, J. Phys. Chem. C 118 (2014) 1229–1239.

[59] F.M.C. Batista, F.A. La Porta, L. Gracia, E. Cerdeiras, L. Mestres, M. Siu Li, N. C. Batista, J. Andrés, E. Longo, L.S. Cavalcante, A joint experimental and theoretical study on the electronic structure and photoluminescence properties of $Al_2(WO_4)_3$ powders, J. Mol. Struct. 1081 (2015) 381–388.

[60] A. Beltrán, L. Gracia, E. Longo, J. Andrés, First-principles study of pressure-induced phase transitions and electronic properties of Ag_2MoO_4, J. Phys. Chem. C 118 (2014) 3724–3732.

[61] H.J. Monkhorst, J.D. Pack,, Special points for Brillouin-x. One integrations, Phys. Rev. B: Condens. Matter 13 (1976) 5188–5192.

[62] F. Cora, A. Patel, N.M. Harrison, R. Dovesi, C.R.A. Catlow, An ab initio Hartree–Fock study of the cubic and tetragonal phases of bulk tungsten trioxide, J. Am. Chem. Soc. 118 (1996) 12174–12182.

[63] CRYSTAL Basis set. ⟨http://www.crystal.unito.it/Basis_Sets/Ptable.html⟩, 2016 (accessed 10.02.16).

[64] Basis set. ⟨http://www.tcm.phy.cam.ac.uk/ mdt26/basis_sets/Ba_basis.txt⟩, 2016 (accessed 10.02.16).

[65] G. Wulff, Zur Frage der Geschwindigkeit Des Wachstums und Der Auflosung der Krystallflachen, Krist. Miner. 34 (1901) 449–530.

[66] K. Momma, F. Izumi, VESTA 3 for three-dimensional visualization of crystal, volumetric and morphology data, J. Appl. Cryst. 44 (2011) 1272–1276.

[67] A. Kuzmin, J. Purans, Local atomic and electronic structure of tungsten ions in AWO_4 crystals of scheelite and wolframite types, Radiat. Meas. 33 (2001) 583–586.

[68] F. Toa, Z. Wang, L. Yao, W. Cai, X. Li, Shape-controlled synthesis and characterization of YF_3 truncated octahedral nanocrystals, Cryst. Growth Des. 7 (2007) 854–858.

[69] C. Herring, Some theorems on the free energies of crystal surfaces, Phys. Rev. 82 (1981) 87–93.

[70] J.W. Gibbs, A.W. Smith, On the equilibrium of heterogeneous substances, Trans. Conn. Acad. Arts Sci. 3 (1875) 108–248.

[71] X. Wang, H. Xu, H. Wang, H. Yan, Morphology-controlled $BaWO_4$ powders via a template-free precipitation technique, J. Cryst. Growth 284 (2005) 254–261.

[72] Y. Liu, Y. Chu, Surfactant-assisted synthesis of single crystal $BaWO_4$ octahedral microparticles, Mater. Chem. Phys. 92 (2005) 59–63.

[73] B. Xie, Y. Wu, Y. Jiang, F. Li, J. Wu, S. Yuan, W. Yu, Y. Qian, Shape-controlled synthesis of $BaWO_4$ crystals under different surfactants, J. Cryst. Growth 235 (2002) 283–286.

[74] L.D. Marks, Modified wulff constructions for twinned particles, J. Cryst. Growth 61 (1983) 556–566.

[75] A.S. Barnard, P. Zapol, Effects of particle morphology and surface hydrogenation on the phase stability of TiO_2, Phys. Rev. B 70 (2004) 235403.

[76] L. Li, F. Abild-Pedersen, J. Greeley, J.K. Nørskov, Surface tension effects on the reactivity of metal nanoparticles, J. Phys. Chem. Lett. 6 (2015) 3797–3801.

[77] D. Errandonea, J. Pellicer-Porres, F.J. Manjón, A. Segura, Ch Ferrer-Roca, R. S. Kumar, O. Tschauner, J. López-Solano, P. Rodríguez-Hernández, S. Radescu, A. Mujica, A. Muñoz, G. Aquilanti, Determination of the high-pressure crystal structure of $BaWO_4$ and $PbWO_4$, Phys. Rev. B 73 (2006) 224103.

[78] Y. Hu, Z. Gao, W. Sun, X. Liu, Anisotropic surface energies and adsorption behaviors of scheelite crystal, Colloids Surf. A 415 (2012) 439–448.

[79] Z.Y. Gao, W. Sun, Y.H. Hu, X.-W. Liu, Surface energies and appearances of commonly exposed surfaces of scheelite crystal, Trans. Nonferr. Met. Soc. 23 (2013) 2147–2152.

[80] T.G. Cooper, N.H. de Leeuw, A combined ab initio and atomistic simulation study of the surface and interfacial structures and energies of hydrated scheelite: introducing a $CaWO_4$ potential model, Surf. Sci. 531 (2003) 159–176.

[81] H.-Y. Jung, Y.-D. Huh, A two-dimensional four-fold symmetric $SrMoO_4$ dendrite, CrystEngComm 17 (2015) 1398.

CRYSTAL
Research&Technology

Cryst. Res. Technol. **51**, No. 10, 634–644 (2016) / DOI 10.1002/crat.201600227

Original Paper

On the morphology of $BaMoO_4$ crystals: A theoretical and experimental approach

Marisa C. Oliveira[1,2], *Lourdes Gracia*[1], *Içamira C. Nogueira*[3], *Maria Fernanda C. Gurgel*[4], *Jose Manuel R. Mercury*[5], *Elson Longo*[2], *and Juan Andrés*[1,*]

Received 18 July 2016, revised 4 August 2016, accepted 15 August 2016

$BaMoO_4$ crystals were obtained by a co-precipitation method, and their structures were characterized by X-ray diffraction and Rietveld refinement techniques. Field emission scanning electron microscopy was utilized to investigate the morphology of the as-synthesized aggregates.- Through systematic first principle calculations within the density functional theory method at the B3LYP level, we investigated the structure; the surface stability of the (001), (101), (110), (100), (111), and (112) surfaces; and the morphological transformations of $BaMoO_4$. The relative surfaces energies were further varied to predict a complete map of the available morphologies through a Wulff construction approach. This revealed that the obtained experimental and theoretical morphologies coincided when the surface energy values of the (001) surface decreased while those of the (100) and (101) facets increased simultaneously. Analysis of the surface structures showed that the electronic properties were associated with the presence of undercoordinated $[BaO_x]$ ($x = 4$, 5, and 6) and $[MoO_y]$ ($y = 3$) clusters. The presented results provide a comprehensive catalog of the morphologies most likely to be present under realistic conditions, and will serve as a starting point for future studies on the surface chemistry of $BaMoO_4$ crystals.

1 Introduction

Barium molybdate ($BaMoO_4$) is a prototypical member of the molybdate family with a scheelite-type tetragonal structure. This compound has been prepared by a plethora of synthetic routes including solid-state reactions, Czochralski techniques, spontaneous crystallization, microwave-assisted synthesis, hydrothermal synthesis, co-precipitation, microemulsion, and complex polymerization. [1–15] Of these procedures, co-precipitation has been demonstrated to be one of the most effective approaches to synthesize inorganic compounds with interesting morphologies and regular particle size. [16–23].

The morphology of a given material is related to the stability of their various corresponding exposed surfaces, which can be rigorously described by their surface energies. In this context, first principle calculations have been gradually developed and employed for the study of crystal morphology. This has enabled the understanding of the atomic and electronic properties of a crystal surface, which has provided some insight into the features of single crystal facets relevant to subsequent technological applications. [24, 25] In particular, these applications for $BaMoO_4$ can be further enhanced or optimized by tailoring the surface atomic structures. [26–28].

It is well known that the morphologies of $BaMoO_4$ are sensitive to the synthesis conditions, and a number of different shapes of $BaMoO_4$ crystals have been synthesized and studied such as penniform-like, [29] flower-like, [30] nest-like, [31] and shuttle-like [32, 33] shapes. Our group are engaged in a research project devoted to developed and apply a working methodology, based on the joint use of experimental findings and first-principles calculations, to obtain the electronic, structural and energetic properties controlling

---

[*] Corresponding author: e-mail: andres@qfa.uji.es

[1] Departament de Química Física i Analítica, Universitat Jaume I, 12071 Castelló de la Plana, Spain

[2] CDMF-UFSCar, Universidade Federal de São Carlos, P.O. Box 676, 13565-905, São Carlos, SP, Brazil

[3] Departament de Física, Universidade Federal do Amazonas, 69077–000, Manaus, AM, Brazil

[4] Department de Química, Universidade Federal de Goiás, 75704-020, Catalão, GO, Brazil

[5] PPGEM-IFMA, Instituto Federal do Maranhão, 65030-005, São Luís, MA, Brazil

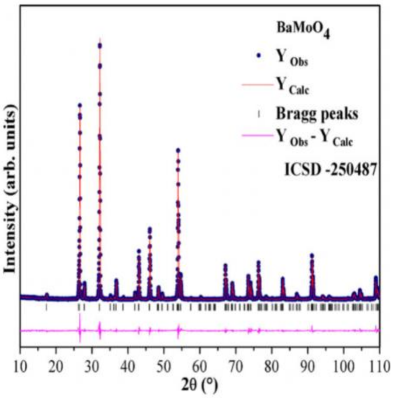

Fig. 1 Rietveld refinements of the $BaMoO_4$ crystals synthesized at 80 °C using the co-precipitation method.), XRD pattern using Cu $K\alpha$ radiation ($\lambda = 1.5406$ Å) in a 2θ range from 10° to 110°.

the morphology and the transformation mechanism of complex crystals. Very recently this strategy has been used in $BaWO_4$ crystals. [34] This work follows a joint experimental and theoretical strategy on another scheelite based material, $BaMoO_4$ crystals, to obtain a complete map of the morphologies available for this material. In addition, based on these results, we are able to rationalize how the different surfaces change their energies throughout the synthesis process, and we are able to propose the path by which the experimental and theoretical morphologies of $BaMoO_4$ can match.

This paper is divided into three sections. Next, our results are presented and discussed and our main conclusions. Next, our results the experimental details and the computational model and method used, are summarized in the final section.

2 Results and discussion

2.1 X-Ray diffraction measurements and Rietveld refinements

Figure 1 shows the Rietveld refinement plots for the observed patterns versus the calculated patterns of the $BaMoO_4$ crystals obtained using a co-precipitation method.

The measured diffraction patterns were well adjusted to the ICSD N°. 250487. [35] All the diffraction peaks can be readily indexed to the pure scheelite-type tetragonal structure of $BaMoO_4$ (space group: $I4_1/a$). No additional phase peaks were observed in the resolution range, indicating that the pure tetragonal phase $BaMoO_4$ can be obtained. The strong and sharp diffraction peaks suggested the synthesized crystals were well-crystallized. To confirm that the structure of the $BaMoO_4$ crystals was tetragonal and to determine the lattice parameters, cell volume, and atomic coordinates, a structural refinement using the Rietveld method was performed for the $BaMoO_4$ crystals.

The quality of the structural refinement was checked using the statistical parameters R_{wp}, R_{Bragg}, R_p, and χ^2 (12.50%, 5.78%, 8.67% and 1.36%, respectively). The low deviations of these parameters, which indicates the good quality of the structural refinement and numerical results. A previous work, including structural refinement data, showed that all the $(Ba_{1-x}Sr_x)MoO_4$ crystals were crystallized in a scheelite-type tetragonal structure with the $I4_1/a$ space group, and four molecular formula per unit-cell ($Z = 4$). [35] Our results (a, $b = 5.5830(9)$ Å, $c = 12.8270(7)$ Å) closely agree with the lattice parameters reported for $x = 0$ of the solid solution, namely a, $b = 5.58483(2)$ Å, $c = 12.82922(9)$ Å. Variations in the atomic coordinates related to oxygen atoms were observed in Table 1. This is possible because the Ba and Mo positions were fixed by the crystal symmetry and only the atomic positions for oxygen were refined. [36].

Figure 2 illustrates a schematic representation of a single conventional $1\times1\times1$ cell for $BaMoO_4$. The lattice parameters and atomic positions were confirmed using Rietveld refinement to model this unit cell. In terms of cluster organization, the Mo atoms are surrounded by four oxygen atoms $[MoO_4]$ in a tetrahedral configuration and Ba atoms are surrounded by eight oxygen atoms in a deltahedral configuration $[BaO_8]$. [8].

For comparison purposes, the calculated and experimental values of the lattice parameters (a and c) and the atomic coordinates of the oxygen atoms are presented in Table 1.

These results are in good agreement with previous experimental observations and calculations. [14, 35, 37–44]. In addition, theoretical and experimental results can be compared with previous studies of other scheelite-type materials, [45, 46] where the calculations describe precisely the evolution of the crystal structure on pressure phases and help to understand the electronic and structural properties.

2.2 Surface study

The surface energy values, E_{surf}, for (001), (101), (110), (100), (111), and (112) surfaces were calculated in order to correlate the theoretical and experimental studies.

Table 1 Calculated and experimental values of the lattice parameters (a and c) and atomic coordinates x, y, z of the oxygen.

	Cell parameters		Oxygen coordinates		
Data	a (Å)	c (Å)	x	y	z
Theo. (this work)	5.5927	12.4055	0.2311	0.1218	0.0460
Exp. (this work)	5.583(09)	12.827(07)	0.233(29)	0.126(67)	0.057(48)
Exp. [35]	5.5848	12.8292	0.2283	0.1353	0.0489
Theo [37, 38]	5.5364	12.7153	-	-	-
Exp. [39]	5.5479	12.7432	-	-	-
Exp. [40]	5.5622	12.8188	-	-	-
Exp. [41, 42]	5.5877	12.8067	-	-	-
Exp. [43]	5.573	12.786	-	-	-
Exp. [44]	5.580	12.810	-	-	-
Ep. [14]	5.5802	12.821	-	-	-
Interatomic distance(˚A)	Calculated		Experimental		Difference
Ba-O	2.7249		2.718(40)		−0.006
Ba-O	2.7610		2.848(42)		0.087
Mo-O	1.7855		1.708(97)		−0.076

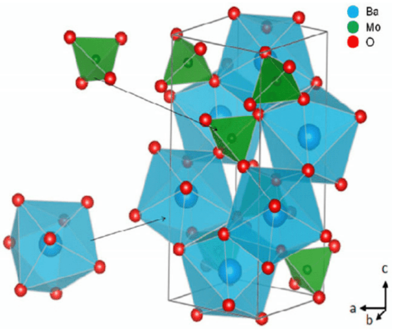

Fig. 2 A polyhedral representation of the BaMoO4 unit cell. The local coordination corresponding to the deltahedral $[BaO_8]$ and tetrahedral $[MoO_4]$ clusters is depicted for both the Ba and Mo atoms, respectively.

Surface energy is defined as the energy per unit area required for forming the surface relative to the bulk and is calculated according to:

$$E_{surf} = \frac{E_{slab} - nE_{bulk}}{2A}$$

where E_{slab} is the total energy of the 2D slab, nE_{bulk} is the energy of the corresponding amount of the bulk $BaMoO_4$ units, and A represents the surface area, which is created on each side of the 2D slab and is repeated periodically. After the corresponding optimization process and convergence tests in thickness, slab models consisting of four molecular units containing 24 atoms were obtained. All these surfaces are presented in figure 3 with the coordination number, i.e., clusters of the most exposed Ba and Mo atoms.

Considering the surface atom distributions, we note that the surfaces (101), (111), and (112) are exposed to a vacuum by the Mo and O atoms, while the (001), (100), and (110) surfaces are exposed by the Ba and O atoms. Exposed Mo atoms can be coordinated to three or four oxygen atoms, forming $[MoO_3]$ or $[MoO_4]$ clusters, respectively. Exposed Ba atoms can be coordinated to four, five, or six oxygen atoms, forming $[BaO_4]$, $[BaO_5]$, or $[BaO_6]$ clusters, respectively.

Analysis of the results shows that the most stable surface, the (001) surface, presents exposed $[BaO_6]$ clusters, corresponding to the presence of two oxygen vacancies compared to the bulk. However, in the (100), (110), (101), and (111) surfaces there are undercoordinated $[BaO_5]$ clusters associated to the presence of three oxygen

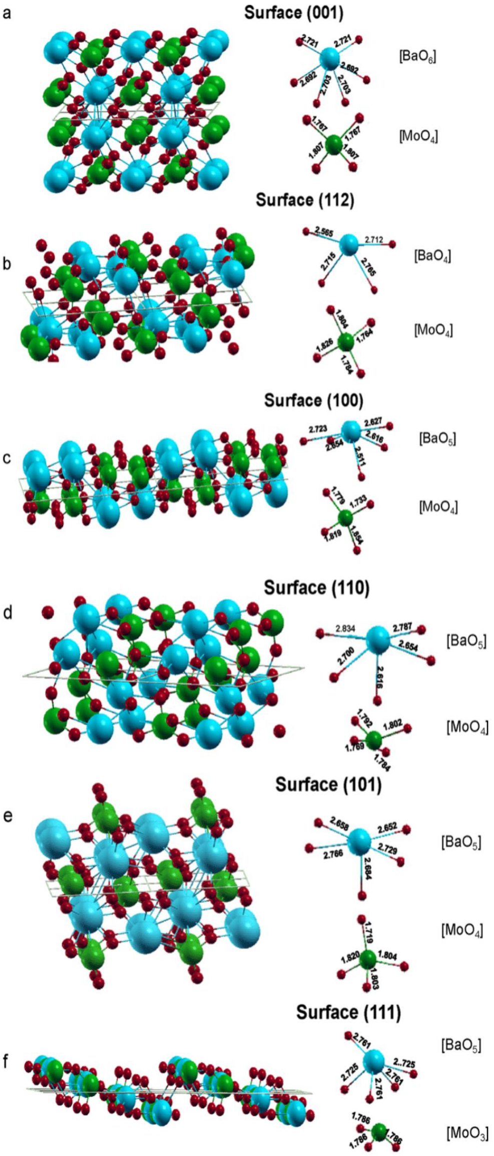

Fig. 3 Schematic representations of surfaces: a) (001), b) (112), c) (100), d) (110), e) (101), and f) (111). The values for the Ba–O and Mo–O bond distances of the exposed Ba and Mo atoms are given in Å.

vacancies. On the (112) surface there are four oxygen vacancies, i.e., undercoordination at [BaO$_4$]. Only the (111) surface presents [MoO$_3$] clusters, implying a breaking of a Mo–O bond compared to the bulk. Since the bonding interaction of a Mo–O bond is stronger than a Ba–O bond, the stability of this surface is reduced compared to the rest of the surfaces.

2.3 Morphologies of the BaMoO$_4$ crystals

The conventional approach to the quantitative study of morphology is through the determination of the surface energy of each surface, as defined by the Wulff construction [47–49] using the *ab initio* calculated surface energies. From the Wulff construction, it is derived that the surfaces with the lowest surface energies control the crystal morphology of BaMoO$_4$. [42, 43].

The FE-SEM images of the BaMoO$_4$ crystals synthesized at 80 °C by the co-precipitation method are shown in figure 4. The micro-structured BaMoO$_4$ crystals were obtained immediately after the reaction between the (Ba^{2+}) and (MoO_4^{2-}) ions. The speed of nucleation was very fast.

The BaMoO$_4$ crystals exhibited a large quantity of particles with an agglomerate nature and polydisperse sizes. The particles were of a considerable length with a surface with many notches and well-formed perpendicular branches (see figure 4**).**

The order of the stability of the BaMoO$_4$ surfaces according to the theoretical calculations is (001) > (112) > (100) > (110) > (101) > (111) and the ideal morphology of BaMoO$_4$ is controlled by (001), (112), and (100), being their contribution 15.1%, 70.9%, and 14.0%, respectively. Based on the results of the experimental micrographs (see figure 4), it is possible to modify the ideal morphology by tuning the values for the surface energies of the different facets using the Wulff construction. [47–50] Analysis of the theoretical results showed that when the relative stability of the facets changes (increases or decreases), more than one type of facet will appear in the resulting morphology. The available morphologies reflecting a change in the values of the surface energy, i.e., modifying the stability of the surfaces to generate the corresponding morphology, are depicted in figure 5. In order to obtain a similar morphology to the experimental FE-SEM images, the values of the surface energy for the (001) were increased and the surface energy for (100) and (101) decreases, simultaneously (see right-hand side of figure 5).

Recently, Gao et al. [51] reported that the surfaces of scheelite crystal have predominantly exposed surfaces, (001), (112), and (100) in the morphologies, with the (112) crystal surface as the most commonly exposed surface. [52–54] This result is in agreement with present result our and whose obtained in the previous study on BaWO$_4$. [34] A comparison between BaWO$_4$ and BaMoO$_4$ shows that ideal morphology of both scheelites is similar. However, the experimental FE-SEM images are different for both materials, i.e. 99.5% contribution of (112), 0.4% of (100) and 0.1% of (001) in BaWO$_4$ while 46.5% of (101), 46.9% of (100), 5.8% of (112) and 0.8% of (001) are found for BaMoO$_4$.

Another important aspect that should be considered when studying solid materials is a distinction between the surface energy, E_{surf}, and the surface tension, σ. The surface tension is "surface stress" represented by a work force per unit area in the surface layer. [55, 56] The surface tension can be obtained using the thermodynamic stability model described by the equation $\sigma = \partial E_{tot}/\partial A$, where E_{tot} is the total energy with contributions from the particle bulk and surfaces. To calculate E_{tot}, the uniform dilation with area ΔA (corresponding to a constant ratio between the in-plane lattice parameters, x:y) of the structure must be calculated while optimizing only the internal parameters (without optimization of the in-plane cell parameters). Thus, E_{tot} can be calculated as $\frac{1}{2}(E_{slab} - nE_{bulk})$ for optimized structures and surfaces after dilation. Therefore, by applying two-dimensional dilation to a slab in the surface plane and calculating the total energy as previously described, a change in the total energy (ΔE_{tot}) after dilation was obtained for a given dilation area. The values for the surface energy and tension are listed in Table 2.

The results collected in Table 2 show that the surface (101) presents a low value of surface tension, consistent with the stability provided by the six-fold coordination of the Ba atom. Evidence of this was only observed for the (001) and (101) surfaces.

Growth in the <001> direction, the most stable surface, can be related to the differences in the surface energy, which can drive the morphology of products with high tropism. The interaction of small particles may have promoted growth of the crystals, forming large microstructures by self-assembly due to Oswald's ripening, because so many notches can be seen on the surface of the crystals. [33, 57, 58].

The surface relaxation energy values, which are associated with concerted layer breathing due to the loss of atomic coordination, can be observed in Table 2. The (112) and (110) surfaces are found to be the most prone to relax. The coordination number of the exposed Ba atom is reduced to the middle, [BaO$_4$], compared to the bulk in the (112) surface, while the

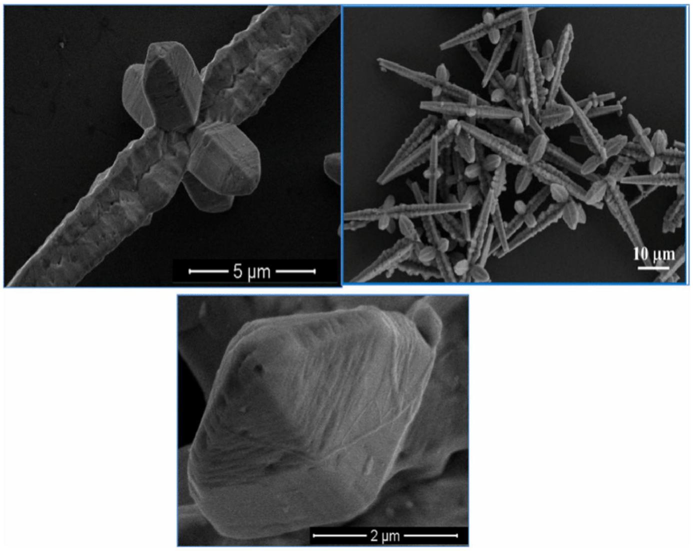

Fig. 4 FE-SEM images of the $BaMoO_4$ crystals.

Table 2 The calculated values of the surface energy, surface tension, change in total energy (ΔE_{tot}) for the area dilation (ΔA), relaxation energy, and gap energy, for each surface.

Surface	E_{suf} (J/m²)	ΔE_{tot} (Hartree)	ΔA (Å²)	σ (J/m²)	Relaxation (%)	E_{gap} (eV)
(001)	0.99	0.035	1.273	0.54	6	5.69
(112)	1.02	0.032	2.385	0.85	62	5.81
(100)	1.17	0.039	2.853	1.04	30	5.38
(110)	1.23	0.033	2.017	1.01	61	5.63
(101)	1.34	0.039	1.562	0.94	37	5.09
(111)	2.23	0.016	4.231	2.51	1	Conductor

$[BaO_5]$ cluster has the longest Ba–O distance (2.834 Å) in (110).

2.4 Band structure for the $BaMoO_4$ bulk and surfaces

The band structures of the $BaMoO_4$ were calculated for 80 k-points along the appropriate high-symmetry paths of the adequate Brillouin zone. Diagrams of the density of state (DOS) were obtained analysis of the corresponding electronic structures shown in figure 6.

The calculated band structure and total DOS projected on atoms for the (001), (112), (100), (110), (101), and (111) surfaces and the bulk $BaMoO_4$ crystal are shown in figure 6 (a–g). It can be easily seen that the upper valence band is composed predominantly of the O 2p states and the bottom of conduction band is mainly attributed to the Mo 4d states and the O 2p states. Based on the literature, AMO_4 oxides with a scheelite structure, such as $BaMoO_4$, contain an M cation exhibiting the closest valence to the nominal value of 6+, showing the covalent property of the crystals, which is mainly contributed by the Mo–O bond. [39].

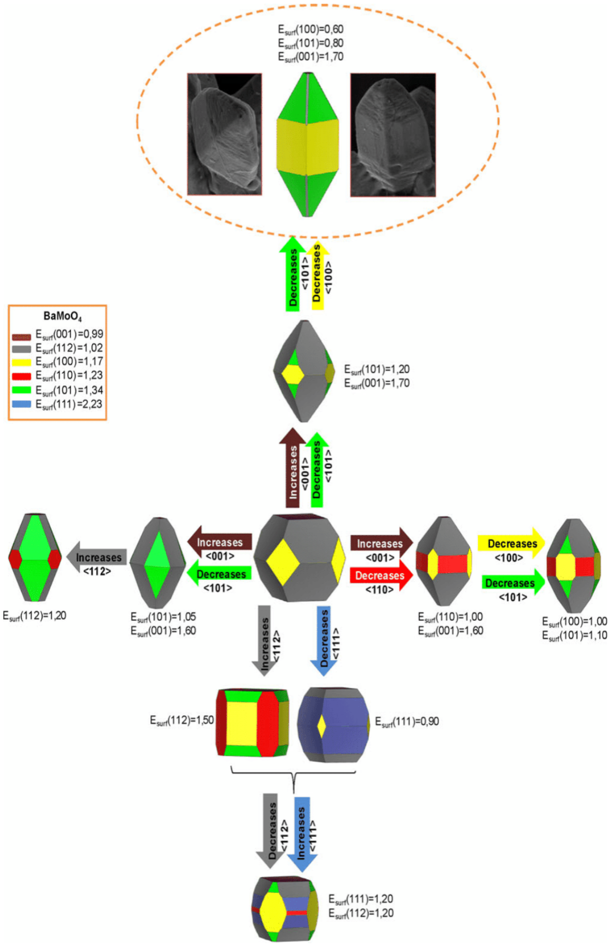

Fig. 5 Crystallographic structures and morphology map for the $BaMoO_4$ crystals (the surface energy units are given in J/m^2). The experimental FE-SEM images (inset) are included for comparison.

In relation to the band structures, the differences in the structural properties of the bulk and the surfaces can be observed. This is due to the reduced coordination of the O atoms in the top layers, which causes spacing between the adjacent layers due to vacancies. The coordination numbers for the exposed metal atoms are presented in figure 3. The essential features of the different surfaces remain constant but significant differences in the distribution of the electronic states is observed for the (001), (100), (110), and (101) surfaces, where the reduced coordination environment of the surface terminated oxygen atoms gives rise to a split-off feature in the O 2p and Mo 4d partial DOS at the bottom of the conduction band. Surface states reduce the bulk band gap (5.8 eV) by 0.1–0.7 eV depending on the specific surface, as can be observed in Table 2. At this stage, a note of caution is mandatory, it is well known that DFT approach underestimates the band gap energy due to its

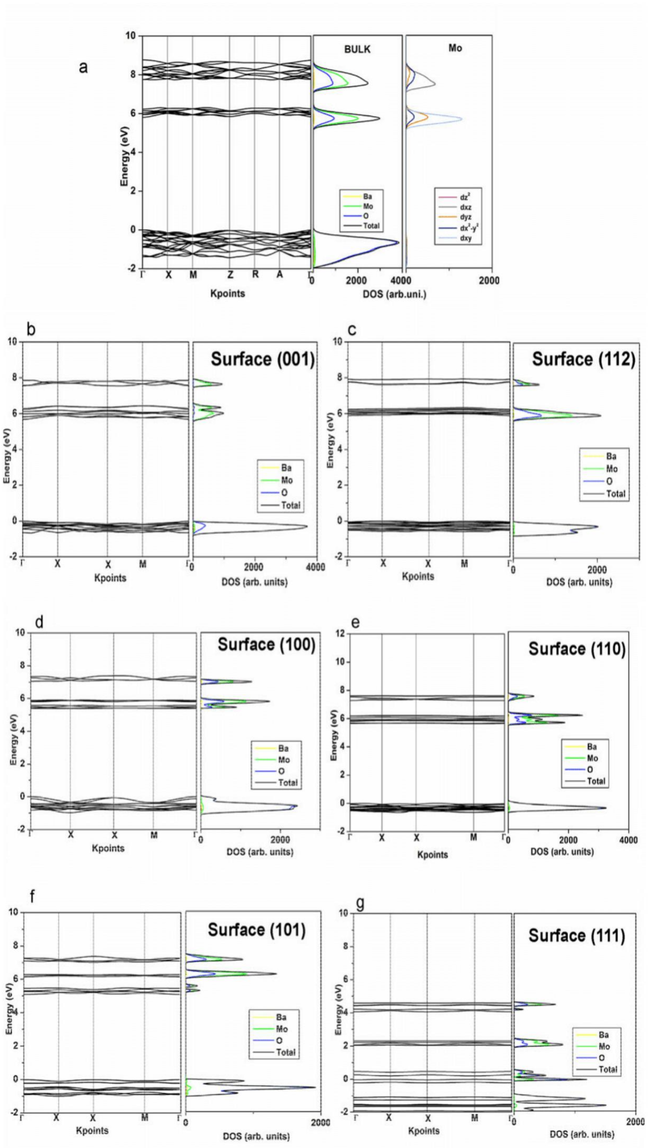

Fig. 6 Calculated band structures and DOS for (a) bulk $BaMoO_4$ and the (b) (001), (c) (112), (d) (100), (e) (110), (f) (101), and (g) (112) surfaces.

independent particle picture. [59–62] All surfaces present an insulating band gap except for the (111) surface, which has a large surface energy value and exhibits a conducting behavior. This can be attributed to the three oxygen vacancies in the undercoordinated [BaO$_5$] cluster and one of them in [MoO$_3$] cluster, being the Mo-O interaction more covalent than Ba–O interaction. This result is similar than in scheelite BaWO$_4$ system. [34].

3 Conclusion

Systematic DFT calculations were carried out to study the structure, surface stability (involving the (001), (101), (110), (100), (111), and (112) surfaces), and morphological transformations of BaMoO$_4$. The experimental simulations complemented the FE-SEM techniques used to investigate the morphology of the as-synthesized BaMoO$_4$ aggregates.

The main conclusions of this work can be summarized as follows. i) A simple preparation route using a co-precipitation method can provide an effective process to synthesize inorganic compounds with interesting morphologies and regular particle sizes with an easy handling process and a short reaction time. ii) The building blocks of the BaMoO$_4$ structure were deltahedral [BaO$_8$] and [MoO$_4$] clusters, i.e., a local coordination structure for both the Ba and Mo atoms. iii) The order of stability of the BaMoO$_4$ surfaces according to theoretical calculations was (001) > (112) > (100) > (110) > (101) > (111). iv) The calculated morphology of the BaMoO$_4$ based on the Wulff construction was (112) (70.9%), (001) (15.1%), and (100) (14.0%) with the (112) crystal surface as the commonly exposed surface. v) The relative energetics of all the surface structures were modulated to obtain a complete map of the morphologies available for BaMoO$_4$, which enabled us to identify where the observed morphology from the FE-SEM images was located on this map. vi) The obtained experimental and theoretical morphologies coincided when the value of the surface energy for the (001) surface decreased while that of the (100) and (101) surfaces simultaneously increased. vi) Analysis of the surface structures suggested that the electronic properties could be associated with the presence of undercoordinated [BaO$_x$] ($x = 4$, 5, and 6) and [MoO$_y$] ($y = 3$) clusters. vi) Finally, the present study could serve as an appropriate model to clarify how knowledge about surface-specific properties could be utilized to design crystal morphologies that exhibit improved performances in various applications.

4 Experimental section

Synthesis of the BaMoO$_4$ crystals: BaMoO$_4$ crystals were synthesized by a simple co-precipitation route at 80 °C. All chemical reagents were of analytical grade and were used without further treatment. Sodium molybdate dihydrate (1 x 10^{-3} mol) ($Na_2MoO_4.2H_2O$, Strem Chemicals, 99.95%) was dissolved in 50 mL of distilled water at 80 °C with vigorous stirring. Then, barium nitrate (1 x 10^{-3} mol) ($Ba(NO_3)_2$, Sigma-Aldrich, 99%), solubilized in 50 mL of distilled water at 80 °C, was added under constant stirring. The pH of the solution was maintained at 7, and the temperature was maintained at 80 °C. Then, there was a rapid formation of a white precipitate. This precipitate was washed with distilled water several times. Finally, it was collected and dried in a conventional furnace at 323 K for 8 h.

Characterization of the BaMoO$_4$: The phase composition of the as-prepared sample was detected by X-ray powder diffraction (XRD, D/MAX/2500PC, Rigaku, Japan), operating at 40 kV and 150 mA, Cu Kα radiation ($\lambda = 1.5406$ Å) in a 2θ range from 10° to 110° with a scan rate of 0.02°/min. Rietveld refinement [63] of the measured XRD pattern was carried out using the general structure analysis (GSAS) program. [64] The diffraction peak profiles were adjusted using the Thompson–Cox–Hastings pseudo-Voigt (pV-TCH) function and by an asymmetry function, as described by Finger et al. [65] The background was corrected using a Chebyschev polynomial of the first order. The strain anisotropy broadening was corrected using the phenomenological model described by Stephens. [66] A field-emission scanning electron microscope (FE-SEM, Inspect F50, FEI Company, Hillsboro, OR) was used to observe the morphology of the particles.

Theoretical Calculations: In this work, we simulated, considering symmetrical slabs (with respect to the mirror plane), the (001), (101), (110), (100), (111), and (112) surfaces of BaMoO$_4$. Morphology studies have been carried out on various metal oxides such as PbMoO$_4$, [67] CaWO$_4$, [68] α-Ag$_2$WO$_4$, [24] and Ag$_3$PO$_4$, [69] as well as Co$_3$O$_4$, Fe$_2$O$_3$, In$_2$O$_3$, [25] α-Ag$_2$MoO$_4$, [70] and BaWO$_4$. [34] All these studies have shown a combination of experimental and theoretical insights into the electronic, structural, and energetic properties controlling the morphology and transformation mechanisms, and the corresponding computational methodology, based on the Wulff construction, can be found in these papers.

The calculations were carried out with the CRYSTAL14 computer program [71] within the framework of the density functional theory (DFT) with the hybrid functional B3LYP. [72, 73] The atomic centers were described using the basis sets for the Mo [74] pseudopotential, and the O [74] and Ba [75] (6-31G* basis set) were described by the standards, respectively. The Brillouin zone was sampled using the Monkhorst–Pack method and at different k-point grids according to the system size. The thresholds controlling the accuracy of the calculation of the Coulomb and exchange integrals were set to 10^{-8} (ITOL1 to ITOL4) and 10^{-14} (ITOL5), which assures a convergence in total energy better than 10^{-7} a.u., whereas the percentage of Fock/Kohn–Sham matrix mixing was set to 40 (IPMIX = 40). [76].

Acknowledgements. This work was financially supported by the following Spanish research funding institutions: the CTQ2012-36253-C03-02 project (Ministerio de Economia y Competitividad), and the PrometeoII/2014/022 and ACOMP/2014/270 projects (Generalitat Valenciana) and the following Brazilian research funding institutions: CNPq (INCTMN 573636/2008-7), FAPESP (2013/07296-2, 2012/14468-1, 2013/26671-9, and 2014/04350-9), CAPES/PNPD 1268069 (process A104/2013 and 99999.002998/2014-09), and the Programa de Cooperación Científica con Iberoamerica (Brasil) of Ministerio de Educación (PHBP14-00020). J.A. acknowledges the Ministerio de Economia y Competitividad "Salvador Madariaga" program, PRX15/00261.L.G. acknowledges Banco Santander (Becas Iberoamérica: Jóvenes profesores e investigadores). M.C. acknowledges Generalitat Valenciana for the Santiago Grisolia Program 2015/033.

Key words. $BaMoO_4$, co-precipitation method, morphology, Wulff construction.

References

[1] B. Wu, W. Yang, H. Liu, L. Huang, B. Zhao, C. Wang, G. Xu, and Y. Lin, Spectrochim. Acta A. **123**, 12 (2014).
[2] T. T. Basiev, A. A. Sobol, Y. K. Voronko, and P. G. Zverev, Opt. Mater. **15**, 205 (2000).
[3] D. A. Spassky, S. N. Ivanov, V. N. Kolobanov, V. V. Mikhailin, V. N. Zemskov, B. I. Zadneprovski, and L. I. Potkin, Radiat. Meas. **38**, 607 (2004).
[4] C. S. Lim, J. Lumin. **132**, 1774 (2012).
[5] J. H. Ryu, J. W. Yoon, and K. B. Shim, J. Alloys Compd. **413**, 144 (2006).
[6] C. Zhang, L. Zhang, C. Song, G. Jia, S. Huo, and S. Shen, J. Alloy Compd. **589**, 185 (2014).
[7] G. R. Tian and S. X. Sun, Cryst. Res. Technol. **45**, 188 (2010).
[8] M. Ghaed-Amini, M. Bazarganipour, M. Salavati-Niasari, and K. Saberyan, Trans. Nonferrous Met. Soc. China. **25**, 3967 (2015).
[9] W. -L. Feng, Y. Jin, Y. Wu, D. -F. Li, and A. -K. Cai, J. Lumin. **134**, 614 (2013).
[10] Y. Mi, Z. Huang, Z. Zhou, F. Hu, and Q. Meng, Chem. Lett. **38**, 404 (2009).
[11] Y. Sun, J. Ma, J. Fang, C. Gao, and Z. Liu, Ceram. Int., **37**, 683 (2011).
[12] A. P. A. Marques, D. M.A. de Melo, C. A. Paskocimas, P. S. Pizani, M. R. Joya, E. R. Leite, and E. Longo, J. Solid State Chem. **179**, 671 (2006).
[13] M. F. C. Abreu, F. V. Motta, R. C. Lima, M. S. Li, E. Longo, and A. P. de A. Marques, Ceram. Int. **40**, 6719 (2014).
[14] A. Gholami and M. Maddahfar, J. Mater. Sci.: Mater. Electron. **27**, 6773 (2016).
[15] J. C. Sczancoski, L. S. Cavalcante, N. L. Marana, R. O. da Silva, R. L. Tranquilin, M. R. Joya, P. S. Pizani, J. A. Varela, J. R. Sambrano, M. Siu Li, E. Longo, and J. Andrés, Curr. Appl. Phys. **10**, 614 (2010).
[16] Z. Shahri, M. Bazarganipour, and M. Salavati-Niasari, Superlattice. Microst. **63**, 258 (2013).
[17] T. Gholami, M. Salavati-Niasari, M. Bazarganipour, and E. Noori, Superlattice. Microst. **61**, 33 (2013).
[18] M. Salavati-Niasari, B. Shoshtari-Yeganeh, and M. Bazarganipour, Superlattice. Microst. **58**, 20 (2013).
[19] E. Noori, M. Bazarganipour, M. Salavati-Niasari, and T. Gholami, J. Clust Sci. **24**, 1171 (2013).
[20] M. Goudarzi, M. Bazarganipour, and M. Salavati-Niasari, Rsc Adv. **4**, 46517 (2014).
[21] S. Mandizadeh, M. Bazarganipour, and M. Salavati-Niasari, Ceram. Int. **40**, 15685 (2014).
[22] M. Ghaed-Amini, M. Bazarganipour, and M. Salavati-Niasari, J. Ind. Eng. Chem. **21**, 1089 (2015).
[23] S. Gholamrezaei, M. Salavati-Niasari, M. Bazarganipour, M. Panahi-Kalamuei, and S. Bagheri, Adv. Powder Technol. **25**, 1585 (2014).
[24] J. Andrés, L. Gracia, A. F. Gouveia, M. M. Ferrer, and E. Longo, Nanotechnology. **26**, 405703 (2015).
[25] M. M. Ferrer, A. F. Gouveia, L. Gracia, E. Longo, and J. Andrés, Modelling Simul. Mater. Sci. Eng. **24**, 025007 (2016).
[26] S. S. Ding, M. Lei, H. Xiao, G. Liu, Y. C. Zhang, K. Huang, C. Liang, Y. J. Wang, R. Zhang, D. Y. Fan, H. J. Yang, and Y. G. Wang, J. Alloy. Compd. **579**, 549 (2013).
[27] M. Lei, C. X. Ye, S. S. Ding, K. Bi, H. Xiao, Z. B. Sun, D. Y. Fan, H. J. Yang, and Y. G. Wang, J. Alloy. Compd. **639**, 102 (2015).
[28] L. Ma, Y. Sun, P. Gao, Y. Yin, Z. Qin, and B. Zhou, Mater. Lett. **64**, 1235 (2010).
[29] H. Shi, L. Qi, J. Ma, and N. Wu, Adv. Funct. Mater. **15**, 442 (2005).
[30] H. Shi, X. Wang, N. Zhao, L. Qi L, and J. Ma, J. Phys. Chem. B. **110**, 748 (2006).
[31] Z. Luo, H. Li, H. Shu, K. Wang, J. Xia, and Y. Yan, Cryst. Growth Des. **8**, 2275 (2008).
[32] Y. Yin, Z. Gan, Y. Sun, B. Zhou, X. Zhang, D. Zhang, and P. Gao, Mater. Lett. **64**, 789 (2010).
[33] L. K. Bharat, S. H. Lee, and J. S. Yu, Mater. Res. Bull. **53**, 49 (2014).
[34] M. C. Oliveira, L. Gracia, I. C. Nogueira, M. F. C. Gurgel, J. M. R. Mercury, E. Longo, and J. Andrés, Ceram. Inter. **42**, 10913 (2016).

[35] I. C. Nogueira, L. S. Cavalcante, P. F. S. Pereira, M. M. de Jesus, J. M. Rivas Mercury, N. C. Batista, M. S. Li, and E. Longo, J. Appl. Cryst. **46**, 1434 (2013).

[36] O. Gomis, J. A. Sans, R. Lacomba-Perales, D. Errandonea, Y. Meng, J. C. Chervin, and A. Polian, Phys. Rev. B. **86**, 054121 (2012).

[37] H. Zhao, F. Zhang, X. Guo, Q. Zhang, and T. Liu, J. Phys. Chem. Solids **71**, 1639 (2010).

[38] X. Guo, Q. Zhang, T. Liu, M. Song, J. Yin, H. Zhang, and X. Wang, Nucl. Instrum. Meth. B. **267**, 1093 (2009).

[39] V. Nassif, R. E. Carbonio, and J. A. Alonso, J. Solid State Chem. **146**, 266 (1999).

[40] V. Thangadurai, C. Knittlmayer, and W. Weppner, Mater. Sci. Eng. B. **106**, 228 (2004).

[41] A. Phuruangrat, T. Thongtem, and S. Thongtem, Superlattice. Microst. **52**, 78 (2012).

[42] A. Phuruangrat, T. Thongtem, and S. Thongtem, J. Phys. Chem. Solids. **70**, 955 (2009).

[43] T. Thongtem, A. Phuruangrat, and S. Thongtem, Mater. Lett. **62**, 454 (2008).

[44] Z. Luo, H. Li, H. Shu, K. Wang, and J. Xia, Y. Yan, Mater. Chem. Phys. **110**, 17 (2008).

[45] D. Errandonea, L. Gracia, R. Lacomba-Perales, A. Polian, and J. C. Chervin, J. Appl. Phys. **113**, 123510 (2013).

[46] R. Vilaplana, O. Gomis, F. J. Manjón, P. Rodríguez-Hernández, A. Muõoz, D. Errandonea, S. N. Achary, and A. K. Tyag, J. Appl. Phys. **112**, 103510 (2012).

[47] G. Wulff, Z. Kristallogr. Miner. **34**, 449 (1901).

[48] C. Herring, Phys. Rev. **82**, 87 (1981).

[49] J. W. Gibbs, Trans. Conn. Acad. Of Arts Sci. **3**, 108 (1875).

[50] T. Wang, X. Tian, Y. Yang, Y. -W. Li, J. Wang, M. Beller, and H. Jiao, Phys. Chem. Chem. Phys. **18**, 6005 (2016).

[51] Z. Y. Gao, W. Sun, Y. -H. Hu, and X. -W. Liu, T. Nonferr. Metal. Soc. **23**, 2147 (2013).

[52] T. G. Cooper and N. H. de Leeuw, Surf. Sci. **531**, 159 (2003).

[53] P. Mogilevsky, T. A. Parthasarathy, and M. D. Petry, Acta Mater. **52**, 5529 (2004).

[54] H. -Y. Jung and Y. -D. Huh, Crystengcomm. **17**, 1398 (2015).

[55] A. S. Barnard and P. Zapol, Phys. Rev. B. **70**, 235403 (2004).

[56] L. Li, F. Abild-Pedersen, J. Greeley, and J. K. Nørskov, J. Phys. Chem. Lett. **6**, 3797 (2015).

[57] M. Li, Y. Guan, Y. Yin, X. Cui, S. Rong, G. Jin, Y. Hao, and Q. Wu, Superlattice. Microst. **80**, 222 (2015).

[58] E. -K. Ryu and Y. -D. Huh, Bull. Korean Chem. Soc. **29**, 503 (2008).

[59] J. P. Perdew, Int. J. Quantum Chem. **28**, 497 (1985).

[60] A. J. Cohen, P. M.-Sánchez, and W. Yang, Chem. Rev. **112**, 289 (2012).

[61] P. Mori-Sánchez, A. J. Cohen, and W. Yang, Phys. Rev. Lett. **100**, 146401 (2008).

[62] D. Bagayoko, AIP Advances. **4**, 127104 (2014).

[63] H. M. Rietveld, J. Appl. Cryst. **2**, 65 (1969).

[64] A. C. Larson, R. B. V. Dreele, "General Structure Analysis System (Gsas)". Report Laur. Los Alamos National Laboratory: New Mexico Usa; (2004). User Manual.

[65] W. Finger, D. E. Cox, and A. P. Jephcoat, J. Appl. Cryst. **27**, 892 (1994).

[66] P. W. Stephens, J. Appl. Cryst. **32**, 281 (1999).

[67] M. R. D. Bomio, R. L. Tranquilin, F. V. Motta, C. A. Paskocimas, R. M. Nascimento, L. Gracia, J. Andrés, and E. Longo, J. Phys. Chem. C. **117**, 21382 (2013).

[68] V. M. Longo, L. Gracia, D. G. Stroppa, L. S. Cavalcante, M. Orlandi, A. J. Ramirez, E. R. Leite, J. Andrés, A. Beltrán, J. A. Varela, and E. Longo, J. Phys. Chem. C. **115**, 20113 (2011).

[69] G. Botelho, J. Andres, L. Gracia, L. S. Matos, and E. Longo, Chempluschem. **81**, 202 (2016).

[70] M. T. Fabbro, C. Saliby, L. R. Rios, F. A. La Porta, L. E. Gracia, M. S. Li, J. Andrés, L. P. S. Santos, and E. Longo, Sci. Technol. Adv. Mater. **16**, 065002 (2015).

[71] R. Dovesi, V. R. Saunders, C. Roetti, R. Orlando, C. M. Zicovich-Wilson, F. Pascale, B. Civalleri, K. Doll, N. M. Harrison, I. J. Bush, Ph. D'Arco, M. Llunel, M. Causà, and Y. Noël, Crystal 14. University Of Torino: Torino Italy; (2014). User Manual.

[72] A. D. Becke, J. Chem. Phys. **98**, 5648 (1993).

[73] C. T. Lee, W. T. Yang, and R. G. Parr, Phys. Rev. B: Condens. Matter. **37**, 785 (1988).

[74] http://Www.Crystal.Unito.It/Basis_Sets/Oxygen.Html, http://Www.Crystal.Unito.It/Basis_Sets/Molibdenum.Html.

[75] http://Www.Tcm.Phy.Cam.Ac.Uk/~Mdt26/Basis_Sets/Ba_Basis.Txt.

[76] H. J. Monkhorst and J. D. Pack, Phys. Rev. B: Condens. Matter. **13**, 5188 (1976).

Applied Surface Science

ELSEVIER

ARTICLE

Geometry, electronic structure, morphology, and photoluminescence emissions of $BaW_{1-x}Mo_xO_4$ (x=0, 0.25, 0.50, 0.75, and 1) solid solutions: theory and experiment in concert

Marisa Carvalho Oliveira[a,b], Juan Andrés[a]*, Lourdes Gracia[c], Michelle Suzane M. P. de Oliveira[d], Jose Manuel R. Mercury[d], Elson Longo[b] and Içamira Costa Nogueira[e]

[a]Departamento de Química Física y Analítica, Universitat Jaume I, 12071 Castelló de la Plana, Spain;
[b]CDMF-UFSCar, Universidade Federal de São Carlos, P.O. Box 676, 13565-905 São Carlos, SP, Brazil;
[c]Departamento de Química Física, Universitat de València, 46100 Burjassot, Spain;
[d]PPGEM-IFMA, Instituto Federal do Maranhão, CEP 65030-005, São Luís, MA, Brazil;
[e]Departamento de Física, UFAM, 3000-Japiim, Manaus, AM 69077-000, Brazil

Abstract

The design of a solid solution with tunable electro-optical properties and multifunctionality is a promising strategy for developing novel materials. In this work, $BaW_{1-x}Mo_xO_4$ (x=0, 0.25, 0.5, 0.75, and 1) solid solutions have been successfully prepared for the first time by a co-precipitation method. Their crystal structure and phase composition were determined by X-ray diffraction and Rietveld refinements. Fourier transform infrared and micro Raman spectroscopy in combination with field-emission scanning electron microscopy (FE-SEM) were used to describe the microstructures and chemical compositions of the synthesized materials. The influence of chemical composition on morphology and photoluminescence (PL) emission has been analyzed. The geometry, electronic structures, and morphologies of $BaW_{1-x}Mo_xO_4$ (x=0, 0.25, 0.5, 0.75, and 1) solid solutions were investigated by first-principles quantum-mechanical calculations based on the density functional theory. By using Wulff construction and the values of the surface energies for the (112), (001), (110), (101), (100), and (111) surfaces, a complete map of the available morphologies for the $BaW_{1-x}Mo_xO_4$ solid solutions was obtained. These results show a qualitative agreement between the experimental morphologies obtained using the FE-SEM images and the computational models. The substitution of W^{6+} by Mo^{6+} enhances the electron-transfer process due to a stronger Mo(4d)-O(2p) hybridization compared to W(5d)-O(2p) for the W/Mo-O superficial bonds, and is responsible for the change in morphology from $BaWO_4$ to $BaMoO_4$. Such a fundamental study, which combines multiple experimental methods and first-principles calculations, has provided valuable insight into obtaining a basic understanding of the local structures, bonding, morphologies, band gaps, and electronic and optical properties of the $BaW_{1-x}Mo_xO_4$ (x=0, 0.25, 0.5, 0.75, and 1) solid solutions.

1. Introduction

Alkaline earth molybdate and tungstate ($AMoO_4$ and AWO_4, A = Ba, Sr, or Ca) are inorganic compounds having the scheelite-type ABO_4 structure, and exhibit interesting properties for a wide range of applications such as scintillators, luminescent materials, electro-optical devices, and catalysts [1], [2], [3], [4], [5].

From a structural point of view, in the tetragonal scheelite structure (space group I41/a), each hexavalent metal cation, Mo^{6+} or W^{6+}, is tetrahedrally coordinated to four oxygen anions, yielding [MoO_4] or [WO_4] clusters. The alkaline earth bivalent metal cations, A^{2+}, are located between these tetrahedral clusters, forming an eightfold coordination with the oxygen anions, i.e., [AO_8] clusters [6] or [MoO_4]/[WO_4] clusters being the building blocks of their 3-D structures. The versatility of this family of complex oxide crystals is owing to the fact that their physical and chemical properties depend on their composition, which in turn allows the tuning of the final properties by changing the chemical composition. Very recently, L. Liu et al. [7] have obtained different morphologies by adjusting the relative concentrations of solute, water, and ethanol, while the mechanisms through which these morphologies were formed have been analyzed by using *in situ* scanning electron microscopy and atomic force microscopy.

Our group has been engaged in a research project devoted to the study of the structural, morphological, and optical properties of $BaWO_4$ [8] and $BaMoO_4$ [9] microcrystals by using a combination of theoretical calculations and experimental techniques [10]. As an extension of these studies, in this work, we focus our attention on $BaW_{1-x}Mo_xO_4$ solid solutions, in which both $BaWO_4$ and $BaMoO_4$ have the scheelite structure. When the W^{6+} cations in $BaWO_4$ are partially replaced by the Mo^{6+} cations, the formation of a $BaW_{1-x}Mo_xO_4$ solid solution is expected, and its structural, electronic, and optical properties can be tailored over a broad range, with the Mo/W ratio $0 \leq x \leq 1$, opening the door to finding new materials that can exhibit a wide range of technologically relevant properties. Recently, Bouzidi et al. [11] have prepared $BaW_{1-x}Mo_xO_4$ solid solutions (x = 0.00, 0.05, 0.10, 0.15, and 0.20) by a solid state reaction method, while Vidya et al. [12] have prepared $AMo_{0.5}W_{0.5}O_4$ (where A=Ba, Sr, or Ca) by a single-step modified combustion technique.

Based on the above considerations, in this work, we seek to fulfill a four-fold objective. The first is to report, for the first time, the synthesis of novel $BaW_{1-x}Mo_xO_4$ (x=0, 0.25, 0.5, 0.75, and 1) solid solutions by employing a co-precipitation method. Secondly, X-ray diffraction (XRD), Fourier transform infrared (FT-IR), and micro Raman (MR) spectroscopy, in combination with field-emission scanning electron microscopy (FE-SEM) and Rietveld refinements, were employed to characterize the samples and determine the effect of their chemical composition on the morphology and photoluminescence (PL) emissions. The third aim is to investigate the geometry, electronic structure, and properties of $BaW_{1-x}Mo_xO_4$ using the density functional theory (DFT). The fourth aim is to apply a joint experimental and theoretical strategy developed by us to obtain a complete map of the morphologies available for the $BaW_{1-x}Mo_xO_4$ solid solutions. Based on these results, we hope to understand how the different surfaces change their energies throughout the synthesis process, and propose a mechanism by which the experimental and theoretical morphologies of the $BaW_{1-x}Mo_xO_4$ solid solutions match. We believe that these novel results are of significant relevance, since they may inspire the efficient synthesis of these and related molybdate/tungstate solid solutions and provide critical information to expand our fundamental understanding of the effect of substitution of W by Mo in these compounds.

This paper contains three more sections. The next section is the experimental section (synthesis and characterization), where the computational details are given. In section three, the results are presented and discussed. The main conclusions are summarized in the fourth and final section.

2. Experimental procedures

2.1. Synthesis

$BaW_{1-x}Mo_xO_4$ (x = 0, 0.25, 0.50, 0.75, and 1) solid solutions were synthesized by a co-precipitation method at 80 °C. Sodium tungstate dihydrate ($Na_2WO_4.2H_2O$, Stream Chemical, 99.5%, 1×10^{-3} mol) and sodium molybdate dihydrate ($Na_2MoO_4.2H_2O$, Stream Chemical, 99.95%, 1×10^{-3} mol) were dissolved in 50 mL of distilled water at 80 °C by vigorous stirring. Then, 1×10^{-3} mol of barium nitrate ($Ba(NO_3)_2$, Sigma-Aldrich, 99%), solubilized in 50 mL of distilled water at 80 °C, was added to the previously mentioned solution. The solution was maintained at 80 °C until the $BaW_{1-x}Mo_xO_4$ crystals precipitated. This precipitate was washed with distilled water several times, collected, and dried in a conventional furnace at 50 °C for 8 h.

2.2. Characterization

To determine the phase composition and crystal structure of the as-synthesized $BaW_{1-x}Mo_xO_4$ (x = 0, 0.25, 0.50, 0.75, and 1) crystals, X-ray powder diffraction (XRD) was employed in combination with Rietveld refinements [13] and the General Structure Analysis System program [14]. The measurements were carried out using a D/MAX/2500PC diffractometer (Rigaku, Japan) operating at 40 kV and 150 mA with CuKα radiation (λ= 1.5406A) in the 2ϑ range 10° to 110° at a scan rate of 0.02°/min. The diffraction peak profiles were adjusted using the Thompson–Cox–Hastings pseudo-Voigt (pV-TCH) function and an asymmetry function described by Finger et al. [15]. The background was corrected using a Chebyshev polynomial of the first order. The strain anisotropy broadening was corrected using the phenomenological model described by Stephens [16]. The high-quality powder diffraction data in combination with the Rietveld method allowed the refinement of a structural model (atomic coordinates, site occupancies, and atomic displacement parameters), as well as the profile parameters (lattice constants, peak shape, sample height, and background).

The morphologies of the particles were observed with a field-emission scanning electron microscope, model InspectF50 (FEI Company, Hillsboro, USA), operated at 15 kV. The Fourier transform infrared spectroscopy (FT-IR) patterns were recorded in the range 250–1100 cm^{-1} using KBr pellets as a reference in a Bomen-Michelson spectrophotometer in the transmittance mode (model MB-102). Micro Raman (MR) spectroscopy was conducted on a Horiba Jobin-Yvon (Japan) spectrometer coupled to a charge-coupled device detector and Ar-ion laser (MellesGriot, United States) operating at 514.5 nm with a maximum power of 200 mW. The spectra were measured in the range 48–1100 cm^{-1}. The PL spectra were measured with a Monospec 27 monochromator (Thermal Jarrel Ash, United States) coupled to a R446 photomultiplier (Hamamatsu Photonics, Japan). A Kr ion laser (Coherent Innova 200 K, United States) (λ = 350 nm) was used as the excitation source. The incident laser beam power on the sample was maintained at 15 mW. All the measurements were performed at room temperature.

2.3. Computational details

Quantum-mechanical calculations using DFT at the B3LYP hybrid functional level [17], [18] have been carried out by means of the CRYSTAL14 computer code [19]. This method has been successfully employed in various studies of the bulk and surface electronic and structural properties of perovskite [20], [21], molybdate [22], [23], [9], and tungstate based materials [24], [25], [26], [8], as well as Ag_2CrO_4 [27], and $LaVO_4$ [28].

The atomic centers were described using pseudopotential basis sets for the Mo [29] atom and large-core effective core potentials derived by Hay and Wadt, modified by Cora *et al.*[30] for the W atom; while the O [31] and Ba [32] atoms were described by the standard all-electron-basis sets (6-31G* basis set).

The irreducible edge of the Brillouin zones was sampled using the Monkhorst–Pack method [33] at different k-point grids according to the system size. The thresholds controlling the accuracy of the calculation of the Coulomb and exchange integrals were set to 10^{-8} (ITOL1 to ITOL4) and 10^{-14} (ITOL5), which assures a convergence in total energy better than 10^{-7} a.u., whereas the percentage of Fock/Kohn–Sham matrix mixing was set to 40 (IPMIX = 40) for the calculation of the equilibrium geometries and electronic properties of the $BaW_{1-x}Mo_xO_4$ structures.

The initial cell and atomic position parameters used in the optimization process were taken from the results of Rietveld refinements of $BaWO_4$ and $BaMoO_4$. The scheelite structure is characterized by barium atoms bonded to eight oxygen atoms, resulting in [BaO_8] bisdisphenoid clusters, and the molybdenum or tungsten atoms coordinated to four oxygen atoms in a tetrahedral configuration, i.e., forming [MoO_4] or [WO_4] clusters.

The scheelite $BaWO_4$ conventional unit cell containing 24 atoms is showed in **Fig. 1(a)**. There are four W atoms in the structure generated from the *4a* Wyckoff position by symmetry operations.

In order to investigate the energetics of the Mo^{6+} distribution, several representative cells were generated, differing in the positions of the Mo^{6+} cations. In the most stable arrangement, the Mo^{6+} ions lie far apart, and the corresponding structures for $BaW_{1-x}Mo_xO_4$ (x=0.25, 0.5, 0.75, and 1) are depicted in **Fig. 1(b)**, **1(c)**, **1(d)**, and **1(e)**, respectively.

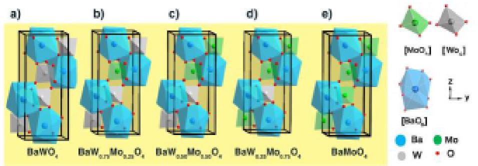

Figure 1. Unit cell representation of $BaW_{1-x}Mo_xO_4$ crystals: (a) x = 0, (b) x=0.25, (c) x =0.50, (d) x = 0.75, and (e) x=1. The constituent clusters: [MoO_4], [WO_4] and [BaO_8] are depicted.

The surface models containing 4, 4, 4, 8, 4, and 4 molecular units for the (001), (101), (110), (100), (111), and (112) surfaces of $BaW_{1-x}Mo_xO_4$ (x= 0, 0.25, 0.50, 0.75, and 1), respectively, were used in the calculations, and are shown in **Fig. 2**. These surfaces were modeled using symmetrical slabs (with respect to the mirror plane), and all of them were terminated with the O planes. After the corresponding optimization process and thickness convergence tests, the resulting slab models consisted of four molecular units containing 24 ions on the (001), (101), (110), (111), and (112) surfaces, while the (100) surface was modeled containing 48 ions, considering a thickness of the surface not lower than 7 Å.

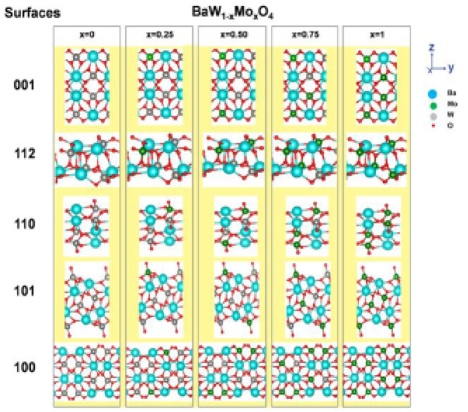

Figure 2. Schematic representations of the different surfaces of $BaW_{1-x}Mo_xO_4$ (x = 0, 0.25, 0.50, 0.75, and 1) solid solutions.

The surface calculations were based on the equilibrium morphology of a crystal predicted by the classic Wulff construction, which minimizes the total surface energy at a fixed volume, providing a simple correlation between the surface energy (E_{surf}) of the (hkl) plane and its distance r_{hkl} in the normal direction from the center of the crystallite [34].

The surface energy (E_{surf}) is defined as the total energy per repeating cell of the slab (E_{slab}) minus the total energy of the perfect crystal per molecular unit for each percentage of solid solution, i.e., 0, 25, 50, 75, and 100% (E_{bulk}) multiplied by the number of molecular units on the surface (N) and divided by the surface area, A, per repeating cell of the two sides of the slab, as shown in equation (1).

$$E_{suf} = \frac{1}{2A}\left(E_{slab} - N \cdot E_{bulk}\right) \qquad (1)$$

3. Results and discussion

3.2. X-Ray diffraction and Rietveld refinements

The structural study of the $BaW_{1-x}Mo_xO_4$ (x = 0, 0.25, 0.50, 0.75, and 1) solid solutions was performed by means of XRD (**Fig. 3**) and Rietveld refinements (**Fig. S1**).

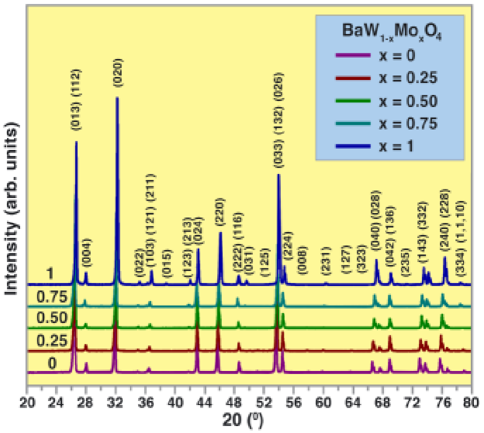

Figure 3. X-ray diffraction patterns of $BaW_{1-x}Mo_xO_4$ (x=0, 0.25, 0.50, 0.75, and 1) crystals.

An analysis of the XRD patterns displayed in **Fig. 3** shows that all the peaks can be indexed perfectly to a scheelite-type-tetragonal structure, with the space group symmetry I41/a and four molecular formula units per unit cell (Z = 4) [35]. The XRD peak patterns and Rietveld refinement plots of these crystals show good agreement between the experimentally observed XRD patterns and the theoretically fitted results (see **Fig. S1(a-c)**). The XRD patterns illustrate that all the diffraction peaks for the $Ba(W_{1-x}Mo_x)O_4$ crystals are monophasic, without the presence of secondary phases. Thus, it was proved that the substitution of W^{6+} by Mo^{6+} in the $BaWO_4$ crystal lattice forms $Ba(W_{1-x}Mo_x)O_4$ solid solutions. The occupation sites of W^{6+} and Mo^{6+} for each solid solution in the crystal lattice, as calculated by the Rietveld refinements, are presented in Table 1. The good quality for the structural refinements is evidenced by the low deviations of the statistical parameters (R_{wp}, R_p, R_{Bragg} and ^{2}). These parameters are listed in Table 1 and suggest that the measured diffraction patterns are in good agreement with the ICSD entry No. 155511 [35].

For comparison, first-principles calculations were used to determine the lattice parameters (**Table 1**) and atomic coordinates (Table S1) of the oxygen anions. These results are in good agreement with previous experimental observations. An analysis of the results shows that the substitution of W^{6+} by Mo^{6+} induces variations in the atomic coordinates of the oxygen atoms (see Table S1), indicating the existence of structural and electronic distortions in the $[WO_4]$, $[MoO_4]$, and $[BaO_8]$ clusters, as well as changes in the lattice parameters and a reduction in the unit cell volume.

Table 1. Lattice parameters, unit cell volume, and statistical parameters of the $BaW_{1-x}Mo_xO_4$ (x = 0.25, 0.50, and 0.75) solid solutions obtained by Rietveld refinements and calculations.

		Lattice Parameters			
Sample $BaW_{1-x}Mo_xO_4$	Cell volume (Å)^3	α = β = γ = 90°			
		Experimental		Theoretical	
		a =b (Å)	c (Å)	a = b (Å)	c (Å)
x=0	401.42	5.614(9)	12.732(6)	5.581(4)	12.412(6)
x=0.25	401.27	5.608(0)	12.759(0)	5.588(1)	12.445(0)
x=0.50	400.81	5.599(3)	12.783(9)	5.594(1)	12.477(8)
x=0.75	400.53	5.591(4)	12.811(0)	5.599(7)	12.519(2)
x=1	399.83	5.583(0)	12.827(0)	5.602(6)	12.574(6)
ICSD 155511 BaWO$_4$	398.48	5.603(4)	12.693(7)		

R_{Bragg}(%) = 6.95^a, 6.83^b, 6.29^c; χ^2(%) = 1.14^a, 1.20^b, 1.27^c; R_{wp}(%) = 13.64^a, 14.85^b , 16.28^c; R_p(%) = 8.71^a, 9.94^b, 11.07^c

3.2. Vibrational analysis

Molybdate and tungstate crystals with the scheelite-type tetragonal structure present 26 different vibration modes: $\Gamma(\text{Raman + infrared}) = 3A_g + 5A_u + 5B_g + 3B_u + 5E_g + 5E_u$, with A_g, B_g, and E_g being the Raman-active modes. Furthermore, the odd modes (A_u and E_u) are the active vibrational modes in the infrared spectra [36]. The experimental/theoretical spectra are shown in **Fig. 4 (a-f)**.

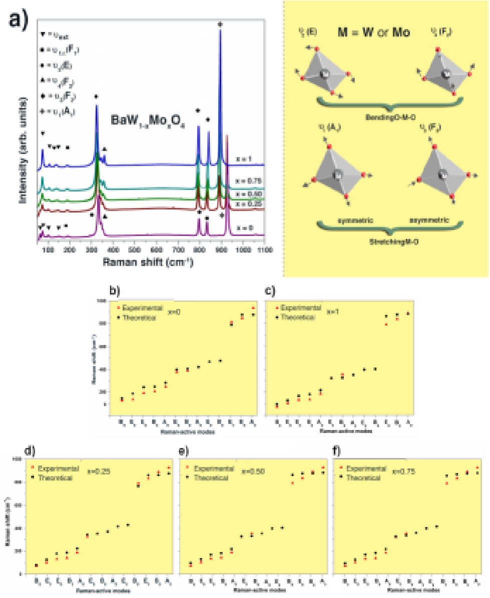

Figure 4. . MR spectra of $BaW_{1-x}Mo_xO_4$ (x=0, 0.25, 0.50, 0.75, and 1) solid solutions. (a) experimental spectra. In (b) x = 0, (c) x= 1, (d) x=0.25, (e) x = 0.50 and f) x = 0.75, the calculated values are compared with the experimental Raman-active modes.

The Raman spectra of the scheelite structures can be interpreted in terms of the modes of the $[MO_4]^{2-}$ (M= Mo or W) tetrahedra, which can be considered as the constituent units in the structures. Thus, these modes can be classified either as internal vibrations (the $[MO_4]^{2-}$ (M= Mo or W) center of mass does not move) or as external vibrations (motion of the Ba^{2+} cations and the movements of the $[MO_4]^{2-}$ tetrahedra as rigid units). The corresponding representation for the tetrahedral symmetry is composed of four internal modes $\nu_1(A_1) + \nu_2(E) + \nu_4(F_2)$, one free rotation mode $\nu_{fr}(F_1)$, and one translation mode $\nu_3(F_2)$; however, only some of these modes are active in the IR spectrum, namely, ν_3, $\nu_4(F_2)$ [37].

In the FTIR spectrum of $BaW_{1-x}Mo_xO_4$ (x = 0.25, 0.50, and 0.75), the $3B_u$ vibrations are silent modes; one A_u and one E_u modes are acoustic vibrations. The experimental FTIR spectra are illustrated in **Fig. S2.** A metal-oxygen band in the MO_4^{2-} cluster (M=Mo and W) appears in the FTIR spectrum (see **Fig. (S2)**), corresponding to the internal modes indicated as the antisymmetric stretching ($\nu_3(F_2)$) vibrations at 811–830 cm^{-1} and the bending vibration ($\nu_4(F_2)$), observed as a strong band at about 380 cm^{-1}.

The experimental and calculated Raman-active modes are shown in **Fig. 4 (a-f)**, indicating the existence of a strong interaction between the ions, which arises from the stretching and bending vibrations of the shorter metal–oxygen bonds within the anionic groups [38]. A comparison between the relative positions of the Raman-active modes for the $BaW_{1-x}Mo_xO_4$ (x = 0.25, 0.50, and 0.75) solid solutions are shown in **Fig. 4 (b-f).** DFT calculations using the B3LYP functional tend to overestimate the values of the vibrational frequencies; therefore, a scaling factor of 0.96 was used [39]. The calculations reveal the presence of three modes (A_g, E_g, and B_g, at approximately 452-375 cm^{-1}) not experimentally observed. A plausible explanation for this result can be that these modes have a very low intensity and are not easily detectable by experimental techniques.

Two high-frequency bands centered at 927 cm^{-1} for $BaWO_4$ and 894 cm^{-1} for $BaMoO_4$ are also present in $BaW_{1-x}Mo_xO_4$ (x = 0.25, 0.50, and 0.75) solid solutions, which correspond to intense peaks in the Raman (A_g) mode and are assigned to the symmetric stretching $\nu_1(A_1)$ of the bonds [←O←M→O→] (M=Mo and W), while the two Raman (B_g and E_g internal) modes at 836 and 792 cm^{-1} are attributed to the asymmetric stretching $\nu_3(F_2)$ of the bonds (→O→M→O→).

The peaks located at 357 and 324 cm^{-1} are assigned ($\nu_4(F_2)$, $\nu_2(E)$) to the rotational modes (E_g, B_g) as the bending modes. The free rotational $\nu_{fr}(F_1)$ mode at about 188 cm^{-1}, in addition to the external peaks (ν_{ext}) corresponding to the motions of MO_4^{2-} and Ba^{2+} are shown at approximately 74, 107, 126, and 143 cm^{-1}, which are assigned to rotational (A_g, E_g) and translational modes (B_g).

3.3. Photoluminescence emissions

The PL spectra of the $BaW_{1-x}Mo_xO_4$ (x=0.25, 0.50, and 0.75) solid solutions using the same excitation at 350 nm are depicted in **Fig. 5.**

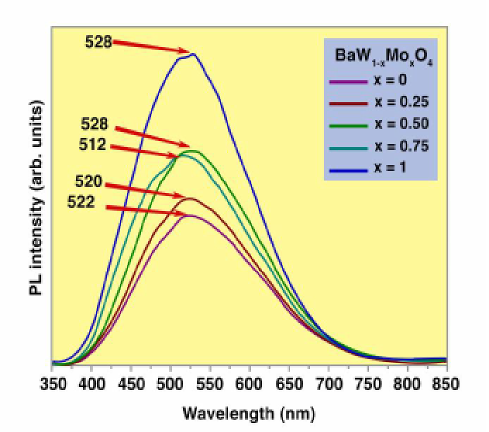

Figure 5. PL spectra of $BaW_{1-x}Mo_xO_4$ (x=0,0.25,0.50,0.75,1) crystals.

All the compositions (x =0, 0.25, 0.50, 0.75, and 1) exhibit PL emission peaks centered at 522, 520, 528, 512, and 528 nm, respectively. We note that the emission is attributed to the charge transfer in the $[MO_4]^{2-}$ (M= Mo and W) complex. The wide visible emission originates from the charge-transfer transition between the O 2p orbital and the empty d orbital of the $[MO_4]^{2-}$ (M= Mo and W) tetrahedral structure, with excitation energies located within the band gap [40], [41], i.e., self-trapping electron states. The one ground state is $^1A_1$ and the four single excited states are $^1A(^1T_1)$, $^1E(^1T_1)$, $^1E(^1T_2)$, and $^1B(^1T_2)$ [42], [43] .

The PL curves shown in **Fig. 5** represent a different type of electronic transition that can be associated with a specific structural arrangement of $[WO_4]$ or $[MoO_4]$ clusters, and can also be observed in the experimental results obtained from the Raman spectra that show two high-frequency bands at 927 cm^{-1} and 894 cm^{-1} for $BaWO_4$ and $BaMoO_4$, respectively, as well as for the $BaW_{1-x}Mo_xO_4$ (x = 0.25, 0.50, and 0.75) solid solution. In addition, we believe that the differences in the PL emission intensities presented in **Fig. 5** are induced by the substitution of W^{+6} by Mo^{+6} as the $BaW_{1-x}Mo_xO_4$ (x = 0.25, 0.50, and 0.75) solid solutions form, which can be associated with the influence of the chemical composition and electronic transition, as discussed in the next section.

3.4. Electronic properties

The local coordination of the superficial Mo^{6+} and W^{6+} is fundamental for describing the order of stability of the different surfaces of the $BaW_{1-x}Mo_xO_4$ (x=0, 0.25, 0.5, 0.75, and 1) solid solutions. The cleavage process associated with the slab model induces the presence of under-coordinated cations at the surface plane. Then, it is possible to find a relationship between the geometry, electronic structure, and surface energy values in order to discuss the order of stability of the investigated models.

We note that all the surfaces expose the superficial $[BaO_6]$ or $[BaO_5]$ clusters. However, the (001), (112), (101), (110), and (100) surfaces present $[MO_4]$ (M= Mo or W) clusters, while the (111) surface shows superficial $[MO_3]$ (M= Mo or W) clusters, implying the breaking of a M-O bond compared to the bulk compound. An analysis of both the (001) and (112) surfaces reveals the presence of two-coordinated superficial O anions, Ba-O-M (M=Mo or W) on the (001) surface, while on the (112) surface, we observe the appearance of two types of superficial O anions with a coordination of one, O-M, or two, Ba-O-M (M=Mo or W). Then, the (001) surface exhibits just one dangling bond per exposed oxygen anion, while the (112) surface presents oxygen anions with the lowest coordination numbers.

The calculated values of the surface energy, relaxation, and gap energy for the different surfaces of the $BaW_{1-x}Mo_xO_4$ (x=0, 0.25, 0.5, 0.75, and 1) solid solutions are presented in **Table 2.** The inversion in the stability order between the (001) and (112) surfaces with respect to pure $BaWO_4$ can be associated with the inclusion of Mo^{6+} in the crystalline structure of $BaW_{1-x}Mo_xO_4$, inducing a stronger Mo(4d)-O(2p) hybridization compared to W(5d)-O(2p) for the superficial bonds that stabilize the dangling bond effect. This fact enhances the electron-transfer process on the surface plane, facilitated by the presence of the Mo^{6+} cation. Therefore, we can argue that the (001) surface becomes more stable than the (112) surface in $BaW_{0.75}Mo_{0.25}O_4$, $BaW_{0.5}Mo_{0.5}O_4$, $BaW_{0.25}Mo_{0.75}O_4$, and $BaMoO_4$ due to the smallest contribution of the dangling bond effect to the value of E_{surf}.

Table 2. Calculated values of the surface energy, relaxation, and gap energy for each surface of $BaW_{1-x}Mo_xO_4$ solid solutions for x=0, 0.25, 0.5, 0.75, and 1.

Surface	Mo percentage	E_{suf} (J/m^2)	Relaxation (%)	E_{gap} (eV)
(001)	0%	1.02		
	25%	0.55	7	5.92
	50%	0.54	14	5.97
	75%	0.54	20	5.69
	100%	0.99		
(112)	0%	0.92		
	25%	0.65	5	6.14
	50%	0.64	9	5.57
	75%	0.63	12	5.54
	100%	1.02		
(100)	0%	1.22		
	25%	1.09	4	5.49
	50%	1.09	8	5.48
	75%	1.08	10	5.33
	100%	1.17		
(110)	0%	1.10		
	25%	0.80	4	6.15
	50%	0.79	7	6.14
	75%	0.80	10	5.49
	100%	1.23		
(101)	0%	1.31		
	25%	0.91	4	6.16
	50%	0.89	8	6.21
	75%	0.90	12	5.31
	100%	1.34		
(111)	0%	2.06		
	25%	1.91	1	Conductor
	50%	1.89	1	
	75%	1.90	1	
	100%	2.23		

The calculated band structure and density of states (DOS) projected for the atoms and orbitals of $BaW_{0.5}Mo_{0.5}O_4$ corresponding to the (001), (101), (110), and (112) surfaces are displayed in **Fig. 6.** An analysis of the band structure and projected DOS presented here shows that the band gap values (see Table 2) are in the range 0.1–0.8 eV, and depend significantly on the local coordination of both Mo^{6+} and W^{6+} at the different surfaces. The main contribution to the valence band (VB) region is due to the 2p orbitals of the oxygen anions and a predominance of the dx^2-y^2 and dz^2 states of Mo^{6+} and W^{6+} found in the conduction band (CB) region.

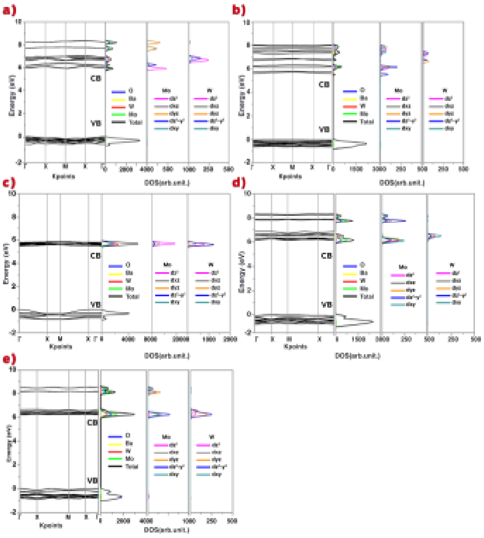

Figure 6. The band structure and density of states projected on atoms and orbitals for (a) (001), (b) (112), (c) (100), (d) (110) and (e) (101) surfaces at $BaW_{0.5}Mo_{0.5}O_4$.

In addition, theoretical methodology can contribute to an explanation for the optical properties, since a reduction in the band gap value is observed mainly in the cases of the (100) and (101) surfaces. The density of states projected on the atoms as a function of layer position for the (100) and (101) surfaces of the $BaW_{1-x}Mo_xO_4$ (x = 0.25, 0.50, and 0.75) solid solutions is presented in **Fig. 7.**

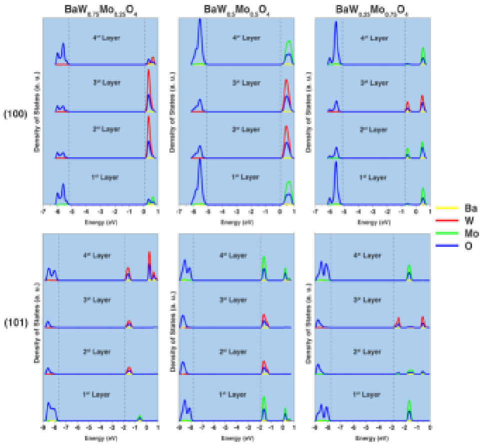

Figure 7. Density of states projected on atoms as a function of layer position at (100) and (101) surfaces.

An analysis of Figure 7 shows that for the (100) and (101) surfaces the distribution of the energy levels of each layer of the $BaW_{1-x}Mo_xO_4$ (x=0.25, 0.50, 0.75) solid solution is related to the electron transfer from the O anions to the d orbitals of Mo^{6+} or W^{6+}, which are the electronic transitions associated with the PL emissions. Furthermore, it was observed that the isoelectronic replacement of Mo^{6+} by W^{6+} perturbs the energy-level distribution in the vicinity of the band-gap region, narrowing the corresponding excitation energy, mainly for the CB, since the 4d valence orbitals of Mo^{6+} have a lower energy than those of W^{6+} (5d). However, the results show that both the metals contribute equally in the lower energy region of the CB, suggesting a competition for the electron trapping mechanism, i.e., the excited electrons from the O (2p) levels can be located in both the $[MoO_4]$ and $[WO_4]$ clusters, which could be related to the non-linear wavelength displacement observed in the experimental PL emissions (**Fig. 5**).

3.5. Morphology

The conventional approach to the quantitative study of changes in morphology is by applying the Wulff construction using the calculated surface energies [34]. In previous publications, $BaWO_4$ and $BaMoO_4$ have been described in detail, and it was noted that the ideal morphology for the $BaWO_4$ and $BaMoO_4$ systems is defined mainly by their (112), (001), and (100) facets [9], [9], as presented in other scheelite crystals [44].

In order to describe the effects of the isoelectronic replacement of W^{6+} by Mo^{6+} on the morphology, the Wulff construction was applied to the intermediary composition of the $BaW_{1-x}Mo_xO_4$ solid solution. The ideal morphology of $BaW_{0.75}Mo_{0.25}O_4$ is based on 79.24% of (112), 18.72% (001), and 2.04% (101). The ideal morphology of $BaW_{0.50}Mo_{0.50}O_4$ involves 79.41% of (112), 18.47% (001), and 2.12% (101). Finally, 80.81% of (112), 17.91% (001), and 1.28% (101) constitute the ideal morphology for the $BaW_{0.25}Mo_{0.75}O_4$ system. These calculated morphologies for the $BaW_{1-x}Mo_xO_4$ system for x=0, 0.25, 0.50, 0.75, and 1 are presented in **Fig. 8.**

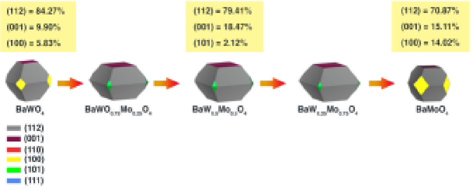

Figure 8. Ideal morphologies of $BaW_{1-x}Mo_xO_4$ (x=0, 0.25, 0.50, 0.75 and 1) solid solutions.

In this study, the effect induced by the substitution in the $BaW_{1-x}Mo_xO_4$ solid solution is the alteration of the order of stability between the (001) and (112) surfaces, as well as between the (100) and (110) surfaces. This effect on the exposed surfaces and relative surface energy values can be observed in Table 3.

Table 3. Surface energy values of the ideal morphology for the $BaW_{1-x}Mo_xO_4$ (x=0, 0.25, 0.5, 075, and 1) solid solution. The values in parentheses indicate the increased/decreased surface energy with Mo content.

Surfaces	Surface Energy (E_{surf})					
	$BaWO_4$	$BaW_{0.75}Mo_{0.25}O_4$	$BaW_{0.5}Mo_{0.5}O_4$	$BaW_{0.25}Mo_{0.75}O_4$	$BaMoO_4$	$\Delta Total_{(BMO-BWO)}$
112	0.92	0.65 (-0.27)	0.64 (-0.01)	0.63 (-0.01)	1.02 (+0.39)	(+0.10)
001	1.02	0.55 (-0.47)	0.54(-0.01)	0.54 (0)	0.99 (+0.45)	(-0.03)
110	1.10	0.80 (-0.30)	0.79 (-0.01)	0.80 (+0.01)	1.23 (+0.43)	(+0.13)
100	1.22	1.08 (-0.14)	1.09 (+0.01)	1.09 (0)	1.17 (+0.08)	(-0.05)
101	1.31	0.91 (-0.40)	0.89 (-0.02)	0.90 (+0.01)	1.34 (+0.44)	(+0.03)
111	2.06	1.91 (-0.15)	1.89 (- 0.02)	1.90 (+0.01)	2.23 (+0.33)	(+0.17)

Table 3 lists the values of the surface energies values obtained for the $BaW_{1-x}Mo_xO_4$ (x=0, 0.25, 0.50, 0.75, and 1) solid solution, as well as the changes (increase or decrease) in surface energy for all the compositions. From the analysis of the corresponding surfaces, the order of stability of the $BaWO_4$ system is: (112) > (001) > (110) > (100) > (101) > (111); however, in the $BaW_{1-x}Mo_xO_4$ system, for x=0.25, there is a different order of stability, as follows: (001) > (112) > (110) > (101) > (100) > (111), which is maintained for the other solid solutions at x=0.50 and 0.75. This inversion in the (001) and (112) surface energy values, as well as those of (101) and (100), can be attributed to the presence of more Mo atoms in the system, as shown in **Fig. 7.** Thus, the morphology control and transformation mechanisms provide insights into the electronic, structural, and energetic properties.

In order to better understand the disappearance of the (112) surface in the experimental micrographs passing from x=0.25 to 0.50 and 0.75, the morphologies of the $BaW_{1-x}Mo_xO_4$ (x= 0.25, 0.50, and 0.75) solid solution have been depicted in **Fig. 9.** The ideal morphology changes by tuning the values of E_{surf} of the different surfaces, and a comparison between the theoretical and experimental morphologies for $BaW_{1-x}Mo_xO_4$ (x=0.25, 0.50, 0.75) is presented at the top of **Fig. 9.**

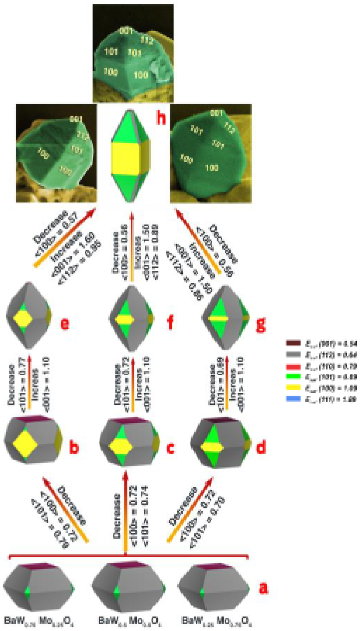

Figure 9. Equilibrium shapes of $BaW_{1-x}Mo_xO4$ (x= 0.25, 0.50, 0.75) solid solutions via the Wulff construction principle. Experimental micrographs are also included for comparison purposes. Surface energy is in J m^{-2}.

Fig. 9 shows a schematic representation map of the morphologies of the $BaW_{1-x}Mo_xO_4$ (x= 0.25, 0.50, and 0.75) solid solution, in which the transformations are obtained by tuning the surface energies of the different surfaces.

In this work, three ideal morphologies were considered (**Fig. 9(a)**), based on the results presented in Table 3, that indicate insignificant differences in surface energy values for the compositions x =0.25, 0.50, and 0.75; therefore, we assume only an ideal morphology.

In order to obtain a morphology similar to that observed in the FE-SEM images, it is necessary to make a morphological modulation of the theoretical surface energies values. In this case, we started with the ideal morphology *a* and decreased the (100) surface energy value to 0.72 J/m^2, while simultaneously decreasing the corresponding value for (101) to 0.79 J/m^2, generating the shape *b*. The shapes *c* and *d* were created by decreasing the surface energy values to 0.74 and to 0.70 J/m^2 respectively. An increase in the (001) surface energy value to 1.10 J/m^2 and a simultaneous decrease in the (101) surface energy value to 0.77, 0.72, and 0.69 J/m^2 generates the shapes *e, f* and *g*.

Finally, the increase in the surface energy value to 1.50 and to 1.60 J/m^2 for (001) was simulated, simultaneously increasing the (112) surface energy value from 0.64 to 0.95, 0.89, and 0.86 J/m^2, as well as decreasing the energy value for (100) surface to 0.56 J/m^2, generates shape *h*. An important objective of this study is to compare experimental and theoretical results and consider their differences in order to arrive at an understanding of the real system.

Conclusion

The formation of solid solutions $BaW_{1-x}Mo_xO_4$ (x=0, 0.25, 0.5, 075, and 1) by using a simple co-precipitation method was reported for the first time, and their crystal structures and phase compositions were experimentally determined, employing XRD with Rietveld refinements. FT-IR and MR spectroscopy, in combination with FE-SEM, were used to describe the microstructure and chemical composition of the synthesized materials. First-principles calculations were performed to obtain the relative stability of the (112), (001), (110), (101), (100), and (111) surfaces, and Wulff construction was employed to rationalize the crystal morphologies observed in the FE-SEM images. This study is designed to serve as a roadmap of the available morphologies of the $BaW_{1-x}Mo_xO_4$ solid solutions (x=0, 0.25, 0.5, 075, and 1) in order to understand the fundamentals, key advantages, and potential applications of the transformation processes along the synthesis pathway, where the experimental and theoretical morphologies of the $BaW_{1-x}Mo_xO_4$ solid solutions are well-matched. We showed that the substitution of W^{6+} by Mo^{6+} enhances the electron-transfer process due to a stronger Mo(4d)-O(2p) hybridization compared to W(5d)-O(2p) for the W/Mo-O superficial bonds; this is responsible for the change in morphology from $BaWO_4$ to $BaMoO_4$.

The synthetic approach and findings reported here are important for understanding the structure–property relationships of molybdate/tungstate compounds, which have potential applications in the design of novel functional materials.

Acknowledgements

The authors acknowledge the financial support from Generalitat Valenciana for PrometeoII/2014/022, Prometeo/2016/079, ACOMP/2014/270, ACOMP/2015/1202, Ministerio de Economia y Competitividad, project CTQ2015-65207-P, Fundação de Amparo à Pesquisa do Estado de São Paulo (FAPESP) (2013/07296-2).

Programa de Cooperación Cientifica con Iberoamerica (Brasil) of Ministerio de Educación (PHBP14- 00020). M.C. acknowledges Generalitat Valenciana for Santiago Grisolia Program 2015/033. We also wish to thank the Servei d'Informática, Universitat Jaume I, for their generous allocation of computer time.

references

[1] D.A. Spassky, S.N. Ivanov, V.N. Kolobanov, V.V. Mikhailin, V.N. Zemskov, B.I. Zadneprovski, L.I. Potkin, Optical and luminescent properties of the lead and barium molybdates, Radiat. Meas. 38(4–6) (2004) 607-610.

[2] J. Liu, J. Ma, B. Lin, Y. Ren, X. Jiang, J. Tao, X. Zhu, Room temperature synthesis and optical properties of $SrMoO_4$ crystallites by w/o microemulsion, Ceram. Inter. 34(6) (2008) 1557-1560.

[3] T. Thongtem, S. Kungwankunakorn, B. Kuntalue, A. Phuruangrat, S. Thongtem, Luminescence and absorbance of highly crystalline $CaMoO_4$, $SrMoO_4$, $CaWO_4$ and $SrWO_4$ nanoparticles synthesized by co-precipitation method at room temperature, J. Alloy. Compd. 506(1) (2010) 475-481.

[4] Y. Sun, J. Ma, J. Fang, C. Gao, Z. Liu, Photoluminescent improvement of $SrMoO_4$ by the electrochemical formation of Ca^{2+}-doped solid solutions, Inorg. Chem. Commun. 14(8) (2011) 1221-1223.

[5] A.P.A. Marques, F.V. Motta, M.A. Cruz, J.A. Varela, E. Longo, I.L.V. Rosa, $BaMoO_4$:Tb^{3+} phosphor properties: Synthesis, characterization and photophysical studies, Solid State Ionics 202(1) (2011) 54-59.

[6] M.C. Oliveira, L. Gracia, I. C.Nogueira, M.F.C. Gurgel, J.M. R.Mercury, E. Longo, J. Andrés, Synthesis and morphological transformation of $BaWO_4$ crystals: Experimental and theoretical insights, Ceram. Inter. 42 (2016) 10913-10921.

[7] L. Liu, S. Zhang, M.E. Bowden, J. Chaudhuri, J.J.D. Yoreo, In Situ TEM and AFM Investigation of Morphological Controls during the Growth of Single Crystal $BaWO_4$, Cryst. Growth Des. 18(3) (2018) 1367-1375.

[8] M.C. Oliveira, L. Gracia, I.C. Nogueira, M.F.C. Gurgel, J.M.R. Mercury, E. Longo, J. Andrés, Synthesis and morphological transformation of $BaWO_4$ crystals: Experimental and theoretical insights, Ceram. Inter. 42 (2016) 10913-10921.

[9] M.C. Oliveira, L. Gracia, I.a.C. Nogueira, M.F.C. Gurgel, J.M.R. Mercury, E. Longo, J. Andrés, On the morphology of $BaMoO_4$ crystals: A theoretical and experimental approach, Cryst. Res. Technol 51 (2016) 634–644.

[10] M. C. de Oliveira, T. Marinho, L. Gracia, E. Longo, J. Andrés, Analysis for the Morphology Prediction of Materials from First Principles Calculations, in: J. Li, J. Li, Y. Chu (Eds.) Crystal Growth: Concepts, Mechanisms and Applications., Nova Science Publisher, Estados Unidos, 2017.

[11] C. Bouzidi, N. Sdiri, A. Boukhachem, H. Elhouichet, M. Férid, Impedance analysis of $BaMo_{1-x}W_x$O4 ceramics, Superlattice. Microst. 82(Supplement C) (2015) 559-573.

[12] S. Vidya, S. Solomon, J.K. Thomas, Structral, Optical and Dielectric Characterization of Nanocrystalline $AMo_{0.5}W_{0.5}O_4$ (where A=Ba,Sr and Ca) Prepared by Single Step Modified Combustion Technique, Mater. Today- Proc. 2(3) (2015) 904-908.

[13] H. Rietveld, A profile refinement method for nuclear and magnetic structures, J. Appl. Crystallogr. 2(2) (1969) 65-71.

[14] A.C. Larson, R.B. Von Dreele, General Structure Analysis System (GSAS) program, Los Alamos, NM, Rep. N°. LAUR 86–748, Los Alamos National Laboratory, University of California., 2004.

[15] W. Finger, D.E. Cox, A.P. Jephcoat, A correction for powder diffraction peak asymmetry due to axial divergence, J. Appl. Crystallogr. 27 (1994) 892-900.

[16] P. Stephens, Phenomenological model of anisotropic peak broadening in powder diffraction, J. Appl. Crystallogr. 32(2) (1999) 281-289.

[17] C.T. Lee, W.T. Yang, R.G. Parr, Development of the Colle-Salvetti correlation-energy formula into a functional of the electron density, Phys. Rev. B: Condens. Matter 37 (1988) 785-789.

[18] A.D. Becke, Density-functional thermochemistry. III. The role of exact exchange, J. Chem. Phys 98 (1993) 5648-5652.

[19] R. Dovesi, R. Orlando, A. Erba, C.M. Zicovich-Wilson, B. Civalleri, S. Casassa, L. Maschio, M. Ferrabone, M. De La Pierre, P. D'Arco, Y. Noël, M. Causà, M. Rérat, B. Kirtman, CRYSTAL14: A program for the ab initio investigation of crystalline solids, Int. J. Quantum Chem. 114(19) (2014) 1287-1317.

[20] M.L. Moreira, J. Andrés, L. Gracia, A. Beltrán, L.A. Montoro, J.A. Varela, E. Longo, Quantum mechanical modeling of excited electronic states and their relationship to cathodoluminescence of $BaZrO_3$, J. Appl. Phys. 114 (2013) 043714

[21] M.C. Oliveira, L. Gracia, M. de Assis, I.L.V. Rosa, M.F. do Carmo Gurgel, E. Longo, J. Andrés, Mechanism of photoluminescence in intrinsically disordered $CaZrO_3$ crystals: First principles modeling of the excited electronic states, J. Alloy. Compd. 722(Supplement C) (2017) 981-995.

[22] A. Beltrán, L. Gracia, E. Longo, J. Andrés, First-Principles Study of Pressure-Induced Phase Transitions and Electronic Properties of Ag2MoO4, J. Phys. Chem. C 118 (2014) 3724-3732.

[23] M.T. Fabbro, C. Saliby, L.R. Rios, F.A.L. Porta, L.E. Gracia, M.S. Li, J. Andrés, L.P.S. Santos, E. Longo, Identifying and rationalizing the morphological, structural, and optical properties of B-Ag_2MoO_4 microcrystals, and the formation process of Ag nanoparticles on their surfaces: combining experimental data and first-principles calculations, Sci. Technol. Adv. Mater 16 (2015) 065002.

[24] L. Gracia, V. M. Longo, L. S. Cavalcante, A. Beltrán, W. Avansi, M. S. Li, V. R. Mastelaro, J. A. Varela, E. Longo, J. Andrés, Presence of excited electronic state in $CaWO_4$ crystals provoked by a tetrahedral distortion: An experimental and theoretical investigation, J. Appl. Phys. 110 (2011) 043501.

[25] F.M.C. Batista, F.A.L. Porta, L. Gracia, E. Cerdeiras, L. Mestres, M.S. Li, N.C. Batista, J. Andrés, E. Longo, L.S. Cavalcante, A joint experimental and theoretical study on the electronic structure and photoluminescence properties of $Al_2(WO_4)_3$ powders, J. Mol. Struct. 1081 (2015) 381-388.

[26] E. Longo, D.P. Volanti, V.M. Longo, L. Gracia, I.C. Nogueira, M.A.P. Almeida, A.N. Pinheiro, M.M. Ferrer, L.S. Cavalcante, J. Andrés, Toward an Understanding of the Growth of Ag Filaments on α-Ag_2WO_4 and Their Photoluminescent Properties: A Combined Experimental and Theoretical Study, J. Phys. Chem. C 118 (2014) 1229-1239.

[27] G.S. Silva, L. Gracia, M.T. Fabbro, L.P. Serejo dos Santos, H. Beltrán-Mir, E. Cordoncillo, E. Longo, J. Andrés, Theoretical and Experimental Insight on Ag_2CrO_4 Microcrystals: Synthesis, Characterization, and Photoluminescence Properties, Inorg. Chem. 55(17) (2016) 8961-8970.

[28] A.F. Gouveia, M.M. Ferrer, J.R. Sambrano, J. Andrés, E. Longo, Modeling the atomic-scale structure, stability, and morphological transformations in the tetragonal phase of $LaVO_4$, Chem. Phys. Lett. 660 (2016) 87-92.

[29] http://Www.Crystal.Unito.It/Basis_Sets/Molibdenum.Html.

[30] F. Cora, A. Patel, N.M. Harrison, R. Dovesi, C.R.A. Catlow, An Ab Initio Hartree-Fock Study of the Cubic and Tetragonal Phases of Bulk Tungsten Trioxide, J. Am. Chem. Soc. 118 (1996) 12174-12182.
[31] http://Www.Crystal.Unito.It/Basis_Sets/Oxygen.Html.
[32] http://Www.Tcm.Phy.Cam.Ac.Uk/~Mdt26/Basis_Sets/Ba_Basis.Txt.
[33] H.J. Monkhorst, J.D. Pack, Special points for Brillouin-zone integrations, Phys. Rev. B 13(12) (1976) 5188.
[34] G. Wulff, Xxv. zur frage der geschwindigkeit des wachsthums und der auflösung der krystallflächen, Z. Krist.-Cryst. Mater. 34(1) (1901) 449-530.
[35] D. Errandonea, J. Pellicer-Porres, F.J. Manjón, A. Segura, C. Ferrer-Roca, R.S. Kumar, O. Tschauner, J. López-Solano, P. Rodríguez-Hernández, S. Radescu, A. Mujica, A. Muñoz, G. Aquilanti, Determination of the high-pressure crystal structure of $BaWO_4$ and $PbWO_4$, Phys. Rev. B 73(22) (2006) 224103.
[36] T.T. Basiev, A.A. Sobol, Y.K. Voronko, P.G. Zverev, Spontaneous Raman spectroscopy of tungstate and molybdate crystals for Raman lasers, Opt. Mater. 15(3) (2000) 205-216.
[37] K. Nakamoto, Infrared and Raman Spectra of Inorganic and Coordination Compounds, fourth ed ed., Wiley,, New York, 1986.
[38] S. Vidya, S. Solomon, J.K. Thomas, Structral, Optical and Dielectric Characterization of Nanocrystalline $AMo_{0.5}W_{0.5}O_4$ (where A=Ba,Sr and Ca) Prepared by Single Step Modified Combustion Technique, Materials Today: Proceedings 2(3) (2015) 904-908.
[39] J.B. Foresman, E. Frisch, Exploring Chemistry with Electronic Structure Methods, Frequency Calculations. Gaussian, Inc., Pittsburgh. P.A, 1996, pp. 61-90.
[40] M. Li, Y. Guan, Y. Yin, X. Cui, S. Rong, G. Jin, Y. Hao, Q. Wu, Controllable synthesis of 3D $BaXO_4$ (X=W, Mo) microstructures by adjusting nucleation stage and their photoluminescence properties, Superlattice. Microst. 80(Supplement C) (2015) 222-228.
[41] A. Phuruangrat, T. Thongtem, S. Thongtem, Precipitate synthesis of $BaMoO_4$ and $BaWO_4$ nanoparticles at room temperature and their photoluminescence properties, Superlattices and Microstructures 52(1) (2012) 78-83.
[42] T. Thongtem, A. Phuruangrat, S. Thongtem, Characterization of $MMoO_4$ (M=Ba, Sr and Ca) with different morphologies prepared using a cyclic microwave radiation, Mater. Lett. 62(3) (2008) 454-457.
[43] T. Thongtem, A. Phuruangrat, S. Thongtem, Synthesis of $CaWO_4$, $SrWO_4$ and $BaWO_4$ with nanosized particles using cyclic microwave radiation, J. Ceram. Process. Res. 9(3) (2008) 258-261.
[44] Z.Y. Gao, W. Sun, Y.H. Hu, X.-W. Liu, Surface energies and appearances of commonly exposed surfaces of scheelite crystal, T. Nonferr. Metal. Soc 23 (2013) 2147-2152.

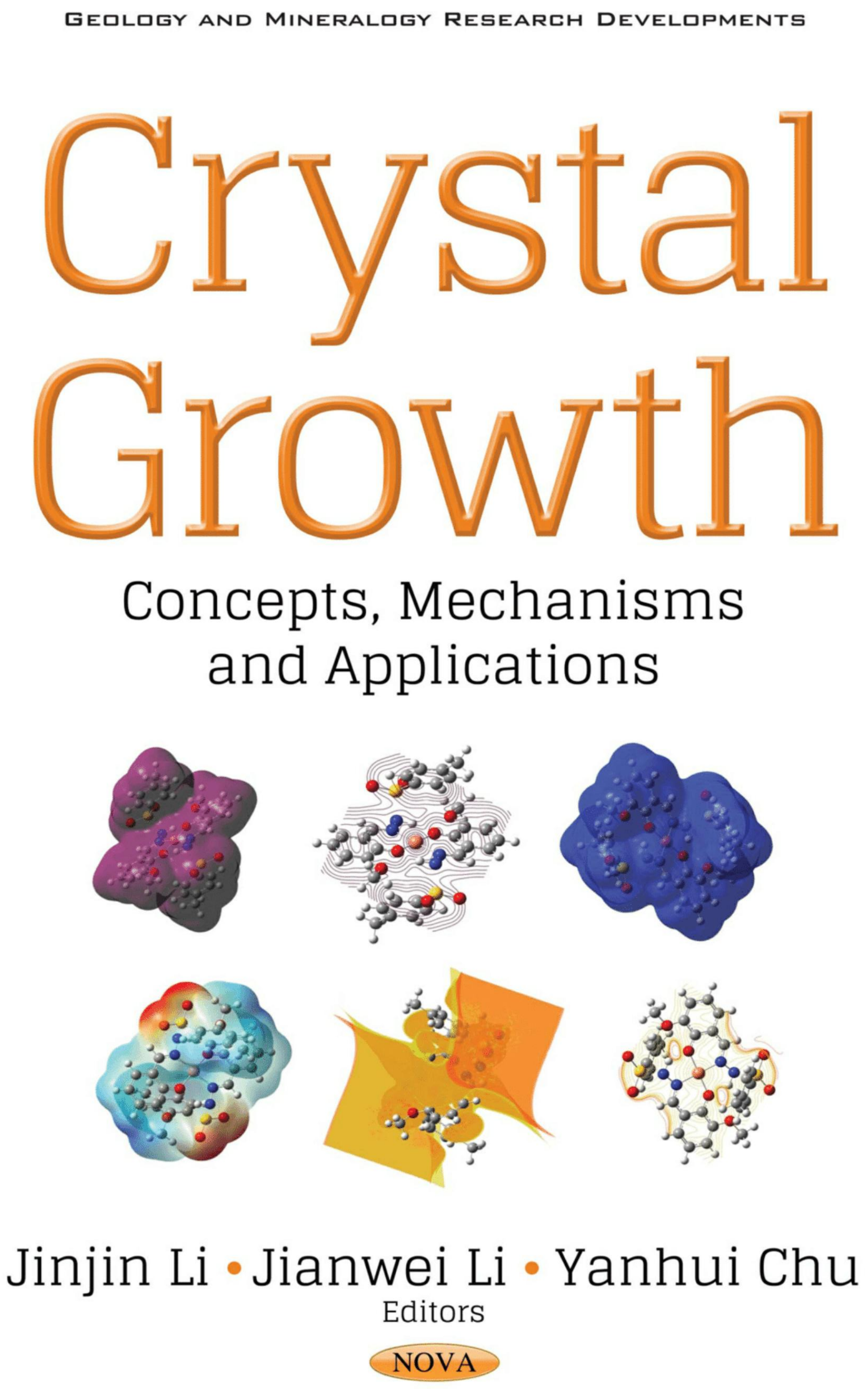

GEOLOGY AND MINERALOGY RESEARCH DEVELOPMENTS

Crystal Growth

Concepts, Mechanisms and Applications

Jinjin Li • Jianwei Li • Yanhui Chu
Editors

NOVA

GEOLOGY AND MINERALOGY RESEARCH DEVELOPMENTS

CRYSTAL GROWTH

CONCEPTS, MECHANISMS AND APPLICATIONS

JINJIN LI
JIANWEI LI
AND
YANHUI CHU
EDITORS

nova
science publishers
New York

In: Crystal Growth
Editors: J. Li, J. Li and Y. Chu

ISBN: 978-1-53612-203-9

Chapter 3

ANALYSIS FOR THE MORPHOLOGY PREDICTION OF MATERIALS FROM FIRST PRINCIPLES CALCULATIONS

Marisa Carvalho de Oliveira[1,2]**,**
Thiago Marinho Duarte[1,3]**,** ***Lourdes Gracia***[4,*]**,**
Elson Longo[2] ***and Juan Andres***[1]
[1]Departmentof Analytical and Physical Chemistry,
University Jaume I (UJI), Castelló, Spain
[2]CDMF-UFSCar, Federal University of São Carlos,
São Carlos, SP, Brazil
[3]Department of Chemistry, Federal University of Paraíba,
João Pessoa, PB, Brazil
[4]Department of Physical Chemistry, University of Valencia,
Burjassot, Spain

---

[*] Corresponding author: Email: Lourdes.Gracia@uv.es, lgracia@uji.es.

ABSTRACT

As various physical and chemical processes occur at surfaces, an understanding of surface structures and the factors that affect morphology is mandatory. The control of (nano)crystal morphology is a complex and difficult process that depends on both the internal structures of the crystals and external growth conditions, such as the synthesis process, the solvents used, and the process additives. The morphologies of (nano)crystals grown under or near equilibrium conditions are governed mainly by surface energies, resulting in the formation of simple shapes with well-defined facets to minimize the surface energy. However, surface energy values are not readily acquired experimentally, and computer modeling and simulation are necessary to obtain these values. Such techniques are powerful tools for exploring the morphological mechanisms at the atomistic/molecular level. The observed (nano)crystal morphologies are often interpreted in terms of Wulff constructions, which offers a simple method to determine the equilibrium (nano)crystal shape. As recently developed by our research group, first-principles calculations can be used to explicitly predict the evolution of morphologies in different environments.

The complete set of morphologies obtained theoretically may serve as a guide for researchers analyzing electron microscopy images to gain a further understanding of how to control crystal shapes synthetically by tuning the surface chemistry and by controlling the relative surface energy values. Then, this feature chapter introduces recent work, based on combined experimental findings and first-principles calculations, to provide a deeper knowledge of the electronic, structural, and energetic properties controlling the morphology and the transformation mechanisms of different (nano)materials, such $BaWO_4$, $BaMoO_4$, $CaZrO_3$, and $BaSnO_3$. These considerations reveal a close resemblance between experimental and calculated morphologies, but also elaborate on some of the current and future trends to illustrate why (nano)morphology is at the core of current scientific development in chemistry and physics, and the appropriate handling of complexity is discussed along these lines.

Keywords: morphology, surface energy, Wulff construction, complex metallic oxides

INTRODUCTION

Morphologies and exposed surfaces are important factors that influence the application of (nano)materials (Tian et al. 2007), directly affecting their efficiency in various devices (Lieber 1998). Steady-state morphologies of micro/nanocrystal particles with several exposed facets present different physical and chemical characteristics owing to crystal anisotropy, i.e., different crystal planes exhibit different anisotropic responses towards various mechanical, physical, and chemical activities like hardness, piezoelectricity, and reactivity (Schmidt et al. 2012); (Dandekar et al. 2013). These characteristics are controlled by the synthesis parameters of the materials, such as reagent concentration, precursor pH, reaction temperature and time, and synthesis method.

Morphological control of (nano)crystals and understanding the mechanism for morphology evolution have been meaningful topics of research in materials science and nanoscience, as obtaining a fundamental understanding of the stability of (nano)crystal surface structures and morphology–structure–function relationships is of considerable importance for further development of highly stable and functional materials for practical applications. In particular, the activity of nanocrystals as catalysts depends strongly on the surface structures of the facets enclosing the crystals (Ahmadi et al. 1996); (Lee et al. 2006b); (Lee et al. 2006a); (Gao, Ju, et al. 2013); (Li and Shen 2014), (Araújo et al. 2014); (Wang et al. 2015).

Morphologies, preferred orientations, and crystal facets are characterized experimentally using scanning electron microscopy, selected-area electron diffraction, and high-resolution transmission electron microscopy. The relative growth rates of (nano)crystal faces cause crystal morphology transformations because of the appearance and/or disappearance of faces. These transformations are due to geometric constraints imposed by the (nano)crystal structure and are associated with the relative surface energy values of each face. Among the influential factors, surface chemistry, including surface energy, tension, and configuration, has a significant impact on the final (nano)crystal morphology.

A significant challenge in the development of functional (nano)materials is understanding the shape-selective growth of (nano)crystals to synthetize (nano)crystals with controlled shapes. A solid fundamental understanding will allow for better design and control of these syntheses and will enable larger-scale production of (nano)crystals with targeted shapes. Further, establishment of a pathway between (nano)crystal morphology and the arrangement of atoms in a (nano)crystal lattice will allow development of shape control for the rational design of external morphologies. Very recently, Zhuang, Tkalych and Carter (2016) (Zhuang et al. 2016), explored the correlation between experimental catalytic activity and three surface properties (surface energy, work function, and potential of zero charge) of 15 traditional and novel catalysts. These authors discovered a strong volcano-shaped correlation between the catalytic activity and the surface energy, indicating that the surface energy can be used as a novel, efficient descriptor of catalytic activity because it reflects the degree of coordinative unsaturation of the surface atoms and, thus, the reactivity of the surface.

Morphology-controlled synthesis of inorganic materials on the nano/micrometer scale has progressed considerably in the past decade (Huang, Rej, et al. 2014). Many facet-dependent properties have been discovered owing to the successful synthesis of nanocrystals with a series of well-defined morphologies. Control of nanocrystal morphology is important in various applications, such as heterogeneous catalysis (Ahmadi et al. 1996); (Zaera 2013), solar cells (Huynh et al. 1999), light-emitting diodes (Schlamp et al. 1997); (Mattoussi et al. 1998), and biological labeling (Bruchez et al. 1998); (Chan et al. 1998). In particular, recent advances in colloidal synthesis have realized controlled preparation of catalytic nanocrystals with various types of uniform morphologies. For example, morphology-dependent catalytic behavior of oxide nanocrystals has been often observed, and oxide nanocrystals are being explored as novel model catalysts for fundamental studies of metal oxide catalysts, such as CeO_2 and TiO_2 (Dinh et al. 2009); (Pan et al. 2011); (Zheng et al.

2011); (Gordon et al. 2012); (Zhou et al. 2012); (Qiao et al. 2013); (Huang 2013); (Huang and Gao 2014), (Huang 2016).

Nanocrystals with well-defined crystallographic facets (Zhou et al. 2012); (Wu et al. 2013); (Kuang et al. 2014) have been designed for improved catalytic (Hu et al. 2008); (Han, Jin, et al. 2009), optical (Wang, Li, et al. 2014), magnetic (Luo et al. 2014), and electrochemical properties (Yu et al. 2013); (Tan et al. 2015). In particular, high-energy facets that contain abundant unsaturated coordination atoms exhibit high reactivity (Jiang et al. 2005); (Tian et al. 2007); (Fan et al. 2008); (Liao et al. 2008a); (Liao et al. 2008b); (Ma et al. 2008b); (Ma et al. 2008a); (Tian et al. 2008); (Yang et al. 2008); (Tian et al. 2009); (Xie et al. 2009); (Xu et al. 2009), (Yang et al. 2009); (Leng et al. 2010), because active facets usually have higher densities of unsaturated, dangling, or distorted atoms than inert facets (Pal et al. 2015), resulting in higher surface reactivity (Yang et al. 2008); (Miao et al. 2013); (Roy et al. 2013); (Xu et al. 2013), (Roy et al. 2013). In this context, shape-controlled synthesis of inorganic nanocrystals with exposed high-energy or reactive facets has attracted intensive interest over the past decade, owing to their fascinating shape dependent properties (Jun et al. 2006); (Tao et al. 2008); (Wang et al. 2008), as well as their great importance in fundamental studies and technological applications (Tian et al. 2007); (Jiang et al. 2010); (Liu, Khare, et al. 2011).

Thermodynamics usually ensures that crystal facets evolve to have the lowest surface energy during a crystal growth process. Owing to the fact that high-index faces possess high surface energies, high-energy facets decrease quickly during the crystal growth process, and the crystal spontaneously evolves into a specific shape with exposed facets that minimize the surface energy of the crystal. Consequently, only (nano)crystals enclosed by low-index facets and with low surface energy are obtained. High-energy facets of micro/nanocrystals, which possess high densities of unsaturated coordination sites, usually exhibit higher surface reactivity than low-index facets owing to differences in exposed (dangling) bonds, surface defects, and electronic structure (Van Santen 2009); (Pal et al. 2015). Further, such high-energy facets are expected to exhibit extraordinary performances in energy and environmental applications, (Yang et al. 2008); (Dai et al. 2009); (Han, Jin, et al. 2009); (Han, Kuang, et al. 2009); (Xiao et al. 2012); (Hu et al. 2016); (Wang et al. 2016). However, as high-energy facets disappear easily during conventional crystal growth, few high-energy facets are exposed on the crystal surface (Liu, Yu, et al. 2011); (Zhang et al. 2013). Therefore, the synthesis and control of (nano)crystals enclosed by high-index facets are still challenging research topics (Zhou et al. 2011); (Wang, Han, et al. 2012); (Wang, Zang, et al. 2012).

A prerequisite for application of nanocrystals as model catalysts is to obtain well-defined surface structures for metal oxide nanocrystals with different morphologies. Presently, morphologies are determined experimentally using microscopy-based techniques in combination with Wulff construction models, which can be obtained from first-principles calculations, to identify the facets exposed on nanocrystals (Han, Kuang, et al. 2009); (Tan et al. 2011); (Liu et al. 2013); (Lin et al. 2014). For example, uniform cubic and octahedral nanocrystals of CeO_2 with a cubic fluorite structure are enclosed with six {100} facets and eight {111} facets, respectively. However, this approach encounters some difficulties in determining the exposed facets for nanocrystals with low symmetries (Vantomme et al. 2005); (Sayle et al. 2011); (Agarwal et al. 2013); (Wang et al. 2013).

Up to now, based on a geometrical approach, the Wulff construction model has had a fundamental role in the theoretical characterization of nano(crystal) morphologies. Instead, as was recently recognized by Marks and Peng (2016) (Marks et al. 2016), the seminal paper of Wulff (1901) (Wulff 1901) titled "On the question of speed of growth and dissolution of crystal surfaces" envisaged the possibility of kinetic control of morphologies based on a mathematical relationship between the surface energy and the growth rate (which is not necessarily correct). Consequently, substantial efforts have been devoted to understanding and predicting the structure and stability of complex oxide surfaces by utilizing state-of-the-art experimental techniques and advanced theoretical approaches, (Freund et al. 1996); (Noguera 2000a); (Goniakowski et al. 2008); (Noguera et al. 2013).

However, there remains a lack of fundamental understanding of the surface structure, composition, and stability of certain complex oxides, particularly ternary oxides. This can be attributed to the inherent complexity of these materials, which renders experimental preparation and characterization of oxide surfaces extremely arduous, especially the preparation of different crystallographic orientations of ionic polar surfaces, for which cleavage is not a favorable option. It is also very challenging to address these materials from a theoretical perspective, as in addition to surface nonstoichiometry, certain facets are dipolar, necessitating special treatment that involves the creation of surface defects (Davies et al. 1994); (Wander et al. 2001); (Barbier et al. 2008); (Eglitis et al. 2008). Nevertheless, theoretical frameworks providing fresh insight into the structure and stability of ternary complex oxide surfaces are a vital step towards realizing the true potential of complex oxide nanostructures and thin films.

The development of a particular morphology for a growing crystal depends on the relative rate of growth along different crystallographic directions. Different growth rates of the crystal planes determine the appearance of the crystal. A crystal consists of a finite number of low-energy faces that are represented by their Miller indices and interplanar spacing. Although studies have provided some insight into the factors that control crystal growth and ultimately determine the morphologies of crystals, shape evolution mechanisms are mostly speculative and based on experimental results. Thus, there is an urgent call for a theoretical understanding of the relationship between the growth environment and the resulting crystal morphology.

Density functional theory (DFT) calculations, as an effective tool for exploring surface chemistry, have been widely used to investigate the underlying mechanism by which growth environments affect crystal morphologies (Piskorz et al. 2012). For instance, Yang et al. used DFT calculations to predict that anatase TiO_2 with high (001) exposure can be successfully synthesized by using fluorine ions as an agent to control surface energies (Yang et al. 2008). Barnard et al. carried out a series of investigations on the shape transitions of TiO_2 nanocrystals using DFT calculations (Barnard et al. 2005).

Further strengthening of theory and simulation in this research area, with a focus on understanding morphology, can guide the efficient synthesis of outstanding materials. First-principles investigations are well established in the study of the morphology and surface properties of various materials, from simple to complex metal oxides (Beltrán et al. 2003); (Leite et al. 2003); (Barnard et al. 2008); (Seyed-Razavi et al. 2010); (Gurlo 2011); (Longo et al. 2011); (Stroppa et al. 2011); (Barnard 2012); (Kim, Lee, et al. 2012); (Li et al. 2012); (Piskorz et al. 2012); (Bomio et al. 2013); (Karim et al. 2013); (Lee et al. 2013); (Tompsett et al. 2013); (Hörmann et al. 2014); (Li, Zhang, et al. 2014); (Stroppa et al. 2014); (Whiteside et al. 2014); (Barmparis et al. 2015); (Kanaki et al. 2015); (Suleiman et al. 2015). There are several insightful reviews that report experimental results and theoretical calculations on the most important aspects that govern crystal shape modulation in semiconductors and in metal nanoparticles (Lovette et al. 2008); (Chen et al. 2009); (Jiang et al. 2010); (Lee et al. 2010); (Seyed-Razavi et al. 2010). In addition, there are good reviews on theoretical methods for surface chemistry (Groß 2009) and the modeling of nanoparticles (Barnard 2010).

Here, we apply a recent experimental and theoretical strategy by combining experimental findings and first-principles calculations, based on Wulff constructions, to determine the electronic, structural, and energetic properties that control the morphology and the transformation mechanism of complex crystals (Ferrer et al. 2016) (Andrés et al. 2015). In this work, we provide a comprehensive set of first-principles computations that quantify the stability of all relevant $BaWO_4$, $BaMoO_4$, $CaZrO_3$, and $BaSnO_3$ crystal surfaces, which allows us to obtain a complete map of available morphologies. In addition, based on these results, we are able to rationalize how the energies of different surfaces change throughout the synthesis process, and we are able to propose a path for which the experimental and theoretical morphologies match. Using corrected surface energies, a straightforward understanding was provided by Wulff constructions. We have introduced computational methodology for modeling different complex metal oxides, as discussed in detail below. Our research seeks to capture the structure and thermodynamics of these systems using an atomistic level description, allowing us to derive general stability rules for the (nano)morphologies of $BaWO_4$, $BaMoO_4$, $CaZrO_3$, and $BaSnO_3$ to rationalize the outcome of previous as-synthesized morphologies, and to provide predictive guidelines for future experimental work. Furthermore, we consider the advantages, disadvantages, and possible difficulties of this approach.

COMPUTATIONAL METHODOLOGY AND MODELING

First-principles calculations were conducted within the framework of DFT using the CRYSTAL14 software package (R. Dovesi 2014). The gradient-corrected correlation functional by Lee, Yang, and Parr (Lee et al. 1988) combined with Becke's exchange functional (B3LYP) (Becke 1993) was used for $BaMoO_4$, $BaWO_4$ and $CaZrO_3$ calculations. This method has been successfully employed in various studies on the bulk and surface electronic and structural properties of perovskite (Moreira et al. 2013), tungstate (L. Gracia et al. 2011); (Longo et al. 2014); (Batista et al. 2015), Ag_2CrO_4 (Silva et al. 2016), $LaVO_4$ (Gouveia et al. 2016), and molybdate-based materials (Beltrán et al. 2014); (Fabbro et al. 2015). The Brillouin zone was sampled using the Monkhorst–Pack method at different k-point grids according to the system size. The thresholds controlling the accuracy of the Coulomb and exchange integral calculations were set to 10^{-8} (ITOL1 to ITOL4) and 10^{-14} (ITOL5), which assures a convergence in the total energy of better than 10^{-7} a.u., whereas the percentage of Fock/Kohn–Sham matrix mixing was set to 40 (IPMIX = 40) (Monkhorst et al. 1976).

The atomic centers were described using pseudopotential basis sets for the Mo (http://Www.Crystal.Unito.It/Basis_Sets/Molibdenum.Html) atom in $BaMoO_4$ and large-core effective core potentials derived by Hay and Wadt and modified by Cora et al. (Cora et al. 1996) for the W atom in $BaWO_4$. Meanwhile, the O (http://Www.Crystal.Unito.It/Basis_Sets/Oxygen.Html) and Ba (http://Www.Tcm.Phy.Cam.Ac.Uk/˜Mdt26/

Basis_Sets/Ba_Basis.Txt) atoms in each system were described by standard all-electron basis sets (6-31G* basis set). In $CaZrO_3$, all-electron basis set were used to describe the atomic orbitals of the Ca (Valenzano et al. 2006), Zr (L et al. 2011), and O (Cora 2005) atoms. In $BaSnO_3$, the PBESOL0 functional (Adamo et al. 1999) was used and the Ba, Sn, and O atoms were described by SC_HAYWSC-31(1d)G_baranek (Sophia et al. 2013), ECP28MDF-411(51d)G_baranek (Dovesi et al.), and 8-411(1d)G_baranek (Dovesi et al.), respectively, by optimizing the outer valence shell functions (Duarte et al. 2016).

The surface energy, E_{surf} (Andrés et al. 2015); (Ferrer et al. 2016), was calculated using the following equation:

$$E_{surf} = \frac{E_{slab} - n \cdot E_{bulk}}{2A}$$

where $n \cdot E_{bulk}$ is the number of surface molecular units multiplied by the energy of the bulk, E_{slab} is the total energy of the surface slab per molecular unit, and A is the surface area. The equilibrium shape of a crystal can be calculated by using Wulff constructions that minimize the total surface free energy for a fixed volume, providing a simple relationship between the surface energy, E_{surf}, of an (hkl) plane and its distance from the center of the crystallite in the normal direction (Wulff 1901).

For nonstoichiometric slabs in the $BaSnO_3$ system, the surface energy was determined by accounting for the simultaneous existence of two types of surface terminations in the surface modeling:

$$E_{surf} = \frac{E_{term_A} + E_{term_B} - n \cdot E_{bulk}}{4A}$$

where E_{term_A} and E_{term_B} are the total energies of the two terminations. The number 4 denotes the creation of four surfaces upon crystal cleavage (Bandura et al. 2010).

The Visualization for Electronic and Structural Analysis (VESTA) program (Momma et al. 2011) was utilized to obtain morphologies for $BaMoO_4$, $BaWO_4$, $CaZrO_3$, and $BaSnO_3$ crystals. Band structures were calculated for 80 K points along the appropriate high-symmetry paths of an adequate Brillouin zone. Density of state (DOS) plots were obtained to analyze the corresponding electronic structures.

APPLICATIONS: MORPHOLOGY MAPPING OF METAL OXIDES

The following studies have used a combination of experimental and theoretical investigations to gain insights into the electronic, structural, and energetic properties controlling the morphology and transformation mechanisms. The corresponding computational methodology, based on Wulff constructions (Wulff 1901), can be found in each study.

$BaWO_4$

Barium tungstate ($BaWO_4$) is a semiconductor in the family of scheelites with crystallized tetragonal structures that belong to the $I4_1/$ space group with C^6_{4h} symmetry. In this structure, Ba atoms are coordinated to eight O atoms, whereas W atoms exhibit tetragonal coordination by O atoms; thus, the building blocks of the $BaWO_4$ crystal are deltahedral $[BaO_8]$ and tetrahedral $[WO_4]$ clusters (Phuruangrat et al. 2012), (Luo et al. 2007), (Anicete-Santos et al. 2011).

The (001), (101), (110), (100), (111), and (112) surfaces of $BaWO_4$ were simulated by considering symmetrical slabs (with respect to the mirror plane). All surfaces were terminated with O planes. After the optimization process and thickness convergence tests, the resulting slab models consisted of four molecular units containing 24 atoms. We note that the (101), (111), and (112) surfaces are terminated with W and O atoms, whereas the other listed surfaces have Ba−O termination. The W surface atoms are coordinated to three or four O atoms, forming [WO_3] or [WO_4] clusters, respectively, whereas the Ba surface atoms are coordinated to three, five, or six O atoms, forming [BaO_3], [BaO_5], or [BaO_6] clusters, respectively.

Presently, equilibrium morphology models are derived from calculated surface energies (Gibbs et al. 1875); (Wulff 1901); (Herring 1981), using the assumption that the crystal faces with the lowest surface energies control the crystal morphology (Xie et al. 2002); (Liu et al. 2005); (Wang et al. 2005). As surface stability depends on the atomic configurations of the exposed facets (Marks 1983), the local coordination of both the W and Ba atoms controls the crystal morphology of $BaWO_4$ and the corresponding behavior of each surface.

The E_{gap} values of the surfaces follow the same order of stability as the $BaWO_4$ surfaces obtained using theoretical calculations (Table 1), namely, (112) > (001) > (110) > (100) > (101) > (111). This result is in agreement with our present results and those obtained in previous studies on $BaMoO_4$. A comparison between $BaWO_4$ and $BaMoO_4$ shows that the ideal morphology of both scheelites is similar. However, experimental field emission scanning electron microscopy (FE-SEM) images of these materials are different, i.e., contributions of 99.5% of (112), 0.4% of (100), and 0.1% of (001) were found for $BaWO_4$ (Oliveira et al. 2016a), whereas contributions of 46.5% of (101), 46.9% of (100), 5.8% of (112), and 0.8% of (001) were found for $BaMoO_4$ (Oliveira et al. 2016b).

Crystal morphologies can be modified by tuning the surface energy values for various facets using the Wulff theorem and the related construction method (Wulff 1901). Taking into account the (001), (101), (110), (100), (111), and (112) facets, various possible crystal morphologies for $BaWO_4$ are displayed in Figure 1(a-b).

Table 1. Calculated surface energy, surface tension, gap energy, and change in total energy (ΔE_{tot}) for a given dilation area (ΔA) for each surface

Surface	E_{suf}(J/m^2)	ΔE_{tot}(Hartree)	ΔA(Å^2)	Δ (J/m^2)	E_{gap}(eV)
(112)	0.92	0.034	2.350	0.73	6.60
(001)	1.02	0.034	1.263	0.57	6.52
(110)	1.10	0.034	1.982	0.85	6.45
(100)	1.22	0.039	2.803	1.09	6.47
(101)	1.31	0.039	1.537	0.91	6.17
(111)	2.06	0.020	4.161	2.58	conductor

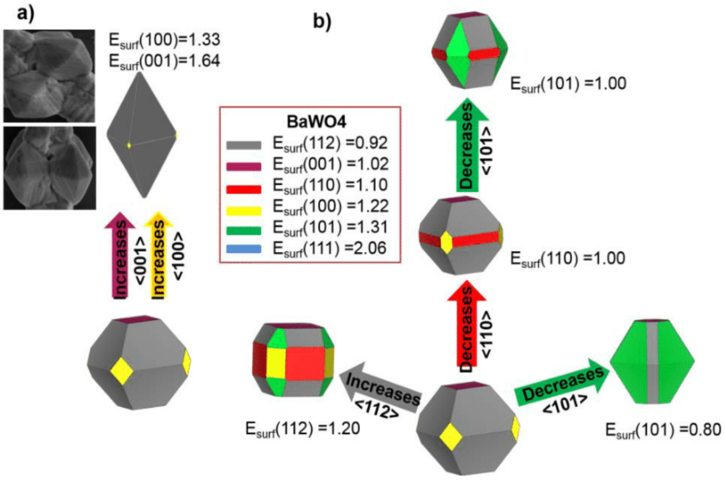

Figure 1. Morphology map for $BaWO_4$ with (001), (112), (100), (101), (111), and (110) crystal planes. Surface energies are expressed in Joules per square meter. a) Experimental FE-SEM images of the studied $BaWO_4$ microcrystal samples are included for comparison. b) Equilibrium crystal shapes predicted by Wulff constructions by tuning the surfaces energy values.

Analysis of the theoretical results indicates that the most stable surfaces are the (112), (001), and (100) facets (Gao, Sun, et al. 2013), which can form a truncated octahedron corresponding to the ideal morphology (shown in the central part of Figure 1). When the relative stability of the facets changes (increases or decreases), more than one facet type appears in the resulting morphology, producing morphological variations. A truncated cube can be obtained if the surface energy of (112) is increased to 1.20 J/m^2, whereas an edge-truncated octahedron can be produced if the surface energy of (101) is decreased to 0.80 J/m^2 The FE-SEM images in Figure 1(a) show well-faceted crystals obtained experimentally that can be compared with the predicted morphologies. Good agreement between the experimental and theoretical morphologies is obtained when the surface energy values for the (001) and (100) facets increase simultaneously (Figure 1). Thus, variations in the ratios between surface energy values affect morphology, and thus, these values can be used to obtain correlations with experimental results.

$BaMoO_4$

Barium molybdate ($BaMoO_4$) is a prototypical member of the molybdate family with a scheelite-type tetragonal structure (Ryu et al. 2006); (Wu et al. 2007), (Sczancoski et al. 2010), similar to $BaWO_4$ (Nogueira et al. 2013). The morphology of a simulated $BaMoO_4$ system was calculated using Wulff constructions for the surface energy values, E_{surf}, of the (001), (101), (110), (100), (111), and (112) surfaces (Table 2). Considering the surface atom distributions, we note that the most stable surface, (001), has exposed [BaO_6] clusters, corresponding to the presence of two oxygen vacancies compared with the bulk structure. However, on the (100), (110), (101), and (111) surfaces, there are undercoordinated [BaO_5] clusters associated with the presence of three oxygen vacancies. On the (112) surface, there are four oxygen vacancies, i.e., undercoordination at [BaO_4]. Only the (111) surface has [MoO_3] clusters, implying breakage of a Mo–O bond in comparison with the bulk structure. As the bonding interaction of a Mo–O bond is stronger than that of a Ba–O bond, the stability of this surface is reduced compared with those of the other surfaces.

According to theoretical calculations, the order of stability found for $BaMoO_4$ surfaces is (001) > (112) > (100) > (110) > (101) > (101) > (111). The ideal morphology of $BaMoO_4$ is controlled by the (001), (112), and (100) surfaces, which have contributions of 15.1%, 70.9%, and 14.0%, respectively, based on experimental micrographs.

The available morphologies, as depicted in Figure 2(a-b), reflect changes in the surface energy values, i.e., modifying the stability of the surface generates the corresponding morphology. Recently, Gao et al. (2013) (Gao, Sun, et al. 2013) reported that the surfaces of scheelite crystals predominantly consist of exposed (001), (112), and (100) surfaces, with the (112) crystal surface as the most commonly exposed surface.

Table 2. Calculated surface energy (E_{surf}), surface tension (σ), and change in total energy (ΔE_{tot}) for the dilation area (ΔA) and gap energy of each surface

Surface	E_{suf} (J/m^2)	ΔE_{tot} (Hartree)	ΔA ($Å^2$)	σ (J/m^2)	E_{gap} (eV)
(001)	0.99	0.035	1.273	0.54	5.69
(112)	1.02	0.032	2.385	0.85	5.81
(100)	1.17	0.039	2.853	1.04	5.38
(110)	1.23	0.033	2.017	1.01	5.63
(101)	1.34	0.039	1.562	0.94	5.09
(111)	2.23	0.016	4.231	2.51	Conductor

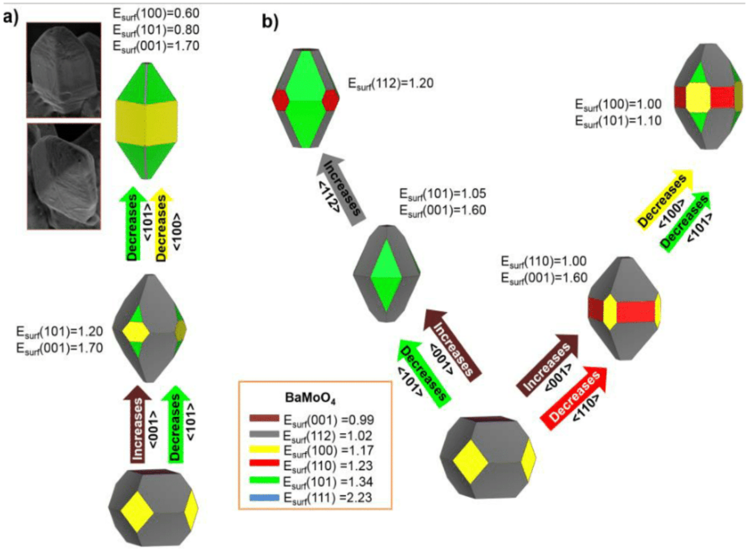

Figure 2. Crystallographic structures and morphology map for $BaMoO_4$ crystals. Surface energies are expressed in Joules per square meter). a) Experimental FE-SEM images and b) equilibrium crystal shapes predicted by Wulff constructions by tuning the surfaces energy values.

The essential features of the different surfaces are constant, but significant differences in the distribution of the electronic states are observed for the (001), (100), (110), and (101) surfaces, where the reduced coordination environment of the surface-terminated oxygen atoms gives rise to split-off features in the O 2p and Mo 4d partial DOS at the bottom of the conduction band. Further, surface states reduce the bulk band gap (5.8 eV) by 0.1–0.7 eV, depending on the specific surface.

$CaZrO_3$

Calcium zirconate ($CaZrO_3$) is a multifunctional material that has many applications and has been investigated frequently, both theoretically and experimentally (Dravid et al. 1987); (Stoch et al. 2012); (Hou 2013);

(M.G.Brik et al. 2013); (Boobalan et al. 2015). $CaZrO_3$ is a perovskite-type material with an orthorhombic structure of space group *Pcmn* (Rosa et al. 2015).

The variation in the equilibrium shapes for these systems obtained using Wulff constructions (Wulff 1901) can be a powerful tool for evaluating the morphology. When the relative stability of the facets changes (increases or decreases), more than one facet type can appear in the resulting morphology, producing morphological variations (Figure 3). The computed surface energy and band gap values for the (121), (100), (010), (101), (001), (111), and (011) surfaces are summarized in Table 3. Analysis of the theoretical results indicates a band gap value of 6.23 eV for bulk $CaZrO_3$.

All surfaces are Ca–O-terminated, with [CaO_4] or [CaO_5] as exposed clusters, and the stability order is (121) > (100) > (010) > (101) > (001) > (111) > (011), and the ideal morphology of $CaZrO_3$ is controlled by the (121), (100), (101), (001), and (010) facets, as can be seen in Figure 3.

Based on the theoretical results, the ideal morphology of $CaZrO_3$ is controlled by the (001), (121), (101), (010) and (100) facets, which have contributions of 11.3%, 56.2%, 11.5%, 7.5%, and 13.5%, respectively. An analysis of the results shows that the present equilibrium morphology models are consistent with the atomic configurations and the local coordination atoms for each surface.

Table 3. Surface energy and band gap values for the (121), (100), (010), (101), (001), (111), and (011) surfaces of $CaZrO_3$ crystals

Surface	E_{suf} (J/m^2)	Area (Å)	E_{gap} (eV)
(121)	1.25	91.13	6.61
(100)	1.26	44.21	6.41
(010)	1.28	32.23	5.62
(101)	1.39	64.41	6.39
(001)	1.37	44.87	6.28
(111)	1.52	72.03	5.64
(011)	1.99	55.25	5.69

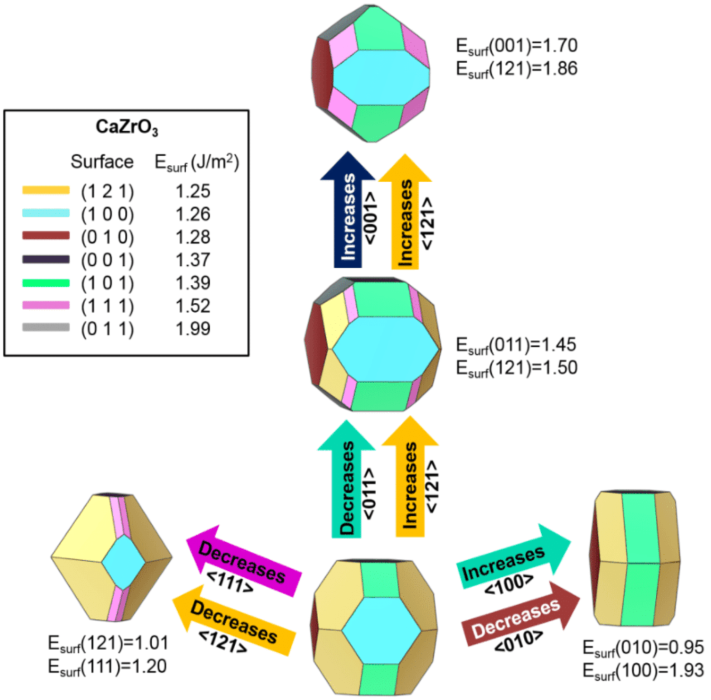

Figure 3. Morphology map for $CaZrO_3$ based on Wulff constructions. Surface energies are expressed in Joules per square meter.

BaSnO$_3$

$BaSnO_3$ exhibits a wide of interesting properties with potential technological applications as capacitor dielectrics, gas sensors for a large variety of molecules (Murugaraj et al. 1997); (Ostrick et al. 1997); (Kreuer 1999); (Aydi et al. 2008); (Kim, Kim, et al. 2012); (Wang, Chesnaud, et al. 2012); (Bevillon et al. 2014); (Hadjarab et al. 2015); (Li et al. 2015); (Marikutsa et al. 2015); (Zhu et al. 2016), humidity detectors, and photocatalysts for dye degradation (Lu et al. 2007); (Liu et al. 2012); (Sales et al. 2014). The properties of this material are correlated with its morphology (Zhang et al. 2017). Moreover, various other synthesis parameters, such as pH, surfactant additives, ion concentration, and synthesis method, can significantly alter the morphology (Kumar et al. 2006); (Sales et al. 2014); (Wang, Liang, et al. 2014); (Huang et al. 2015).

$BaSnO_3$ is a cubic perovskite with space group *Pm3m*, in which the Sn^{4+} cations are located at the centers of regular oxygen octahedra, forming SnO_6 clusters, whereas the local coordination of the Ba^{2+} cations forms a BaO_{12} dodecahedral cluster (Huang et al. 2015); (Duarte et al. 2016). The aim of this study was to understand how BSO morphologies are formed and behave in stoichiometric and nonstoichiometric slabs.

Nonstoichiometric and symmetric slabs for (001), (011), and (111) slabs of $BaSnO_3$ are presented in Figure 4(a). The (001) surface is neutral, with only two terminations and alternating BaO and SnO_2 layers, depicted as A and B. However, the (011) and (111) surfaces have polar characteristics, and studies of similar perovskites have demonstrated that some treatments, such as charge neutrality achieved by imposing a zero net charge on the unit cell, are not very effective at eliminating the generated dipole momentum (Pojani et al. 1999); (Noguera 2000b); (Bottin et al. 2003). In the case of the (011) surface, as an alternative option, a neutral slab can be obtained. For nonsymmetrical surfaces with O–O termination, it is possible to remove oxygen atoms from the top and bottom of the slab, whereas for symmetric and nonstoichiometric surfaces with BaSnO termination, it is possible to remove Ba or Sn atoms, or both, and O atoms at the top and bottom of the slab (Bottin et al. 2003), as shown by pictures C and D in Figure 4(a). The (111) surface is formed by successive layers of BaO_3 and Sn atoms (pictures E and F, Figure 4(a)), following the polarity compensation criterion that the formal charge of the various (111) surfaces of $BaSnO_3$ must be equal to half of the bulk value, i.e., ±2 (Liu et al. 2009).

The simulation data are summarized in Table 4.

A variety of surface reconstructions are reported for $BaSnO_3$-like systems, for both stoichiometric (Charlton et al. 2000); (Liborio et al. 2005) and nonstoichiometric surfaces (Pojani et al. 1999); (Eglitis 2013); (Eglitis 2015), with the (001) surface being the most studied surface.

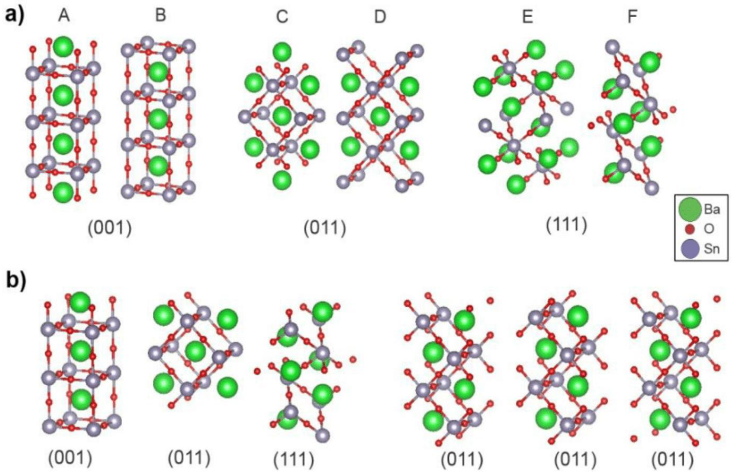

Figure 4. a) Nonstoichiometric and symmetric slabs for (001), (011), and (111) surfaces, and b) stoichiometric slabs for (001), (011), and (111) surfaces.

Table 4. Surface energy values for nonstoichiometric and symmetric slabs of $BaSnO_3$

Termination	**Surface**	***n***	**E_{surf} $(J\cdot m^{-2})$**	**Area (Å^2)**	**Thickness (Å)**
Ba-O/Sn-O	(0 0 1)	7	1.37	16.918	12.20
Ba-O/Sn	(0 1 1)	8	2.33	23.926	11.18
Sn/BaO_3	(1 1 1)	11	3.74	23.303	11.94

Table 5 presents surface energy data for stoichiometric slabs. In this case, the (001) surface is BaO-terminated, whereas the (011) surfaces is SnO- and O_2-terminated. It is possible to observe that there is not a great variation of slab stability (011). Thus, the contribution of different slab thicknesses or even different positions of the outermost oxygen atom is assumed to be small.

Table 5. Surface energy values for stoichiometric and symmetric slabs of $BaSnO_3$

Termination	Surface	*n*	E_{surf} ($J{\cdot}m^{-2}$)	Area ($Å^2$)	Thickness (Å)
Ba-O/Sn-O	(0 0 1)	3	1.37	16.92	10.12
BaSnO	(0 1 1)	4	1.69	23.93	11.05
Sn-BaO3	(1 1 1)	5	3.05	23.30	10.84

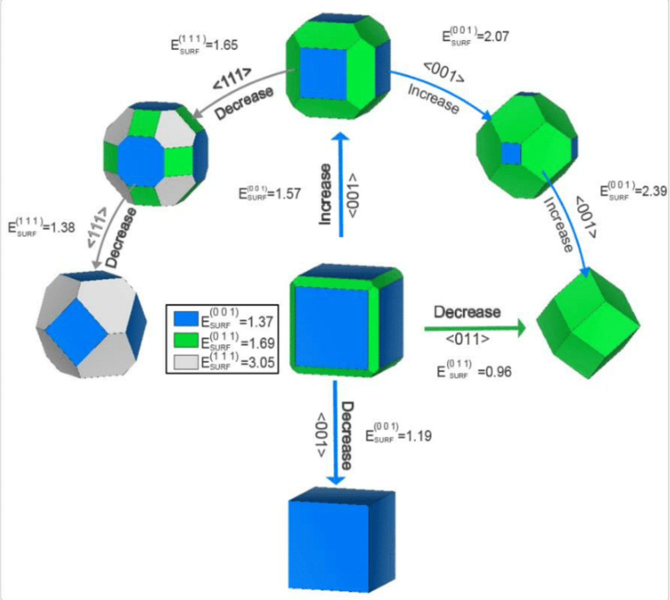

Figure 5. Morphology map for $BaSnO_3$ based on Wulff constructions. Surface energies are expressed in Joules per square meter.

The stability order for stoichiometric and nonstoichiometric slabs is the same: (001) > (011) > (111), although the stability of the stoichiometric (011) surface is higher than that of the corresponding nonstoichiometric slab. Therefore, based on the surface energy values in Table 5, a morphology map was constructed for $BaSnO_3$, as shown in Figure 5, where the ideal morphology is controlled by the (001) surface.

CONCLUSION

"It is a test of true theories not only to account for but to predict phenomena" W. Whewell, 1847 in *The Philosophy of the Inductive Sciences*, *Founded Upon Their History* (Whewell 1847).

Computer modeling is highly likely to play a part in understanding the shape of (nano)crystals and in predicting morphological transformations. We have introduced first-principles surface models for all relevant low-index surfaces of $BaWO_4$, $BaMoO_4$, $CaZrO_3$, and $BaSnO_3$. By simulating clean surfaces with different chemical natures and translating surface stabilities into equilibrium morphologies, we have realized almost the entire range of available morphologies, thereby lending microscopic understanding to experimental results.

Rather than individual values, the most important outcome of these simulations is the general, chemical trends they have revealed. The predicted morphologies were compared with experimentally observed morphologies. To achieve a given morphology, the relative values of the surface energies were changed. In this way, predictive atomistic simulations should likely play an increasingly important role. Therefore, synthesis processes should be controlled to reduce/increase the presence of various surfaces. It has been established that the proposed procedure is easy to apply, provides accurate predictions of crystal morphologies, and can be applied to complex systems.

It should be noted that our calculations have been carried out in a vacuum, and this can be considered a simple approximation. Recent studies show improvements in this area, such as the inclusion of solvent or consideration of specific interactions with surfactants present in the synthesis environment. For example, calculation of the surface Gibbs free energy per unit surface area for an *i*-terminated surface, including variations in entropy and temperature, was recently reported by Kim and Kim to analyze changes in morphology as a function of partial pressure of O_2. Moreover, the authors analyzed the equilibrium crystal shape of $BaZrO_3$ and space charge formation in the (011) surface of $BaZrO_3$ (Kim et al. 2017). Further, Jiang et al. (Jiang et al. 2016) have performed first-principles calculations to clarify the effect of hydrogen adsorption on the surface facets of Pd–Cu nanocrystals. The results indicate that adsorbates could largely modify the equilibrium surface energy, and Wulff constructions based on corrected surface energies are consistent with the experiments, providing microscopic insight into the behavior of nanocrystals at realistic gas pressures. Such an approach is promising for shaping nanocatalysts by gas-assisted treatments. Qi et al. (Qi et al. 2014) have performed DFT calculations to study the surface chemistry of ionic liquids adsorbed on TiO_2 facets. The results of this study revealed how ionic liquids achieve the synthesis of shape-controlled nanocrystals by tuning the surface chemistry, which is a valuable step toward the ultimate goal of controlling the synthesis of inorganic nanomaterials.

We strongly believe in the philosophy of natural sciences, where experiments should inspire predictive models that in turn are verified or disproved by more experiments. Rather than just showing qualitative agreement between theory and experiment, it is more important to be able to predict phenomena, and we urge authors to consider going beyond just reporting results (and referees to allow predictive hypotheses to be included).

ACKNOWLEDGMENTS

This work was supported by the following Spanish research funding projects: *PrometeoII*/2014/022, ACOMP/2014/270, and ACOMP72015/ 1202 (Generalitat-Valenciana); Ministerio de Economia y Competitividad (CTQ2015-652017-P); and Programa de Cooperacion Cientifica con Iberoamerica (Brasil) of Ministerio de Educacion (PHBP14-00020); and CAPES/DGPU (project 312/15 and process 99999.000374/2015-04), as well as the following Brazilian research funding institutions: Federal University of Paraíba and Federal University of São Carlos. M.C. acknowledges Generalitat Valenciana for the Santiago Grisolia Program 2015/033. We also acknowledge Servei Informatica, Universitat Jaume I for a generous allotment of computer time.

REFERENCES

Adamo, Carlo. & Vincenzo, Barone. (1999). "Toward reliable density functional methods without adjustable parameters: The PBE0 model." *The Journal of Chemical Physics*, *110*, 6158-6170. doi: doi: 10.1063/1.478522.

Agarwal, Shilpa., Leon, Lefferts., Barbara, L. Mojet., Michel Ligthart, D. A. J., Emiel, J. M. Hensen., David, R. G. Mitchell., Willem, J. Erasmus., Bruce, G. Anderson., Ezra, J. Olivier., Johannes, H. Neethling. & Abhaya, K. Datye. (2013). "Exposed Surfaces on Shape-Controlled Ceria Nanoparticles Revealed through AC-TEM and Water–Gas Shift Reactivity." *ChemSusChem*, *6* (10), 1898-1906. doi: 10.1002/cssc.201300651.

Ahmadi, T. S., Wang, Z. L., Green, T. C., Henglein, A. & El-Sayed, M. A. (1996). "Shape controlled synthesis of colloidal platinum nanoparticles." *Science*, *272* (5270), 1924–1926.

Andrés, J., Gracia, L., Gouveia, A. F., Ferrer, M. M. & Longo, E. (2015). "Effects of surface stability on the morphological transformation of metals and metal oxides as investigated by first-principles calculations." *Nanotechnology*, *26*, 405703.

Anicete-Santos, M., Picon, F. C., Nahum Alves, C., Pizani, P. S., Varela, J. A. & Longo, E. (2011). "The Role of Short-Range Disorder in $BaWO_4$ Crystals in the Intense Green Photoluminescence." *J. Phys. Chem. C*, *115*, 12180-12186.

Araújo, V. D., Tranquilin, R. L., Motta, F. V., Paskocimas, C. A., Bernardi, M. I. B., Cavalcante, L. S., Andres, J., Longo, E. & Bomio, M. R. D. (2014). "Effect of polyvinyl alcohol on the shape, photoluminescence and photocatalytic properties of $PbMoO_4$ microcrystals." *Materials Science in Semiconductor Processing*, *26*, 425-430. doi: http://dx.doi.org/10.1016/j.mssp.2014.05.027.

Aydi, Abdelhedi., Souad, Chkoundali., Hamadi, Khemakhem., Annie, Simon. & Régnault, Von Der Mühll. (2008). "X-ray diffraction, dielectric measurements and Raman spectroscopy: Studies of the $(1-x)CaSnO_3 - xNaNbO_3$ solid solution." *Journal of Alloys and*

Compounds, *465* (1–2), 222-226. doi: http://dx.doi.org/10.1016/ j. jallcom.2007.10.108.

Bandura, A. V., Evarestov, R. A. & Kuruch, D. D. (2010). "Hybrid HF–DFT modeling of monolayer water adsorption on (001) surface of cubic $BaHfO_3$ and $BaZrO_3$ crystals." *Surface Science*, *604* (19–20), 1591-1597. doi: http://dx.doi.org/10.1016/j.susc.2010.05.030.

Barbier, A., Stierle, A., Finocchi, F. & Jupille, J. (2008). "Stability and stoichiometry of (polar) oxide surfaces for varying oxygen chemical potential." *J. Phys.: Condens. Matter*, *20*, 184014.

Barmparis, Georgios D., Zbigniew, Lodziana., Nuria, Lopez. & Ioannis, N. Remediakis. (2015). "Nanoparticle shapes by using Wulff constructions and first-principles calculations." *Beilstein Journal of Nanotechnology*, *6*, 361-368. doi: 10.3762/bjnano.6.35.

Barnard, A. S. (2010). "Modelling of nanoparticles: approaches to morphology and evolution." *Reports on Progress in Physics*, *73* (8), 086502. doi: 10.1088/0034-4885/73/8/086502.

Barnard, A. S. & Kirkland, A. I. (2008). "Combining Theory and Experiment in Determining the Surface Chemistry of Nanocrystals." *Chemistry of Materials*, *20* (17), 5460-5463. doi: 10.1021/cm8001892.

Barnard, A. S., Zapol, P. & Curtiss, L. A. (2005). "Modeling the Morphology and Phase Stability of TiO_2 Nanocrystals in Water." *Journal of Chemical Theory and Computation*, *1* (1), 107-116. doi: 10.1021/ct0499635.

Barnard, Amanda S. (2012). "Direct Comparison of Kinetic and Thermodynamic Influences on Gold Nanomorphology." *Accounts of Chemical Research*, *45* (10), 1688-1697. doi: 10.1021/ar3000184.

Batista, F. M. C., La Porta, F. A., Gracia, L., Cerdeiras, E., Mestres, L., Siu Li, M., Batista, N. C., Andrés, J., Longo, E. & Cavalcante, L. S. (2015). "A joint experimental and theoretical study on the electronic structure and photoluminescence properties of $Al_2(WO_4)_3$ powders." *Journal of Molecular Structure*, *1081*, 381-388.

Becke, A. D. (1993). "Density-functional thermochemistry. III. The role of exact exchange." *J. Chem. Phys*, *98*, 5648-5652. doi: 10.1063/ 1.464913.

Beltrán, A., Andrés, J., Longo, E. & Leite, E. R. (2003). "Thermodynamic argument about SnO_2 nanoribbon growth." *Applied Physics Letters*, *83* (4), 635-637. doi: 10.1063/1.1594837.

Beltrán, A., Gracia, L., Longo, E. & Andrés, J. (2014). "First-Principles Study of Pressure-Induced Phase Transitions and Electronic Properties of $Ag2MoO_4$." *J. Phys. Chem. C*, *118*, 3724-3732.

Bevillon, Emile., Jessica, Hermet., Guilhem, Dezanneau. & Gregory, Geneste. (2014). "How dopant size influences the protonic energy landscape in $BaSn_{1-x}MxO_{3-x/2}$ (M = Ga, Sc, In, Y, Gd, La)." *Journal of Materials Chemistry A*, *2* (2), 460-471. doi: 10.1039/C3TA12870A.

Bomio, M. R. D., Tranquilin, R. L., Motta, F. V., Paskocimas, C. A., Nascimento, R. M., Gracia, L., Andres, J. & Longo, E. (2013). "Toward Understanding the Photocatalytic Activity of $PbMoO_4$ Powders with Predominant (111), (100), (011), and (110) Facets. A Combined Experimental and Theoretical Study." *The Journal of Physical Chemistry C*, *117* (41), 21382-21395. doi: 10.1021/jp407416h.

Boobalan, K., Varun, A., Vijayaraghavan, R., Chidambaram, K. & Kamachi Mudali, U. (2015). "Facile, scalable synthesis of nanocrystalline calcium zirconate by the solution combustion method." *Ceramics International*, *41*, 3069–3074.

Bottin, François., Fabio, Finocchi. & Claudine, Noguera. (2003). "Stability and electronic structure of the (1×1) $SrTiO_3$ (110) polar surfaces by first-principles calculations." *Physical Review B*, *68* (3), 035418.

Bruchez, M., Moronne, M., Gin, P., Weiss, S. & Alivisatos, A. P. (1998). "Semiconductor Nanocrystals as Fluorescent Biological Labels." *Science*, *281*, 2013–2016.

Chan, W. C. W. & Shuming, N. (1998). "Quantum Dot Bioconjugates for Ultrasensitive Nonisotopic Detection." *Science*, *281* (5385), 2016-2018. doi: 10.1126/science.281.5385.2016.

Charlton, G., Brennan, S., Muryn, C. A., McGrath, R., Norman, D., Turner, T. S. & Thornton, G. (2000). "Surface relaxation of $SrTiO_3$ (001)." *Surface Science*, *457* (1–2), L376-L380. doi: http://dx.doi.org/10.1016/S0039-6028(00)00403-9.

Chen, Jingyi., Byungkwon, Lim., Eric, P. Lee. & Younan, Xia. (2009). "Shape-controlled synthesis of platinum nanocrystals for catalytic and electrocatalytic applications." *Nano Today*, *4* (1), 81-95. doi: http://dx.doi.org/10.1016/j.nantod.2008.09.002.

Cora, F. (2005). "The performance of hybrid density functionals in solid state chemistry: the case of $BaTiO_3$." *Mol. Phys.*, *103*, 2483-2496.

Cora, F., Patel, A., Harrison, N. M., Dovesi, R. & Catlow, C. R. A. (1996). "An Ab Initio Hartree-Fock Study of the Cubic and Tetragonal Phases of Bulk Tungsten Trioxide." *J. Am. Chem. Soc.*, *118*, 12174-12182.

Dai, Yunqian., Claire, M. Cobley., Jie, Zeng., Yueming, Sun. & Younan, Xia. (2009). "Synthesis of Anatase TiO_2 Nanocrystals with Exposed {001} Facets." *Nano Letters*, *9* (6), 2455-2459. doi: 10.1021/nl901181n.

Dandekar, Preshit., Zubin, B. Kuvadia. & Michael, F. Doherty. (2013). "Engineering Crystal Morphology." *Annual Review of Materials Research*, *43* (1), 359-386. doi: 10.1146/annurev-matsci-071312-121623.

Davies, Mark J., Stephen, C. Parker. & Graeme, W. Watson. (1994). "Atomistic simulation of the surface structure of spinel." *Journal of Materials Chemistry*, *4* (6), 813-816. doi: 10.1039/JM9940400813.

Dinh, Cao-Thang., Thanh-Dinh, Nguyen., Freddy, Kleitz. & Trong-On, Do. (2009). "Shape-Controlled Synthesis of Highly Crystalline Titania Nanocrystals." *ACS Nano*, *3* (11), 3737–3743.

Dovesi, R., Saunders, V. R., Orlando C. Roetti, R., Zicovich-Wilson, C. M., Civalleri F. Pascale, B., Doll, K., Harrison, N. M., Bush, I. J., D'Arco, Ph., Llunel, M. & Causa, Y. N. http:// www.crystal.unito.it/basis-sets.php.

Dovesi, R., Saunders, V. R., Roetti, C., Orlando, R., Zicovich-Wilson, C. M., Pascale, F., Civalleri, B., Doll, K., Harrison, N. M., Bush, I. J., D'Arco, Ph., Llunel, M., Caus`a, M., No¨e, Y. (2014). CRYSTAL14. edited by University Of Torino. Torino- Italy.

Dravid, V. P., Notis, M. R. & Lyman, C. E. (1987). "Electron microscopy of boundary structure in calcium zirconate." *journal of materials science*, *22*, 4546-4549.

Duarte, Thiago M., Prescila, G. C. Buzolin., Ieda, M. G. Santos., Elson, Longo. & Julio, R. Sambrano. (2016). "Choice of hybrid functional and basis set optimization to calculate the structural, electronic, mechanical, and vibrational properties of $BaSnO_3$." *Theoretical Chemistry Accounts*, *135* (6), 151. doi: 10.1007/s00214-016-1901-1.

Eglitis, R. I. (2013). "Ab initio calculations of the atomic and electronic structure of $BaZrO_3$ (111) surfaces." *Solid State Ionics*, *230*, 43-47. doi: http://dx.doi.org/10.1016/j.ssi.2012.10.023.

Eglitis, R. I. & David, Vanderbilt. (2008). "First-principles calculations of atomic and electronic structure of $SrTiO_3$ (001) and (011) surfaces." *Physical Review B*, *77* (19), 195408.

Eglitis, Roberts I. (2015). "Theoretical Modelling of the Energy Surface (001) and Topology of $CaZrO_3$ Perovskite." *Ferroelectrics*, *483* (1), 75-85. doi: 10.1080/00150193.2015.1058690.

Fabbro, M. T., Saliby, C., Rios, L. R., La Porta, F. A., Gracia, L. E., Li, M. S., Andrés, J., Santos, L. P. S. & Longo, E. (2015). "Identifying and rationalizing the morphological, structural, and optical properties of B-Ag_2MoO_4 microcrystals, and the formation process of Ag nanoparticles on their surfaces: combining experimental data and first-principles calculations." *Sci. Technol. Adv. Mater*, *16*, 065002.

Fan, Dongbo., John Thomas, P. & Paul, O'Brien. (2008). "Pyramidal Lead Sulfide Crystallites With High Energy {113} Facets." *Journal of the American Chemical Society*, *130* (33), 10892-10894. doi: 10.1021/ja804516q.

Ferrer, M. M., Gouveia, A. F., Gracia, L., Longo, E. & Andrés, J. (2016). "A 3D platform for the morphology modulation of materials: first principles calculations on the thermodynamic stability and surface structure of metal oxides: Co_3O_4, α-Fe_2O_3, and In_2O_3." *Modelling Simul. Mater. Sci. Eng.*, *24*, 025007.

Freund, H. J., Kuhlenbeck, H. & Staemmler, V. (1996). "Oxide surfaces." *Rep. Prog. Phys.*, *59*, 283-347.

Gao, Qiang., Yi-Ming, Ju., Duo, An., Min-Rui, Gao., Chun-Hua, Cui., Jian-Wei, Liu., Huai-Ping, Cong. & Shu-Hong, Yu. (2013). "Shape-

Controlled Synthesis of Monodisperse PdCu Nanocubes and Their Electrocatalytic Properties." *ChemSusChem*, *6* (10), 1878-1882.

Gao, Z. Y., Sun, W., Hu, Y. H. & Liu, X. W. (2013). "Surface energies and appearances of commonly exposed surfaces of scheelite crystal." *T. Nonferr. Metal. Soc*, *23*, 2147-2152.

Gibbs, J. W. & Smith, A.W. (1875). "On the Equilibrium of Heterogeneous Substances." *Trans. Conn. Acad. of Arts Sci.*, *3*, 108-248.

Goniakowski, Jacek., Fabio, Finocchi. & Claudine, Noguera. (2008). "Polarity of oxide surfaces and nanostructures." *Reports on Progress in Physics*, *71* (1), 016501. doi: 10.1088/0034-4885/71/1/016501.

Gordon, Thomas R., Matteo, Cargnello., Taejong, Paik., Filippo, Mangolini., Ralph, T. Weber., Paolo, Fornasiero. & Christopher, B. Murray. (2012). "Nonaqueous Synthesis of TiO_2 Nanocrystals Using TiF4to Engineer Morphology, Oxygen Vacancy Concentration, and Photocatalytic Activity." *Journal of the American Chemical Society*, *134* (15), 6751-6761. doi: 10.1021/ja300823a.

Gouveia, Amanda F., Mateus, M Ferrer., Júlio, R Sambrano., Juan, Andrés. & Elson, Longo. (2016). "Modeling the atomic-scale structure, stability, and morphological transformations in the tetragonal phase of $LaVO_4$." *Chemical Physics Letters*, *660*, 87-92.

Groß, Axel. (2009). *Theoretical Surface Science:A Microscopic Perspective*. 2nd ed ed. Germany: Berlin: Springer.

Gurlo, Aleksander. (2011). "Nanosensors: towards morphological control of gas sensing activity. SnO_2, $In2O_3$, ZnO and WO_3case studies." *Nanoscale*, *3* (1), 154-165. doi: 10.1039/c0nr00560f.

Hadjarab, B., Trari, M. & Kebir, M. (2015). "Physical characterization of the semiconducting deficient perovskite $BaSnO_{3-\delta}$." *Materials Science in Semiconductor Processing*, *29*, 283-287. doi: http://dx.doi.org/10.1016/j.mssp.2014.04.041.

Han, Xiguang., Mingshang, Jin., Shuifen, Xie., Qin, Kuang., Zhiyuan, Jiang., Yaqi, Jiang., Zhaoxiong, Xie. & Lansun, Zheng. (2009). "Synthesis of Tin Dioxide Octahedral Nanoparticles with Exposed High-Energy {221} Facets and Enhanced Gas-Sensing Properties."

Angewandte Chemie International Edition, *48* (48), 9180-9183. doi: 10.1002/anie.200903926.

Han, Xiguang., Qin, Kuang., Mingshang, Jin., Zhaoxiong, Xie. & Lansun, Zheng. (2009). "Synthesis of Titania Nanosheets with a High Percentage of Exposed (001) Facets and Related Photocatalytic Properties." *Journal of the American Chemical Society*, *131* (9), 3152-3153. doi: 10.1021/ja8092373.

Herring, C. (1981). "Some Theorems on the Free Energies of Crystal Surface." *Phys. Rev*, *82*, 87-93.

Hörmann, N. G. & Groß, A. (2014). "Stability, composition and properties of Li_2FeSiO_4 surfaces studied by DFT." *Journal of Solid State Electrochemistry*, *18* (5), 1401-1413. doi: 10.1007/s10008-013-2189-x.

Hou, Z. F. (2013). "Ab initio calculations of elastic modulus and electronic structures of cubic $CaZrO_3$." *Physica B-Condensed Matter.*, *403*, 2624-2628.

http://Www.Crystal.Unito.It/Basis_Sets/Molibdenum.Html.

http://Www.Crystal.Unito.It/Basis_Sets/Oxygen.Html.

http://Www.Tcm.Phy.Cam.Ac.Uk/~Mdt26/Basis_Sets/Ba_Basis.Txt.

Hu, Linhua., Qing, Peng. & Yadong, Li. (2008). "Selective Synthesis of Co_3O_4 Nanocrystal with Different Shape and Crystal Plane Effect on Catalytic Property for Methane Combustion." *J. Am. Chem. Soc.*, *130*, 16136-16137.

Hu, Yidong., Gang, Chen., Chunmei, Li., Yansong, Zhou., Jingxue, Sun., Sue, Hao. & Zhonghui, Han. (2016). "Fabrication of {010} facet dominant $BiTaO_4$ single-crystal nanoplates for efficient photocatalytic performance." *Journal of Materials Chemistry A*, *4* (14), 5274-5281. doi: 10.1039/C6TA00468G.

Huang, Chuande., Xiaodong, Wang., Quan, Shi., Xin, Liu., Yan, Zhang., Fei, Huang. & Tao, Zhang. (2015). "A Facile Peroxo-Precursor Synthesis Method and Structure Evolution of Large Specific Surface Area Mesoporous $BaSnO_3$." *Inorganic Chemistry*, *54* (8), 4002-4010. doi: 10.1021/acs.inorgchem.5b00269.

Huang, Michael H., Sourav, Rej. & Shih-Chen, Hsu. (2014). "Facet-dependent properties of polyhedral nanocrystals." *Chemical Communications*, *50* (14), 1634. doi: 10.1039/c3cc48527g.

Huang, Weixin. (2013). "Crystal Plane-Dependent Surface Reactivity and Catalytic Property of Oxide Catalysts Studied with Oxide Nanocrystal Model Catalysts." *Topics in Catalysis*, *56* (15), 1363-1376. doi: 10.1007/s11244-013-0139-6.

Huang, Weixin. (2016). "Oxide Nanocrystal Model Catalysts." *Accounts of Chemical Research*, *49* (3), 520-527. doi: 10.1021/ acs.accounts. 5b00537.

Huang, Weixin. & Yuxian, Gao. (2014). "Morphology-dependent surface chemistry and catalysis of CeO_2 nanocrystals." *Catal. Sci. Technol.*, *4* (11), 3772-3784. doi: 10.1039/c4cy00679h.

Huynh, Wendy U., Xiaogang, Peng. & Paul Alivisatos, A. (1999). "CdSe Nanocrystal Rods/Poly(3-hexylthiophene) Composite Photovoltaic Devices." *Adv. Mater.*, *11* (11), 923-927.

Jiang, Ying., Hengbo, Li., Zhemin, Wu., Wenying, Ye., Hui, Zhang., Yong, Wang., Chenghua, Sun. & Ze, Zhang. (2016). "*In Situ* Observation of Hydrogen-Induced Surface Faceting for Palladium–Copper Nanocrystals at Atmospheric Pressure." *Angewandte Chemie International Edition*, *55* (40), 12427-12430. doi: 10.1002/anie. 201605956.

Jiang, Zhi-Yuan., Qin, Kuang., Zhao-Xiong, Xie. & Lan-Sun, Zheng. (2010). "Syntheses and Properties of Micro/Nanostructured Crystallites with High-Energy Surfaces." *Advanced Functional Materials*, *20* (21), 3634-3645. doi: 10.1002/adfm.201001243.

Jiang, Zhi-Yuan., Tao, Xu., Zhao-Xiong, Xie., Zhi-Wei, Lin., Xi, Zhou., Xin, Xu., Rong-Bin, Huang. & Lan-Sun, Zheng. (2005). "Molten Salt Route toward the Growth of ZnO Nanowires in Unusual Growth Directions." *The Journal of Physical Chemistry B*, *109* (49), 23269-23273. doi: 10.1021/jp054566r.

Jun, Young-wook., Jin-sil, Choi. & Jinwoo, Cheon. (2006). "Shape Control of Semiconductor and Metal Oxide Nanocrystals through

Nonhydrolytic Colloidal Routes." *Angewandte Chemie International Edition*, *45* (21), 3414-3439. doi: 10.1002/anie.200503821.

Kanaki, Elisavet., Sebastian, Gohr., Carsten, Müller. & Beate, Paulus. (2015). "Theoretical study on the morphology of MgF_2 nanocrystals at finite temperature and pressure." *Surface Science*, *632*, 158-163. doi: http://dx.doi.org/10.1016/j.susc.2014.10.007.

Karim, Altaf., Sonia, Fosse. & Kristin, A. Persson. (2013). "Surface structure and equilibrium particle shape of the $LiMn_2O_4$ spinel from first-principles calculations." *Physical Review B*, *87* (7), 075322.

Kim, Hyung Joon., Useong, Kim., Tai, Hoon Kim., Jiyeon, Kim., Hoon, Min Kim., Byung-Gu, Jeon., Woong-Jhae, Lee., Hyo, Sik Mun., Kwang, Taek Hong., Jaejun, Yu., Kookrin, Char. & Kee, Hoon Kim. (2012). "Physical properties of transparent perovskite oxides $(Ba,La)SnO_3$ with high electrical mobility at room temperature." *Physical Review B*, *86* (16), 165205.

Kim, Ji-Su. & Yeong-Cheol, Kim. (2017). "Equilibrium crystal shape of $BaZrO_3$ and space charge formation in the (011) surface by using ab-initio thermodynamics." *Journal of the Korean Physical Society*, *70* (1), 75-80. doi: 10.3938/jkps.70.75.

Kim, Yongseon., Hyundeok, Lee. & Shinhoo, Kang. (2012). "First-principles and experimental investigation of the morphology of layer-structured $LiNiO_2$ and $LiCoO_2$." *Journal of Materials Chemistry*, *22* (25), 12874-12881. doi: 10.1039/C2JM31145C.

Kreuer, K. D. (1999). "Aspects of the formation and mobility of protonic charge carriers and the stability of perovskite-type oxides." *Solid State Ionics*, *125* (1–4), 285-302. doi: http://dx.doi.org/10.1016/S0167-2738(99)00188-5.

Kuang, Qin., Xue, Wang., Zhiyuan, Jiang., Zhaoxiong, Xie. & Lansun, Zheng. (2014). "High-Energy-Surface Engineered Metal Oxide Micro- and Nanocrystallites and Their Applications." *Accounts Of Chemical Research*, 308-318 (2), 308-318.

Kumar, Ashok., Choudhary, R. N. P., Singh, B. P. & Awalendra, K. Thakur. (2006). "Effect of strontium concentration on electrical conduction properties of Sr-modified $BaSnO_3$." *Ceramics*

International, *32* (1), 73-83. doi: http://dx.doi.org/10.1016/ j.ceramint. 2004.12.010.

Valenzano, L., Civalleri, B., Chavan, S., Bordiga, S., Nilsen, M. H., Jakobsen, S., Lillerud, K. P. & Lamberti, C. (2011). "Disclosing the Complex Structure of UiO-66 Metal Organic Framework: A Synergic Combination of Experiment and Theory." *Chem. Mater.*, *23*, 1700–1718.

Gracia, L., Longo, V. M., Cavalcante, L. S., Beltrán, A., Avansi, W., Li, M. S., Mastelaro, V. R., Varela, J. A., Longo, E. & Andrés, J. (2011). "Presence of excited electronic state in $CaWO_4$ crystals provoked by a tetrahedral distortion: An experimental and theoretical investigation." *J. Appl. Phys.*, *110*, 043501.

Lee, C. T., Yang, W. T. & Parr, R. G. (1988). "Development of the Colle-Salvetti correlation-energy formula into a functional of the electron density." *Phys. Rev. B: Condens. Matter*, *37*, 785-789. doi: 10.1103/ PhysRevB.37.785.

Lee, Eunseok. & Kristin, A Persson. (2013). "First-principles study of the nano-scaling effect on the electrochemical behavior in $LiNi_{0.5}Mn_{1.5}O_4$." *Nanotechnology*, *24*, 424007.

Lee, Hyunjoo., Susan, E. Habas., Sasha, Kweskin., Derek, Butcher., Gabor, A. Somorjai. & Peidong, Yang. (2006a). "Morphological Control of Catalytically Active Platinum Nanocrystals." *Angewandte Chemie International Edition*, *45*, 7824 –7828. doi: 10.1002/anie. 200603068.

Lee, Hyunjoo., Susan, E. Habas., Sasha, Kweskin., Derek, Butcher., Gabor, A. Somorjai. & Peidong, Yang. (2006b). "Morphological Control of Catalytically Active Platinum Nanocrystals." *Angewandte Chemie International Edition*, *118*, 7988-7992.

Lee, Kwangyeol., Minsik, Kim. & Heonjo, Kim. (2010). "Catalytic nanoparticles being facet-controlled." *Journal of Materials Chemistry*, *20* (19), 3791-3798. doi: 10.1039/B921857B.

Leite, E. R., Giraldi, T. R., Pontes, F. M., Longo, E., Beltrán, A. & Andrés, J. (2003). "Crystal growth in colloidal tin oxide nanocrystals induced by coalescence at room temperature." *Applied Physics Letters*, *83* (8), 1566-1568. doi: 10.1063/1.1605241.

Leng, Mei., Mingzhu, Liu., Yibo, Zhang., Zhenqing, Wang., Chao, Yu., Xiangguang, Yang., Hongjie, Zhang. & Cheng, Wang. (2010). "Polyhedral 50-Facet Cu_2O Microcrystals Partially Enclosed by {311} High-Index Planes: Synthesis and Enhanced Catalytic CO Oxidation Activity." *Journal of the American Chemical Society*, *132* (48), 17084-17087. doi: 10.1021/ja106788x.

Li, Pan., Xian, Zhao., Chun-Jiang, Jia., Honggang, Sun., Yanlu, Li., Liming, Sun., Xiufeng, Cheng., Li, Liu. & Weiliu, Fan. (2012). "Mechanism of Morphology Transformation of Tetragonal Phase $LaVO_4$ Nanocrystals Controlled by Surface Chemistry: Experimental and Theoretical Insights." *Crystal Growth & Design*, *12* (10), 5042-5050. doi: 10.1021/cg3009927.

Li, Yong. & Wenjie, Shen. (2014). "Morphology-dependent nanocatalysts: Rod-shaped oxides." *Chem. Soc. Rev.*, *43* (5), 1543-1574. doi: 10.1039/c3cs60296f.

Li, Yuhan., Jingping, Zhang., Fengmei, Yang., Jing, Liang., Hao, Sun., Shuwei, Tang. & Rongshun, Wang. (2014). "Morphology and surface properties of $LiVOPO_4$: a first principles study." *Physical Chemistry Chemical Physics*, *16* (44), 24604-24609. doi: 10.1039/C4CP03628J.

Li, Yuwei., Lijun, Zhang., Yanming, Ma. & David, J. Singh. (2015). "Tuning optical properties of transparent conducting barium stannate by dimensional reduction." *APL Materials*, *3* (1), 011102. doi: 10.1063/1.4906785.

Liao, Hong-Gang., Yan-Xia, Jiang., Zhi-You, Zhou., Sheng-Pei, Chen. & Shi-Gang, Sun. (2008a). "Shape-Controlled Synthesis of Gold Nanoparticles in Deep Eutectic Solvents for Studies of Structure-Functionality Relationships in Electrocatalysis." *Angewandte Chemie International Edition*, *120*, 9240-9243. doi: 10.1002/anie.200803202.

Liao, Hong-Gang., Yan-Xia, Jiang., Zhi-You, Zhou., Sheng-Pei, Chen. & Shi-Gang, Sun. (2008b). "Shape-Controlled Synthesis of Gold Nanoparticles in Deep Eutectic Solvents for Studies of Structure–

Functionality Relationships in Electrocatalysis." *Angew. Chem*, *47*, 9100–9103.

Liborio, M. L., Sánchez, G. C., Paxton, T. A. & Finnis, W. M. (2005). "Stability of Sr adatom model structures for $SrTiO_3$ (001) surface reconstructions." *Journal of Physics: Condensed Matter*, *17* (23), L223.

Lieber, Charles M. (1998). "One-Dimensional Nanostructures: Chemistry, Physics & Applications." *Solid State Communications*, *107* (11), 607-616.

Lin, Yuyuan., Zili, Wu., Jianguo, Wen., Kenneth, R. Poeppelmeier. & Laurence, D. Marks. (2014). "Imaging the Atomic Surface Structures of CeO_2 Nanoparticles." *Nano Letters*, *14* (1), 191-196. doi: 10.1021/nl403713b.

Liu, Bin., Ankur, Khare. & Eray, S. Aydil. (2011). "TiO2–B/Anatase Core–Shell Heterojunction Nanowires for Photocatalysis." *ACS Applied Materials & Interfaces*, *3* (11), 4444-4450. doi: 10.1021/am201123u.

Liu, Gang., Jimmy, C. Yu., Gao, Qing Lu. & Hui-Ming, Cheng. (2011). "Crystal facet engineering of semiconductor photocatalysts: motivations, advances and unique properties." *Chemical Communications*, *47* (24), 6763-6783. doi: 10.1039/C1CC10665A.

Liu, Lichen., Xianrui, Gu., Zeyang, Ji., Weixin, Zou., Changjin, Tang., Fei, Gao. & Lin, Dong. (2013). "Anion-Assisted Synthesis of TiO_2 Nanocrystals with Tunable Crystal Forms and Crystal Facets and Their Photocatalytic Redox Activities in Organic Reactions." *The Journal of Physical Chemistry C*, *117* (36), 18578-18587. doi: 10.1021/jp4064774.

Liu, Qinzhuang., Bing, Li., Jianjun, Liu., Hong, Li., Zhongliang, Liu., Kai, Dai., Guangping, Zhu., Peng, Zhang., Feng, Chen. & Jianming, Dai. (2012). "Structure and band gap tuning of transparent $(Ba_{1-x}Sr_x)SnO_3$ thin films epitaxially grown on MgO substrates." *EPL*, *98* (4), 47010.

Liu, Wei., Chuncheng, Wang., Jie, Cui. & Zhen-Yong, Man. (2009). "Ab initio calculations of the (111) polar surfaces." *Solid State*

Communications, *149* (43–44), 1871-1876. doi: http://dx.doi.org/ 10. 1016/j.ssc.2009.08.006.

Liu, Y. & Chu, Y. (2005). "Surfactant-assisted synthesis of single crystal BaWO4 octahedral microparticles." *Mater. Chem. Phys*, *92*, 59-63.

Longo, E., Volanti, D. P., Longo, V. M., Gracia, L., Nogueira, I. C., Almeida, M. A. P., Pinheiro, A. N., Ferrer, M. M., Cavalcante, L. S. & Andrés, J. (2014). "Toward an Understanding of the Growth of Ag Filaments on α-Ag_2WO_4 and Their Photoluminescent Properties: A Combined Experimental and Theoretical Study." *J. Phys. Chem. C*, *118*, 1229-1239.

Longo, Valéria M., Lourdes, Gracia., Daniel, G. Stroppa., Laécio, S. Cavalcante., Marcelo, Orlandi., Antônio, J. Ramirez., Edson, R. Leite., Juan, Andrés., Armando, Beltrán., José, A. Varela. & Elson, Longo. (2011). "A Joint Experimental and Theoretical Study on the Nanomorphology of $CaWO_4$ Crystals." *The Journal of Physical Chemistry C*, *115* (41), 20113-20119. doi: 10.1021/jp205764s.

Lovette, Michael A., Andrea, Robben Browning., Derek, W. Griffin., Jacob, P. Sizemore., Ryan, C. Snyder. & Michael, F. Doherty. (2008). "Crystal Shape Engineering." *Industrial & Engineering Chemistry Research*, *47* (24), 9812-9833. doi: 10.1021/ie800900f.

Lu, Wensheng. & Helmut, Schmidt. (2007). "Preparation and characterization of $BaSnO_3$ powders by hydrothermal synthesis from tin oxide hydrate gel." *Journal of Materials Science*, *42* (24), 10007-10013. doi: 10.1007/s10853-007-2069-9.

Luo, Tao., Qiang-Qiang, Meng., Chao, Gao., Xin-Yao, Yu., Yong, Jia., Bai, Sun., Zhen, Jin., Qun-Xiang, Li., Jin-Huai, Liu. & Xing-Jiu, Huang. (2014). "Sub-20 nm-Fe_3O_4 square and circular nanoplates: synthesis and facet-dependent magnetic and electrochemical properties." *Chemical Communications*, *50* (100), 15952-15955. doi: 10.1039/C4CC06064D.

Luo, Z., Li, H., Xia, J., Zhu, W., Guo, J. & Zhang, B. (2007). "Controlled synthesis of different morphologies of BaWO4 crystals via a surfactant-assisted method." *J. Cryst. Growth.*, *300*, 523-529.

M.G.Brik, C. G. Ma. & Krasnenko, V. (2013). “First-principles calculations of the structural and electronic properties of the cubic $CaZrO_3$ (001) surfaces.” *Surface Science*, *608*, 146-153.

Ma, Yanyun., Qin, Kuang., Zhiyuan, Jiang., Zhaoxiong, Xie., Rongbin, Huang. & Lansun, Zheng. (2008a). “Synthesis of Trisoctahedral Gold Nanocrystals with Exposed High-Index Facets by a Facile Chemical Method.” *Angew. Chem*, *120*, 9033–9036.

Ma, Yanyun., Qin, Kuang., Zhiyuan, Jiang., Zhaoxiong, Xie., Rongbin, Huang. & Lansun, Zheng. (2008b). “Synthesis of Trisoctahedral Gold Nanocrystals with Exposed High-Index Facets by a Facile Chemical Method.” *Angewandte Chemie International Edition*, *47* (46), 8901-8904. doi: 10.1002/anie.200802750.

Marikutsa, Artem., Marina, Rumyantseva., Alexander, Baranchikov. & Alexander, Gaskov. (2015). “Nanocrystalline $BaSnO_3$ as an Alternative Gas Sensor Material: Surface Reactivity and High Sensitivity to SO_2.” *Materials*, *8* (9), 5311.

Marks, L. D. & Peng, L. (2016). “Nanoparticle shape, thermodynamics and kinetics.” *Journal of Physics: Condensed Matter*, *28* (5), 053001. doi: 10.1088/0953-8984/28/5/053001.

Marks, L. D. (1983). “Modified Wulff constructions for twinned particles.” *J. Crys. Growth*, *61*, 556-566.

Mattoussi, Hedi., Leonard, H. Radzilowski., Bashir, O. Dabbousi., Edwin, L. Thomas., Moungi, G. Bawendi. & Michael, F. Rubner. (1998). “Electroluminescence from heterostructures of poly(phenylene vinylene) and inorganic CdSe nanocrystals.” *Journal of Applied Physics*, *83* (12), 7965-7974. doi: 10.1063/1.367978.

Miao, Jianwei. & Bin, Liu. (2013). “Anatase TiO_2 microspheres with reactive {001} facets for improved photocatalytic activity.” *RSC Advances*, *3* (4), 1222-1226. doi: 10.1039/C2RA22312K.

Momma, K. & Izumi, F. (2011). “ VESTA 3 for three-dimensional visualization of crystal, volumetric and morphology data.” *J. Appl. Cryst.*, *44*, 1272-1276.

Monkhorst, H. J. & Pack, J. D. (1976). “Special points for Brillouin-x.one integrations.” *Phys. Rev. B: Condens. Matter.*, *13*, 5188-5192.

Moreira, Mário L., Juan, Andrés., Lourdes, Gracia., Armando, Beltrán., Luciano, A. Montoro., José, A. Varela. & Elson, Longo. (2013). "Quantum mechanical modeling of excited electronic states and their relationship to cathodoluminescence of $BaZrO_3$." *J. Appl. Phys.*, *114*, 043714 doi: 10.1063/1.4816247.

Murugaraj, P., Kreuer, K. D., He, T., Schober, T. & Maier, J. (1997). "High proton conductivity in barium yttrium stannate $Ba_2YSnO_{5.5}$." *Solid State Ionics*, *98* (1–2), 1-6. doi: http://dx.doi.org/10.1016/S0167-2738(97)00102-1.

Nogueira, I. C., Cavalcante, L. S., Pereira, P. F. S., de Jesus, M. M., Rivas Mercury, J. M., Batista, N. C., Li, M. S. & Longo, E. (2013). "Rietveld refinement, morphology and optical properties of $(Ba_{1-x}Sr_x)MoO_4$ crystals." *J. Appl. Cryst.*, *46*, 1434.

Noguera, Claudine. (2000a). "Polar oxide surfaces." *J. Phys.: Condens. Matter*, *12*, R367–R41.

Noguera, Claudine. (2000b). "Polar oxide surfaces." *J. Phys.: Condens. Matter*, *12*, R367–R341. doi: 10.1088/0953-8984/12/31/201.

Noguera, Claudine. & Jacek, Goniakowski. (2013). "Polarity in Oxide Nano-objects." *Chemical Reviews*, *113* (6), 4073-4105. doi: 10.1021/cr3003032.

Oliveira, M. C., Gracia, L., Nogueira, I. C., Gurgel, M. F. C., Mercury, J. M. R., Longo, E. & Andrés, J. (2016a). "Synthesis and morphological transformation of $BaWO_4$ crystals: Experimental and theoretical insights." *Ceram. Inter.*, *42*, 10913-10921.

Oliveira, Marisa Carvalho., Lourdes, Gracia., Ic¸amira C. Nogueira., Maria, Fernanda C. Gurgel., Jose, Manuel R. Mercury., Elson, Longo. & Juan, Andrés. (2016b). "On the morphology of $BaMoO_4$ crystals: A theoretical and experimental approach." *Cryst. Res. Technol*, *51*, 634–644.

Ostrick, Bernhard., Maximilian, Fleischer. & Hans, Meixner. (1997). "High-Temperature Hall Measurements on $BaSnO_3$Ceramics." *Journal of the American Ceramic Society*, *80* (8), 2153-2156. doi: 10.1111/j.1151-2916.1997.tb03102.x.

Pal, Jaya. & Tarasankar, Pal. (2015). "Faceted metal and metal oxide nanoparticles: design, fabrication and catalysis." *Nanoscale*, *7* (34), 14159-14190. doi: 10.1039/C5NR03395K.

Pan, Jian., Gang, Liu., Gao, Qing Max Lu. & Hui-Ming, Cheng. (2011). "On the True Photoreactivity Order of {001}, {010}, and {101} Facets of Anatase TiO_2 Crystals." *Angewandte Chemie International Edition*, *50* (9), 2133-2137. doi: 10.1002/anie.201006057.

Phuruangrat, A., Thongtem, T. & Thongtem, S. (2012). "Precipitate synthesis of $BaMoO_4$ and BaWO4 nanoparticles at room temperature and their photoluminescence properties." *Superlattice. Microst*, *52*, 78-83.

Piskorz, Witold., Joanna, Gryboś., Filip, Zasada., Piotr, Zapała., Sylvain, Cristol., Jean-François, Paul. & Zbigniew, Sojka. (2012). "Periodic DFT Study of the Tetragonal ZrO_2 Nanocrystals: Equilibrium Morphology Modeling and Atomistic Surface Hydration Thermodynamics." *The Journal of Physical Chemistry C*, *116* (36), 19307-19320. doi: 10.1021/jp3050059.

Pojani, Ariana., Fabio, Finocchi. & Claudine, Noguera. (1999). "Polarity on the $SrTiO_3$ (111) and (110) surfaces." *Surface Science*, *442* (2), 179-198. doi: http://dx.doi.org/10.1016/S0039-6028(99)00911-5.

Qi, Kezhen., Di, Li., Jiaqi, Fu., Lianjie, Zhu., Xiaochuan, Duan., Qing, Qin., Guichang, Wang. & Wenjun, Zheng. (2014). "Elucidating Ionic Liquid Environments That Affect the Morphology of TiO_2 Nanocrystals: A DFT+D Study." *The Journal of Physical Chemistry C*, *118* (40), 23320-23327. doi: 10.1021/jp503891s.

Qiao, Zhen-An., Zili, Wu. & Sheng, Dai. (2013). "Shape-Controlled Ceria-based Nanostructures for Catalysis Applications." *ChemSusChem*, *6*, 1821 – 1833 1. doi: 10.1002/cssc.v6.10/issuetoc.

Rosa, I. L. V., Oliveira, M. C., Assis, M., Ferrer, M., André, R. S., Longo, E. & Gurgel, M. F. C. (2015). "A theoretical investigation of the structural and electronic properties of orthorhombic $CaZrO_3$." *Ceramics International*, *41* (2), 3069–3074.

Roy, Nitish., Youngku, Sohn. & Debabrata, Pradhan. (2013). "Synergy of Low-Energy {101} and High-Energy {001} TiO_2 Crystal Facets for

Enhanced Photocatalysis." *ACS Nano*, *7* (3), 2532-2540. doi: 10.1021/nn305877v.

Ryu, J. H., Yoon, J. W. & Shim, K. B. (2006). "Microwave-assisted synthesis of $BaMoO_4$ nanocrystallites by a citrate complex method and their anisotropic aggregation." *J. Alloy Compd*, *413*, 144-149.

Sales, Herbet Bezerra., Valérie, Bouquet., Stéphanie, Députier., Sophie, Ollivier., Francis, Gouttefangeas., Maryline, Guilloux-Viry., Vincent, Dorcet., Ingrid, Távora Weber., Antônio, Gouveia de Souza. & Iêda, Maria Garcia dos Santos. (2014). "$Sr_{1-x}Ba_xSnO_3$ system applied in the photocatalytic discoloration of an azo-dye." *Solid State Sciences*, *28*, 67-73. doi: http://dx.doi.org/10.1016/j.solidstatesciences.2013.12.007.

Sayle, Thi X. T., Beverley, J. Inkson., Ajay, Karakoti., Amit, Kumar., Marco, Molinari., Gunter, Mobus., Stephen, C. Parker., Sudipta, Seal. & Dean, C. Sayle. (2011). "Mechanical properties of ceria nanorods and nanochains; the effect of dislocations, grain-boundaries and oriented attachment." *Nanoscale*, *3* (4), 1823-1837. doi: 10.1039/C0NR00980F.

Schlamp, M. C., Xiaogang, Peng. & Alivisatos, A. P. (1997). "Improved efficiencies in light emitting diodes made with CdSe(CdS) core/shell type nanocrystals and a semiconducting polymer." *Journal of Applied Physics*, *82* (11), 5837-5842. doi: 10.1063/1.366452.

Schmidt, C. & Ulrich, J. (2012). "Morphology prediction of crystals grown in the presence of impurities and solvents — An evaluation of the state of the art." *Journal of Crystal Growth*, *353* (1), 168-173. doi: http://dx.doi.org/10.1016/j.jcrysgro.2012.05.001.

Sczancoski, J. C., Cavalcante, L. S., Marana, N. L., Silva, R. O. D., Tranquilin, R. L., Joya, M. R., Pizani, P. S., Varela, J. A., Sambrano, J. R., Li, M. S., Longo, E. & Andrés, J. (2010). "Electronic structure and optical properties of $BaMoO_4$ powders." *Curr. Appl. Phys*, *10*, 614-624.

Seyed-Razavi, Alireza., Ian, K. Snook. & Amanda, S. Barnard. (2010). "Origin of nanomorphology: does a complete theory of nanoparticle evolution exist?" *Journal of Materials Chemistry*, *20* (3), 416-421. doi: 10.1039/B915383G.

Silva, Gabriela S., Lourdes, Gracia., Maria, T. Fabbro., Luis, P. Serejo., dos, Santos., Hector, Beltrán-Mir., Eloisa, Cordoncillo., Elson, Longo., & Juan, Andrés. (2016). "Theoretical and Experimental Insight on Ag_2CrO_4 Microcrystals: Synthesis, Characterization, and Photoluminescence Properties." *Inorganic Chemistry*, *55* (17), 8961-8970. doi: 10.1021/ acs.inorgchem.6b01452.

Sophia, Gustavo., Philippe, Baranek., Christian, Sarrazin., Michel, Rérat. & Roberto, Dovesi. (2013). "First-principles study of the mechanisms of the pressure-induced dielectric anomalies in ferroelectric perovskites." *Phase Transitions*, *86* (11), 1069-1084. doi: 10.1080/ 01411594. 2012.754442.

Stoch, P., Szczerba, J., Lis, J., Madej, D. & Pędzich, Z. (2012). "Crystal structure and ab initio calculations of $CaZrO_3$." *Journal of the European Ceramic Society*, *32* (3), 665-670.

Stroppa, Daniel G., Luciano, A. Montoro., Armando, Beltrán., Tiago, G. Conti., Rafael, O. da Silva., Juan, Andrés., Edson, R. Leite. & Antonio, J. Ramirez. (2011). "Dopant Segregation Analysis on Sb:SnO_2 Nanocrystals." *Chemistry – A European Journal*, *17* (41), 11515-11519. doi: 10.1002/chem.201100972.

Stroppa, Daniel G., Luciano, A. Montoro., Antonio, Campello., Lourdes, Gracia., Armando, Beltran., Juan, Andres., Edson, R. Leite. & Antonio, J. Ramirez. (2014). "Prediction of dopant atom distribution on nanocrystals using thermodynamic arguments." *Physical Chemistry Chemical Physics*, *16* (3), 1089-1094. doi: 10.1039/C3CP53427H.

Suleiman, Ibrahim A., Marian, W. Radny., Michael, J. Gladys., Phillip, V. Smith., John, C. Mackie., Eric, M. Kennedy. & Bogdan, Z. Dlugogorski. (2015). "Thermodynamic stability and structure of cuprous chloride surfaces: a DFT investigation." *Physical Chemistry Chemical Physics*, *17* (10), 7038-7045. doi: 10.1039/C4CP05340K.

Tan, Chih-Shan., Shih-Chen, Hsu., Wei-Hong, Ke., Lih-Juann, Chen. & Michael, H. Huang. (2015). "Facet-Dependent Electrical Conductivity Properties of Cu_2O Crystals." *Nano Letters*, *15* (3), 2155-2160. doi: 10.1021/acs.nanolett.5b00150.

Tan, Joyce Pei Ying., Hui, Ru Tan., Chris, Boothroyd., Yong, Lim Foo., Chao Bin, He. & Ming, Lin. (2011). "Three-Dimensional Structure of CeO_2 Nanocrystals." *The Journal of Physical Chemistry C*, *115* (9), 3544-3551. doi: 10.1021/jp1122097.

Tao, Andrea R., Susan, Habas. & Peidong, Yang. (2008). "Shape Control of Colloidal Metal Nanocrystals." *Small*, *4* (3), 310-325. doi: 10.1002/smll.200701295.

Tian, N., Zhou, Z. Y., Sun, S. G., Ding, Y. & Wang, Z. L. (2007). "Synthesis of Tetrahexahedral Platinum Nanocrystals with High-Index Facets and High Electro-Oxidation Activity." *Science*, *316* (5825), 732-735. doi: 10.1126/science.1140484.

Tian, Na., Zhi-You, Zhou. & Shi-Gang, Sun. (2008). "Platinum Metal Catalysts of High-Index Surfaces: From Single-Crystal Planes to Electrochemically Shape-Controlled Nanoparticles." *The Journal of Physical Chemistry C*, *112* (50), 19801-19817. doi: 10.1021/ jp8040 51e.

Tian, Na., Zhi-You, Zhou. & Shi-Gang, Sun. (2009). "Electrochemical preparation of Pd nanorods with high-index facets." *Chemical Communications*, (12), 1502-1504. doi: 10.1039/B819751B.

Tompsett, David A., Steve, C. Parker., Peter, G. Bruce. & Saiful Islam, M. (2013). "Nanostructuring of β-MnO_2: The Important Role of Surface to Bulk Ion Migration." *Chemistry of Materials*, *25* (4), 536-541. doi: 10.1021/cm303295f.

Valenzano, L., Torres, F. J., Doll, K., Pascale, F., Zicovich-Wilson, C. M. & Dovesi, R. (2006). "Ab Initio study of the vibrational spectrum and related properties of crystalline compounds; the case of $CaCO_3$ calcite." *Z. Phys. Chem.*, *220*, 893-912.

Van Santen, Rutger A. (2009). "Complementary Structure Sensitive and Insensitive Catalytic Relationships." *Accounts of Chemical Research*, *42* (1), 57-66. doi: 10.1021/ar800022m.

Vantomme, Aurélien., Zhong-Yong, Yuan., Gaohui, Du. & Bao-Lian, Su. (2005). "Surfactant-Assisted Large-Scale Preparation of Crystalline CeO_2 Nanorods." *Langmuir*, *21* (3), 1132-1135. doi: 10.1021/ la047 751p.

Wander, A., Schedin, F., Steadman, P., Norris, A., McGrath, R., Turner, T. S., Thornton, G. & Harrison, N. M. (2001). "Stability of Polar Oxide Surfaces." *Physical Review Letters*, *86* (17), 3811-3814.

Wang, Chao., Hideo, Daimon., Taigo, Onodera., Tetsunori, Koda. & Shouheng, Sun. (2008). "A General Approach to the Size- and Shape-Controlled Synthesis of Platinum Nanoparticles and Their Catalytic Reduction of Oxygen." *Angewandte Chemie International Edition*, *47* (19), 3588-3591. doi: 10.1002/anie.200800073.

Wang, Lan., Ling, Zang., Jincai, Zhao. & Chuanyi, Wang. (2012). "Green synthesis of shape-defined anatase TiO_2 nanocrystals wholly exposed with {001} and {100} facets." *Chemical Communications*, *48* (96), 11736-11738. doi: 10.1039/C2CC36005E.

Wang, Lei., Haibo, Li., Shuling, Xu., Qiaoli, Yue. & Jifeng, Liu. (2014). "Facet-dependent optical properties of nanostructured ZnO." *Materials Chemistry and Physics*, *147* (3), 1134-1139. doi: 10.1016/j.matchemphys.2014.06.069.

Wang, Liangbing., Songtao, Zhao., Chenxuan, Liu., Chen, Li., Xu, Li., Hongliang, Li., Youcheng, Wang., Chao, Ma., Zhenyu, Li. & Jie, Zeng. (2015). "Aerobic Oxidation of Cyclohexane on Catalysts Based on Twinned and Single-Crystal $Au_{75}Pd_{25}$Bimetallic Nanocrystals." *Nano Letters*, *15* (5), 2875-2880. doi: 10.1021/nl5045132.

Wang, Shengping., Lifang, Zhao., Wei, Wang., Yujun, Zhao., Guanglin, Zhang., Xinbin, Ma. & Jinlong, Gong. (2013). "Morphology control of ceria nanocrystals for catalytic conversion of CO_2 with methanol." *Nanoscale*, *5* (12), 5582-5588. doi: 10.1039/C3NR00831B.

Wang, Wanjun., Shijing, Liang., Kaining, Ding., Jinhong, Bi., Jimmy, C. Yu., Po, Keung Wong. & Ling, Wu. (2014). "Microwave hydrothermal synthesis of $MSnO_3$ (M^{2+}=Ca^{2+}, Sr^{2+}, Ba^{2+}): effect of M^{2+} on crystal structure and photocatalytic properties." *Journal of Materials Science*, *49* (4), 1893-1902. doi: 10.1007/s10853-013-7880-x.

Wang, X., Xu, H., Wang, H. & Yan, H. (2005). "Morphology-controlled $BaWO_4$ powders via a template-free precipitation technique." *J. Crys. Growth*, *284*, 254-261.

Wang, Xue., Xiguang, Han., Shuifen, Xie., Qin, Kuang., Yaqi, Jiang., Subing, Zhang., Xiaoliang, Mu., Guangxu, Chen., Zhaoxiong, Xie. & Lansun, Zheng. (2012). "Controlled Synthesis and Enhanced Catalytic and Gas-Sensing Properties of Tin Dioxide Nanoparticles with Exposed High-Energy Facets." *Chemistry – A European Journal*, *18* (8), 2283-2289. doi: 10.1002/chem.201103280.

Wang, Yanzhong., Anthony, Chesnaud., Emile, Bevillon. & Guilhem, Dezanneau. (2012). "Properties of Y-doped $BaSnO_3$ proton conductors." *Solid State Ionics*, *214*, 45-55. doi: http://dx.doi.org/ 10. 1016/j.ssi. 2012.02.045.

Wang, Zhenni., Guang, Yang., Zhaorui, Zhang., Mingshang, Jin. & Yadong, Yin. (2016). "Selectivity on Etching: Creation of High-Energy Facets on Copper Nanocrystals for CO_2 Electrochemical Reduction." *ACS Nano*, *10* (4), 4559-4564. doi: 10.1021/ acsnano.6b00602.

Whewell, William. (1847). The Philosophy of the Inductive Sciences Founded Upon their History. New York, London: Johnson Reprint Corporation.

Whiteside, Alexander., Craig, A. J. Fisher., Stephen, C. Parker. & Saiful Islam, M. (2014). "Particle shapes and surface structures of olivine $NaFePO_4$ in comparison to $LiFePO_4$." *Physical Chemistry Chemical Physics*, *16* (39), 21788-21794. doi: 10.1039/C4CP02356K.

Wu, Binghui. & Nanfeng, Zheng. (2013). "Surface and interface control of noble metal nanocrystals for catalytic and electrocatalytic applications." *Nano Today*, *8* (2), 168-197. doi: 10.1016/ j.nantod. 2013.02.006.

Wu, X., Du, J., Li, H., Zhang, M., Xi, B., Fan, H., Zhu, Y. & Qian, Y. (2007). "Aqueous mineralization process to synthesize uniform shuttle-like BaMoO4 microcrystals at room temperature." *J. Solid State Chem.*, *180*, 3288-3295.

Wulff, G. (1901). "On the question of speed of growth and dissolution of crystal surfaces." *Kristallogr. Miner*, *34*, 449-530.

Xiao, Xiaoling., Xiangfeng, Liu., Hu, Zhao., Dongfeng, Chen., Fengzhen, Liu., Junhui, Xiang., Zhongbo, Hu. & Yadong, Li. (2012). "Facile

Shape Control of Co_3O_4 and the Effect of the Crystal Plane on Electrochemical Performance." *Advanced Materials*, *24* (42), 5762-5766. doi: 10.1002/adma.201202271.

Xie, B., Wu, Y., Jiang, Y., Li, F., Wu, J., Yuan, S., Yu, W. & Qian, Y. (2002). "Shape-controlled synthesis of $BaWO_4$ crystals under different surfactants." *J. Crys. Growth*, *235*, 283-286.

Xie, Xiaowei., Yong, Li., Zhi-Quan, Liu., Masatake, Haruta. & Wenjie, Shen. (2009). "Low-temperature oxidation of CO catalysed by Co_3O_4 nanorods." *Nature*, *458* (7239), 746-749. doi: 10.1038/nature07877.

Xu, Hua., Pakpoom, Reunchan., Shuxin, Ouyang., Hua, Tong., Naoto, Umezawa., Tetsuya, Kako. & Jinhua, Ye. (2013). "Anatase TiO_2 Single Crystals Exposed with High-Reactive {111} Facets Toward Efficient H_2 Evolution." *Chemistry of Materials*, *25* (3), 405-411. doi: 10.1021/ cm303502b.

Xu, Tao., Xi, Zhou., Zhiyuan, Jiang., Qin, Kuang., Zhaoxiong, Xie. & Lansun, Zheng. (2009). "Syntheses of Nano/Submicrostructured Metal Oxides with All Polar Surfaces Exposed via a Molten Salt Route." *Crystal Growth & Design*, *9* (1), 192-196. doi: 10.1021/cg8002096.

Yang, Hua Gui., Gang, Liu., Shi, Zhang Qiao., Cheng Hua, Sun., Yong, Gang Jin., Sean, Campbell Smith., Jin, Zou., Hui, Ming Cheng. & Gao, Qing Lu. (2009). "Solvothermal Synthesis and Photoreactivity of Anatase TiO_2 Nanosheets with Dominant {001} Facets." *Journal of the American Chemical Society*, *131* (11), 4078-4083. doi: 10.1021/ ja808790p.

Yang, Hua Gui., Cheng, Hua Sun., Shi, Zhang Qiao., Jin, Zou., Gang, Liu., Sean Campbell, Smith., Hui, Ming Cheng. & Gao, Qing Lu. (2008). "Anatase TiO_2 single crystals with a large percentage of reactive facets." *Nature*, *453* (7195), 638-641. doi: 10.1038/nature06964.

Yu, Xin-Yao., Qiang-Qiang, Meng., Tao, Luo., Yong, Jia., Bai, Sun., Qun-Xiang, Li., Jin-Huai, Liu. & Xing-Jiu, Huang. (2013). "Facet-dependent electrochemical properties of Co_3O_4 nanocrystals toward heavy metal ions." *Scientific Reports*, *3*, 2886. doi: 10.1038/srep02886.http://www.nature.com/articles/srep02886#supplementary-information.

Zaera, Francisco. (2013). "Shape-Controlled Nanostructures in Heterogeneous Catalysis." *ChemSusChem*, *6*, 1797 – 1820. doi: 10. 1002/cssc.20130039810.1002/cssc.v6.10/issuetoc.

Zhang, Da., Jing, Li., Qigang, Wang. & Qingsheng, Wu. (2013). "High {001} facets dominated BiOBr lamellas: facile hydrolysis preparation and selective visible-light photocatalytic activity." *Journal of Materials Chemistry A*, *1* (30), 8622-8629. doi: 10.1039/C3TA11390F.

Zhang, Luo., Xiaoyan, Wang., Zhongju, Zhang. & Xin, Wang. (2017). "Effect of surface chemistry on morphology evolution of $LaPO_4$: Experiment and density functional theory calculations." *Computational Materials Science*, *127*, 22-28. doi: http://dx.doi.org/10.1016/ j.commatsci. 2016. 10.024.

Zheng, Zhaoke., Baibiao, Huang., Jibao, Lu., Xiaoyan, Qin., Xiaoyang, Zhang. & Ying, Dai. (2011). "Hierarchical TiO_2 Microspheres: Synergetic Effect of {001} and {101} Facets for Enhanced Photocatalytic Activity." *Chemistry - A European Journal*, *17* (52), 15032-15038. doi: 10.1002/chem.201101466.

Zhou, Kebin. & Yadong, Li. (2012). "Catalysis Based on Nanocrystals with Well-Defined Facets." *Angewandte Chemie International Edition*, *51* (3), 602-613. doi: 10.1002/anie.201102619.

Zhou, Zhi-You., Na, Tian., Jun-Tao, Li., Ian, Broadwell. & Shi-Gang, Sun. (2011). "Nanomaterials of high surface energy with exceptional properties in catalysis and energy storage." *Chemical Society Reviews*, *40* (7), 4167-4185. doi: 10.1039/C0CS00176G.

Zhu, Liangzheng., Zhipeng, Shao., Jiajiu, Ye., Xuhui, Zhang., Xu, Pan. & Songyuan, Dai. (2016). "Mesoporous $BaSnO_3$ layer based perovskite solar cells." *Chemical Communications*, *52* (5), 970-973. doi: 10.1039/ C5CC08156D.

Zhuang, Houlong., Alexander, J. Tkalych. & Emily, A. Carter. (2016). "Surface Energy as a Descriptor of Catalytic Activity." *The Journal of Physical Chemistry C*, *120* (41), 23698-23706. doi: 10.1021/ acs.jpcc. 6b09687.

Journal of Physics and Chemistry of Solids 114 (2018) 141–152

Contents lists available at ScienceDirect

Journal of Physics and Chemistry of Solids

journal homepage: www.elsevier.com/locate/jpcs

Experimental and theoretical study to explain the morphology of $CaMoO_4$ crystals

F.K.F. Oliveira [a], M.C. Oliveira [b], L. Gracia [c], R.L. Tranquilin [a], C.A. Paskocimas [a], F.V. Motta [a], E. Longo [d], J. Andres [b], M.R.D. Bomio [a,*]

[a] LSQM- Laboratorio de Síntese Química de Materiais, DEMat, Universidade Federal do Rio Grande do Norte - UFRN, P.O. Box 1524, 59078-970 Natal, RN, Brazil
[b] Departament de Química Física i Analítica, Universitat Jaume I, 12071 Castello de la Plana, Spain
[c] Department of Physical Chemistry, University of Valencia, 46100 Burjassot, Spain
[d] CDMF-UFSCar, Universidade Federal de São Carlos, P.O. Box 676, 13565-905 São Carlos, SP, Brazil

ARTICLE INFO

Keywords:
$CaMoO_4$
Microwave-assisted hydrothermal method
Morphology
Wulff construction

ABSTRACT

$CaMoO_4$ crystals were prepared by a controlled co-precipitation method and processed in a domestic microwave-assisted hydrothermal system with two different surfactants (ethyl 4-dimethylaminobenzoate and 1,2,4,5-benzenetetracarboxylic dianhydride). The corresponding structures were characterized by X-ray diffraction and Rietveld refinement techniques, Fourier transform infrared spectroscopy, ultraviolet–visible absorption spectroscopy, and photoluminescence measurements. Field emission scanning electron microscopy was used to investigate the morphology of the as-synthesized aggregates. The structure, the surface stability of the (001), (112), (100), (110), (101), and (111) surfaces of $CaMoO_4$, and their morphological transformations were investigated through systematic first-principles calculations within the density functional theory method at the B3LYP level. Analysis of the surface structures showed that the electronic properties were associated with the presence of undercoordinated $[CaO_x]$ ($x = 5$ and 6) and $[MoO_y]$ ($y = 4$ and 3) clusters. The relative surfaces energies were tuned to predict a complete map of the morphologies available through a Wulff construction approach. The results reveal that the experimental and theoretical morphologies obtained coincide when the surface energies of the (001) and (101) surfaces increase, while the surface energy of the (100) facet decreases simultaneously. The results provide a comprehensive catalog of the morphologies most likely to be present under realistic conditions, and will serve as a starting point for future studies on the surface chemistry of $CaMoO_4$ crystals.

1. Introduction

Calcium molybdate ($CaMoO_4$) belongs to the scheelite family with its $AMoO_4$ formula, where A is Ca, Sr, or Ba, and has a tetragonal structure with space group $I4_1/a$ [1,2]. This type of structure is composed of dodecahedral $[CaO_8]$ clusters and tetrahedral $[MoO_4]$ clusters connected via common vertices. In turn, $[CaO_8]$ polyhedra are connected via the edges and form a 3D framework [2–4] in which the Ca—O—Mo moiety can act as a "hinge," allowing the $[MoO_4]$ cluster more rotational freedom [5] to generate a structural disorder at the $[CaO_8]$ and $[MoO_4]$ clusters throughout the scheelite lattice [6,7].

$CaMoO_4$ (nano)crystals have received great attention, and many different preparation methods have been reported, such as solid-state reaction [8,9], citrate complex methods [10,11], a galvanic cell method [12], sol-gel methods [13,14], an ultrasound method [15], hydrothermal methods [16,17], a free surfactant sonochemical method [18], chemical deposition [19–22], precipitation [23], co-precipitation [24–27], and microwave-hydrothermal [2,11,28–33]. From the theoretical point of view, the geometry, electronic properties, and optical properties of $CaMoO_4$ have been investigated by density functional theory (DFT) methods [34–36].

In recent years, the search for the relationship between morphology and properties has attracted increasing attention to the field of material research. The performance of various crystal facets is linked to unique surface features such as local electronic structure [37], atomic termination [38], atomic population [39], coordination patterns [40], dangling

---

* Corresponding author.
E-mail address: mauricio.bomio@ct.ufrn.br (M.R.D. Bomio).

https://doi.org/10.1016/j.jpcs.2017.11.019
Received 20 June 2017; Received in revised form 22 November 2017; Accepted 24 November 2017

bonds [41], and internal electric strain [42], as well as surface energies [43]. Particularly, the activity of nanocrystals used as catalysts depends strongly on the surface structure of facets enclosing these crystals [44–49], and makes it possible to increase catalytic activity and selectivity by optimization of the structure of the catalytically active site. In addition, according to Ruditskiy et al. [50], the shape control of nanocatalysts helps to optimize the catalytic applicability and reduces the costs of the material. Therefore, changing the morphology of the as-synthesized (nano)crystals and further controlling their properties are great challenges for their application. However, the control of the final morphology and surface structure, which is a complex and difficult task, is highly dependent on the crystal internal structures, synthesis method, and external growth conditions, such as the concentration of the constituents, surfactants, additives, solvents, etc. In this study, surface energies of six different surfaces, (001), (112), (110), (101), (100), and (111), of the $CaMoO_4$ crystal were calculated with use of DFT. The predominant cleavage surfaces, the preferentially expressed crystal surfaces, and the corresponding morphologies were predicted theoretically, and these were then compared with the observations based on field emission scanning electron microscopy (FE-SEM) images.

In this work, we seek to fulfill a twofold objective. Firstly, the synthesis and characterization of $CaMoO_4$ crystals was done with and without different surfactants (ethyl 4-dimethylaminobenzoate [EDA] and 1,2,4,5-benzenetetracarboxylic dianhydride [BTD]) by a co-precipitation method and with processing in a domestic microwave-assisted hydrothermal system at 140 °C for 1, 2, 4, and 8 min. These samples were structurally characterized by X-ray diffraction (XRD), Fourier transform infrared (FT-IR) spectroscopy, FE-SEM, ultraviolet–visible (UV–vis) absorption spectroscopy, and photoluminescence (PL) measurements. Secondly, we intend to provide detailed microscopic information on the evolution of the final morphology with the surfactant used throughout the synthesis. Shape control was achieved by precise tuning of the experimental parameters, such as the presence of surfactants and time.

We believe that these results can arouse enough interest since they will contribute to broadening of the fundamental knowledge of the morphology of compounds based on $CaMoO_4$. To do so, a recent experimental and theoretical strategy was applied, based on the joint use of experimental findings and first-principles calculations at the DFT level. The Wulff construction is used to obtain the electronic, structural, and energetic properties that control the morphology and the transformation mechanism of metals, binary oxides, and complex crystals [51–54]. This strategy was recently used in $BaWO_4$ [55], $BaMoO_4$ [56], and α-$AgVO_3$ [57] crystals. In this context, Ng and Fan [58] reported a simple method to prepare uniform β-Ag_2MoO_4 crystals with well-defined shapes, which is expected to catalyze more extensive studies on the photocatalytic properties of the material.

This work follows this procedure to obtain a complete map of available morphologies for $CaMoO_4$ crystals. In addition, on the basis of these results, we are able to rationalize how the different surfaces change their energies throughout the synthesis process, and we are able to propose a path by which the experimental and theoretical morphologies of $CaMoO_4$ can match. With corrected surface energies, a straightforward understanding was provided by Wulff construction.

The rest of the article is divided into three sections. In the next section, we describe, in detail, the materials and methods for synthesizing and processing $CaMoO_4$ powders, as well as the computational method and model systems used to perform the first-principles calculations. Section 3 contains the results and discussion. The article ends with the main conclusions of our work.

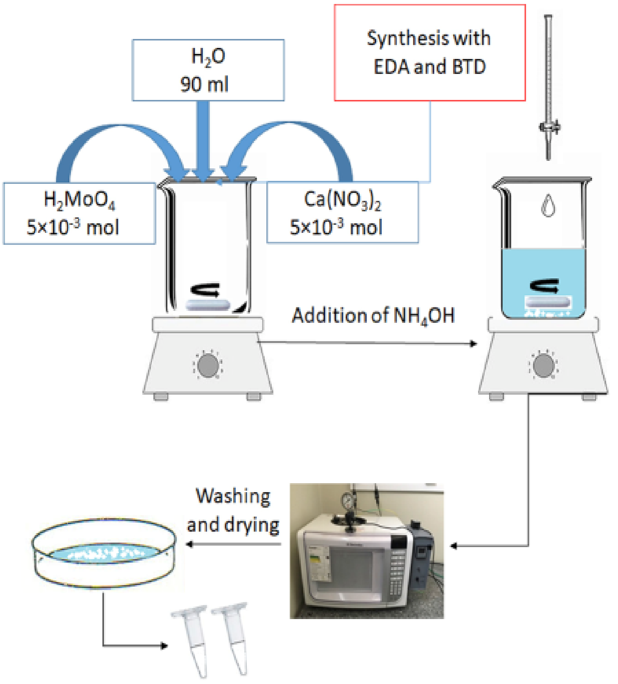

Fig. 1. The synthesis process for $CaMoO_4$ crystals. BTD, 1,2,4,5-benzenetetracarboxylic dianhydride; EDA, ethyl 4-dimethylaminobenzoate.

2. Materials and methods

2.1. Synthesis and processing of $CaMoO_4$ powders

$CaMoO_4$ powders were synthesized by a co-precipitation method in distilled water and processed in a microwave-assisted hydrothermal system for different times (1, 2, 4, and 8 min). Two different surfactants were used during the synthesis: Ethyl 4-dimethylaminobenzoate (EDA) and 1,2,4,5-benzenetetracarboxylic dianhydride (BTD). In addition, the samples were also synthesized without the surfactant, as a reference. A schematic representation of the synthesis of $CaMoO_4$ crystals is illustrated in Fig. 1.

A typical experimental procedure was as follows: 5×10^{-3} mol of molybdic acid, H_2MoO_4 (85%purity, Synth), and 5×10^{-3} mol of calcium nitrate, $Ca(NO_3)_2$ (99.5% purity, Sigma-Aldrich), were dissolved in 90 mL of water, and the mixture was stirred for 15 min. Then 5 mL of ammonium hydroxide, NH_4OH, was added to this solution until the pH reached 14 to intensify the rate of hydrolysis between Mo and Ca ions, as shown in Eqs. (1) and (2):

$$H_2MoO_{4\,(s)} + Ca(NO_3)_{2\,(s)} \xrightarrow{H_2O} 2H^+_{(aq)} + 2NO^-_{3\,(aq)} + Ca^{2+}_{(aq)} + MoO^{2-}_{4\,(aq)} \quad (1)$$

$$Ca^{2+}_{(aq)} + MoO^{2-}_{4\,(aq)} \rightarrow CaMoO_{4\,(s)} \quad (2)$$

Subsequently, processing was done with a microwave-assisted hydrothermal system (2.45 GHz, maximum power of 800 W). The solution was transferred into a Teflon autoclave and processed at 140 °C for 1, 2, 4, and 8 min. The pressure into the autoclave was stabilized at 3.4 bar. The solution obtained was washed with distilled water ten times to neutralize the solution (pH ≈ 7). Finally, the precipitates were dried at 100 °C for 24 h.

2.2. Characterizations of $CaMoO_4$ powders

$CaMoO_4$ powders were structurally characterized by XRD patterns, which were obtained with a Bruker/D2 PHASER with Cu-Kα radiation in the 2θ range from 10° to 75° at a rate of 0.02°/min. The lattice parameters a and c were calculated by adjustment of the experimental diffractogram with use of the program MAUD [56]. The average crystallite sizes and microstrain were calculated by the Williamson-Hall method [59–61].

FT-IR spectra were recorded at room temperature with a Shimadzu IRTracer-100 instrument. The morphology of the powders was observed by FE-SEM (Zeiss Auriga). UV–vis spectra were recorded with a Shimadzu UV-2600 spectrophotometer in reflectance mode. PL spectra were measured with a Thermo Jarrell Ash Monospec 27 monochromator and a Hamamatsu R446 photomultiplier. The 350.7 nm line of a krypton ion laser (Coherent Innova 90 K) was used as the excitation source, with the output power of the laser kept at 200 mW. All measurements were taken

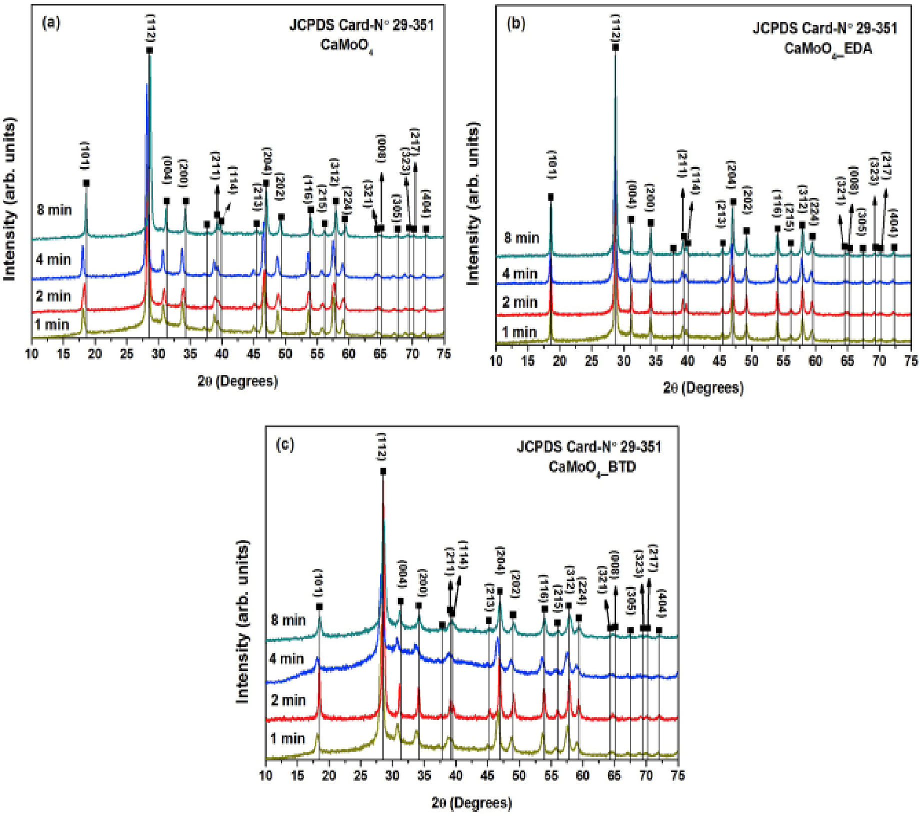

Fig. 2. X-ray diffraction patterns of $CaMoO_4$ crystals at 1, 2, 4, and 8 min: (a) $CaMoO_4$, (b) $CaMoO_4$ prepared with ethyl 4-dimethylaminobenzoate, and (c) $CaMoO_4$ prepared with 1,2,4,5-benzenetetracarboxylic dianhydride.

at room temperature.

2.3. Computational method

Theoretical procedures and computational methods involving first-principles calculations related to the $CaMoO_4$ structure were performed with the hybrid functional B3LYP and the periodic DFT framework [62,63] with use of the CRYSTAL14 software package [64].

Mo cations [65] were described by a pseudopotential basis set, while O anions [66] and Ca cations [67] were described by standard (6-31d1G) basis sets.

For bulk and surface calculations, the diagonalization of the Fock matrix was performed at adequate *k*-point grids in the reciprocal space. The thresholds controlling the accuracy of the calculation of the Coulomb and exchange integrals were set to 10^{-8} (ITOL1 to ITOL4) and 10^{-14} (ITOL5), and the percentage of mixing Fock/Kohn-Sham matrices was set to 40 (IPMIX keyword) [68].

Surface energies were determined from the equilibrium shape by a classic Wulff construction [69] that minimizes the total surface free energy at a fixed volume, providing a simple correlation between the surface energy (E_{surf}) of the (*hkl*) plane and the distance (r_{hkl}) in the normal direction from the center of the crystallite. The Wulff construction has been successfully used in materials science to obtain the morphology of materials, including $PbMoO_4$, $CaWO_4$, Ag_3PO_4, α-Ag_2MoO_4, $BaMoO_4$, $BaWO_4$, Ag_2CrO_4, and $LaVO_4$ [54,56,70–75]. The surface energy (E_{surf}) is defined as the total energy per repeating slab cell (E_{slab}) minus the total energy of the perfect crystal per molecular unit ($E_{bulk/atom}$) multiplied by the number of molecular units of the surface (N_s) and divided by the surface area per repeating cell of the two sides of the slab.

3. Results and discussion

3.1. XRD analyses

Fig. 2 show the XRD patterns obtained at different times (1, 2, 4, and 8 min) for $CaMoO_4$ powders processed in a microwave-assisted hydrothermal system at 140 °C. The XRD patterns revealed that all diffraction peaks of $CaMoO_4$ powders can be indexed to the scheelite-type tetragonal structure without the presence of secondary phases, in agreement with Joint Committee on Powder Diffraction Standards (JCPDS) card no. 29-351 [76]. Moreover, the relative intensities and sharp diffraction of all peaks indicated that the materials are well crystallized, suggesting an ordered structure at long range.

3.2. Rietveld refinement analysis

The Rietveld method is based on the construction of diffraction patterns calculated according to the structural model [77]. The Rietveld refinement was performed with MAUD [78], and the refined parameters were the lattice parameters, background, profile, half-width parameters (*u*, *v*, *w*), and crystallite size [79]. The results for all the powders were obtained by the Rietveld method with use of Crystallography Open Database entry 9009632 [80]. Table 1 shows the lattice parameters, cell volume, and positions of the atoms. An analysis of the results reveals small differences with the reported data [80]. Nevertheless, it is important to note the variations in the position of the oxygen anions (Table 2). These variations are associated with distortions of the Ca—O and/or Mo—O bond lengths, and consequently with different levels of distortion of the $[CaO_8]$ and/or $[MoO_4]$ clusters in the lattice.

Table 1
Rietveld refinement and Williamson-Hall data for the as-synthesized $CaMoO_4$ crystals.

Sample	*t* (min)	*a* (Å)	*c* (Å)	*V* (Å^3)	D_{hkl} (nm)	ε_{hkl}
$CaMoO_4$	1	5.235	11.458	314.05	46	0.003
	2	5.220	11.428	311.42	41	0.003
	4	5.233	11.451	313.56	30	0.002
	8	5.225	11.437	312.25	34	0.003
$CaMoO_4$ (EDA)	1	5.234	11.454	313.71	40	0.003
	2	5.235	11.456	313.94	43	0.002
	4	5.235	11.457	313.98	36	0.003
	8	5.234	11.453	313.75	66	0.004
$CaMoO_4$ (BTD)	1	5.225	11.432	312.11	27	0.003
	2	5.237	11.459	314.22	34	0.002
	4	5.227	11.433	312.52	30	0.004
	8	5.236	11.458	314.16	43	0.006
COD entry	9009632	5.222	11.425	314.16	–	–

t is the synthesis time, *a* and *c* are lattice parameters, *V* is the unit cell volume, D_{hkl} is the average crystallite size, and ε_{hkl} is the microstrain.
BTD, 1,2,4,5-benzenetetracarboxylic dianhydride; COD, Crystallography Open Database; EDA, ethyl 4-dimethylaminobenzoate.

The $CaMoO_4$ microstrain (ε_{hkl}) and crystallite sizes (D_{hkl}) were analyzed by the Williamson-Hall method. It is represented by Eq. (3):

$$\frac{\beta_{hkl}\cos\theta}{\lambda} = \frac{1}{D_{hkl}} + \frac{(\varepsilon_{hkl})\varepsilon\sin\theta}{\lambda} \tag{3}$$

where β_{hkl} is the full width at half maxima (FWHM) of XRD patterns, θ is the diffraction angle, λ is the wavelength of the X-Rays, D_{hkl} is the average crystallite size, and ε_{hkl} is the micro-strain.

Table 1 and Fig. S1, Fig.S2, and Fig.S3 show the results for crystallite size and microstrain for pure $CaMoO_4$, $CaMoO_4$ prepared with EDA ($CaMoO_4$_EDA), and $CaMoO_4$ prepared with BTD ($CaMoO_4$_BTD) obtained at different processing times of 1, 2, 4, and 8 min in the microwave-assisted hydrothermal system at 140 °C. For $CaMoO_4$ samples, a large difference in crystallite size and microstrain was not observed. For $CaMoO_4$_EAD processed at 140 °C for 8 min, the crystallite size and microstrain increase, probably due to distortion in the crystalline lattice promoted by the surfactant EDA. For $CaMoO_4$_BTD processed at 140 °C for 1 and 2 min, we can conclude that the surfactant BTD acts as a

Table 2
Atomic coordinates for $CaMoO_4$ crystalline structures.

Sample	*t* (min)	Atom	*x*	*y*	*z*
$CaMoO_4$	1	Ca	0	0.25	0.625
		Mo	0	0.25	0.125
		O	0.1553	−0.00767	0.208195
	2	Ca	0	0.25	0.625
		Mo	0	0.25	0.125
		O	0.149	0.0069	0.2089
	4	Ca	0	0.25	0.625
		Mo	0	0.25	0.125
		O	0.1569	−0.03105	0.206959
	8	Ca	0	0.25	0.625
		Mo	0	0.25	0.125
		O	0.15834	−0.04248	0.21528
$CaMoO_4$ (EDA)	1	Ca	0	0.25	0.625
		Mo	0	0.25	0.125
		O	0.15561	−0.01478	0.20835
	2	Ca	0	0.25	0.625
		Mo	0	0.25	0.125
		O	0.15246	−0.00021	0.20929
	4	Ca	0	0.25	0.625
		Mo	0	0.25	0.125
		O	0.15403	−0.0172	0.20952
	8	Ca	0	0.25	0.625
		Mo	0	0.25	0.125
		O	0.15309	−0.00562	0.20944
$CaMoO_4$ (BTD)	1	Ca	0	0.25	0.625
		Mo	0	0.25	0.125
		O	0.14878	−0.05927	0.206735
	2	Ca	0	0.25	0.625
		Mo	0	0.25	0.125
		O	0.15667	−0.00845	0.20904
	4	Ca	0	0.25	0.625
		Mo	0	0.25	0.125
		O	0.17313	−0.04003	0.214182
	8	Ca	0	0.25	0.625
		Mo	0	0.25	0.125
		O	0.15335	−0.02341	0.204194

BTD, 1,2,4,5-benzenetetracarboxylic dianhydride; EDA, ethyl 4-dimethylaminobenzoate.

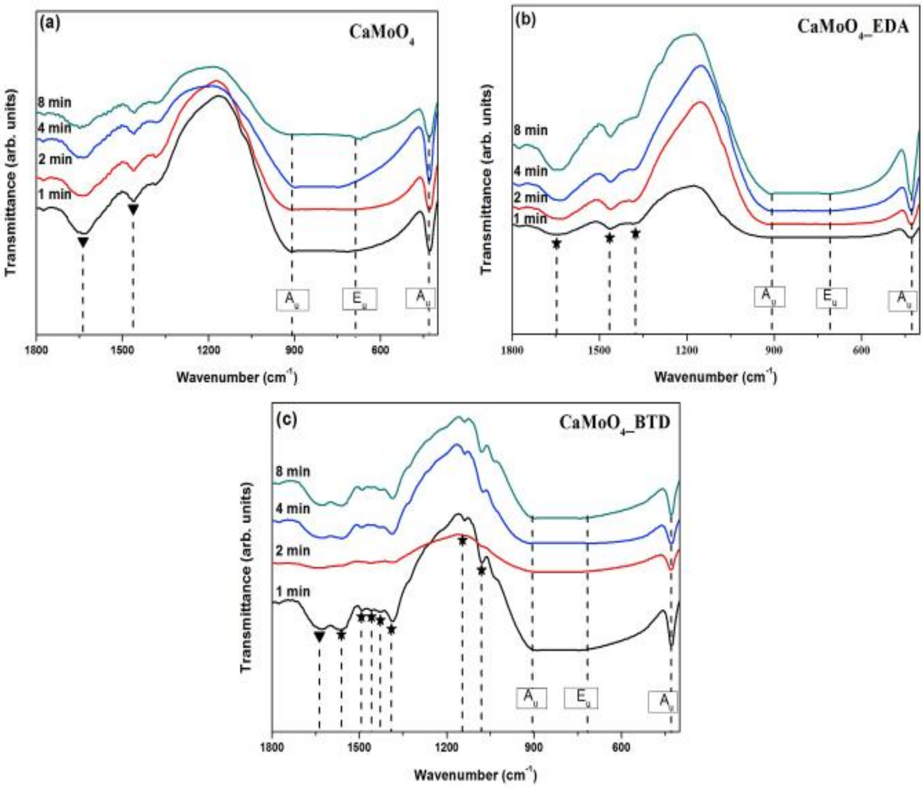

Fig. 3. Fourier transform infrared patterns of $CaMoO_4$ crystals at 1, 2, 4, and 8 min: (a) $CaMoO_4$, (b) $CaMoO_4$ prepared with ethyl 4-dimethylaminobenzoate ($CaMoO_4$_EDA), and (c) $CaMoO_4$ prepared with 1,2,4,5-benzenetetracarboxylic dianhydride ($CaMoO_4$_BTD).

Table 3
Experimental and theoretical results for Raman-active and infrared-active modes (cm^{-1}) of $CaMoO_4$.

Raman Experimental												
B_g	Eg	Eg	Ag	Bg	Eg	Ag	Bg	B_g	E_g	Eg	B_g	A_g
–	–	–	205	–	263	333	339	393	401	797	844	878 [78]
110	145	189	205	219	263	333	339	393	401	797	844	878 [80]
112	143	190	205	214	267	322	328	391	402	792	845	877 [81]
111.5	143	189.5	204.5	214	267	321.5	327.5	391	402.5	792	845.5	877 [83]
111	145	189	205	–	267	323	–	391	402	793	847	878 [82]
Theoretical												
116.8	159.8	196.6	226.5	231.7	303.6	337.3	346.3	432.5	441	819.5	864.5	896[a]

Infrared							
Experimental							
E_u	Au	Eu	Au	Eu	Au	Au	Eu
–	–	–	–	–	430	–	820 [79]
–	–	–	–	405	430	–	827 [7]
–	–	240	280	330	428	790	878 [1]
–	–	–	–	–	411–423	720–970 [26]	
–	–	–	–	–	423	743–895 [32]	
–	–	–	–	–	430	790–900[a]	
Theoretical							
158.8	195.3	209.1	250.7	327.5	470.7	785.3	808.7[a]

[a] Present work.

growth control agent because of the smaller crystallites than for pure $CaMoO_4$. On the other hand, for $CaMoO_4$_BTD processed at 140 °C for 4 and 8 min, BTD enhances the lattice distortion parameter *c*.

3.3. FT-IR analysis

The scheelite-type tetragonal structure exhibits 26 different vibration modes: ($\Gamma = 3A_g + 5A_u + 5B_g + 3B_u + 5E_g + 5E_u$), but eight of them ($4A_u$ and $4E_u$) are active in the infrared, while the other 13 modes (A_g, B_g, and E_g) are Raman active [81].

Fig. 3 shows the FT-IR spectra of the $CaMoO_4$ crystals in the range from 1800 to 400 cm^{-1}. Three types of vibration modes are seen ($1E_u$ and $2A_u$), while the other vibration modes are not identified because they are located in the lower region (400–100 cm^{-1}). An analysis of the results reveals the presence of an intense absorption band, around 660–910 cm^{-1}, corresponding to E_u and A_u modes that are associated with the antisymmetric stretch of the tetrahedral [MoO_4] clusters. At 432 cm^{-1}, a less intense A_u mode, corresponding to antisymmetric vibrations of the O—Mo—O angles, is observed. However, in FT-IR analysis it is possible to perceive some differences in the simple $CaMoO_4$. In Fig. 3(a), the peaks between 1630 and 1450 cm^{-1} are attributed to the presence of CO_2 in the atmosphere [1], while in Fig. 3(b), the peak around 1357 cm^{-1} is assigned to the presence of a tertiary amine organic group resulting from EDA. In Fig. 3(c), in the region from 1380 to 560 cm^{-1}, the vibration corresponding to the out-of-plane bending of CH_2 is observed, while the wide band between 1134 and 1070 cm^{-1} is associated with the presence of anhydride [C—C(=O)—O—C(=O)—C] groups from BTD. At 1650 cm^{-1}, a band associated with the O—H bond of the water molecule was identified [82], while at 1450 cm^{-1}, a band corresponding to C—O bonds was identified [1,2].

The theoretical and experimental frequencies for the infrared and Raman spectra are shown in Table 3, and the comparison and analysis of the results shows they are agreement with the results previously reported in the literature [1,2,26,32,81–86].

Theoretical analysis predicts that seven of these modes ($2A_g + 3B_g + 2E_g$) are internal motions of tetrahedral [MoO_4] clusters and octahedral [CaO_8] clusters, while the other six ($1A_g + 2B_g + 3E_g$) are external pure lattice modes of the [MoO_4] tetrahedra (translational and rotational motions between ions in the lattice) [87]. In principle, there is a strong interaction between the O—Ca—O and O—Mo—O moieties of adjacent clusters, which are structurally ordered at short range; and intense and sharp bands are exhibited at low intensities as observed at 116.8 cm^{-1} (B_g) and 159.8 and 196.6 cm^{-1} (E_g). Internal motions of MoO_4 tetrahedra such as symmetric bending at 441.0 cm^{-1} (E_g) and 432.5 cm^{-1} (B_g) or antisymmetric bending at 346.3 cm^{-1} (B_g), 337.3 cm^{-1} (A_g), 303.6 cm^{-1} (E_g), and 231.7 cm^{-1} (B_g) can be observed. However, strong intense bands at 896.0, 864.5, and 819.5 cm^{-1} are attributed to internal/optical modes A_g, B_g, and E_g, respectively. The A_g mode was observed at 896.0 cm^{-1} and was assigned to symmetric stretching vibrations of [MoO_4] clusters, and the B_g and E_g modes at 864.5 and 819.5 cm^{-1} were assigned to antisymmetric stretching vibrations of the O—Mo—O moieties (Fig. 4).

3.4. UV–vis analysis

The optical band gap energy (E_{gap}) was calculated by the method proposed by Wood and Tauc [88]. The band gap energy for all $CaMoO_4$ particles synthesized at 140 °C for different times, with and without surfactants, was calculated, and the values are listed in Table 4 and Fig. S4, Fig.S5, and Fig.S6.

Roca et al. [89]. describe that the exponential optical absorption profile and E_{gap} are controlled by the degree of structural order-disorder in the lattice. In our study, the UV–vis spectra evidenced changes of band gap energies with the increase of the heating time. The results agree with those reported in the literature [1,2] regarding the presence of intermediary energy levels between the valence band and the conduction band [72,85,90]. The formation of this intermediate energy level inside the band gap can be described by the degree of order and disorder of the crystalline structure [90]. Therefore, as can be seen in Tables 1 and 4, the increase in structural disorder and the volume of $CaMoO_4$ synthesized in presence of EDA promotes a wide intermediate level compared with the pure $CaMoO_4$ and $CaMoO_4$_BTD, having as a consequence a reduction in the band gap energy.

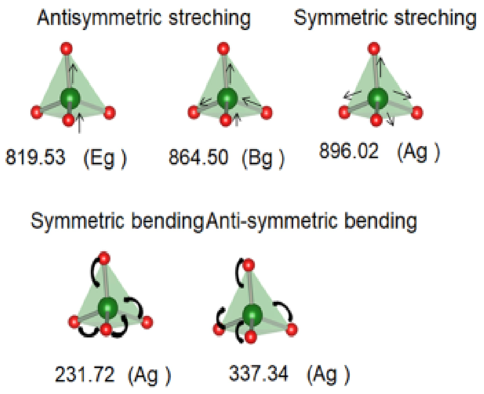

Fig. 4. Theoretical Raman-active modes of $CaMoO_4$.

3.5. Representations of the unit cell, surfaces, and cluster coordination

Fig. 5 shows a schematic representation of the tetragonal structure (space group $I4_1/a$) of the $CaMoO_4$ unit cell with atomic positions and lattice parameters obtained from the Rietveld refinement data (Tables 1 and 2) in which different clusters are depicted; that is, the local coordination of Ca and Mo atoms for the bulk (Fig. 5) and surfaces (Fig. 6).

In the bulk, Mo cations are coordinated by four oxygens, yielding [MoO_4] clusters with a tetrahedral configuration. These clusters are distorted because of the displaced positions of the O ions, yielding a variation in the O—Mo—O angles of the ideal tetrahedral configuration.

The (001), (112), (100), (110), (101), and (111) surfaces of $CaMoO_4$ were modeled by an unreconstructed slab model using an optimized equilibrium geometry. All surfaces are exposed to a vacuum by the Mo and O ions, while the Ca and O ions are the exposed centers on the (111) surface. In addition to the atomic configuration of the exposed facets, the coordination environment has a large effect on the stabilization of the surfaces. Since the bonding interaction of a Mo—O bond is stronger than that of a Ca—O bond, the stability of the (111) surface is reduced

Table 4
Optical band gap energy for $CaMoO_4$ without and with the surfactants ethyl 4-dimethylaminobenzoate (EDA) and 1,2,4,5-benzenetetracarboxylic dianhydride (BTD).

Samples	*t* (min)	E_{gap} (eV)
$CaMoO_4$	1	3.71
	2	3.71
	4	3.74
	8	3.75
$CaMoO_4$ (EDA)	1	3.51
	2	3.65
	4	3.66
	8	3.25
$CaMoO_4$ (BTD)	1	3.66
	2	3.71
	4	3.66
	8	3.68

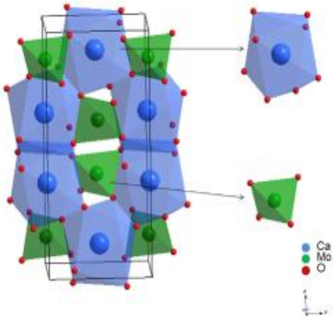

Fig. 5. The bulk structure of $CaMoO_4$, showing $[CaO_8]$ and $[MoO_4]$ clusters as building blocks of the material.

compared with that of the rest of the surfaces because of the presence of two oxygen vacancies; that is, under coordination at the $[MoO_2]$ cluster. Only the (112) surface presents $[CaO_5]$ clusters, implying a breaking of a Ca—O bond compared with the bulk.

The local coordination of the superficial Ca and Mo cations and the distance to the closer O ions are shown in Fig. 6.

3.6. Morphology study

Table 5 lists the surface energies, area, and relaxation energy during the optimization process for each surface. According to the DFT calculations, the stability of the surfaces is in the order (001)>(112)>(110)>(101)>(100)>(111).

Table 5
E_{surf}, area, and relaxation energy during the optimization process.

Surface	E_{surf} (J/m^2)	A (Å^2)	Relaxation energy (%)
(001)	0.72	27.385	14
(112)	0.75	50.054	70
(110)	0.93	41.898	70
(101)	1.01	32.637	74
(100)	1.15	59.253	43
(111)	4.56	88.157	1

These results can be explained in terms of local order (at short distance), taking into account the vacancies of the O ions in the superficial Mo ($[MoO_4]$ and $[MoO_2]$) and Ca ($[CaO_6]$ and $[CaO_5]$) clusters. This information was used to map the available morphologies of $CaMoO_4$, assuming different values for the surface energy of different facets, and then the transformations between the different morphologies were associated with the relative surface energy of each surface. Fig. 7 illustrates the good agreement between the experimental FE-SEM images and the theoretical morphologies.

By modulating the relationship between the surface stabilities of the different faces, we obtained Fig. 7, which can be used to obtain correlations with the experimental results. This map displays the available morphologies of $CaMoO_4$ crystals resulting from a change in the relative stability of the facets. We started with the ideal morphology, and when the surface energies of the (001) and (101) surfaces increased, shape A was obtained (bottom of Fig. 7). When the surface energy of the (101) surface decreased, with simultaneous increase of the surface energy of (112) surfaces, shape B was obtained (top of Fig. 7). Other possibilities were observed when the surface energy of the (101) facet decreases and that of the (112) surface increases (middle of Fig. 7). Experimentally, EDA was determinant, because an interaction occurred on the structure, allowing two types of facets to be exposed in the resulting morphology. The experimental morphology was simulated by means of two paths: the first from shape A to shape A1, increasing the surface energy of the (001) surface to 1.37 J/m^2 and decreasing the corresponding value of the (100)

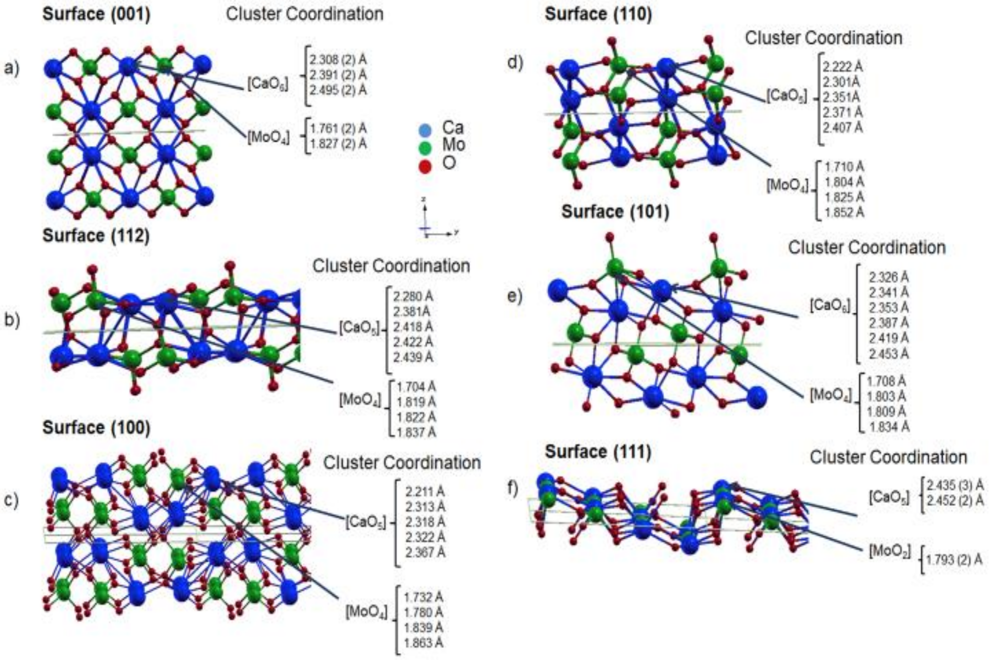

Fig. 6. The surfaces and Ca—O and Mo—O bond distances of the exposed atoms: (a) (001), (b) (112), (c) (100), (d) (110), (e) (101), and (f) (111).

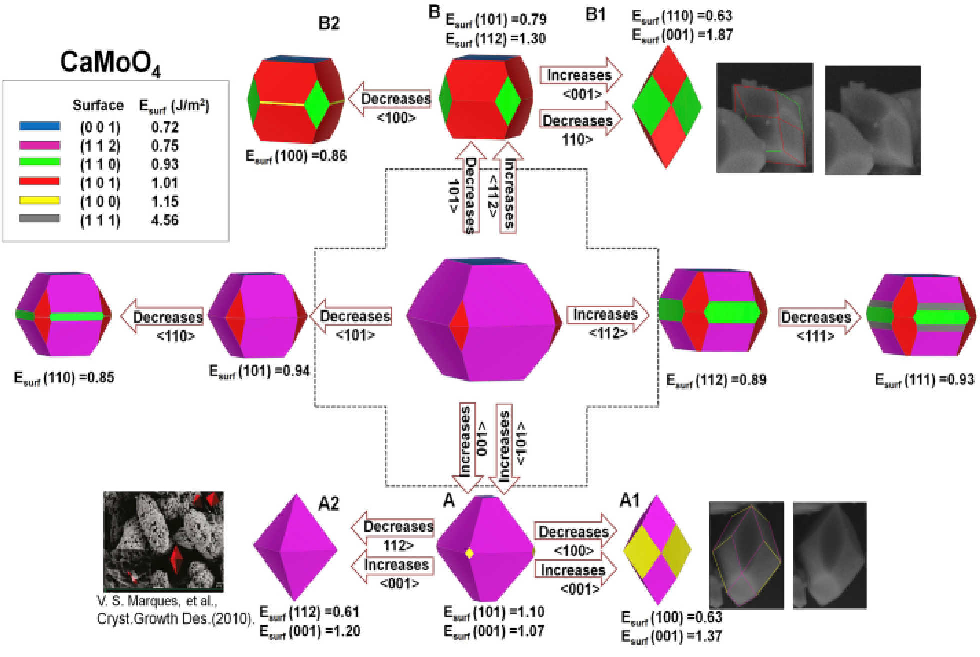

Fig. 7. Map of morphologies of $CaMoO_4$ with crystal planes (001), (112), (110), (101), (100), and (111).

surface to 0.63 J/m^2. The second path was obtained from shape B to shape B1, increasing the surface energy of the (001) surface to 1.87 J/m^2 and decreasing the corresponding value of the (110) surface to 0.63 J/m^2. The A2 morphology generated is similar to that synthesized by Ghaed-Amini et al. [91] and Marques et al. [2].

Therefore, the theoretical morphologies can be controlled by the different surface energies, and it is well known that morphologies can undergo changes because of differences in the environment in which they are synthesized. These differences may include the presence of surfactants and impurities, and differences in solvents, temperature, and synthetic routes.

3.7. Band structure and density of states

The computed band structure and total density of states (DOS) projected onto the atoms and orbitals of the $CaMoO_4$ structures, surfaces, and bulk are shown in Fig. 8.

An analysis of the DOS indicates that the upper part of the valence band consists mainly of O orbitals($2p_x$, $2p_y$ and $2p_z$) and lesser contributions of Ca and Mo orbitals. The lower part of the conduction band is derived mostly from Mo 4 d orbitals ($4d_z^2$, $4d_{x-y}^{22}$, $4d_{xy}$, $4d_{xz}$, $4d_{yz}$). The direct band gap energy of 4.92 eV (from Γ to Γ) is obtained for the bulk. An analysis of the projected DOS reveals that the top of the valance band is produced by a major contribution of the O $2p_z$ and $2p_z$ states, and the top of the conduction is due to Mo $4d_z^2$ states and minor contribution of $4d_{x-y}^{22}$ states (see Fig. 8(h)).

Calculations yielded a direct band gap energy for the (001), (112), (110), (101), and (100) surfaces very similar to that in the bulk crystal, with variations of 0.1–0.3 eV depending on the specific surface. However, the (111) surface has a conducting character, indicating a certain instability, possibly due to the breaking of coordination in $[MoO_4]$ clusters with two vacancies.

3.8. PL analysis

The PL spectra of the $CaMoO_4$ as-synthesized powders with and without surfactants, (EDA and BTD) are shown in Fig. 9.

Broad emission bands associated with a multilevel process (i.e., involving the participation of numerous states within the band gap of the material [28]) can be observed.

Through the deconvolution of the PL spectra of pure $CaMoO_4$, $CaMoO_4$_EDA, and $CaMoO_4$_BTD (Fig. 9), it was possible to discovery three curves centered at 459 nm (blue), 529 nm (green), and 610 nm (orange), which covered all the visible electromagnetic spectrum. These results show the same behavior of PL for pure $CaMoO_4$ and $CaMoO_4$_EDA samples. On the other hand, $CaMoO_4$_BTD samples reveal an elevated percentage of the blue area, indicating a higher concentration of shallow defects than in pure $CaMoO_4$ and $CaMoO_4$_EDA samples, which favors equally the blue and green areas.

The blueshift in the PL is related to the changes in the morphology of the $CaMoO_4$ particles, from peanut-like for pure $CaMoO_4$ to spheres for $CaMoO_4$_EDA and dumbbell-like and flower-like for $CaMoO_4$_BTD (Fig. S7) and theoretical models (Fig. 7). However, other factors may also be involved in the PL, such as particle aggregation and differences in the size. On the other hand, we believe that the blueshift in $CaMoO_4$_BTD samples may be related to a preferential growth of the A1 structure described on the map of morphologies (Fig. 7), consequently promoting a higher concentration of shallow defects. Hence, the morphology and the PL in this study varied significantly with the heat treatment time, morphology, and surfactant used during the synthesis.

4. Conclusions

In summary, we have developed a morphology-controlled synthesis of $CaMoO_4$ crystals by means of a simple co-precipitation method and with

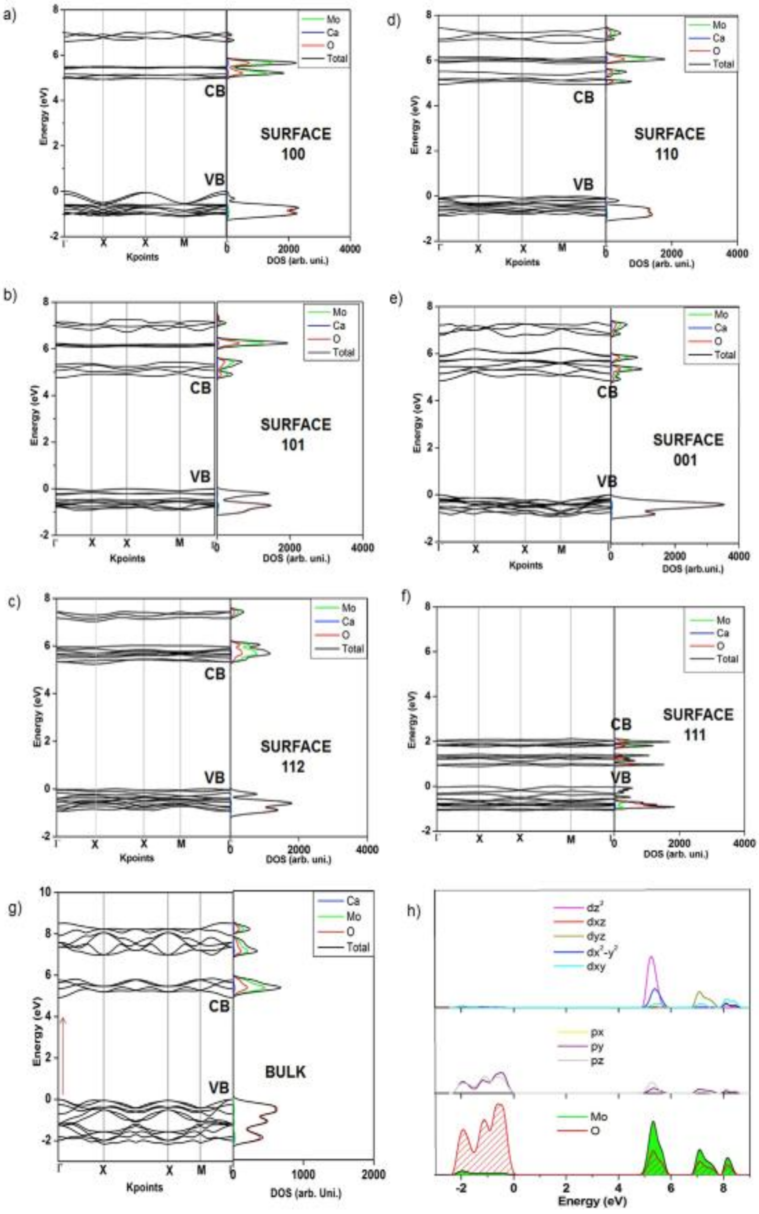

Fig. 8. Theoretical band structure and projected density of states (DOS): (a) the (100) surface, (b) the (101) surface, (c) the (112) surface, (d) the (110) surface, (e) the (001) surface, (f) the (111) surface, (g) bulk projected on atoms, and (h) bulk projected on orbitals.

processing in a domestic microwave-assisted hydrothermal system with and without use of different surfactants (EDA and BTD). The as-synthesized samples were characterized by XRD and Rietveld refinement techniques, FT-IR spectroscopy, UV–vis absorption spectroscopy, and PL measurements, while FE-SEM was used to investigate the morphology of the crystals. The effects of reaction conditions, including the presence of surfactant and reaction time, on the properties and morphology of $CaMoO_4$ were investigated systematically.

The available morphologies of $CaMoO_4$ comprise a complete array of polyhedral geometries that are achieved by modulation of the surface energies by use of a Wulff construction, and they can be fine-tuned to find the path to link the experimental morphologies (obtained by FE-SEM)

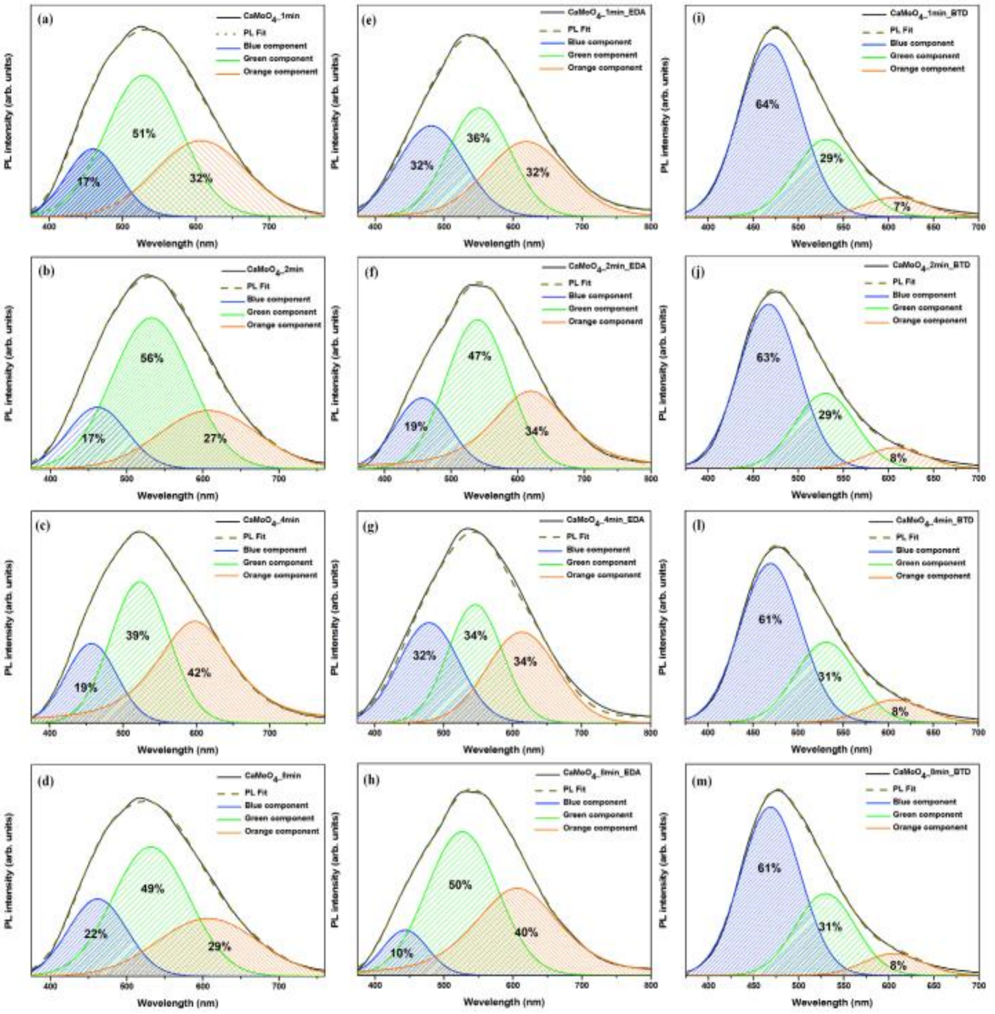

Fig. 9. Photoluminescence (PL) spectra patterns of $CaMoO_4$ microcrystals synthesized by the microwave-assisted hydrothermal method at 140 °C: (a) $CaMoO_4$ 1 min, (b) $CaMoO_4$ 2 min (c) $CaMoO_4$ 4 min, (d) $CaMoO_4$ 8 min, (e) $CaMoO_4$ prepared with ethyl 4-dimethylaminobenzoate ($CaMoO_4$_EAD) 1 min, (f) $CaMoO_4$_EAD 2 min (g) $CaMoO_4$_EAD 4 min, (h) $CaMoO_4$_EAD 8 min, (i) $CaMoO_4$ prepared with 1,2,4,5-benzenetetracarboxylic dianhydride ($CaMoO_4$_BTD) 1 min, (j) $CaMoO_4$_BTD 2 min, (l) $CaMoO_4$_BTD 4 min, and (m) $CaMoO_4$_BTD 8 min.

and theoretical morphologies. The surface energies for six different surfaces, (001), (112), (100), (110), (101), and (111), of the $CaMoO_4$ crystal were calculated with use of DFT. On the basis of the calculation results, the predominantly exposed surfaces in the morphologies of $CaMoO_4$ crystals and their morphological transformations were predicted. By tuning the surface energies, we obtained a complete map of the morphologies available for $CaMoO_4$, which enabled us to identify where the observed morphology from the FE-SEM images was located on this map. The experimental and theoretical morphologies obtained coincide when the surface energy of the (001) surface decreases and the surface energies of the (100) and (101) surfaces simultaneously increase. The present work is expected to catalyze more extensive studies on the different properties of this material. In particular, with the changes of experimental parameters that can be used for tuning the morphology of $CaMoO_4$ crystals, we anticipate that $CaMoO_4$ crystals with other exotic shapes will be unraveled in time. It is also likely that the concepts identified in this work can be extrapolated to the shape-controlled preparation of other related materials.

Acknowledgments

The authors thank the following Brazilian research financing institutions for financial support: National Council for Scientific and Technological Development - CNPq (Processo 402127/2013-7), São Paulo Research Foundation - FAPESP (Processo 2013/07296-2), Programa de Pos-Graduação em Ciência e Engenharia de Materiais (PPGCEM-UFRN), Generalitat Valenciana (PrometeoII/2014/022, ACOMP/2014/270, and ACOMP/2015/1202), Ministerio de Economía y

Competitividad, Spain (project CTQ2015-65207-P), and Programa de Cooperacion Científica con Iberoamerica (Brazil) of the Ministerio de Educacion, Spain (PHBP14-00020). J.A. acknowledges the Ministerio de Economia y Competitividad, "Salvador Madariaga" program, PRX15/00261. M.C.O acknowledges the Generalitat Valencia for the Santiago Grisolia program 2015/033.

Appendix A. Supplementary data

Supplementary data related to this article can be found at https://doi.org/10.1016/j.jpcs.2017.11.019.

References

[1] G. Botelho, I. Nogueira, E. Moraes, E. Longo, Study of structural and optical properties of $CaMoO_4$ nanoparticles synthesized by the microwave-assisted solvothermal method, Mater. Chem. Phys. 183 (2016) 110–120.

[2] V. Marques, L. Cavalcante, J. Sczancoski, A. Alcântara, M.O. Orlandi, E. Moraes, E. Longo, J.A. Varela, M. Siu Li, M. Santos, Effect of different solvent ratios (water/ethylene glycol) on the growth process of $CaMoO_4$ crystals and their optical properties, Cryst. Growth Des. 10 (2010) 4752–4768.

[3] A.K. Parchur, A.I. Prasad, A.A. Ansari, S.B. Rai, R.S. Ningthoujam, Luminescence properties of Tb3+-doped $CaMoO_4$ nanoparticles: annealing effect, polar medium dispersible, polymer film and core-shell formation, Dalton Trans. 41 (2012) 11032–11045.

[4] A.K. Parchur, R.S. Ningthoujam, Preparation and structure refinement of Eu3+ doped $CaMoO_4$ nanoparticles, Dalton Trans. 40 (2011) 7590–7594.

[5] W. Miller, C.W. Smith, D.S. Mackenzie, K.E. Evans, Negative thermal expansion: a review, J. Mater. Sci. 44 (2009) 5441–5451.

[6] F.A. Rabuffetti, S.P. Culver, L. Suescun, R.L. Brutchey, Structural disorder in $AMoO_4$ (A = Ca, Sr, Ba) scheelite nanocrystals, Inorg. Chem. 53 (2014) 1056–1061.

[7] S.P. Culver, R.L. Brutchey, Thermally activated rotational disorder in $CaMoO_4$ nanocrystals, CrystEngComm 18 (2016) 4485–4488.

[8] D. Gao, Y. Li, X. Lai, Y. Wei, J. Bi, Y. Li, M. Liu, Fabrication and luminescence properties of Dy^{3+} doped $CaMoO_4$ powders, Mater. Chem. Phys. 126 (2011) 391–397.

[9] J. Brübach, T. Kissel, M. Frotscher, M. Euler, B. Albert, A. Dreizler, A survey of phosphors novel for thermography, J. Lumin. 131 (2011) 559–564.

[10] J.H. Chung, S.Y. Lee, K.B. Shim, S.-Y. Kweon, S.-C. Ur, J.H. Ryu, Blue upconversion luminescence of $CaMoO_4:Li^{+}/Yb^{3+}/Tm^{3+}$ phosphors prepared by complex citrate method, Appl. Phys. A 108 (2012) 369–373.

[11] J.H. Ryu, J.-W. Yoon, C.S. Lim, W.-C. Oh, K.B. Shim, Microwave-assisted synthesis of $CaMoO_4$ nano-powders by a citrate complex method and its photoluminescence property, J. Alloys Compd. 390 (2005) 245–249.

[12] D. Gao, X. Lai, C. Cui, P. Cheng, J. Bi, D. Lin, Oxidant-assisted preparation of $CaMoO_4$ thin film using an irreversible galvanic cell method, Thin Solid Films 518 (2010) 3151–3155.

[13] G. Li, Z. Wang, Z. Quan, C. Li, J. Lin, Growth of highly crystalline $CaMoO_4:Tb^{3+}$ phosphor layers on spherical SiO_2 particles via sol-gel process: structural characterization and luminescent properties, Cryst. Growth Des. 7 (2007) 1797–1802.

[14] H. Wu, Y. Hu, W. Zhang, F. Kang, N. Li, G. Ju, Sol–gel synthesis of Eu3+ incorporated $CaMoO_4$: the enhanced luminescence performance, J. Sol-Gel Sci. Technol. 62 (2012) 227–233.

[15] Y. Zhang, L. Wang, D. Chu, H. Sun, A. Wang, Z. Ma, L. Yang, Y. Zhuang, Y. Bai, Fabrication of coupled twin-shaped hollow hemispherical calcium molybdate via a facile ultrasound-assisted approach, CrystEngComm 17 (2015) 2444–2449.

[16] S. Dutta, S. Som, S. Sharma, Luminescence and photometric characterization of K^{+} compensated $CaMoO_4:Dy^{3+}$ nanophosphors, Dalton Trans. 42 (2013) 9654–9661.

[17] Y.-S. Luo, X.-J. Dai, W.-D. Zhang, Y. Yang, C.Q. Sun, S.-Y. Fu, Controllable synthesis and luminescent properties of novel erythrocyte-like $CaMoO_4$ hierarchical nanostructures via a simple surfactant-free hydrothermal route, Dalton Trans. 39 (2010) 2226–2231.

[18] S.S. Hosseinpour-Mashkani, S.S. Hosseinpour-Mashkani, A. Sobhani-Nasab, Synthesis and characterization of rod-like $CaMoO_4$ nanostructure via free surfactant sonochemical route and its photocatalytic application, J. Mater. Sci. Mater. Electron. 27 (2016) 4351–4355.

[19] J. Liu, X. Huang, Y. Li, Z. Li, A general route to thickness-tunable multilayered sheets of sheelite-type metal molybdate and their self-assembled films, J. Mater. Chem. 17 (2007) 2754–2758.

[20] X. Choa, W. Ling, L. Hao, Z. Ding-Bing, Y. Tao-Kai, $CaMoO_4$ Hollow microspheres: ionic liquid-assisted synthesis and optical properties, Chin. J. Inorg. Chem. 23 (2007) 1941–1946.

[21] C. Xu, D. Zou, H. Guo, F. Jie, T. Ying, Luminescence properties of hierarchical $CaMoO_4$ microspheres derived by ionic liquid-assisted process, J. Lumin. 129 (2009) 474–477.

[22] P. Yu, G.-B. Hu, Y.-F. Tian, D.-Q. Xiao, Y. Liu, Q.-W. Guo, Synthesis and photoluminescent properties of nanocrystalline $CaMoO_4$ thin film via chemical solution processing, J. Nanosci. Nanotechnol. 8 (2008) 2651–2654.

[23] M. Laguna, N.O. Nunez, A.I. Becerro, M. Ocana, Morphology control of uniform $CaMoO_4$ microarchitectures and development of white light emitting phosphors by Ln doping (Ln = Dy^{3+}, Eu^{3+}), CrystEngComm 19 (2017) 1590–1600.

[24] Y.L. Yang, X.M. Li, W.L. Feng, W.L. Li, C.Y. Tao, Synthesis and characteristic of $CaMoO_4$: Eu^{3+} red phosphor for W-LED by co-precipitation, J. Inorg. Mater. 25 (2010) 1015.

[25] Y. Yang, X. Li, W. Feng, W. Yang, W. Li, C. Tao, Effect of surfactants on morphology and luminescent properties of $CaMoO_4:Eu^{3+}$ red phosphors, J. Alloys Compd. 509 (2011) 845–848.

[26] T. Thongtem, S. Kungwankunakorn, B. Kuntalue, A. Phuruangrat, S. Thongtem, Luminescence and absorbance of highly crystalline $CaMoO_4$, $SrMoO_4$, $CaWO_4$ and $SrWO_4$ nanoparticles synthesized by co-precipitation method at room temperature, J. Alloys Compd. 506 (2010) 475–481.

[27] Y. Xiang, J. Song, G. Hu, Y. Liu, Synthesis of $CaMoO_4$ hierarchical structures via a simple slow-release co-precipitation method, Appl. Surf. Sci. 349 (2015) 374–379.

[28] V.M. Longo, L.S. Cavalcante, E.C. Paris, J.C. Sczancoski, P.S. Pizani, M.S. Li, J. Andres, E. Longo, J.A. Varela, Hierarchical assembly of $CaMoO_4$ nano-octahedrons and their photoluminescence properties, J. Phys. Chem. C 115 (2011) 5207–5219.

[29] L. Wang, Y. Sun, C. Li, Y. Wang, X. Ma, Y. Wang, S. Li, Z. Zhang, P. Ma, G. Cui, Morphology-controlled $CaMoO_4$ nanorods via a facile microwave-assisted EDTA chelating agent process, Cryst. Res. Technol. 47 (2012) 1231–1236.

[30] Y. Sun, C. Li, Z. Zhang, X. Ma, L. Wang, Y. Wang, M. Song, P. Ma, L. Jiang, Y. Guo, Persimmon-like $CaMoO_4$ micro/nanomaterials: a rapid microwave-assisted fabrication, characterization, and the growth mechanism, Solid State Sci. 14 (2012) 219–224.

[31] A. Phuruangrat, T. Thongtem, S. Thongtem, Synthesis of nanocrystalline metal molybdates using cyclic microwave radiation, Mater. Sci. Pol. 28 (2010) 557–563.

[32] A. Phuruangrat, T. Thongtem, S. Thongtem, Preparation, characterization and photoluminescence of nanocrystalline calcium molybdate, J. Alloys Compd. 481 (2009) 568–572.

[33] T. Thongtem, A. Phuruangrat, S. Thongtem, Characterization of $MMoO_4$ (M = Ba, Sr and Ca) with different morphologies prepared using a cyclic microwave radiation, Mater. Lett. 62 (2008) 454–457.

[34] C. Bouzidi, K. Horchani-Naifer, Z. Khadraoui, H. Elhouichet, M. Ferid, Synthesis, characterization and DFT calculations of electronic and optical properties of $CaMoO_4$, Phys. B Condens. Matter 497 (2016) 34–38.

[35] T. Liu, J. Chen, F. Yan, Optical polarized properties related to the oxygen vacancy in the $CaMoO_4$ crystal, J. Lumin. 129 (2009) 101–104.

[36] C. Pu, T. Liu, Q. Zhang, Study of the electronic structures of $CaMoO_4$ crystal related to oxygen vacancy, Phys. Status Solidi (b) 245 (2008) 1586–1589.

[37] A.P. Kaushik, B. Lukose, P. Clancy, The role of shape on electronic structure and charge transport in faceted PbSe nanocrystals, ACS Nano 8 (2014) 2302–2317.

[38] N. Erdman, K.R. Poeppelmeier, M. Asta, O. Warschkow, D.E. Ellis, L.D. Marks, The structure and chemistry of the TiO_2-rich surface of $SrTiO_3$ (001), Nature 419 (2002) 55–58.

[39] B. Lv, Z. Liu, H. Tian, Y. Xu, D. Wu, Y. Sun, Single-crystalline dodecahedral and octodecahedral α-Fe_2O_3 particles synthesized by a fluoride anion–assisted hydrothermal method, Adv. Funct. Mater. 20 (2010) 3987–3996.

[40] H.G. Yang, C.H. Sun, S.Z. Qiao, J. Zou, G. Liu, S.C. Smith, H.M. Cheng, G.Q. Lu, Anatase TiO_2 single crystals with a large percentage of reactive facets, Nature 453 (2008) 638–641.

[41] W. Liu, J.-g. Wang, W. Li, X. Guo, L. Lu, X. Lu, X. Feng, C. Liu, Z. Yang, A shortcut for evaluating activities of TiO_2 facets: water dissociative chemisorption on TiO_2-B (100) and (001), Phys. Chem. Chem. Phys. 12 (2010) 8721–8727.

[42] J. Jiang, K. Zhao, X. Xiao, L. Zhang, Synthesis and facet-dependent photoreactivity of BiOCl single-crystalline nanosheets, J. Am. Chem. Soc. 134 (2012) 4473–4476.

[43] Z. Zongyan, L. Zhaosheng, Z. Zhigang, Surface properties and electronic structure of low-index stoichiometric anatase TiO_2 surfaces, J. Phys. Condens. Matter 22 (2010), 175008.

[44] Q. Gao, Y.-M. Ju, D. An, M.-R. Gao, C.-H. Cui, J.-W. Liu, H.-P. Cong, S.-H. Yu, Shape-controlled synthesis of monodisperse PdCu nanocubes and their electrocatalytic properties, ChemSusChem 6 (2013) 1878–1882.

[45] L. Wang, S. Zhao, C. Liu, C. Li, X. Li, H. Li, Y. Wang, C. Ma, Z. Li, J. Zeng, Aerobic oxidation of cyclohexane on catalysts based on twinned and single-crystal $Au_{75}Pd_{25}$ bimetallic nanocrystals, Nano Lett. 15 (2015) 2875–2880.

[46] H. Lee, S.E. Habas, S. Kweskin, D. Butcher, G.A. Somorjai, P. Yang, Morphological control of catalytically active platinum nanocrystals, Angew. Chem. Int. Ed. 45 (2006) 7824–7828.

[47] T.S. Ahmadi, Z.L. Wang, T.C. Green, A. Henglein, M.A. El-Sayed, Shape-controlled synthesis of colloidal platinum nanoparticles, Science 272 (1996) 1924–1925.

[48] X.-F. Wang, G.-H. Peng, N. Li, Z.-H. Liang, X. Wang, J.-L. Wu, Hydrothermal synthesis and luminescence properties of 3D walnut-like CaMoO 4: Eu 3+ red phosphors, J. Alloys Compd. 599 (2014) 102–107.

[49] V.D. Araújo, R.L. Tranquilin, F.V. Motta, C.A. Paskocimas, M.I.B. Bernardi, L.S. Cavalcante, J. Andres, E. Longo, M.R.D. Bomio, Effect of polyvinyl alcohol on the shape, photoluminescence and photocatalytic properties of $PbMoO_4$ microcrystals, Mater. Sci. Semicond. Process. 26 (2014) 425–430.

[50] A. Ruditskiy, H.-C. Peng, Y. Xia, Shape-controlled metal nanocrystals for heterogeneous catalysis, Annu. Rev. Chem. Biomol. Eng. 7 (2016) 327–348.

[51] J. Andres, G. Lourdes, G. Amanda Fernandes, F. Mateus Meneghetti, L. Elson, Effects of surface stability on the morphological transformation of metals and metal oxides as investigated by first-principles calculations, Nanotechnology 26 (2015), 405703.

[52] M.M. Ferrer, A.F. Gouveia, L. Gracia, E. Longo, J. Andres, A 3D platform for the morphology modulation of materials: first principles calculations on the thermodynamic stability and surface structure of metal oxides: Co_3O_4, α-Fe_2O_3, and In_2O_3, Model. Simul. Mater. Sci. Eng. 24 (2016), 025007.

[53] G.S. Silva, L. Gracia, M.T. Fabbro, L.P. Serejo dos Santos, H. Beltran-Mir, E. Cordoncillo, E. Longo, J. Andres, Theoretical and experimental insight on

Ag_2CrO_4 microcrystals: synthesis, characterization, and photoluminescence properties, Inorg. Chem. 55 (2016) 8961–8970.

[54] A.F. Gouveia, M.M. Ferrer, J.R. Sambrano, J. Andres, E. Longo, Modeling the atomic-scale structure, stability, and morphological transformations in the tetragonal phase of $LaVO_4$, Chem. Phys. Lett. 660 (2016) 87–92.

[55] M.C. Oliveira, L. Gracia, I.C. Nogueira, M.F.C. Gurgel, J.M.R. Mercury, E. Longo, J. Andres, Synthesis and morphological transformation of $BaWO_4$ crystals: experimental and theoretical insights, Ceram. Inter. 42 (2016) 10913–10921.

[56] M.C. Oliveira, L. Gracia, I.C. Nogueira, M.F.C. Gurgel, J.M.R. Mercury, E. Longo, J. Andres, On the morphology of $BaMoO_4$ crystals: a theoretical and experimental approach, Cryst. Res. Technol. 51 (2016) 634–644.

[57] R.C. de Oliveira, C.C. de Foggi, M.M. Teixeira, M.D.P. da Silva, M. Assis, E.M. Francisco, B.N.A.d.S. Pimentel, P.F.d.S. Pereira, C.E. Vergani, A.L. Machado, J. Andres, L. Gracia, E. Longo, Mechanism of antibacterial activity via morphology change of α-$AgVO_3$: theoretical and experimental insights, ACS Appl. Mater. Interfaces 9 (13) (2017) 11472–11481.

[58] C.H.B. Ng, W.Y. Fan, Crystal origami: preparation of β-Ag_2MoO_4 concave and convex crystals with high-index facets, ChemNanoMat 3 (2017) 178–182.

[59] S. Ishihara, N. Iyi, Y. Tsujimoto, S. Tominaka, Y. Matsushita, V. Krishnan, M. Akada, J. Labuta, K. Deguchi, S. Ohki, M. Tansho, T. Shimizu, Q. Ji, Y. Yamauchi, J.P. Hill, H. Abe, K. Ariga, Hydrogen-bond-driven 'homogeneous intercalation' for rapid, reversible, and ultra-precise actuation of layered clay nanosheets, Chem. Commun. 49 (2013) 3631–3633.

[60] A.K. Parchur, A.A. Ansari, B.P. Singh, T.N. Hasan, N.A. Syed, S.B. Rai, R.S. Ningthoujam, Enhanced luminescence of CaMoO4:Eu by core@shell formation and its hyperthermia study after hybrid formation with Fe3O4: cytotoxicity assessment on human liver cancer cells and mesenchymal stem cells, Integr. Biol. 6 (2014) 53–64.

[61] A. Khorsand Zak, W.H. Abd Majid, M.E. Abrishami, R. Yousefi, X-ray analysis of ZnO nanoparticles by Williamson–Hall and size–strain plot methods, Solid State Sci. 13 (2011) 251–256.

[62] A.D. Becke, Density-functional thermochemistry. III. The role of exact exchange, J. Chem. Phys. 98 (1993) 5648–5652.

[63] C. Lee, W. Yang, R.G. Parr, Development of the Colle-Salvetti correlation-energy formula into a functional of the electron density, Phys. Rev. B 37 (1988) 785.

[64] R. Dovesi, R. Orlando, A. Erba, C.M. Zicovich-Wilson, B. Civalleri, S. Casassa, L. Maschio, M. Ferrabone, M. De La Pierre, P. D'Arco, Y. Noel, M. Causa, M. Rerat, B. Kirtman, CRYSTAL14: a program for the ab initio investigation of crystalline solids, Int. J. Quantum Chem. 114 (2014) 1287–1317.

[65] http://www.crystal.unito.it/Basis_Sets/Molibdenum.Html, Molibdenum basis-sets.

[66] http://www.crystal.unito.it/Basis_Sets/Oxygen.Html, Oxygen basis-sets.

[67] L. Valenzano, F.J. Torres, K. Doll, F. Pascale, C.M. Zicovich-Wilson, R. Dovesi, Ab initio study of the vibrational spectrum and related properties of crystalline compounds; the case of $CaCO_3$ calcite, Zeitschrift für Physikalische Chemie 220 (2006) 893–912.

[68] H.J. Monkhorst, J.D. Pack, Special points for Brillouin-zone integrations, Phys. Rev. B 13 (1976) 5188.

[69] G. Wulff, Xxv. Zur Frage der Geschwindigkeit des Wachsthums und der Auflosung der Krystallflachen, Zeitschrift für Kristallographie-Crystalline Materials 34 (1901) 449–530.

[70] M. Bomio, R. Tranquilin, F. Motta, C. Paskocimas, R. Nascimento, L. Gracia, J. Andres, E. Longo, Toward understanding the photocatalytic activity of $PbMoO_4$ powders with predominant (111),(100),(011), and (110) facets. A combined experimental and theoretical study, J. Phys. Chem. C 117 (2013) 21382–21395.

[71] V.M. Longo, L. Gracia, D.G. Stroppa, L.S. Cavalcante, M. Orlandi, A.J. Ramirez, E.R. Leite, J. Andres, A. Beltran, J.A. Varela, A joint experimental and theoretical study on the nanomorphology of $CaWO_4$ crystals, J. Phys. Chem. C 115 (2011) 20113–20119.

[72] G. Botelho, J. Andres, L. Gracia, L.S. Matos, E. Longo, Photoluminescence and photocatalytic properties of Ag_3PO_4 microcrystals: an experimental and theoretical investigation, ChemPlusChem 81 (2016) 202–212.

[73] M.T. Fabbro, C. Saliby, L.R. Rios, F.A. La Porta, L. Gracia, M.S. Li, J. Andres, L.P. Santos, E. Longo, Identifying and rationalizing the morphological, structural, and optical properties of-Ag_2MoO_4 microcrystals, and the formation process of Ag nanoparticles on their surfaces: combining experimental data and first-principles calculations, Sci. Technol. Adv. Mater. 16 (6) (2015 Dec) 065002–065012.

[74] M.C. Oliveira, L. Gracia, I.C. Nogueira, M.F.C. Gurgel, J.M.R. Mercury, E. Longo, J. Andres, Synthesis and morphological transformation of $BaWO_4$ crystals: experimental and theoretical insights, Ceram. Int. 42 (2016) 10913–10921.

[75] G.S. Silva, L. Gracia, M.T. Fabbro, L.P. Serejo dos Santos, H. Beltrán-Mir, E. Cordoncillo, E. Longo, J. Andrés, Theoretical and experimental insight on Ag_2CrO_4 microcrystals: synthesis, characterization, and photoluminescence properties, Inorg. Chem. 55 (2016) 8961–8970.

[76] P.D. File, Joint Committee on Powder Diffraction Standards, ASTM, Philadelphia, Pa, 1967, pp. 9–185.

[77] R. Roca, J.C. Sczancoski, I.C. Nogueira, M.T. Fabbro, H. Alves, L. Gracia, L.P. Santos, C. De Sousa, J. Andres, G. Luz, Facet-dependent photocatalytic and antibacterial properties of α-Ag_2WO_4 crystals: combining experimental data and theoretical insights, Catal. Sci. Technol. 5 (2015) 4091–4107.

[78] L. Lutterotti, S. Matthies, H.R. Wenk, Maud, Materials analysis using diffraction, Newsl. CPD 21 (1999) 14–15.

[79] H. Rietveld, A profile refinement method for nuclear and magnetic structures, J. Appl. Crystallogr. 2 (1969) 65–71.

[80] S. Grazulis, A. Daskevic, A. Merkys, D. Chateigner, L. Lutterotti, M. Quiros, N.R. Serebryanaya, P. Moeck, R.T. Downs, A. Le Bail, Crystallography Open Database (COD): an open-access collection of crystal structures and platform for world-wide collaboration, Nucleic Acids Res. 40 (2011) D420–D427.

[81] S.P.S. Porto, J.F. Scott, Raman spectra of $CaWO_4$, $SrWO_4$, $CaMoO_4$, and $SrMoO_4$, Phys. Rev. 157 (1967) 716–719.

[82] A. Marques, F. Motta, E. Leite, P. Pizani, J.A. Varela, E. Longo, D. De Melo, Evolution of photoluminescence as a function of the structural order or disorder in $CaMoO_4$ nanopowders, J. Appl. Phys. 104 (2008), 043505.

[83] M. Nicol, J.F. Durana, Vibrational Raman spectra of $CaMoO_4$ and $CaWO_4$ at high pressures, J. Chem. Phys. 54 (1971) 1436–1440.

[84] P.G. Zverev, Vibronic relaxation of Raman modes in $CaMoO_4$ and $PbMoO_4$ molecular ionic crystals, Phys. status solidi C. 1 (2004) 3101–3105.

[85] V.M. Longo, A.T.d. Figueiredo, A.B. Campos, J.W. Espinosa, A.C. Hernandes, C. Taft, J.R. Sambrano, J.A. Varela, E. Longo, Different origins of green-light photoluminescence emission in structurally ordered and disordered powders of calcium molybdate, J. Phys. Chem. A 112 (2008) 8920–8928.

[86] E. Sarantopoulou, C. Raptis, S. Ves, D. Christofilos, G.A. Kourouklis, Temperature and pressure dependence of Raman-active phonons of $CaMoO_4$: an anharmonicity study, J. Phys. Condens. Matter 14 (2002) 8925.

[87] T.T. Basiev, A.A. Sobol, Y.K. Voronko, P.G. Zverev, Spontaneous Raman spectroscopy of tungstate and molybdate crystals for Raman lasers, Opt. Mater. 15 (2000) 205–216.

[88] D.L. Wood, J. Tauc, Weak Absorption tails in amorphous semiconductors, Phys. Rev. B 5 (1972) 3144–3151.

[89] R.A. Roca, J.C. Sczancoski, I.C. Nogueira, M.T. Fabbro, H.C. Alves, L. Gracia, L.P.S. Santos, C.P. de Sousa, J. Andres, G.E. Luz, E. Longo, L.S. Cavalcante, Facet-dependent photocatalytic and antibacterial properties of α-Ag_2WO_4 crystals: combining experimental data and theoretical insights, Catal. Sci. Technol. 5 (2015) 4091–4107.

[90] J.C. Sczancoski, M.D.R. Bomio, L.S. Cavalcante, M.R. Joya, P.S. Pizani, J.A. Varela, E. Longo, M.S. Li, J.A. Andres, Morphology and blue photoluminescence emission of $PbMoO_4$ processed in conventional hydrothermal, J. Phys. Chem. C 113 (2009) 5812–5822.

[91] M. Ghaed-Amini, M. Bazarganipour, M. Salavati-Niasari, Calcium molybdate octahedral nanostructures, hierarchical self-assemblies controllable synthesis by coprecipitation method: characterization and optical properties, J. Ind. Eng. Chem. 21 (2015) 1089–1097.

Journal of Alloys and Compounds 750 (2018) 55–70

Contents lists available at ScienceDirect

Journal of Alloys and Compounds

journal homepage: http://www.elsevier.com/locate/jalcom

Structure, morphology and photoluminescence emissions of $ZnMoO_4$: RE $^{3+}$=Tb^{3+} - Tm^{3+} - X Eu^{3+} (x = 1, 1.5, 2, 2.5 and 3 mol%) particles obtained by the sonochemical method

L.X. Lovisa [a, *], M.C. Oliveira [b], J. Andres [b], L. Gracia [c], M.S. Li [d], E. Longo [e], R.L. Tranquilin [a], C.A. Paskocimas [a], M.R.D. Bomio [a], F.V. Motta [a]

[a] LSQM—Laboratorio de Síntese Química de Materiais, DEMAT, UFRN, Natal, Campus, Lagoa Nova, Natal, RN CEP 59078-900, Brazil
[b] Departament de Química Física i Analítica, Universitat Jaume I, Campus del Riu Sec, Castello E, 12071, Spain
[c] Department of Química-Física, Universitat de Valencia, 46100, Burjassot, Spain
[d] IFSC, USP, Av. Trabalhador São Carlense, 400, CEP 13566-590, São Carlos, SP, Brazil
[e] LIEC, IQ, UNESP, Rua Francisco Degni s/n, CEP 14801-907, Araraquara, SP, Brazil

ARTICLE INFO

Article history:
Received 18 January 2018
Received in revised form
19 March 2018
Accepted 29 March 2018
Available online 30 March 2018

Keywords:
$ZnMoO_4$: Tb^{3+}
Tm^{3+}
Eu^{3+}
Sonochemical method
Photoluminescence

ABSTRACT

$ZnMoO_4$ and $ZnMoO_4$: RE^{3+} = 1% Tb^{3+}, 1% Tm^{3+}, x Eu^{3+} (x = 1, 1.5, 2, 2.5 and 3 mol%) particles were prepared by a sonochemical method. The influence of the dopant content on photoluminescent behavior was investigated. The X-ray diffraction results confirmed the formation of the α-$ZnMoO_4$ phase with a triclinic crystalline structure. The influence of the chemical compositions on photoluminescence emissions has been studied and the results clearly show the specific emissions of Tb^{3+} and Eu^{3+}, simultaneously, with a strong contribution of the matrix. Band gap values are in the range of 3.55–4.25 eV. From the values calculated for the CIE coordinates, it was observed that this material develops an emission tendency in the orange-red region. It has been demonstrated for the first time that the sample $ZnMoO_4$: 1% Tb^{3+}, 1% Tm^{3+}, 2% molEu^{3+}, presented higher photoluminescence intensity. At higher concentrations of RE^{3+}, the quenching effect was observed. The morphology of samples are interpreted based on a comparative analysis of the calculated and experimental field emission scanning electron microscopy (FE-SEM) images. First-principle calculations at a density functional theory level were performed to obtain the values of surface energies and relative stability of the (120), (001), (011), (201), and (100) surfaces by employing the Wulff construction. A complete map of the available morphologies of $ZnMoO_4$ and $ZnMoO_4$:12.5%molEu^{3+} is obtained and a possible explanation for the transformation processes is provided in which the experimental and theoretical morphologies can match. The present study offers a fundamental knowledge that is expected to enable the fabrication of $ZnMoO_4$-based phosphor materials with a controllable emission peak shift and intensity.

1. Introduction

Over the last decades, the interest for molybdates has been increasing due to their potential applications in the most diverse areas, such as biology, photoluminescence, photocatalysis, and lithium ion batteries [1–4]. Rare earth cations, RE^{3+}, doped molybdates present high chemical stability, which allows them to be applied in versatile applications, such as plasma display panels, field emission display, lighting industries and white light emitting diodes [5–9]. Therefore, these materials are considered a new generation of light sources, which have been replacing fluorescent lamps efficiently, due to low energy consumption and fast response.

The doping processes of RE^{3+}, the main members of lanthanide's group, at the lattice of the molybdates are responsible for the appearance of optical properties due to 4f valence shell electrons, while photoluminescence emissions are associated to f-f or 4f-5d transitions [10,11], and the emission wavelength also depends on the splitting of energy level. For example, Eu^{3+} cations are activated phosphors that provoke a strong red emitter signal due to $^5D_0 \rightarrow {}^7F_2$ electric dipole transition [12], while Tb^{3+} cations are activated

---

* Corresponding author.
E-mail address: lauraengmat@hotmail.com (L.X. Lovisa).

https://doi.org/10.1016/j.jallcom.2018.03.394
0925-8388/© 2018 Elsevier B.V. All rights reserved.

phosphors which reads a strong green emission due to the transitions of $^5D_3$-^7F_J in the blue and $^5D_4$-^7F_J in the green region (J = 6, 5, 4, 3, 2) and the transition intensities depend on their critical doping concentrations [13].

On the other hand, it is well known that the co-doping process of RE^{3+} is an adequate procedure to enhance intensity since in this process the energy transfer occurs from one RE^{3+}cation which acts as a sensitizer to another RE^{3+}cation acting as activator. Along this process, the energy transfer between RE^{3+}cations is possible due to a plethora of effects such as resonant energy transfer, energy transfer by non-radiative transition and quantum cutting [14]. Many combinations of sensitizer and activator of RE^{3+} were developed as Er^{3+}–Yb^{3+}, Eu^{3+}–Gd^{3+}, Eu^{3+}–Sm^{3+} and Eu^{3+}–Tb^{3+} [15–21].

For the zinc molybdate, $ZnMoO_4$, as a representative member of molybdate family, recent experimental and theoretical studies have evaluated in detail their phosphorescent behavior at low temperatures and a crystal phosphor model was proposed to explain the corresponding mechanism [22–24]. In addition, the influence of the growth conditions of the $ZnMoO_4$ crystals and the characteristics of the decay are analyzed to find an increase of the luminescence emissions [25]. $ZnMoO_4$ is an inorganic semiconductor that present two types of crystal structures: alpha (α) and beta (β) and has been successfully synthesized by different methods, including the sonochemistry, precipitation and hydrothermal processes [26–29]. The type of phase obtained depends on the conditions of synthesis, time, and temperature processing [30]. The crystals α-$ZnMoO_4$ have a triclinic structure, with space group P1 and group symmetry C_1 [31], in which the Zn cations are coordinated by six oxygen anions that form the distorted octahedral [ZnO_6], while Mo cations are bound to four oxygen anions in a tetrahedral configuration [MoO_4] [32]. The crystals β-$ZnMoO_4$ have a monoclinic structure of the wolframite type, with space group $P_{2/c}$and group symmetry C^4_{2h}. In the monoclinic structure, the Zn and Mo cations are coordinated by six oxygen atoms that form the distorted octahedral [ZnO_6] and [MoO_6], respectively [33].

Mikhailik et al. [34] proposed that the photoluminescent properties of $ZnMoO_4$ are related to self-localized excitons and to electron transitions within the anionic molecular complex $[MoO_4]^{2}$ .The emission bands can be associated to radioactive recombination processes of the electron-hole pairs located in the anionic molecular complex $[MoO_4]^{2}$ and this moiety is considered the main constituent element, which defines the optical properties in the visible ultraviolet energy region [35]. Cavalcante et al. [36] attributed that the differences in photoluminescence emission intensities of $ZnMoO_4$ microcrystals are due to the presence of changes in the particle morphology, crystal size and surface defects. RE^{3+} doped $ZnMoO_4$, $ZnMoO_4$:RE^{3+}, have been widely investigated for possible application in optical devices. According to Ju et al. [37], in their work with $ZnMoO_4$: Tb from the co-precipitation method, concluded that the light flux in green is more significant than in red and blue among materials co-doped due to the intense emission of the $^5D_4 \rightarrow {}^7F_5$ (Tb^{3+}) at 550 nm and that this type of material exhibits excellent thermal and chemical stability [38–40]. Chengaiah et al. [41] evaluated the effect of Dy^{3+} dopant concentration on the $ZnMoO_4$ matrix and observed a mixture of emissions in the yellow and blue regions. Through the determination of the chromaticity coordinates, it was possible to produce a material with emission in white. Ran et al. [42] have already described that the energy transfer efficiency between the Bi^{3+} sensitizer and the Eu^{3+} activator in the $ZnMoO_4$ matrix is associated with the concentration of the dopants and the distance between them, highlighting their performance as photoluminescent material in the use of LEDs white.

In this work, a series of the $ZnMoO_4$ and $ZnMoO_4$: 1% Tb^{+3}, 1% Tm^{+3}, x Eu^{+3} (x = 1, 1.5, 2, 2.5 and 3 mol %) particles were prepared by the sonochemical for the preparation of the $ZnMoO_4$ and $ZnMoO_4$: 1% Tb^{+3}, 1% Tm^{+3}, x Eu^{+3} (x = 1, 1.5, 2, 2.5 and 3 mol%). The synthesized samples were characterized by X-ray diffraction and Rietveld refinements, field emission scanning electron microscopy (FE-SEM) and photoluminescence emissions. They present photoluminescence (PL) emissions and a tunable band gap in the visible light region. The geometries, electronic structures and properties of both $ZnMoO_4$ and $ZnMoO_4$: 12.5% Eu^{3+}systems have been characterized and discussed in relation to their crystal structural characteristics by using the density functional theory (DFT)-based calculations. Next, a joint experimental and theoretical strategy, developed by us, was employed to obtain a complete map of the morphologies available for both systems. Based on these results, and by changing the values of the energy surfaces of (120), (011), (001), (201), (220), (100), (111) and (112) surfaces, we are able to rationalize the different path followed for these system by which the experimental FE-SEM images and theoretical morphologies can match.

The remainder of this paper is organized as follows: Section 2 describes the experimental procedure and computational details, Section 3 exhibits the computational details; Sections 4 and 5 present the results and conclusions, respectively.

2. Experimental procedure and computational details

2.1. Materials

Acid Molybdic (H_2MoO_4), (Alfa Aesar), zinc nitrate ($Zn(NO_3)_2 \cdot 6H_2O$) (Synth), europium oxide (Eu_2O_3) (Alfa Aesar), terbium oxide (Tb_4O_7) (Aldrich), thulium oxide (Tm_2O_3), nitric acid (Synth), ammonium hydroxide (NH_4OH) (Synth) and distilled water were used as received to prepare the $ZnMoO_4$ and $ZnMoO_4$: RE^{3+} particles.

2.2. Preparation

Initially, the oxides (Eu_2O_3, Tb_4O_7 and Tm_2O_3) were dissolved separately in 10 ml of nitric acid to obtain their respective nitrates. Since in the form of oxides, these elements are insoluble in the reaction medium. For the synthesis of the $ZnMoO_4$ and $ZnMoO_4$: RE^{3+} particles, two precursor solutions were prepared: one of molybdenum (solution **A**) and the other of zinc (solution **B**). For the two solutions, the starting reagent was dissolved in 40 ml of distilled water. Solution **A** was exposed to high intensity ultrasound irradiation at 65% amplitude in continuous mode. Then solution **B** was added to solution A during the ultrasound by dripping in the time interval of every 10 min. After the complete dissolution, the dopants (RE^{3+}:Tb^{3+}, Tm^{3+} and Eu^{3+}) in nitrate form were added to the system. Finally, NH_4OH was added to the solution to stabilize the pH at 8. The solution was centrifuged three times in distilled water and then kept in the oven at a temperature of 80 C for 24 h for drying. The particles were calcined at 650 C for 4 h at a heating rate of 10 C/min.

2.3. Characterization

The $ZnMoO_4$ and $ZnMoO_4$:RE^{3+} particles were structurally characterized by XRD using a Shimadzu XRD 7000 instrument with Cu-Kα radiation (λ = 1.5406 Å) in the 2θ range from 10 to 50 at a scanning rate of 0.02 s ^{1}. The morphologies were investigated using field-emission gun scanning electron microscopy (FEG-SEM; Carl Zeiss, Supra 35- VP Model, Germany) operated at 6 kV. The chemical analyzes were performed on the equipment of Energy

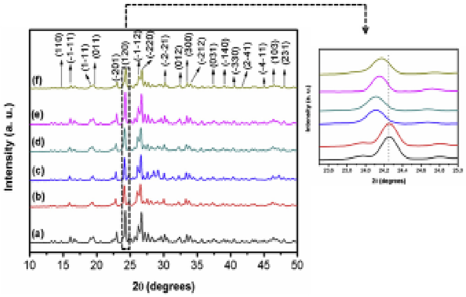

Fig. 1. X-ray diffraction of the $ZnMoO_4$ materials synthesized by the sonochemical method: (a) $ZnMoO_4$, and $ZnMoO_4$: 1% Tb^{3+}, 1% Tm^{3+}, x Eu^{3+} % mol: (b) x = 1%, (c) x = 1.5%, (d) x = 2%, (e) x = 2.5% and (f) x = 3% mol.

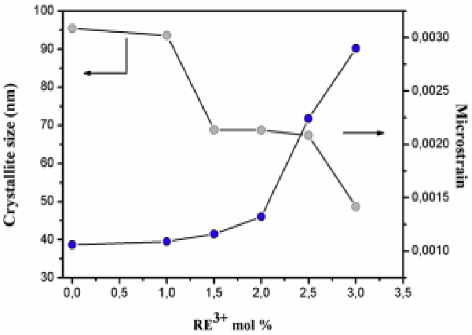

Fig. 2. Relationship between crystallite size and microdeformation according to RE^{3+} concentration.

Dispersive X-ray Fluorescence Spectrometer EDX-720- Shimadzu. The UV–vis diffuse reflectance spectrum was measured at room temperature using a UV–vis spectrometer. The photoluminescence (PL) spectra were acquired with an Ash Monospec 27 monochromator (Thermal Jarrel, U.S.A.) and a R4446 photomultiplier (Hamamatsu Photonics, U.S.A.). The 350 nm beam of a krypton ion laser (Coherent Innova 90 K) was used as the excitation source while its maximum output power was kept at 200 mW. All measurements were performed at room temperature. The time decay measurements were performed on the equipment Fluorolog3 Horiba Jobin Yvon spectrofluorometer equipped with Hamamatsu R928P photomultiplier, SPEX 1934 D phosphorimeter, and a pulsed 150 W Xe–Hg lamp.

2.4. Computational details

Bulk and surfaces of $ZnMoO_4$ and $ZnMoO_4$:12.5% mol Eu^{3+} were calculated by means of the hybrid functional B3LYP within the periodic density functional theory (DFT) framework [43,44], using the CRYSTAL14 software package [45]. Eu center was represented by a small-core effective-core pseudopotential (ECP) [46], while Mo center was described by a Hay–Wadt type (basis [HAYWSC]-31G) [47]. Oxygen [48] and zinc [49] centers were both represented by standards at 6-31G* basis sets.

In the bulk and surface calculations, the exchange–correlation contribution is the result of a numerical integration of the electron density and its gradient, performed over a grid of points. Default values of the tolerances that control the Coulomband exchange series were adopted (ITOL1 = ITOL2 = ITOL3 = ITOL4 = 8, ITOL5 = 14). The Hamiltonian matrix was diagonalized [50], using 36 reciprocal lattice points (k-points), corresponding to a shrinking factor of IS = 4 method for bulk, while 10 k-points grids were used for surfaces. In this work, a triclinic supercell of 144 and 143 atoms which corresponds to 1 2 2 conventional cell, was used to simulate the $ZnMoO_4$ and $ZnMoO_4$:12.5% Eu^{3+}, respectively. It is important to note that for the calculation of the doped materials, $ZnMoO_4$:RE^{3+}, we have a technical problem, i.e. because the % of doping is very small, in the range of 1–3 mol%, it is necessary to use very large unit cells. This fact makes calculations computationally very costly, and it was possible to reach a minimum of doping of 12.5% Eu^{3+}.

Slab models for (120), (011), (001), (201), (220), (100), (111) and (112)surfaces were considered to obtain the surface energy, E_{surf}, values and the morphologies of the $ZnMoO_4$ and $ZnMoO_4$: 12.5% Eu^{3+} systems. Surface calculations were determined from the equilibrium shape by a classic Wulff construction [51] that minimizes the total surface free energy at a fixed volume, providing a simple correlation between the E_{surf} of the (*hkl*) plane and the distance, r (*hkl*),in the normal direction from the center of the crystallite. The Wulff construction has been successfully used in materials science to obtain the morphology of materials, including $PbMoO_4$, α-Ag_2MoO_4 as well as $BaMoO_4$ materials [52–54].

E_{surf} is defined as the total energy per repeating slab cell (E_{slab}) minus the total energy of the perfect crystal per molecular unit ($E_{bulk/atom}$) multiplied by the number of molecular units of the surface (N_s) and divided by the surface area (A) per repeating cell of the two sides of the slab, as shown in equation (1).

$$E_{suf} = \frac{1}{2A}\ E_{slab}\quad Ns \cdot E_{bulk/atom} \tag{1}$$

Table 1
Crystallographic data of $ZnMoO_4$ and $ZnMoO_4$:RE^{3+} samples.

Samples	$ZnMoO_4$	$ZnMoO_4$ (Theoretical)	$ZnMoO_4$: 1% Tb 1% Tm 1% mol Eu^{3+}	$ZnMoO_4$: 1% Tb 1% Tm 1.5% mol Eu^{3+} +	$ZnMoO_4$: 1% Tb 1% Tm 2% mol Eu^{3+}	$ZnMoO_4$: 1% Tb 1% Tm 2.5% mol Eu^{3+}	$ZnMoO_4$: 1% Tb 1% Tm 3% mol Eu^{3+}
a (Å)	9.6822	9.7476	9.6835	9.69991	9.69056	9.70418	9.70166
b (Å)	6. 9487	6.9847	6.9518	6.95539	6.96208	6.96021	6.96096
c (Å)	8.3687	8.3984	8.3551	8.3668	8.37362	8.37270	8.37684
V $(Å)^3$	563.0352	526.5936	562.127	564.4800	564.9384	565.5183	565.7120
α	101.7090	101.3339	101.720	101.6817	101.7214	101.7112	101.6878
β	96.7422	96.8497	96.847	96.8367	96.7110	96.82299	96.81503
θ	106.86	106.9862	106.851	106.8180	106.8245	106.8004	106.8083
D (nm)	95.448	–	93.570	93.570	68.839	68.736	67.342
ε (10^{3})	1.06	–	1.09	1.16	1.32	2.24	2.9
Rwp	6.80	–	8.05	6.93	10.03	8.37	8.54
Rb	3.80	–	11.27	12.21	7.49	13.17	6.83
χ^2	0.56	–	1.40	1.28	0.72	1.50	0.80

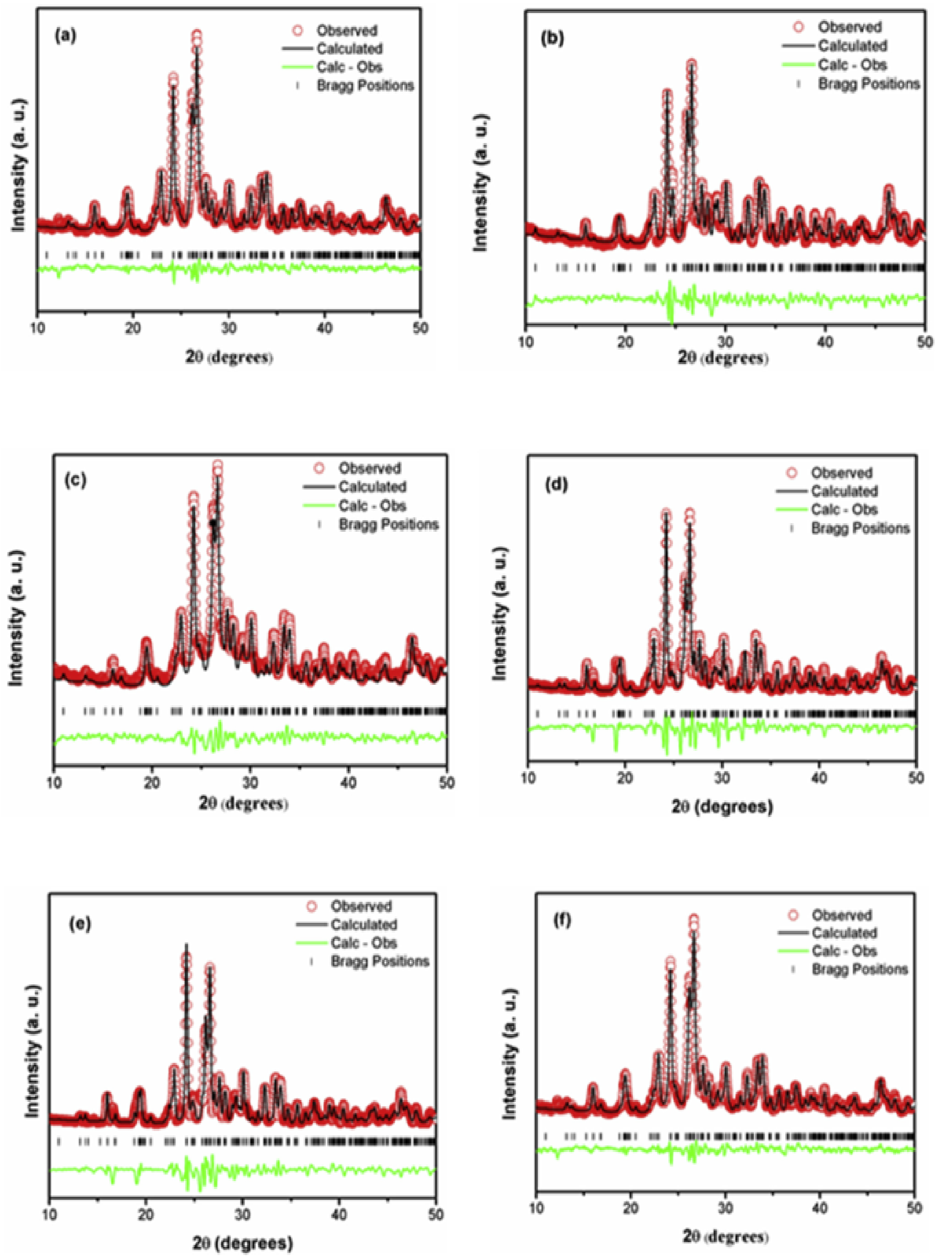

Fig. 3. Structural refinement of the samples (a) $ZnMoO_4$, and $ZnMoO_4$: 1% Tb^{3+}, 1% Tm^{3+}, x Eu^{3+} % mol: (b) 1%, (c) 1.5%, (d) 2%, (e) 2.5% and (f) 3% mol.

3. Results

The XRD pattern presented in Fig. 1 show the diffraction peak characteristics of $ZnMoO_4$. They can be indexed in a triclinic structure of the α type with space group P1in C_1 symmetry (JCPDS-35–0765). The XRD patterns of the samples showed that the $ZnMoO_4$:RE are structurally related to the triclinic crystalline phase. There was no secondary phase formation, indicating that doping occurred successfully.

A decrease in the intensity of the peak (120) at 24.30 is observed in Fig. 1 accompanied by an increase of the amount of dopants in the $ZnMoO_4$ matrix. The structural and electronic distortion in the $[ZnO_6]$ clusters caused by the substitution of RE^{3+} → Zn^{2+}in the structure of $ZnMoO_4$ is evidenced by the

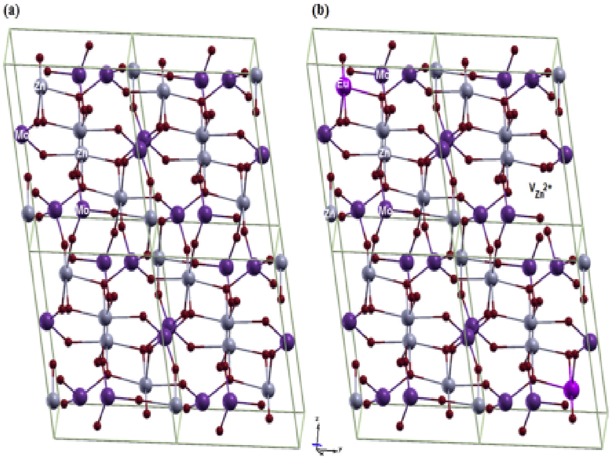

Fig. 4. Theoretical representation of the triclinic 1 2 2 supercell corresponding to (a) $ZnMoO_4$ and (b) $ZnMoO_4$:12.5% molEu^{3+} crystals.

displacement of the peaks to a region of smaller angle according to Fig. 1. This fact can be associated to the difference in the size between the $RE^{3+}$and Zn^{2+}cations. Ju et al. [37] noted that the peaks of the XRD patterns become weak and slightly broad due to the increase of the concentration of Tb^{3+}in $ZnMoO_4$.

The values of the mean crystallite size and the micro strain of $ZnMoO_4$ and $ZnMoO_4:RE^{+3}$are shown in Table 1. The mean crystallite size was estimated by the Scherrer equation (2) [55].

$$D_{hkl} = {}^{0.9\lambda}/_{\beta Cos\theta} \tag{2}$$

Where D_{hkl} is the mean crystallite size, λ is the wavelength, θ is half the Bragg angle and β is the half height of the selected reflection (FWHM). The reduction in the crystallite size is verified when the dopant concentration is increased as shown in Fig. 2. This behavior is first of all due to the distortion caused in the $ZnMoO_4$ lattice by the dopants, which can slow down the growth of the crystals [56]. According to Vidya et al. [57], the dopant provides a lagging force in the grain boundaries. If this generated retarding force is greater than the grain growth force by the formed ion of the lattice (Zn), then the diffusibility is reduced. The micro strain is associated to the synthesis conditions that the materials were formed. For example, the fast precipitation of the $ZnMoO_4$ particles due to the strong attraction force between Zn^{2+}or RE^{3+} and $(MoO_4)^{2+}$ ions due to the addition of NH_4OH. The bonds that form later can generate defects and deformation in the crystals.

The Rietveld refinement method was used to explain possible differences in the structural arrangements induced by the processing of $ZnMoO_4$ and $ZnMoO_4:RE^{3+}$ particles. This refinement was performed by using the general structure analysis Maud program version 2.0. The results of the Rietveld refinements are shown in Fig. 3. The measured diffraction patterns are well matched to ICSD 1528282. The diffractogram corresponding to the experimental and theoretically calculated data are practically identical, as shown in the Calc-Obs line. The results of the refinement are summarized in Table 1. The high quality of the refinement is revealed by the reliability parameters (X^2, *RwpandRp*). The Rietveld method uses the profiles of the intensities obtained by the slow scan measurements of the material from the X-ray diffraction technique.

The cell and atomic position parameters used in the calculations are taken from the results of the Rietveld refinements for both structures (Table 1). An optimization of the cell parameters was performed and the unit cell representation was modeled using a single conventional 1 2 2 cell for $ZnMoO_4$ and $ZnMoO_4:Eu^{3+}$ materials. The X-Window Crystalline Structures and Densities (XCrySDen) program [58] were used to design the periodic model, as showed in Fig. 4(a and b).

The determination of the value of the gap energy (Egap) for the $ZnMoO_4:RE^{3+}$ particles was performed from the UV–Visible spectroscopy by the diffuse reflectance mode. The obtained reflectance data were converted to absorbance [F(R) = α], generating an absorbance versus energy (eV) plot as indicated in Fig. 5. The values of Egap were obtained from the linear extrapolation following the Tauc and Wood method [50].

The electronic transitions in the materials happen through the energy bands and are followed by the emission or absorption of photons in the crystal. For a crystal to have direct electronic transitions, it is necessary to observe the conservation of energy and momentum in the crystal. This condition is favored when the maximum of the valence band (VB) and the minimum of the conduction band (CB) are in the same region of symmetry of the solid. According to different authors [35,59,60], the $ZnMoO_4$crystals exhibit an optical absorption spectrum governed by direct electronic transitions. We calculated and plotted the band structure of $ZnMoO_4$ and $ZnMoO_4$: 12.5% molEu^{3+} along various high-symmetry directions in the first Brillouin zone as shown in Fig. 6(a and b). An analysis of the results displayed in this Figure points out that the doping of Eu^{+3} provokes a decrease of the values for the energy levels belonging to CB with respect to pure $ZnMoO_4$; the energy range is 5.5–6.0 eV and 2-7-3.6 eV for $ZnMoO_4$ and $ZnMoO_4$: 12.5% mol Eu^{3+}, respectively; while the distribution of energy levels within both CB and VB are more compact at $ZnMoO_4$with respect to $ZnMoO_4$: 12.5% mol Eu^{3+}.

The experimental values found for E_{gap} are in the range of3.55 and 4.25 eV, while theoretical calculations predict an indirect gap of 5.28 and 2.67eV for $ZnMoO_4$ and ZnMoO:Eu^{3+}(12.5%) systems, respectively. Fig. 6a–b reveals that the indirect transition is produced along the *k*-points F → G (010–001) from the top of VB to the bottom of CB, although the band structure for the doped system is very flat. The projected total DOS for $ZnMoO_4$ and $ZnMoO_4$:12.5% molEu^{3+} are presented in Fig. 7a and b, respectively. An analysis of

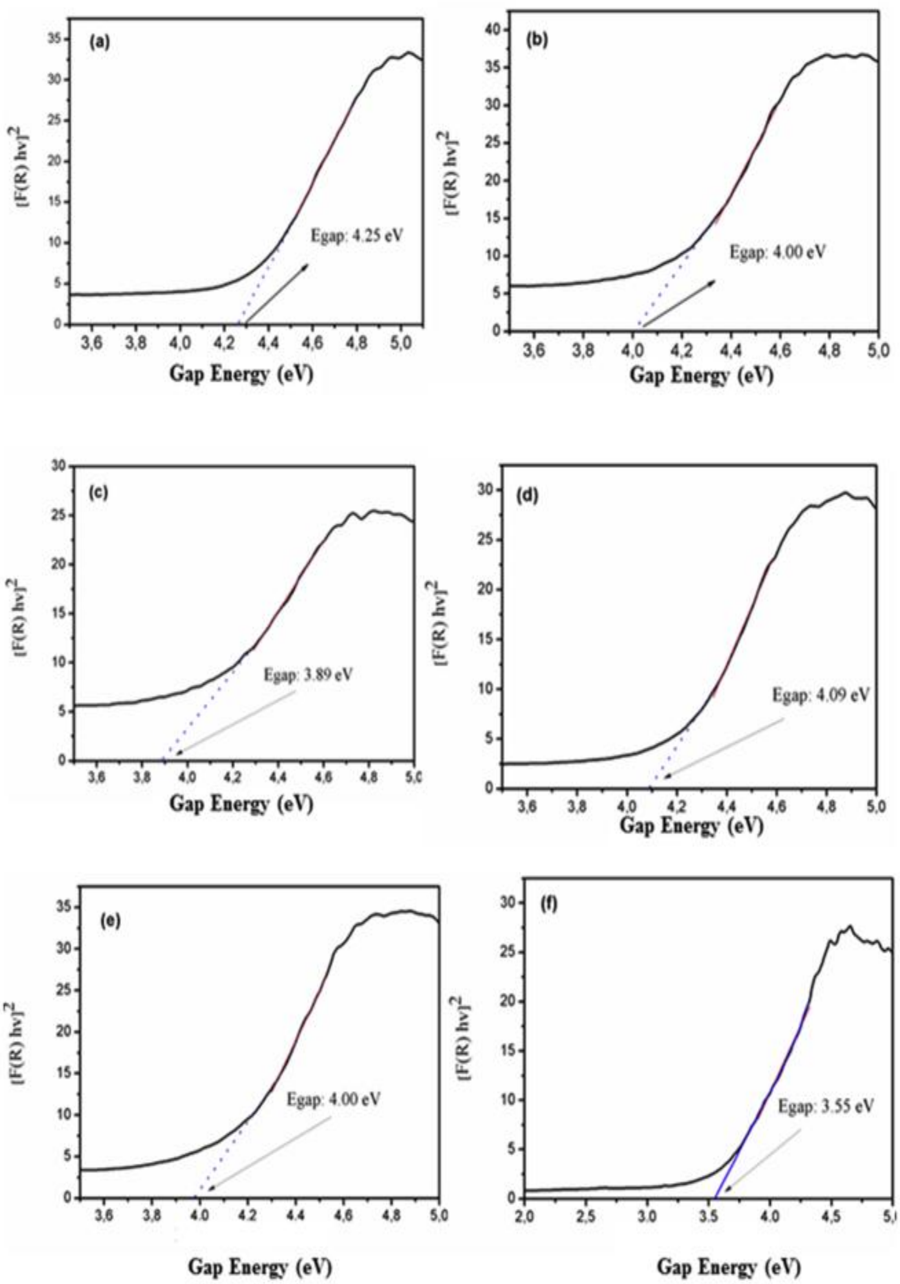

Fig. 5. Determination of the gap energy value by using the Tauc and Wood method: (a) $ZnMoO_4$ and $ZnMoO_4$: 1% Tb^{3+}, 1% Tm^{3+}, x Eu^{3+}% mol: (b) x = 1%, (c) x = 1.5%, (d) x = 2%, (e) x = 2.5% and (f) x = 3% mol.

these figures shows that the VB from 0 to 0.67eV ($ZnMoO_4$) and from 0 to 0.89eV ($ZnMoO_4$: 12.5% molEu^{3+}) are composed mainly of O orbitals (px,py and pz). CB is mainly formed by the Mo and Eu orbitals with a lower contribution of the Zn orbitals (dz^2, dx^2-y^2, dxy, dxz, dyz), located in the range from 5.28 to 6.07eV ($ZnMoO_4$) and from 2.67 to 3.57eV ($ZnMoO_4$: 12.5% molEu^{3+}).

The substitution of the RE^{3+} cations by Zn^{2+} cations promotes an unbalance in the charges within the crystalline structure of $ZnMoO_4$ because the oxidation states of the cations are different. As a way of restoring material neutrality, structural defects occur. The

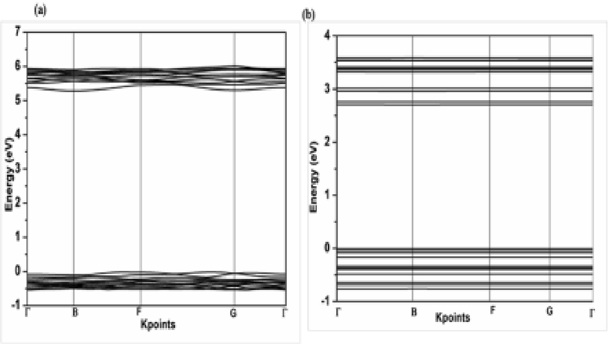

Fig. 6. Band structure of (a) $ZnMoO_4$ and (b) $ZnMoO_4$:12.5 molEu^{3+} crystals.

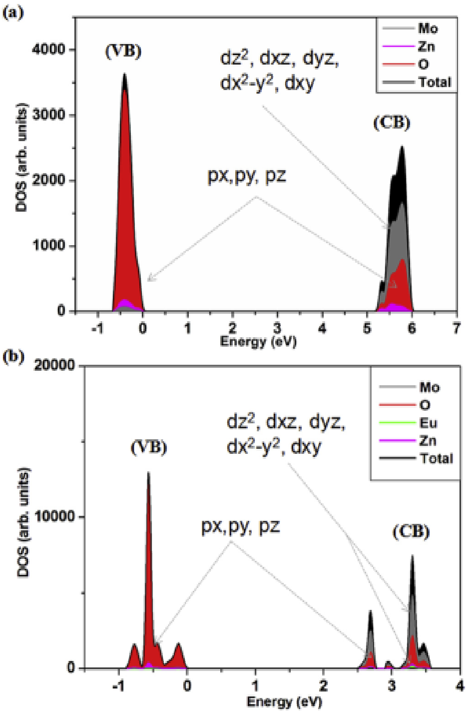

Fig. 7. Projected total DOS of (a) $ZnMoO_4$ and (b) $ZnMoO_4$: 12.5% molEu^{3+}.

RE^{3+} cations when incorporated to the $ZnMoO_4$ matrix causes an excess of positive charges, then, Zn^{2+} vacancies appear [41,61,62]. From an electronic perspective, the presence of these defects promotes the presence of intermediate electronic levels in the forbidden region. This new band gap configuration contributes to electronic transitions occurring at a lower energy level. Fig. S1(of Supporting Information)represents the decrease in the Egap with increasing dopant concentration. It is observed that there is no linearity in the relationship between the two parameters. It is reasonable to consider that other factors may interfere, such as the synthesis method as well as the morphology of the particles.

Fig. 8 presents the photoluminescence emission spectrum of the $ZnMoO_4$ and $ZnMoO_4$:RE^{3+}particles. The samples were excited by a laser of $\lambda = 350$ nm at room temperature. An analysis of the results displayed in Fig. 8 renders a first band of lower intensity located between 370 and 419 nm, which can be associated to the recombination of the hole– electron pairs within the clusters [ZnO_6] with predominant emission in violet. A second band of higher intensity is observed located between 475 nm and 850 nm with a peak at 640 nm. Sczancoski et al. [35] consider that the energy states of the molybdate crystals are formed by oxygen states (2p) located above the VB and molybdenum states (4 d) located under the CB as shows in Fig. 7. The electronic transitions of type Mo (4 d) → O (2p) may present different emissions according to the positioning of the holes in the band structure. This second band was decomposed into four emission bands indicating the contribution of each band of the visible spectrum to the photoluminescence behavior, according to the deconvolutions shown in Fig. 9. The transition corresponding to the first deconvolution band is associated with the shallow holes (near the VB) related to O 2p orbitals with dominance in green. While the orange, red and infrared emissions, corresponding to the second, third and fourth bands, are associated to the deep holes (slightly away from theVB) connected to the O 2p orbital [63].

Wu et al. [64] pointed out that the active vibration modes of the Jahn-Teller T_2 symmetry effect may influence the $[MoO_4]^{2-}$ complex of slightly distorted tetrahedral symmetry, which would result in a structured absorption band for the electronic transitions type $^1A_1 \rightarrow {}^1T_2$. Ding et al. [65] have established that the blue emissions are caused by $^1A_1 \rightarrow {}^1T_2$electronic transitions in groups of intrinsic tetrahedra $[MoO_4]^{2-}$ and green emissions by structural defects of the Frenkel type exist on the surface layer of the crystals.

The origin and the mechanisms responsible for the photoluminescence emissions of molybdates are not yet fully understood. Several hypotheses supported by experimental and theoretical results are reported in the literature to explain this optical property. Campos et al. [66], through theory calculations, propose that the $CaMoO_4$ particles emission processes may be related to the existence of distorted groups [MoO_3] and [MoO_4] in the lattice. These authors have argued that these groups lead to the formation of localized levels of energy in the band gap. Marques et al. [67] associate the dependence of photoluminescent properties with the structural order disorder of molybdate prepared by the polymeric precursor method. Ryu et al. [68] verified that both the degree of crystallization and morphology are two important factors in the photoluminescence emissions of $BaMoO_4$ particles, while Sczancoski et al. [35] suggest that the nature of these emissions are very dependent on the local atomic organizations in the structure.

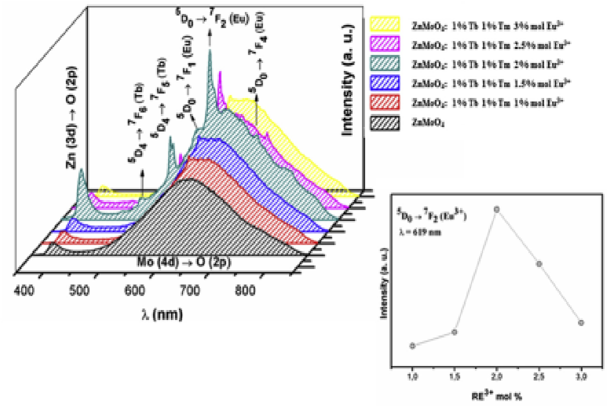

Fig. 8. Photoluminescence emission spectra of the particles (a) $ZnMoO_4$, and $ZnMoO_4$: 1% Tb^{3+}, 1% Tm^{3+}, x Eu^{3+} % mol: (b) x = 1%, (c) x = 1.5%, (d) x = 2%, (e) x = 2.5% and (f) x = 3% mol; detail of quenching effect on transition $^5D_0 \rightarrow {}^7F_2$ (Eu^{3+}).

Fig. 8 shows the emission bands for specific RE^{3+}transitions. For Tb $^{3+}$, they are$^5D_4 \rightarrow {}^7F_j$ (J = 6, 5) located at 490 and 546 nm, respectively. The typical transitions of Eu^{3+} $^5D_0 \rightarrow {}^7F_j$ (J = 1,2 and 4) are positioned at 590, 619 and 624, 702 nm, respectively, while the bands located at 619 and 624 can be attributed to the $^5D_4 \rightarrow {}^7F_2$ (Eu^{3+}) transition. Speghini et al. [69a] proposed that the transitions are dependent on the symmetry of the sites in which the Eu^{3+} is positioned.

The $^5D_0 \rightarrow {}^7F_1$ transition of Eu^{3+} is a magnetic dipole transition. Its intensity is not influenced by the symmetry of the site. The $^5D_0 \rightarrow {}^7F_2$ transition is known as hypersensitive transition and it is greatly influenced by the local symmetry of the Eu^{3+} cation and the nature of the host matrix. As a consequence, Eu^{3+} dopants can also be used as sensitive probes of local structural symmetry [70]. The asymmetric ratio (R) was calculated considering the ratio between the integrals of the areas under curves $^5D_0 \rightarrow {}^7F_2$ and $^5D_0 \rightarrow {}^7F_1$, according to equation (3), to investigate the symmetry environment of the Eu^{3+}cation site.

$$R = \frac{I(5D0 \rightarrow 7F2\,)}{I(5D0 \rightarrow 7F1\,)} \qquad (3)$$

The calculated R was 1.70. It is observed that the peak of emission of electric dipole at 619 nm dominates the peak of emission of magnetic dipole at 590 nm, which is mainly due to the occupation of Eu $^{3+}$ cations without symmetry inversion [71].

The introduction of the RE^{3+} in the $ZnMoO_4$ favors the photoluminescence emissions as it is observed in Fig. 8. For concentrations higher than that one of the sample $ZnMoO_4$: 1% Tb 1% Tm 2% mol Eu^{3+}, a significant drop in intensity can be sensed. This effect is related to a critical concentration which is known as the quenching concentration (see details in Fig. 8). In this critical concentration the distance RE^{3+}- RE^{3+} is reduced, which favors the emergence of non-radioactive transitions by a process of cross relaxation [72]. Non-radioactive transitions are expressed in phonon forms, which result in vibrations within the crystal lattice. Wang [73] states that the concentration of the dopant determines the average distance between the two neighboring activator cations as well as the photoluminescence efficiency of RE^{3+} in doped systems.

A decrease in the emission intensity shows the occurrence of energy migration between RE^{3+}in different sites in the lattice, resulting in concentration quenching. Thus, an optimum concentration for $RE^{3+}$is found to be 4 mol% (X_C = 0.04). The concentration quenching occurs by the non-radiative migration of energy between the RE^{3+}catons. The migration of non-radiative energy can take place from two distinct mechanisms: i. e (i) Forster resonance energy transfer (multipole–multipole interaction) and (ii) Dexter mechanism (exchange interaction) [74].

For the Forster resonance energy transfer to be characterized in a system it is necessary that: the donor (**D**) is in the excited state and that the distance between the donor and the activator ion (**A**) is a factor of great influence for the transfer power. The specific conditions must be fulfilled for this mechanism to take place. Note the following points: (I) the emission range of **D** is partially superimposed on the absorption range of **A**, and (II) the distance (**Rc**) between **D** and **A** must be sufficiently short, since the energy transfer efficiency is proportional to $\frac{1}{Rc^6}$, to allow the interaction of the multipole-multipole emission bands of material [75,76]. The Forster resonance energy transfer can usually happen at distances of up to 100 Å. Dexter (also known as exchange or coalitional energy transfer) is another dynamic quenching mechanism. Dexter energy transfer is a short-range phenomenon (Rc = 10 Å) that decreases with $e^{\,R}$and depends on spatial overlap of donor and quencher molecular orbitals [74].

The critical energy transfer distance (Rc) for $ZnMoO_4$:RE^{3+} was estimated by equation (4) suggested by Blasse [77] from the parameters of the structure, namely the unit cell volume (V), the number of units of the molecular formula per unit cell (Z) and the quenching concentration (Xc).

$$Rc \approx 2\;{\frac{3V}{4Xc\pi Z}}^{\,1/3} \qquad (4)$$

For the $ZnMoO_4$ system: 1% Tb 1% Tm 2% molEu^{3+}, the following values were considered: Z = 6, V = 564.9384 Å^3 and Xc = 0.04, the calculated Rc was 16.50 Å. Normally, the exchange interaction is preferably in an energy transfer process when the value of Rc is between 5 and 10 Å [78]. In case of values higher than 10 Å, there is no indication of exchange interaction in this mechanism. Consequently, other multipolar electrical interactions are responsible for the quenching effect between two more activating ions (RE^{3+}).

To characterize the light emitted by the $ZnMoO_4$ and $ZnMoO_4$:RE^{3+} particles, the chromaticity coordinates (Xc, Yc) were calculated as the basis for the distribution of the photoluminescence emission spectrum as established by the

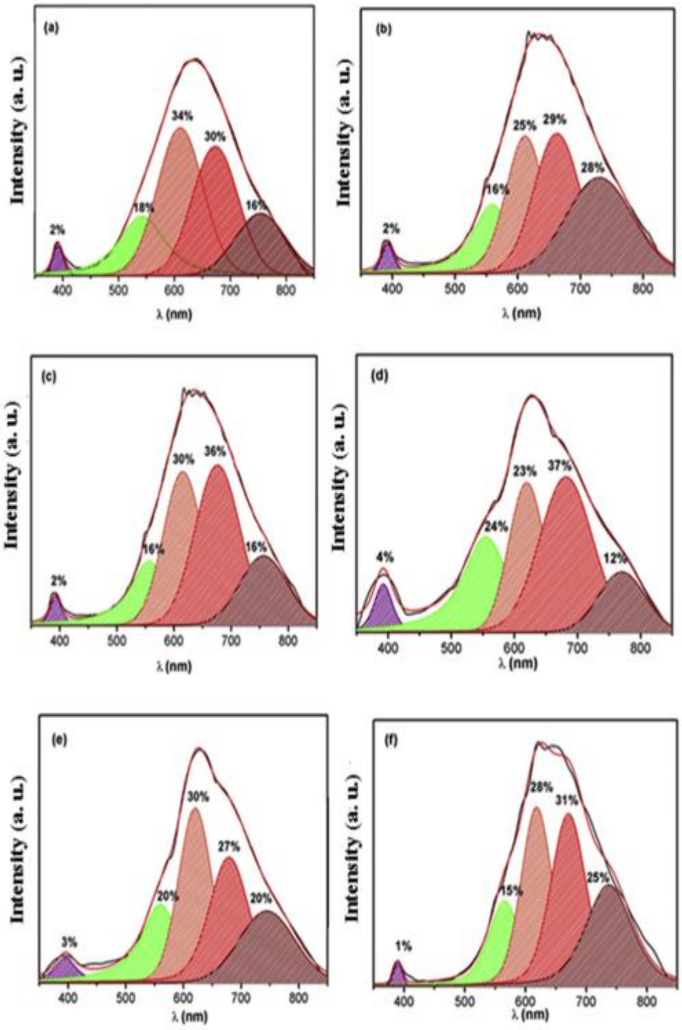

Fig. 9. Deconvolutions of the photoluminescence emission spectra of the particles (a) $ZnMoO_4$; $ZnMoO_4$: 1% Tb^{3+}, 1% Tm^{3+}, x Eu^{3++}% mol: (b) x = 1%, (c) x = 1.5%, (d) x = 2%, (e) x = 2.5% and (f) x = 3% mol.

international commission on illumination (CIE) [79,80]. As well as, the correlative color temperature (CCT) of each sample was estimated using McCamy's empirical formula [81].

$$CCT = \quad 449n^3 + 3525n^2 \quad 6823n + 5520.33 \tag{5}$$

where$n = \frac{(x \quad xe)}{(y \quad ye)}$ is the inverse slope line, $xe = 0.332$ and $ye = 0$.

The color reproduction index (CRI) is a quantity that measures the ability of a light source to reveal the colors of various objects faithfully compared to an ideal or natural light source. This index ranges from 0 to 100%, the closer to 100% the greater the color accuracy of objects. Fig. 10 represents the chromaticity diagram representing the points of the CIE coordinates (Xc, Yc) of all samples. Table 2 shows the CIE, CCT and CRI coordinates of the $ZnMoO_4$and $ZnMoO_4$:RE^{3+} particles.

The decay was recorded for $^5D_0 \rightarrow {}^7F_2$ transition of Eu^{3+} at 614 nm emission. The decay curves of all the $ZnMoO_4$: RE^{3+} samples exhibited bi-exponential decay as shown in Fig. 11 and have been fitted into exponential equation (6). The average lifetime for the bi-exponential decay was calculated from the following formula (7), the calculated decay parameters are listed in Table 3.

$$\mathbf{I} = \mathbf{A_1 exp}^{\frac{-t}{\tau_1}} + \mathbf{A_2 exp}^{\frac{-t}{\tau_2}} \tag{6}$$

Where I is the emission intensity at any time "τ" after switching off the excitation illumination, A_1, A_2 are constant. τ_1, τ_2 are the bi-exponential component of the decay time. The average lifetime for 614 nm emission can be determined by the following formula (6):"

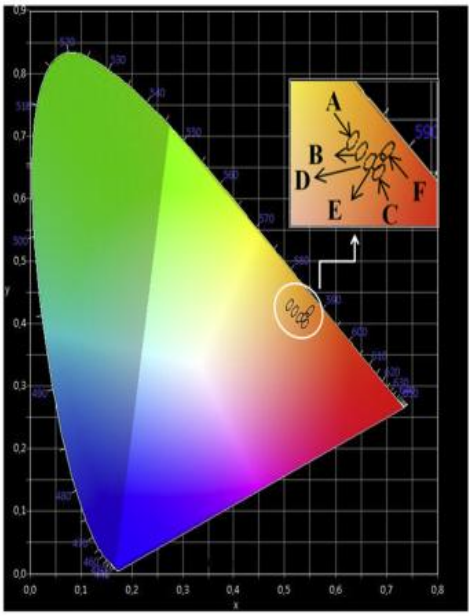

Fig. 10. Chromaticity diagram.

$$\tau = \frac{A_1 \cdot \tau_1{}^2 \;+\; A_2 \cdot \tau_2{}^2}{A_1 \cdot \tau_1 + A_2 \cdot \tau_2} \tag{7}$$

And the energy transfer efficiency from host to RE $^{3+}$ can be calculated according to equation (8) [82]:

$$\mathbf{n} = (1 \quad \frac{\tau}{\tau_0})\mathbf{x}\ 100\% \tag{8}$$

Where τ and τ_0 is the corresponding emission lifetimes of the donor in the presence and absence of the acceptor (RE^{3+}) for the same donor concentration, respectively. The energy transfer efficiency from the host to RE^{3+} in $ZnMoO_4$ is 43% for sample of $ZnMoO_4$: 1% Tb^{3+} 1% Tm^{3+} 2% molEu^{3+}, that exhibited better luminescence.

From the FE-SEM images, it was possible to identify the modifications the morphologies of $ZnMoO_4$ and $ZnMoO_4$:RE^{3+}, as well as to estimate the particle size distribution. Chemical analyzes were performed from the x-ray fluorescence spectroscopy of samples ZnMoO4 and $ZnMoO_4$: 1% Tb^{3+} 1% Tm^{3+} 3% molEu^{3+}, proving the existence of the elements Zn, Mo, O, Eu, Tm and Tb.

For the sample of pure $ZnMoO_4$, it is observed that the particles have plate morphologies, according to the measurements specified in Fig. 12 (I). A similar morphology is found for the sample of $ZnMoO_4$: 1% Tb^{3+} 1% Tm^{3+} 1% molEu^3. For $ZnMoO_4$: 1% Tb^{3+} 1% Tm^{3+}1.5% molEu^{3+}, it was identified octahedral particles with well defined facets. The $ZnMoO_4$: 1% Tb^{3+} 1% Tm^{3+}2% mol Eu^{3+}particles exhibited two different types of morphology and octahedral and cubic shape can be sensed. Through the detail of Fig. 12 (IV), it can be seen the appearance of cubic structures, evidencing the change in the morphology of the particles. The cubic-shaped particles are most relevant for the sample $ZnMoO_4$: 1% Tb^{3+} 1% Tm^{3+} 2.5% Eu^{3+}, confirming the trend presented in the previous sample. Moreover, it was possible to identify other forms: hexagonal and octahedral shapes. The sample $ZnMoO_4$: 1% Tb^{3+} 1% Tm^{3+} 3% Eu^{3+}presented particles with cubic and hexagonal shapes.

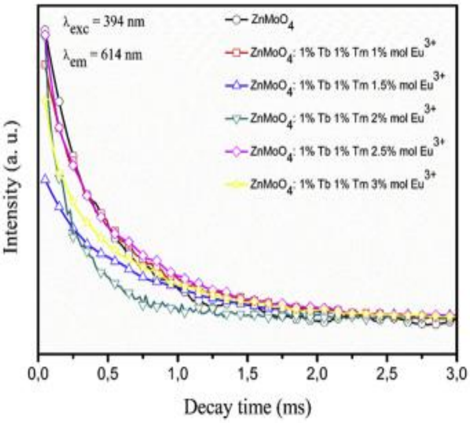

Fig. 11. Decay curves of $ZnMoO_4$ and $ZnMoO_4$: RE^{3+}.

It is well known that the control of the particle growth process is complex and very sensitive to the chemical environment and the internal crystalline structures [83]. The precursor type may be selectively adsorbed on specific exposed surface planes, thereby changing the surface energies and then an inhibition of the appearance of some surface particles along the growth process takes place. Huo [84] stated that the crystallographic planes exposed during the crystal growth process will rapidly decrease during the process as a result of the minimization of the surface energy of the small crystals, which eventually disappear or decrease their participation in the generated morphology. Thus, the surface is generally surrounded by planes with lower surface energies, resulting in slower crystal growth [85].

The equilibrium shape of $ZnMoO_4$and $ZnMoO_4$: RE^{3+}crystals can be calculated using the classic Wulff construction, which minimizes the total surface free energy at a fixed volume, and provides a simple relationship between the Esurf of the (hkl) plane and its distance in the normal direction from the center of the crystallite.

The surface structure and energy values for the (120), (011), (001), (201), (220), (100), (111) and (112) surfaces are described in

Table 2
CIE, CCT and CRI coordinates of $ZnMoO_4$ and $ZnMoO_4$: RE^{3+} samples.

Code	Samples	(Xc, Yc)	CCT (K)	CRI	Color
A	$ZnMoO_4$	(0.51, 0.43)	2256	87	Orange
B	$ZnMoO_4$: 1% Tb 1% Tm 1% mol Eu^{3+}	(0.53, 0.41)	1953	84	
C	$ZnMoO_4$: 1% Tb 1% Tm 1.5% mol Eu^{3+}	(0.54, 0.41)	1876	84	
D	$ZnMoO_4$: 1% Tb 1% Tm 2% mol Eu^{3+}	(0.52, 0.42)	2099	93	
E	$ZnMoO_4$: 1% Tb 1% Tm 2.5% mol Eu^{3+}	(0.54, 0.40)	1818	81	
F	$ZnMoO_4$: 1% Tb 1% Tm 3% mol Eu^{3+}	(0.55, 0.42)	1861	82	

Table 3
Comparison of emission lifetimes of ZnMoO4 and $ZnMoO_4$: RE^{3+}.

Samples	λ_{exc} (nm)	λ_{em} (nm)	A_1	τ_1 (ms)	A_2	τ_2 (ms)	τ (ms)
$ZnMoO_4$	394	614	79.87	0.15	230.29	0.50	0.47
$ZnMoO_4$: 1% Tb 1% Tm 1% mol Eu^{3+}	394	614	1054.57	0.70	655.03	0.21	0.62
$ZnMoO_4$: 1% Tb 1% Tm 1.5% mol Eu^{3+}	394	614	384.89	0.31	522.19	0.89	0.77
$ZnMoO_4$: 1% Tb 1% Tm 2% mol Eu^{3+}	394	614	1251.93	0.28	722.74	0.03	0.26
$ZnMoO_4$: 1% Tb 1% Tm 2.5% mol Eu^{3+}	394	614	620.42	0.09	1260.92	0.63	0.59
$ZnMoO_4$: 1% Tb 1% Tm 3% mol Eu^{3+}	394	614	985.03	0.65	488.45	0.08	0.62

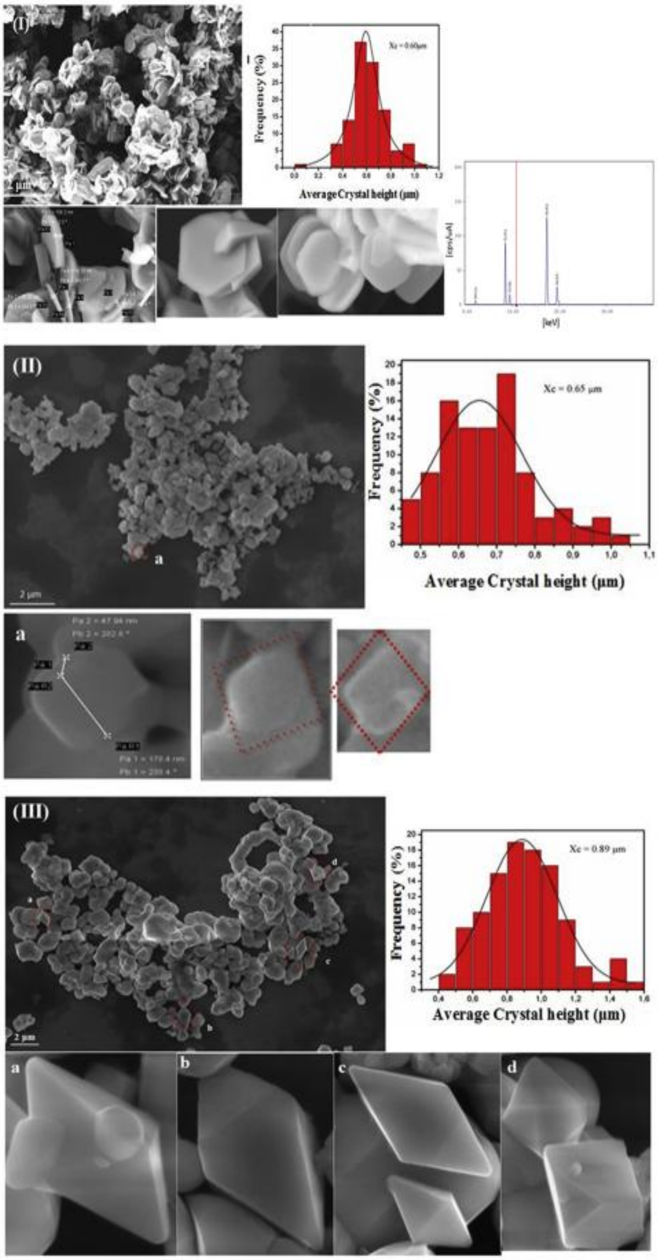

Fig. 12. SEM-FEG images for samples $ZnMoO_4$ (I), and $ZnMoO_4$: 1% Tb^{3+}, 1% Tm^{3+}, x Eu^{3+} 3% mol: x = 1% mol (II), x = 1.5% mol (III), x = 2% mol (IV), x = 2.5% mol (V), and x = 3% mol (VI).

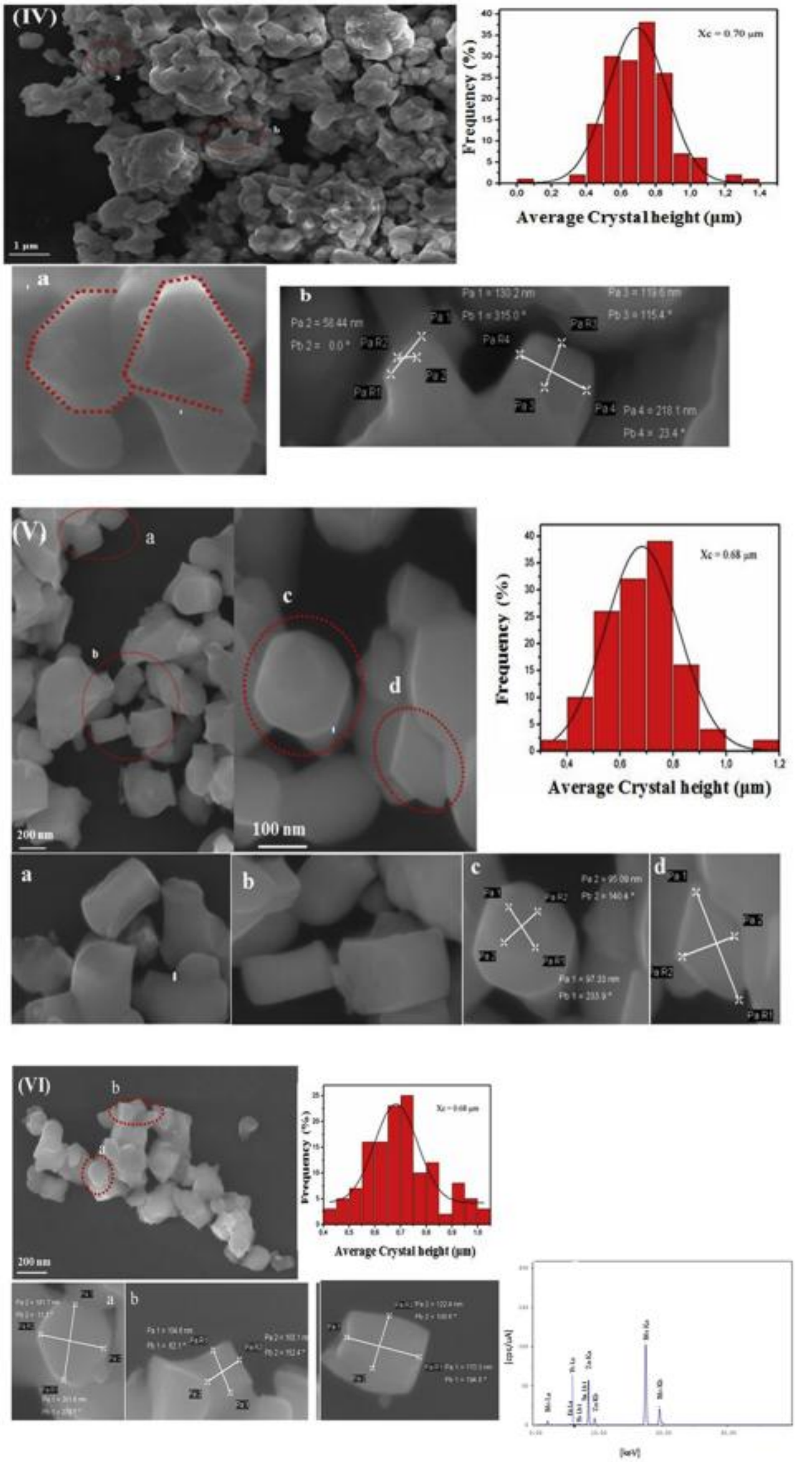

Fig. 12. (*continued*).

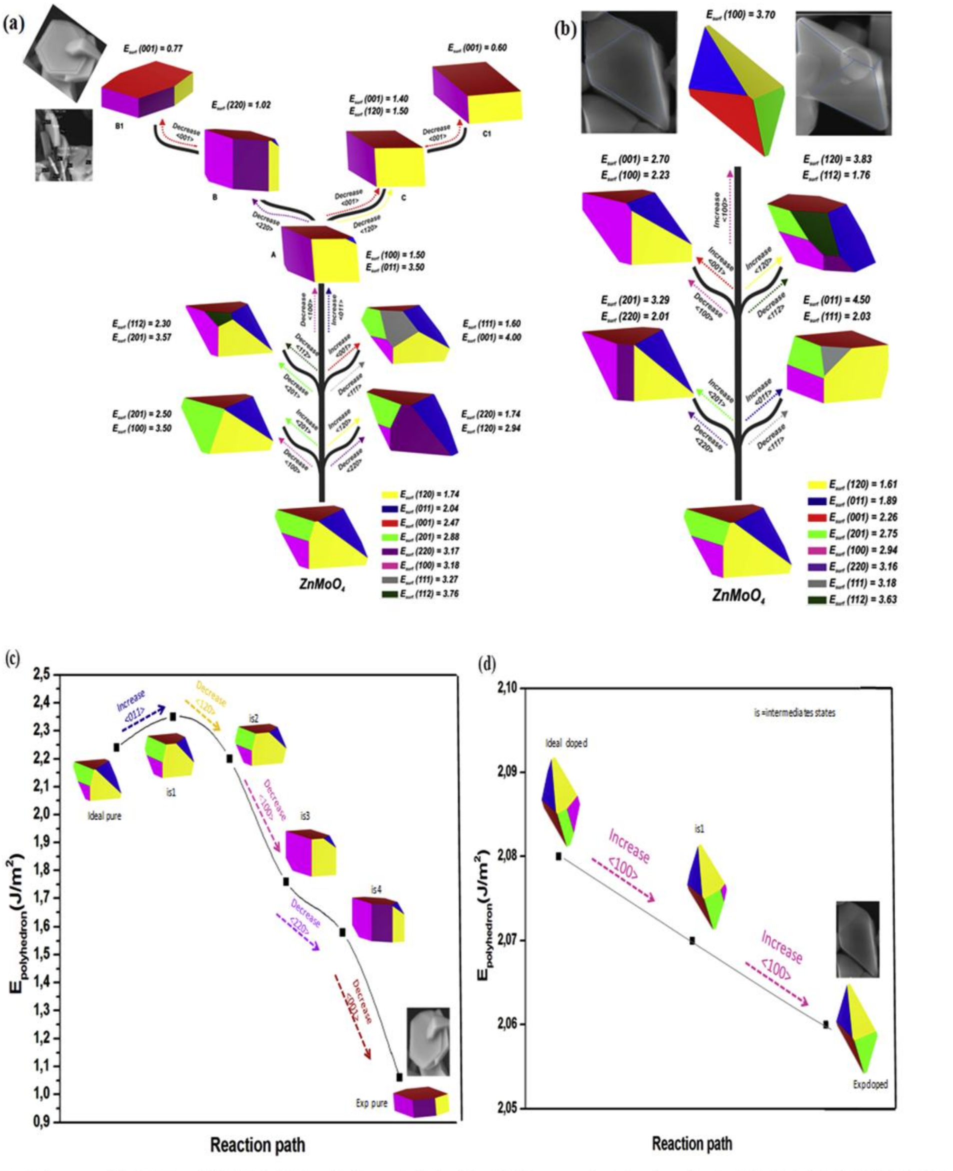

Fig. 13. Morphology map of (a) $ZnMoO_4$ and (b) $ZnMoO_4$:12.5% mol Eu^{3+} crystals obtained from Wulff's construction. The values of $E_{surf}$for (120), (011), (001), (201), (100), (220), (111), and (112) surfaces are employed. Surface energy is in J m^{-2}.

the supplementary information. According to our results, the order of stability is as follows: (120)> (001)> (011) faces in the ideal model. Initially, it was calculated the ideal morphology of $ZnMoO_4$ and $ZnMoO_4$:Eu^{3+} from the Esurf, and it is constituted by 33% (33%) of (120) surface, 23% (24%) of (001) surface, 22% (24%) of (011) surface, 16% (14%) of (201) surface, and 6% (7%) of (100) surface, being the values in parenthesis for $ZnMoO_4$:12.5% molEu^{3+}.

The available morphologies for both $ZnMoO_4$ and $ZnMoO_4$:12.5% mol Eu^{3+}systems can be obtained modifying the relative values of the surface energies or each surface, as it is shown in Fig. 13(a and b). In this map, it is found the experimental morphology obtained for $ZnMoO_4$in the present work, by means of the following paths: from the ideal morphology by increasing and/or decreasing the E_{surf}value of (011), (100), (220) and (001) surfaces as shown in Fig. 13a. The morphology reported by Jia et al. and Wang et al. [86,87] can be reached following the path from A to C and to C1 paths, respectively. Jia et al. synthesized $ZnMoO_4$ by hydrothermal method in conditions of different template agents and the as-prepared products presented varied morphologies for the same crystalline phase (monoclinic), showing in Fig. 13a the corresponding morphology. Wang et al. prepared $ZnMoO_4$via a hydrothermal route with the increase in the monomer concentrations and the influence of temperature on the shape of $ZnMoO_4$ was also investigated, reporting a transition from monoclinic to triclinic phase.

The experimental morphology of $ZnMoO_4$:$Eu^{3+}$was reached by increasing the value of E_{surf} for (100)surface to 3.70 J/m^2as illustrated in Fig. 13b. It is known that a change of morphologies can occur because of the presence of surfactants, impurities, temperature, synthetic routes and other factors. Furthermore, in this work, it is proposed a theoretical strategy for obtaining a reaction path, assuming the creation and screening of alternative reaction routes (intermediates states), to lead to a desired morphology, as presented in Fig. 13(c and d). Therefore, the values of $E_{surf}$from the calculated ideal morphology were used (Fig. 13(c and d))to predict the intermediate states to lead to a desired morphology (experimental), and this strategy allows us to rationalize the different reaction paths to pass the corresponding energy barriers and to control the crystal morphologies.

4. Conclusions

Searching for new classes of inorganic materials, which emerge as a promising option in high-performance applications in the field of photoluminescence, has received special attention. Particularly, oxides doped with rare earth (RE^{3+}) elements present high luminous efficiency, long decay time and emissions in their visible region.

In the present work, $ZnMoO_4$ and $ZnMoO_4$: $RE^{3+} = Tb^{3+}$ - Tm^{3+} - x Eu^{3+} (x = 1, 1.5, 2, 2.5 and 3 mol %)crystals were successfully synthesized using the sonochemical method. XRD observation revealed good crystallinity of the samples prepared without any impurities. All samples showed light emission in the orange–red region. Experimental results and first-principles calculations show a reduction in Egap values provoked by the structural defects and changes of the electronic structure promoted by the introduction of RE^{3+} in the $ZnMoO_4$ lattice. We have for the first time demonstrated that the sample $ZnMoO_4$: 1% Tb^{3+}, 1% Tm^{3+}, 2% Eu^{3+}, present a larger photoluminescence intensity. At higher concentrations of RE^{3+}, the quenching effect was observed. The structural and band gap relationship points out the possibility of band gap engineering in these materials through composition modulation.

FEG-SEM images revealed that both $ZnMoO_4$ and $ZnMoO_4$:12.5% Eu^{3+}samples exhibited similar morphologies. First-principle calculations, at density functional theory level, were performed to obtain the values of surface energies and relative stability of the (120), (001), (011), (201), and (100) surfaces and Wulff construction is employed to rationalize the crystal morphologies found by FE-SEM images. A complete map of the morphologies available for $ZnMoO_4$ and $ZnMoO_4$:12.5% mol Eu^{3+} is obtained and a possible explanation for the transformation processes is provided in which the experimental and theoretical morphologies can match. The present study provided fundamental knowledge on $ZnMoO_4$,and the method of controlling its color emission. Then, a new strategy for the rational structural design of $ZnMoO_4$:RE^{3+} crystals for optoelectronic applications is presented.

Acknowledgements

The authors gratefully acknowledge the financial support of the Brazilian governmental research funding agencies CAPES, CNPq, FAPESP and INCTMN. J.A. acknowledge Generalitat Valenciana for *PrometeoII*/2014/022, ACOMP/2014/270, and ACOMP/2015/1202, and Ministerio de Economía y Competitividad (Spain) project CTQ2015-65207-P for financially supporting this research. M.C. acknowledges Generalitat Valenciana for the Santiago Grisolia Program 2015/033. We also acknowledge the Servei Informatica, Universitat Jaume I for a generous allotment of computer time.

Appendix A. Supplementary data

Supplementary data related to this article can be found at https://doi.org/10.1016/j.jallcom.2018.03.394.

References

[1] Y. Yang, X. Li, W. Feng, W. Yang, W. Li, C. Tao, Effect of surfactants on morphology and luminescent properties of $CaMoO_4$: Eu^{3+} red phosphors, J. Alloys. Compd. 509 (2011) 845.
[2] Y. Jin, J. Zhang, Z. Hao, X. Zhang, Synthesis and luminescence properties of clew-like $CaMoO_4$:Sm^{3+}, Eu^{3+}, J. Alloys. Compd. 509 (2011) L348.
[3] J.H. Chung, S.Y. Lee, K.B. Shim, S.-Y. Kweon, S.-C. Ur, J.H. Ryu, Blue upconversion luminescence of $CaMoO_4$: Li^+/Yb^{3+}/Tm^{3+} phosphors prepared by complex citrate method, Appl. Phys. A 108 (2012) 369.
[4] J. Fei, Q. Sun, J. Li, Y. Cui, J. Huang, W. Hui, H. Hu, Synthesis and electrochemical performance of α-$ZnMoO_4$ nanoparticles as anode material for lithium ion batteries, Mater. Lett. 198 (2017) 4–7.
[5] W.N. Wang, Y. Kaihatsu, F. Iskandar, K. Okuuama, Highly luminous hollow chloroapatite phosphors formed by a template-free aerosol route for solid-state lighting, Chem. Mater. 21 (2009) 4685.
[6] E.F. Schubertand, J.K. Kim, Solid-state light sources getting smart, Science 308 (2005) 1274.
[7] A.A. Talin, K.A. Dean, J.E. Jaskie, Field emission displays: a critical review, Solid State Electron. 45 (2001) 963.
[8] B.V. Ratnam, M. Jayasimhadri, Kiwan Jang, H.S. Lee, Y. Soung-Soo, J.H. Jeong, White light emission from NaCaPO4:Dy3+ phosphor for ultraviolet-based white light-emitting diodes, J. Am. Ceram. Soc. 93 (2010) 3857.
[9] O.S. Wolfbeis, Lanthanide Luminescence, Springer, New York, 2011.
[10] B.G. Wybourne, Optical Spectroscopy of Lanthanides, CRC Press, Taylor and Francis, Boca Raton, USA, 2007.
[11] B.P. Maheshwary, J. Singh, R.A. Singh, Luminescence properties of Eu^{3+} activated $SrWO_4$ nanophosphors-concentration and annealing, RSC Adv. 4 (2015) 32605.
[12] X. Li, Y. Zhang, D. Geng, J. Lian, G. Zhang, Z. Hou, J. Lin, CaGdAlO4:$Tb3^+$/Eu^{3+} as promising phosphors for full-color field emission displays, J. Mater. Chem. C 2 (2014) 9924.
[13] R.S. Ningthoujam, in: S.B. Rai, Y. Dwivedi (Eds.), Enhancement of luminescence by rare earth ions doping in semiconductor host, 6, Nova Science Publishers Inc., 2012, pp. 145–182.
[14] N. Jaina, B.P. Singhb, R.K. Singha, J. Singha, R.A. Singh, Enhanced photoluminescence behaviour of Eu^{3+} activated $ZnMoO_4$ nanophosphors via Tb^{3+} co-doping for light emitting diode, J. Lumin. 188 (2017) 504–513.
[15] A. Pandey, V.K. Rai, V. Kumar, V. Kumar, H.C. Swart, Upconversion based temperature sensing ability of Er^{3+}–Yb^{3+} codoped $SrWO_4$: an optical heating phosphor, Sens. Actuators, B 209 (2015) 352.
[16] J.A. Dorman, J.H. Choi, G. Kuzmanich, J.P. Chang, High-quality white light using core–shell RE^{3+}:$LaPO_4$ (RE = Eu, Tb, Dy, Ce) phosphors, J. Phys. Chem. C 116 (2012) 12854.
[17] B.P. Singh, A.K. Parchur, R.S. Ningthoujam, A.A. Ansari, P. Singh, S.B. Rai, Enhanced photoluminescence in $CaMoO_4$:$Eu^{3+}$by Gd^{3+} co-doping, Dalton

Trans. 43 (2014) 4779.

[18] Y. Jin, J. Zhang, S. Lu, H. Zhao, X. Zhang, X.J. Wang, Fabrication of Eu^{3+} and Sm^{3+} codoped micro/nanosized $MMoO_4$ (M = Ca, Ba, and Sr) via facile hydrothermal method and their photoluminescence properties through energy transfer, J. Phys. Chem. C (2008), 1125860.

[19] M. Yang, Y. Liang, Q. Gui, B. Zhao, D. Jin, M. Lin, L. Yan, H. You, L. Dai, Y. Liu, Multifunctional luminescent nanomaterials from $NaLa(MoO_4)_2$:$Eu^{(3+)/}Tb^{(3+)}$ with tunable decay lifetimes, emission colors, and enhanced cell viability, Sci. Rep. 5 (2015) 11844.

[20] F. Wang, X. Liu, Upconversion multicolor fine-tuning: visible to near-infrared emission from lanthanide-doped $NaYF_4$ nanoparticles, J. Am. Chem. Soc. 130 (2008) 5642.

[21] N. Niu, P. Yang, F. He, X. Zhang, S. Gai, C. Li, Lin, Tunable multicolor and bright white emission of one-dimensional NaLuF4:Yb3+, Ln3+ (Ln = Er, Tm, Ho, Er/Tm, Tm/Ho) microstructures, J. Mater. Chem. vol. 22 (2012) 10889.

[22] V. Ya. Degoda, Ya. P. Kogut, I.M. Moroz, F.A. Danevich, Long time phosphorescence in $ZnMoO_4$ crystals, J. Lumin. 181 (2017) 269–276.

[23] V. Ya. Degoda, Ya. P. Kogut, I.M. Moroz, F.A. Danevich, Thermally stimulated luminescence in $ZnMoO_4$ crystals, J. Lumin. 183 (2017) 424–432.

[24] V. Ya. Degodaa, Ya. P. Koguta, I.M. Moroza, F.A. Danevichb, S.G. Nasonovc, E.P. Makarovc, V.N. Shlegelc, Temperature dependence of luminescence intensity in $ZnMoO_4$ crystals, Mater. Res. Bull. 89 (2017) 139–149.

[25] D. Spassky, V. Nagirnyi, S. Vielhauer, H. Magi, S.G. Nasonov, V.N. Shlegel, A. Belsky, Emission centers in $ZnMoO_4$: influence of growth conditions and decay characteristics, Opt. Mater. 59 (2016) 66–69.

[26] M.A. Patel, B.A. Bhanvase, S.H. Sonawane, Production of cerium zinc molybdate nano pigment by innovative ultrasound assisted approach, Ultrason. Sonochem. 20 (2013) 906–913.

[27] Z. Shahri, M. Bazarganipour, M. Salavati-Niasari, Controllable synthesis of novel zinc molybdate rod-like nanostructures via simple surfactant-free precipitation route, Superlattice. Microst. 63 (2013) 258–266.

[28] C.C. Mardare, D. Tanasic, A. Rathner, N. Muller, A.W. Hassel, Growth inhibition of Escherichia coli by zinc molybdate with different crystalline structure, Phys. Status Solidi A 213 (2016) 1471–1478.

[29] L. Wan, J. Shen, Y. Zhang, X. Li, Novel ZnMoO4/reduced graphene oxide hybrid as a high-performance anode material for lithium ion batteries, J. Alloys. Compd. 708 (2017) 713–721.

[30] S. Dutta, S. Som, S.K. Sharma, Luminescence and photometric characterization of K^+ compensated $CaMoO_4$:Dy^{3+}nanophosphors, Dalton Trans. 42 (2013) 9654.

[31] W. Reichelt, T. Weber, T. Sohnel, S. Dabritz, Mischkristallbildung im System $CuMoO_4$/$ZnMoO_4$, Z. Anorg. Allg. Chem. 626 (2000) 2020–2027.

[32] T. Sohnel, W. Reichelt, H. Oppermann, H.j. Mattauch, A. Simon, Zum System Zn/Mo/O. I. Phasenbestand und Eigenschaften der ternaren Zinkmolybdate; Struktur von $Zn_3Mo_2O_9$, Z. Anorg. Allg. Chem. 622 (1996) 1274.

[33] K. Pavani, A. Ramanan, Influence of 2-aminopyridine on the formation of molybdates under hydrothermal conditions, Eur. J. Inorg. Chem. 2005 (2005) 3080–3087.

[34] V.B. Mikhailik, H. Kraus, D. Wahl, H. Ehrenberg, M.S. Mykhayl, Optical and luminescence studies of ZnMoO4 using vacuum ultraviolet synchrotron readiation, Nucl. Instrum. Meth. Phys. Res. A 562 (2006) 513.

[35] J.C. Sczancoski, L.S. Cavalcante, N.L. Marana, R.O. da Silva, R.L. Tranquilin, M.R. Joya, P.S. Pizani, J.A. Varela, J.R. Sambrano, M. Siu Li, E. Longo, J. Andres, Electronic structure and optical properties of BaMoO4 powders, Curr. Appl. Phys. 10 (2010) 614.

[36] L.S. Cavalcante, J.C. Sczancoski, M. Siu Li, E. Longo, J.A. Varela, β-ZMO microcrystals synthesized by the surfactant-assisted hydrothermal method: growth process and photoluminescence properties, Colloid. Surface. Physicochem. Eng. Aspect. 396 (2012) 346.

[37] X. JU, X. LI, W. LI, W. YANG, C. TAO, Luminescence properties of ZMO:Tb^{3+} green phosphor prepared via co-precipitation, Mater. Lett. 65 (2011) 2642.

[38] P. Li, L. Pang, Z. Wang, Z. Yang, Q. Guo, X. Li, Luminescent characteristics of $LiBaBO_3$:Tb^{3+} green phosphor for white LED, J. Alloys. Compd. 478 (2009) 813.

[39] J. Llanos, R. Castillo, W. Alvarez, Preparation, characterization and luminescence of a new green-emitting phosphor: Gd_2TeO_6 doped with Tb^{3+}, Mater. Lett. 62 (2008) 3597.

[40] X. Li, Z. Yang, L. Guan, Q. Guo, A new yellowish green luminescent material $SrMoO_4$:Tb^{3+}, Mater. Lett. 63 (2009) 1096.

[41] T. Chengaiah, C.K.A. Jayasankar, K. Pavani, T. Sasikala, L.R. Moorthy, Preparation and luminescence characterization of Zn(1-x)MoO_4:xDy^{3+} phosphor for white light-emitting diodes, Optic Commun. 312 (2014) 233.

[42] W. Ran, L. Wang, W. Zhang, F. Li, H. Jiang, W. Li, L. Su, R. Houzong, X. Pana, J. Shi, A super energy transfer process based S-shaped cluster in ZMO phosphors: theoretical and experimental investigation, J. Mater. Chem. C 3 (2015) 8344.

[43] C.T. Lee, W.T. Yang, R.G. Parr, Development of the Colle-Salvetti correlation-energy formula into a functional of the electron density, Phys. Rev. B Condens. Matter 37 (1988) 785–789.

[44] A.D. Becke, Perspective on “Density functional thermochemistry. III. The role of exact exchange”, J. Chem. Phys. 98 (1993) 5648–5652.

[45] R. Dovesi, R. Orlando, A. Erba, C.M. Zicovich-Wilson, B. Civalleri, S. Casassa, et al., CRYSTAL14: a program for the ab initio investigation of crystalline solids, Int. J. Quant. Chem. 114 (2014) 1287–1317.

[46] Access to the site: http://www.crystal.unito.it/Basis_Sets/europium.html.

[47] F. Cora, A. Patel, N.M. Harrison, C. Roetti, C.R.A. Catlow, An ab-initio Hartree-Fock study of alpha-MoO_3, J. Mater. Chem. 7 (1997) 959–967.

[48] C. Gatti, V.R. Saunders, C. Roetti, Crystal field effects on the topological properties of the electron density in molecular crystals: the case of urea, J. Chem. Phys. 101 (1994) 10686–10696.

[49] T. Homann, U. Hotje, M. Binnewies, A. Borger, K.D. Becker, T. Bredow, Composition-dependent band gap in ZnSxSe1-x: a combined experimental and theoretical study, Solid State Sci. 8 (2006) 44–49.

[50] H.J. Monkhorst, J.D. Pack, Special points for Brillouin-zone integrations, Phys. Rev. B 13 (1976) 5188.

[51] G.Wulff. Xxv, Zur frage der geschwindigkeit des wachsthums und der auflosung der krystallflachen, Z. für Kristallogr. - Cryst. Mater. 34 (1901) 449–530.

[52] M. Bomio, R. Tranquilin, F.V. Motta, C.A. Paskocimas, R.M. Nascimento, L. Gracia, J. Andres, E. Longo, Towards understanding the photocatalytic activity of $PbMoO_4$ powders with predominant (111), (100), (011), and (110) facets. A combined experimental and theoretical study, J. Phys. Chem. C 117 (2013) 21382–21395.

[53] M.T. Fabbro, C. Saliby, L.R. Rios, F.A. La Porta, L. Gracia, M.S. Li, Identifying and rationalizing the morphological, structural, and optical properties of beta-Ag2MoO4 microcrystals, and the formation process of Ag nanoparticles on their surfaces: combining experimental data and first-principles calculations, Sci. Technol. Adv. Mater. 16 (2015) 65002–65011.

[54] M.C. Oliveira, et al., On the morphology of $BaMoO_4$ crystals: a theoretical and experimental approach, Cryst. Res. Technol. 51 (2016) 634–644.

[55] H.P. Klug, L.E. Alexander, X-Ray Diffraction Procedures, 1959 (New York).

[56] Y. Gao, Y. Sun, H. Zou, Y. Sheng, X. Zhou, B. Zhang, B. Zhou, Effect of Eu^{3+} doping on the structural and photoluminescence properties of cubic $CaCO_3$, Mater. Sci. Eng. B 203 (2016) 52.

[57] Y.S. Vidya, K.S. Anantharaju, H. Nagabhushana, S.C. Sharma, H.P. Prashantha, C. Shivakumara, Combustion synthesized tetragonal ZrO_2:Eu^{3+} nanophosphors: structural and photoluminescence studies, Spectrochim. Acta Mol. Biomol. Spectrosc. 135 (2015) 241–251.

[58] A. Kokalj, Computer graphics and graphical user interfaces as tools in simulations of matter at the atomic scale, Comput. Mater. Sci. 28 (2003) 155.

[59] D.L. Wood, J. Tauc, Weak absorption tails in amorphous semiconductors, Phys. Rev. B 5 (1972) 3144.

[60] R. Lacomba-Perales, J. Ruiz-Fuertes, D. Errandonea, D. Martınez-Garcıa, A. Segura, Optical absorption of divalent metal tungstates: correlation between the band-gap energy and the cation ionic radius, Eur. Phys. Lett. 83 (2008) 37002.

[61] I.L. Validzic, T.D. Savic, R.M. Krsmanovic, D.J. Jovanovic, M.M. Novakovic, M.C. Popovic, M.I. Comor, Synthesis, strong room-temperature PL and photocatalytic activity of ZnO/$ZnWO_4$ rod-like nanoparticles, Mater. Sci. Eng. B 177 (2012) 645.

[62] J. Ruiz-Fuertes, S. Lopez-Moreno, J. Lopez-Solano, D. Errandonea, A. Segura, R. Lacomba-Perales, A. Munoz, S. Radescu, P. Rodriguez-Hernandez, M. Gospodinov, L.L. Nagornaya, C.Y. Tu, Pressure effects on the electronic and optical properties of AWO_4wolframites (A = Cd, Mg, Mn, and Zn): the distinctive behavior of multiferroic $MnWO_4$, Phys. Rev. B 86 (2012), 125202.

[63] J. Liu, H. Lian, C. Shi, Improved optical photoluminescence by charge compensation in the phosphor system $CaMoO_4$:Eu^{3+}, Opt. Mater. 29 (2007) 1591.

[64] V.M. Longo, L.S. Cavalcante, R. Erlo, V.R. Mastelaro, A.T. de Figueiredo, J.R. Sambrano, S. de Lazaro, A.Z. Freitas, L. Gomes, N.D. Vieira Jr., J.A. Varela, E. Longo, Strong violet–blue light photoluminescence emission at room temperature in $SrZrO_3$: joint experimental and theoretical study, Acta Mater. 56 (2008) 2191.

[65] X.Y. Wu, J. Du, H.B. Li, M.F. Zhang, B.J. Xi, H. Fan, Y.C. Zhu, Y.T. Qian, Aqueous mineralization process to synthesize uniform shuttle-like $BaMoO_4$ microcrystals at room temperature, J. Solid State Chem. 180 (2007) 3288.

[66] S.S. Ding, M. Lei, H. Xiao, G. Liu, Y.C. Zhang, K. Huang, C. Liang, Y.J. Wang, R. Zhang, D.Y. Fan, H.J. Yang, Y.G. Wang, Morphology evolution and photoluminescence of barium molybdate controlled by poly (sodium-4-styrenesulfonate), J. Hernandes Appl. Phys. Lett. 91 (2007), 051923. Journal of Alloys and Compounds 579 (2013) 549.

[67] A.B. Campos, A.Z. Simões, E. Longo, J.A. Varela, V.M. Longo, A.T. de Figueiredo, F.S. De Vicente, A.C. Hernandes, Mechanisms behind blue, green, and red photoluminescence emissions in CaWO4 and CaMoO4 powders, Appl. Phys. Lett. 91 (2017), 051923.

[68] A.P.A. Marques, F.V. Motta, E.R. Leite, P.S. Pizani, J.A. Varela, E. Longo, D.M.A. de Melo, Evolution of photoluminescence as a function of the structural order or disorder in $CaMoO_4$ nanopowders, J. Appl. Phys. 104 (2008), 043505.

[69] J.H. Ryu, J.W. Yoon, C.S. Lim, K.B. Shim, Microwave-assisted synthesis of barium molybdate by a citrate complex method and oriented aggregation, Mater. Res. Bull. 40 (2005) 1468.

[70] A. Speghini, M. Bettinelli, Preparation, structural characterization and luminescence properties of Eu^{3+} - doped nanocrystalline ZrO_2, J. Mater. Res. 20 (2005) 2780–2789.

[71] K. Binnemans, Interpretation of europium(III) spectra, Coord. Chem. Rev. 295 (2015) 1–45.

[72] M. Inokuti, F. Hirayama, Influence of energy transfer by the exchange mechanism on donor luminescence, J. Chem. Phys. 4 (1965) 1978.

[73] F. Wang, X.G. Liu, Recent advances in the chemistry of lanthanide-doped upconversion nanocrystals, Chem. Soc. Rev. 38 (2009) 976.

[74] P. Jena, S.K. Gupta, V. Natarajan, M. Sahu, N. Satyanarayana, M. Venkateswarlu,

Structural characterization and photoluminescence properties of sol–gel derived nanocrystalline $BaMoO_4$:Dy^{3+}, J. Lumin. 158 (2015) 203–210.

[75] G. García-Rosales, et al., Energy transfer from Tb^{3+} to Eu^{3+} ions sorbed on $SrTiO_3$ surface, J. Lumin. 132 (2012) 1299–1306.

[76] L.X. Lovisa, J. Andres, L. Gracia, M.S. Li, C.A. Paskocimas, M.R.D. Bomio, V.D. Araujo, E. Longo, F.V. Motta, Photoluminescent properties of ZrO_2: Tm^{3+}, Tb^{3+}, Eu^{3+} powdersd Acombined experimental and theoretical study, J. Alloys. Compd. 695 (2017) 3094–3103.

[77] G. Blasse, Energy transfer in oxidic phosphors, Philips Res. Rep. 24 (1969) 131.

[78] F. Kang, Y. Zhang, M. Peng, Controlling the energy transfer via multi luminescent centers to achieve white light/tunable emissions in a single-phased X2-Type Y_2SiO_5: Eu^{3+}, Bi^{3+} phosphor for ultraviolet converted LEDs, Inorg. Chem. 54 (2015) 1462.

[79] E.F. Schubert, Light Emitting Diodes, Cambridge University Press, 2003.

[80] R. Robertson, Computation of correlated color temperature and distribution temperature, J. Opt. Soc. Am. 58 (1968) 1528.

[81] C. S. McCamy. Correlated Color Temperature as an Explicit Function of Chromaticity Coordinates, Wappingers Falls, New York 12590-1804.

[82] P. Boutinaud, L. Sarakha, E. Cavalli, M. Bettinelli, P. Dorenbos, R. Mahiou, About red afterglow in Pr^{3+} doped titanate perovskites, J. Phys. D Appl. Phys. 42 (2009) 045106–045112.

[83] F.A. La Porta, A.E. Nogueira, L. Gracia, W.S. Pereira, G. Botelho, T.A. Mulinari, J. Andres, E. Longo, An experimental and theoretical investigation on the optical and photocatalytic properties of ZnS nanoparticles, J. Phys. Chem. Solid. 103 (2017) 179–189.

[84] C.H. Huo, B.S. Wu, P. Gao, Y. Yang, Y.W. Li, H. Jiao, The mechanism of potassium promoter: enhancing the stability of active surfaces, Angew. Chem. 123 (2011) 7541–7544.

[85] C. Burda, X.B. Chen, R. Narayanan, M.A. El- Sayed, Chemistry and properties of nanocrystals of different shapes, Chem. Rev. 105 (2005) 1025–1102.

[86] R.P. Jia, C. Zhang, J.Y. Xu, Morphology-controllable synthesis and characterization of $ZnMoO_4$ nanoparticles, Adv. Mater. Res. 624 (2012) 51–54.

[87] Dongming Wang, Maozhan Huang, Yan Zhuang, Hai-lang Jia, Jianhua Sun, Mingyun Guan, Phase- and morphology-controlled synthesis of zinc molybdate for excellent photocatalytic property, Eur. J. Inorg. Chem. 16 (2017) 4939–4946.

Journal of Alloys and Compounds 722 (2017) 981–995

Contents lists available at ScienceDirect

Journal of Alloys and Compounds

journal homepage: http://www.elsevier.com/locate/jalcom

Mechanism of photoluminescence in intrinsically disordered $CaZrO_3$ crystals: First principles modeling of the excited electronic states

Marisa Carvalho Oliveira [a, b], Lourdes Gracia [c, *], Marcelo de Assis [b], Ieda Lúcia Viana Rosa [b], Maria Fernanda do Carmo Gurgel [d], Elson Longo [b], Juan Andres [a]

[a] *Department of Analytical and Physical Chemistry, University Jaume I (UJI), Castello, E-12071, Spain*
[b] *CDMF-UFSCar, Universidade Federal de São Carlos, PO Box 676, 13565-905, São Carlos, SP, Brazil*
[c] *Department of Physical Chemistry, University of Valencia, Burjassot, E-46100, Spain*
[d] *Department of Chemistry, Universidade Federal de Goias, Regional Catalão, Av. Dr. Lamartine Pinto d eAvelar, 75704-020, Catalão, GO, Brazil*

ARTICLE INFO

Article history:
Received 31 January 2017
Received in revised form
1 June 2017
Accepted 5 June 2017
Available online 28 June 2017

Keywords:
PL emissions
Excited electronic states
DFT calculations
Order-disorder

ABSTRACT

CaZrO3 (CZO) powders obtained by the polymeric precursor method at 400 C, and then, the samples were annealed at different temperatures (400, 600, 800, and 1000 C) and characterized by X-ray diffraction, Raman and ultraviolet–visible spectroscopic methods, along with photoluminescence (PL) emissions. First principle calculations based on the density functional theory (DFT), using a periodic cell models, provide a theoretical framework for understanding the PL spectra based on the localization and characterization of the ground and electronic excited states. Fundamental (singlet, *s*) and excited (singlet, s^*, and triplet, t^*) electronic states were localized and characterized using the ideal and distorted structures of CZO. Their corresponding geometries, electronic structures, and vibrational frequencies were obtained. A relationship between the different morphologies and structural behavior has also been established.

Polarized structures were identified by the redistribution of the $4d_z2$, $4d_{yz}$, and $4d_{xy}$ (Zr) orbitals at the conduction band and the $2p_z$ (O) orbital in the valence band for *s*, s^* and t^*. Analysis of the vibrational eigenvector modes of these electronic states reveals a relationship between them via asymmetric bending and stretching modes that arise from Zr atom displacements due to polyhedral $[ZrO_6]$ distortion. Furthermore, the results provided an insight into the PL emissions of the as-synthesized $CaZrO_3$ and led to the conclusion that the presence of electronically excited states is strongly related to the structural order-disorder effects (polyhedral distortion) at short range for both $[ZrO_6]$ and $[CaO_8]$ clusters.

1. Introduction

The importance of the local structure in determining the observable properties of a material has been discussed since the advent of crystallography [1]. Therefore, the physical and chemical properties of ceramics are intimately linked to their local structure, characterized by the regular and repeating geometry associated with the primitive lattice. While the concept of a crystalline solid as a perfect, periodic structure is at the core of our understanding of a wide range of material properties, disorder is in reality ubiquitous, and can influence various properties drastically. In typical ferroelectric crystals, the polarization and related properties result from structural lattice distortions. For example, in $BaTiO_3$, the off-centering displacement of Ti in the $[TiO_6]$ octahedron is the origin of its exceptional dielectric properties [2]. Very recently, different possibilities to explain the PL emissions in crystalline $Ba(Zr_xTi_{1-x})O_3$ were associated to the isomorphic Zr/Ti substitutions and structural distortions at the $[ZrO_6]$ octahedra [3].

According to the electronic band theory, band formation requires a periodic potential, typically established by regularly spaced atoms in a crystal lattice. When this periodicity is perturbed—for example, when electromagnetic radiation interacts with matter—the structural and electronic order-disorder effects appear, inducing the presence of intermediate states within the band gap, as well as enhancing the anisotropy of the chemical bonds in the materials. These effects are concomitant with the presence of excited electronic states from the ground state after the activation process, determining to a larger extent the efficiency and the

---

* Corresponding author.
E-mail address: lourdes.gracia@uv.es (L. Gracia).

http://dx.doi.org/10.1016/j.jallcom.2017.06.052
0925-8388/© 2017 Elsevier B.V. All rights reserved.

spectral features of emitted radiation. Following the classical paper of Blasse [4], the luminescence of self-activated closed-shell transition metal oxides is basically of charge transfer character.

In this context, PL emission is well suited for the characterization of crystalline materials based on broad band gap semiconductors. In particular, our group is involved in a research project on binary and complex metal oxides as potential alternatives to traditional metal activator based phosphors, because of their advantages of low toxicity, stability, tunable emission color, and low cost. These oxides include TiO_2 [5], ZnO [6], ZnS [7], SnO_2 [8], molybdates [9–11], and tungstates [12,13]. Among the numerous types of perovskite materials (ABO_3), alkaline earth metal perovskite oxides are a veritable gold mine of diverse physical and chemical properties with large technological applications [14–21] based on ferroelectricity, piezoelectricity, non-linear optical behavior, and PL emissions, that arise from the absence of inversion symmetry in a crystal structure [22]. ABO_3 perovskite compounds have a large cation at the A-site, a smaller cation at the B-site, and the oxygen O acts as a bridging ligand, linking the B-site cations to form a three-dimensional cage-like host framework consisting of anionic $[BO_3]$ cages enclosed by 12 B–O-B fragments and filled by A-site guest cations. The ideal structure of perovskite oxides has the cubic space group Pm3m, and the structural variations from the ideal cubic prototype mainly arise from the displacement of the A- and B-site cations and the tilting of the $[BO_6]$ octahedra, based on Glazer's exhaustive classification of the tilted octahedral [23,24].

Symmetry-breaking processes have long played a central role in the design of functional materials. An important example is the rich PL behavior in the ABO_3 perovskite oxides which originate, at least in part, from the structural and electronic order-disorder effects of the $[BO_6]$ octahedra through distortions and rotations. Octahedral rotations provoke changes in the B-O and A-O bond lengths as well as B-O-B and A-O-A bond angles, shifting the positions of the oxygen ions from the edges of the cubic perovskite structure [25]. The overall result is that the unit cell deforms and the structure is no longer cubic but of reduced symmetry, such as orthorhombic, rhombohedral, tetragonal, monoclinic, and triclinic phases, depending on the details of the $[BO_6]$ octahedral rotations and B-site distortions. This influences the electronic and optical properties of materials, behavior of photo-generated charge carriers, including excitation, transfer, and redox reactions, and plays an important role in their technological applications [6,17,26–30]. It should be realised that the absorption transition of the $[BO_6]$ cluster corresponds to an electron transition from a bonding to a nonbonding molecular orbital, i.e. the chemical bond is perturbed, so that the $[BO_6]$ cluster is distorted.

The disorder is considered intrinsic if it is associated with the localization of electrons and electron holes, provoking the presence of different electronic states within the band gap. These electronic states are responsible for the PL behavior. The excitation induced by electromagnetic radiation promotes electrons from the valence band (VB) to the conduction band (CB) by this process. These phenomena originate from the interactions between matter and external incoming light, and an electronic excited state is obtained when a system (crystal) is in an energy level higher than the ground state, e.g., after the absorption of one or more quanta of light (photons). The structure and charge distribution of both fundamental and electronic excited and short-lived states are key to understanding the optical properties. It is necessary to emphasize that PL emissions are microscopic in origin and the structures of these short-lived excited states are difficult to obtain. Excited electronic states reveal information about the electronic structures of the material, but they are short-lived and highly reactive, making the quest to manipulate them extremely demanding.

The difficulties encountered in separating complex factors during experiments are not present when employing theoretical models based on quantum mechanics, which is a reliable tool to describe these systems at the microscopic scale. Consequently, one has to resort to quantum chemical simulations to provide a better understanding of experiments in order to help in ascertaining the geometry and electronic structure of the electronic excited states and therefore prediction, of the PL behavior. However, modeling the structure of excited electronic states and their properties using the first-principles electronic structure methods is still a huge challenge. To overcome this difficulty, numerous efforts by our research group have been made to understand the mechanism of PL emissions in $SrTiO_3$, $SrTiO_3$:Sm, $CaWO_4$, $BaZrO_3$, and $BaZr_{1-x}Hf_xO_3$ solid solutions based on the characterization of excited electronic states [31–37], where the computational cost is significantly reduced by imposing periodic boundary conditions.

Calcium zirconate, $CaZrO_3$ (CZO), has received a lot of attention due to its exceptional dielectric and catalytic properties and PL emissions with applications in diverse areas of science and technology such as hydrogen sensors, luminescence hosts, multilayer capacitors, catalysis, and so on [38–48] CZO presents an orthorhombic structure with 8 and 6-coordination for the Ca and Zr atoms, $[CaO_8]$ and $[ZrO_6]$, respectively, as the constituent building blocks of this material [49]. There are several reports on the electronic structure calculations performed to study CZO in the ground state [50–55]. Recently, Gupta et al. [56] have been performed a spectroscopic and theoretical study to explain the PL emission in the blue region based on the nature of defects, while Moreira et al. [57] employed first-principles calculations to clarify the mechanisms involved in the luminescence emissions observed for disordered $BaZrO_3$, proposing a novel explanation for transitions from a PL and to a radioluminescence emission regime based on crystalline defects.

Nevertheless, no insights about the PL emissions based on the presence of electronic excited states have been obtained. The focus of this article is to expand the theoretical understanding of the phenomena in CZO as a result of an analysis of the electronic excited states. First principles calculations are employed in the present research, and we argue that because our procedure generates models in accord to the experiment, our methodological approach is valid. In addition, a careful examination of the calculated results provides an insight into the physical origin of the process that accounts for the PL behavior of CZO materials. Full details, describing the generation of the atomistic models are presented in the Supplementary Information.

In the present work the focus is the PL mechanism and its relationship with the presence of excited electronic states in intrinsically disordered $CaZrO_3$ crystals, and we seek to fulfill a three-fold objective: synthesis and characterization by X-ray diffraction (XRD), Raman and UV–Vis spectroscopy, and PL emissions of the as-synthesized CZO samples; employment of first principles calculations based on the density functional theory (DFT), at B3LYP level, to localize and characterize (geometry, electronic properties, and vibration frequencies) both ground and excited electronic states of CZO (electronic structures, including density of state (DOS) and band structures were calculated based on optimized geometries); and the achievement of a relationship between structural and electronic order-disorder effects and PL emissions.

The remainder of the paper is organized as follows; the analysis and discussion of both theoretical and PL results are presented in Section 3. The main conclusions are given in Section 4.

2. Experimental procedures and computational details

2.1. Synthesis and characterization

The powder CZO was prepared by the polymeric precursor method, kept for 4 h at 400 C to eliminate any remaining carbon. CZO samples were then annealed at 400, 600, 800 and 1000 C for 2 h. This procedure has been performed to obtain different perovskite-based materials by our research group [27,58]. The annealed samples at 400, 600, 800 and 1000 C were characterized by XRD (Rigaku DMax2500PC) using Cu Kα (λ) 1.5406 Å radiation. The data were collected from 10 to 120 in the 2θ range with 0.5 divergence slit, 0.3 mm receiving slit, in fixed-time mode with 0.02 step size and ls/point. Crystal structures were identified and refined by the Rietveld method using the GSAS software [59]. This software is specially designed to refine simultaneously both the structural and the microstructural parameters through a least squares method. The peak profile function was modeled using the convolution of the Thompson-Cox-Hastings pseudo-Voigt (pV-TCH) with the asymmetry function described by *Finger* et al. [60]. The Rietveld refinement is presented in a previous reported study [61], and provides the network parameters a, b, and c as well as internal coordinates, space group of the CZO and refinement of quality indicators.

PL spectra we are measured with an Ash Monospec 27 monochromator (Thermal Jarrel, U.S.A.) and a R4446 photomultiplier (Hamamatsu Photonics, U.S.A.). The 350 nm excitation wavelength of a krypton ion laser (Coherent Innova 90 K) was used as excitation source, keeping its maximum output power at 200 mW. XRD and Raman spectra, and PL measurements were carried out at room temperature for annealed samples at 400, 600, 800 and 1000 C.

2.2. Computational details

Theoretical calculations were performed using the periodic quantum mechanical method implemented with the computer program CRYSTAL14 [62]. The computational method used is based on density functional theory (DFT) together with the B3LYP functional [63]; [64]. This computational technique has been successful for the study of the electronic and structural properties of various materials including perovskites and several other oxides [36]; [65]. The standards (6-31d1G) all electron basis set were used to describe the atomic orbitals of calcium [66], zirconium [67] and oxygen [68] atoms. The diagonalization of the Fock matrix was performed at 27 or 36 *k*-points grids in the reciprocal space for bulk singlet (s) or excited singlet (s*) and triplet (t*) electronic states, while 9 or 10 *k*-points grids were used for surfaces in singlet (s and s*) or triplet (t*), respectively, of the CZO system. The thresholds controlling the accuracy of the calculation of the Coulomb and exchange integrals were set to 10^{8} (ITOL1 to ITOL4) and 10^{14} (ITOL5), and the percent of Fock/Kohn-Sham matrices mixing was set to 40 (IPMIX keyword) [69]. The XCrysDen program was used as a graphical tool to design the spin density plots and VESTA program was used for the design of morphology.

We use periodic models to find the ground and excited electronic states. A 1 1 1 cell was used as a periodic model to

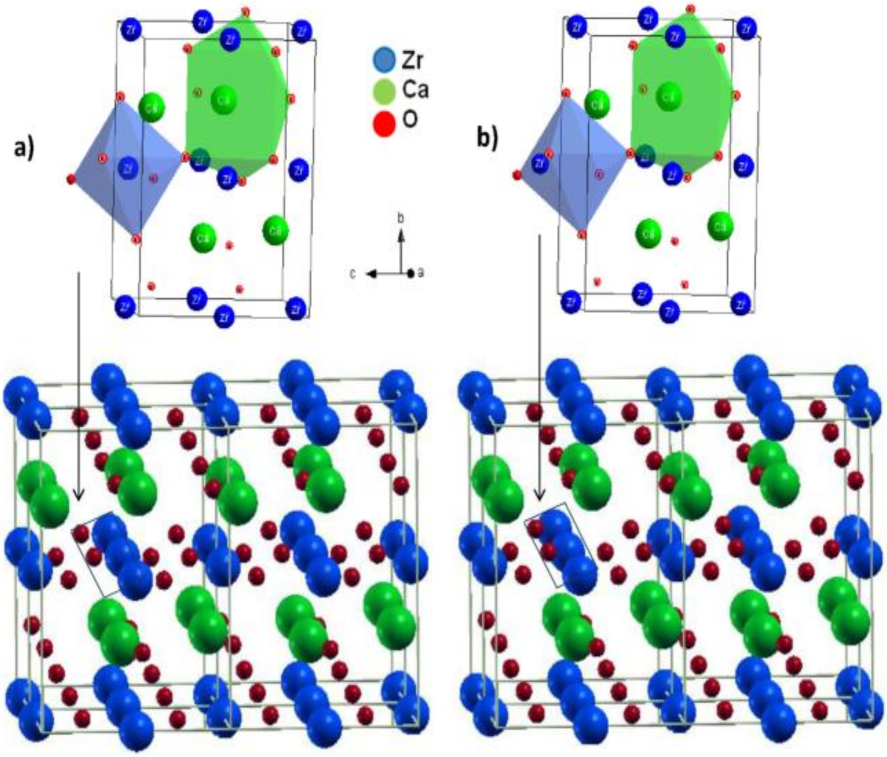

Fig. 1. Cell 1 1 1 for modeling the electronic states of CZO and the corresponding expansion along a and c directions: a) singlet electronic state, s, and b) excited singlet, s*, and triplet, t*, electronic states.

represent the fundamental *s* electronic state, while s* and t* excited electronic states were modeled by shifting the zirconium by a (0.0 0.0 0.2) Å vector from its previous position in the cell (Fig. 1a and b).

CZO presents an orthorhombic structure with space group *Pcmn*. An excited state is obtained by imposing a low and high spin state that must promote an electron from the VB to the CB. Per unit cell, this transaction corresponds to imposing two electrons with the opposite (singlet) and same spin (triplet). It also creates a Frenkel exciton (hole in the VB, electron in the CB). To find the excited electronic states, two arrangements have been explored based in the same model but changing the optimization conditions: i) Zr displacement from the center of a [ZrO_6] octahedron in the orthorhombic CZO, followed by an arising of a spontaneous polarization from this asymmetrical structure, resulting in the Jahn–-Teller effect [70], fixing the cell parameters to obtain the excited singlet, s*; ii) Zr displacement from the center of a [ZrO_6] octahedron, in which the position of the six nearest oxygen atoms surrounding the Zr atom is optimized as well as cell parameters to find the excited triplet, t*, in which, distorted clusters [CaO_8] are also obtained. Then, a series of calculations were carried out on each different electronic states in order to determine their electronic structures and the specific atomic states which make up their corresponding energies. This information is used to understand the transitions associated with PL emission behavior.

Vibrational analysis for ground and excited electronic states in their equilibrium configurations has been made to ensure that there are no imaginary frequencies corresponding to the saddle points on the potential energy surface. It is well known that DFT calculation at B3LYP method tends to overestimate the values of the vibrational frequencies; therefore, a scaling factor of 0.94 is used [71].

Slab models containing in singlet 8 molecular units (in singlet state) and 4 molecular units (in triplet state) for (121), (100), (010), (101), (001), (111), and (011) surfaces, respectively, were considered, after corresponding energy convergence tests. The surface energy is calculated by using the following equation:

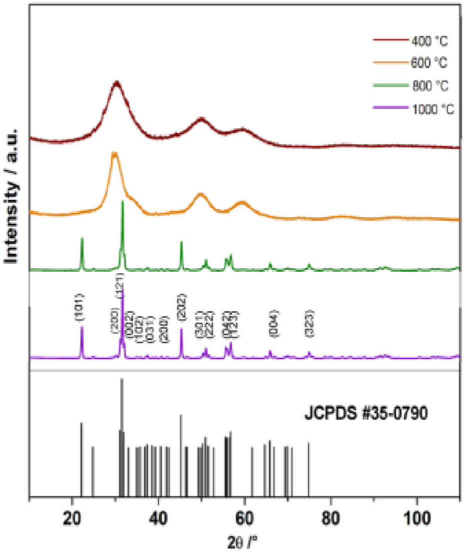

Fig. 2. XRD patterns of the CZO powders annealed at different temperatures for 2 h.

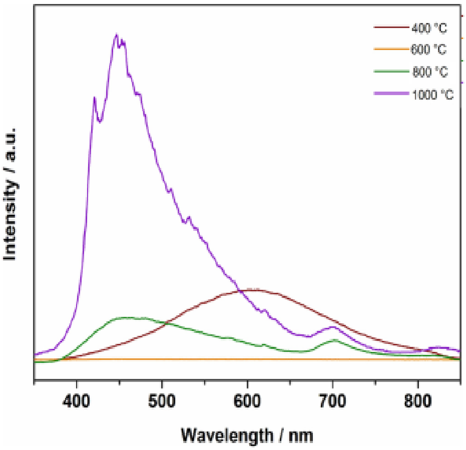

Fig. 3. Photoluminescence spectra of the CZO powder annealed at different temperatures.

$$E_{suf} = \frac{1}{2A}\left(E_{slab} \quad N\, E_{bulk}\right)$$

where A is the surface area of each slab, N is the number of molecular units, E_{slab} is the total energy of the slab, E_{bulk} is the total energy per molecular unit for the CZO unit cell. A classic Wulff construction can be obtained, from calculated E_{surf} values, that minimizes the total surface free energy at a fixed volume.

3. Results and discussion

3.1. X-ray diffraction analysis

The X-ray diffraction patterns for the CZO sample at different temperatures are shown in Fig. 2, and indicate a single phase orthorhombic perovskite with the *Pcmn* space group. The diffraction peaks were indexed based on the JCPDS 35-0790 file and the crystallization of CZO is observed. In annealed samples at 400 and

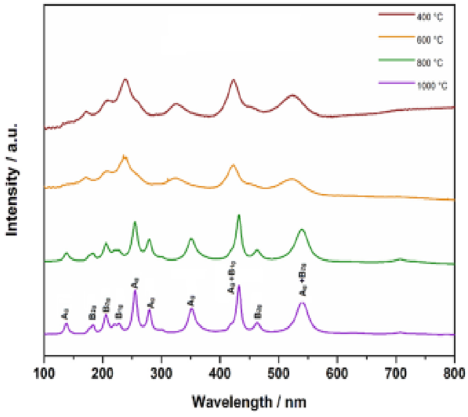

Fig. 4. Raman spectra of CZO powder annealed at different temperatures. The positions of the active modes are indicated.

600 C, the peaks appear more widened and the material is structurally less organized at long range and disordered at short range, involving disordered [CaO_8] and [ZrO_6] clusters, as constituent building blocks of CZO; this behavior can be attributed to structural distortion from the parent high-symmetry structure.

3.2. Photoluminescence properties

Fig. 3 displays the PL emission spectrum of the CZO sample annealed at 1000 C. An emission band extending from 350 to 850 nm and peaking around 450 nm is seen. Additionally, low PL emission intensity was observed at annealed samples at 400 and 800 C, while at 600 C the PL emission is absent. This indicated that the PL behavior of CZO is sensitive to temperature, and a high PL emission requires a certain amount of order together with disorder in the CZO samples. This is also indicated by the diffraction peaks in Fig. 3, which become broader indicating an increase of structural order at short range at both annealed samples at 800 and 1000 C in the lattice. The PL emissions of perovskite-based materials depend on different aspects, among them the excitation wavelength and synthesis method. In the present work both factors are different of those used in the paper by Gupta et al. [56]. Our results are in line with previous results on different perovskite-based materials [27,72].

3.3. Raman spectra

The Raman spectra with ten active modes are shown in Fig. 4.

CZO with the orthorhombic structure and D^{16}_{2h} (*Pcmn*) symmetry group, presents the following irreducible representations at the Γ point of the Brillouin zone and distribution among the following symmetries:

$$8A_u + 10B_{1u} + 8B_{2u} + 10B_{3u} + 7A_g(R) + 5B_{1g}(R) + 7B_{2g}(R) + 5B_{3g}(R) \quad (1)$$

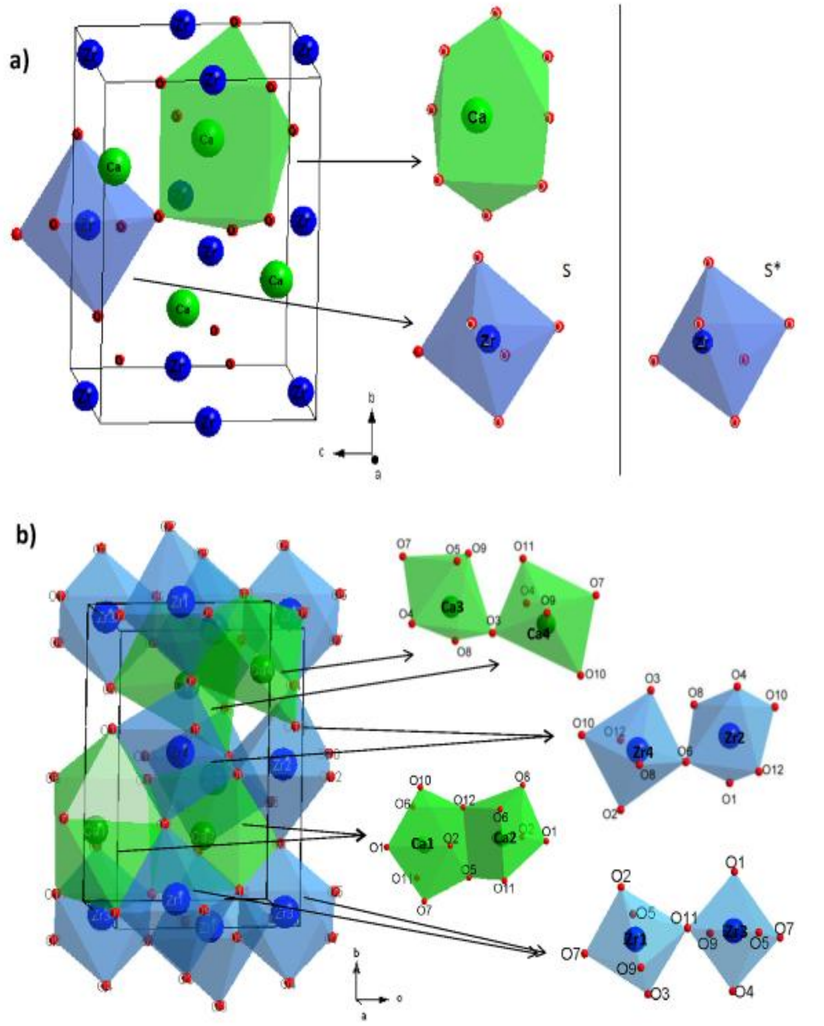

Fig. 5. Electronic states of CZO in terms of cluster constituents: a) singlet and excited singlet electronic states, s and s*, respectively and b) excited triplet electronic state, t*.

Table 1
Bond distances for the fundamental singlet electronic state (s) and excited (s*) and triplet (t*) electronic states 1x and 2x refers to the multiplicity of the bond.

s				t*					
	Bond		(Å)		Bond	(Å)		Bond	(Å)
Ca	O1	1x	2.341	**Ca1**	O1	2.348	**Ca2**	O2	2.348
	O2	2x	2.362		O11	2.433		O12	2.433
	O1	1x	2.461		O6	2.447		O1	2.447
	O2	2x	2.679		O2	2.449		O5	2.449
	O2	2x	2.844		O12	2.583		O8	2.583
					O5	2.669		O6	2.669
					O7	3.050		O9	3.050
					O10	2.814		O11	2.814
				Ca3	O3	2.301	**Ca4**	O4	2.301
					O9	2.346		O7	2.346
					O8	2.381		O10	2.381
					O4	2.408		O3	2.408
					O5	2.573		O11	2.573
					O7	2.656		O9	2.656
					O10	3.027		O6	3.027
					O12	3.272		O8	3.272
Zr	O2	2x	2.100	**Zr1**	O9	2.160	**Zr2**	O12	2.160
	O2	2x	2.091		O2	2.171		O6	2.171
	O1	2x	2.097		O7	2.179		O4	2.179
					O5	2.190		O8	2.190
	s*				O11	2.159		O1	2.194
	Bond		**(Å)**		O3	2.186		O10	2.292
Zr displ.	O2	1x	1.657	**Zr3**	O1	1.995	**Zr4**	O6	1.995
	O2	1x	2.596		O9	2.096		O8	2.096
	O2	1x	1.839		O4	2.128		O3	2.128
	O2	1x	2.455		O7	2.131		O12	2.131
	O1	1x	2.232		O11	2.174		O2	2.174
	O1	1x	2.116		O5	2.294		O10	2.294

a = 5.594 Å, b = 8.021 Å and c = 5.761 Å for s and s* states.
a = 5.673 Å, b = 8.155 Å and c = 5.844 Å for t* state.

where $7A_g + 5B_{1g} + 7B_{2g} + 5B_{3g}$are a total of 24 Raman (R) active modes, $9B_{1u}$+ $7B_{2u}$+ $9B_{3u}$ are the 25 infrared active modes, $8A_u$ are non-active modes, along with three translational modes (B_{1u} +B_{2u} +B_{3u}) [73,74].

The Raman spectra with ten active modes are shown in Fig. 4. The bands in the range 140–300 cm^{-1} are associated with O-Zr-O torsion modes. The bands at 433 and 464 cm^{-1} are related to the O-Zr-O bending modes and the band at 537 cm^{-1} results from the Zr-O stretching mode. The Raman spectrum of annealed sample at 900 °C was previously reported and compared to other experimental studies [75], showing that this kind of system is typically observed in the low wave number range 145–547 cm^{-1} [73], 143–545 cm^{-1} [76], 153–515 cm^{-1} [77].

The appearance of three vibration modes of annealed sample at 1000 °C, which are not present at temperatures of annealed samples at 400 and 600 °C, was noted. This can be associated with the local distortion of the [ZrO_6] octahedra, causing a breakdown of the Raman selection rules and the presence of weak bands in the Raman spectra. Then, the PL emissions can then be related to the appearance of new vibrational modes at 1000 °C.

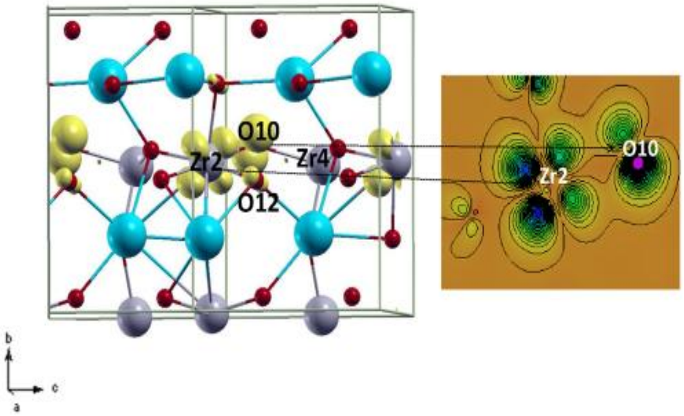

Fig. 6. Spin density localization for the t* state of CZO: a) 3D representation where the spin density is localized (yellow color) in $4d_{z^2}$, $4d_{yz}$ and $4d_{xy}$ of Zr2 atom and $2p_z$ of O10 atom. b) Projection on a plane (passing through Zr2-O10-O12 atoms) in which atoms with highest spin density are included. (For interpretation of the references to colour in this figure legend, the reader is referred to the web version of this article.)

3.4. *Theoretical study*

The ground state of CZO has an orthorhombic structure, with both [ZrO_6] and [CaO_8] clusters as the building blocks. To find excited electronic states, different models have been used to achieve a slight distortion in the [ZrO_6] octahedra. The transformation from the fundamental *s* to *s** states occurs following a displacement of 0.2 Å, for 25% of the Zr atoms along the (001) direction. As a result of Zr atom displacement from the center of the [ZrO_6] octahedron, a spontaneous polarization is produced and a Jahn–Teller effect and asymmetrical relaxation of the six nearest oxygen atoms surrounding the Zr atom in the [ZrO_6] cluster occurs.

However, the transformation from the fundamental *s* to *t** states is produced by a slight distortion of [ZrO_6] and [CaO_8] clusters with a structural order-disorder effect in the Zr-O and Ca-O bonds of CZO. An analysis of the results shows that the transformation from the fundamental *s* to *s** is produced by a slight distortion of [ZrO_6] clusters on a very flat energy surface. For the *t** state an expansion of cell parameters of ~1.5% is found: the *a* parameter increases from 5.594 to 5.673 Å, *b* parameter from 8.021 to 8.155 Å, and *c* parameter from 5.761 to 5.844 Å. In particular, the displacement of the Zr atom causes a slight distortion of both Zr2 and Zr4 clusters, as well as the Ca3 and Ca4 clusters, the latter forming [CaO_{6+2}] clusters. A schematic representation of the unit cells in terms of their cluster constituents is presented in Fig. 5. The Ca-O and Zr-O bond distances for the three systems, *s*, *s**, and *t** configurations are listed in Table 1.

It is important to note that the Zr-O bond distances in the *t** state are stretched and shortened to 2.294 and 1.995 Å, respectively (see Table 1), and this effect can be related to the structural order-disorder effect associated with the appearance of PL at 1000 C.

The characterization of the spin density distribution can be useful for understanding the PL properties of CZO that are based on the behavior of the d-orbitals occupied by unpaired electrons, that is the difference between the contributions from spin alpha and beta to the total electron density. The spin charge density localized in the *t** state is shown in Fig. 6, in which Zr2 and O10 are the atoms with the highest spin density. The spin charge density is mainly located in the $4d_z2$, $4d_{yz}$, and $4d_{xy}$ orbitals of Zr2 and the O10 $2p_z$ orbital.

The results presented in Fig. 6 and Table 1 indicate that the triplet state is achieved by a structural distortion. This order-disorder effect may also be noted in the behavior of PL of CZO, which is highly sensitive to temperature. This behavior is due to the appearance of various electronic levels at this temperature, i.e., intermediate states that are brewing in the band gap. This fact is directly related to the redistribution of local density around Zr and Ca cations that is proportional to the local distortions at both [ZrO_6] and [CaO_8] clusters as well as to torsion movements involving [ZrO_6]-[CaO_8] frameworks. In this way, different types of defects can generate intermediate states and directly influence the band gap.

The PL analysis shows an intracluster organization (short range order), but indicates a disorder between the clusters (medium range order). At medium range the interactions occur by orientation and are associated with the rotation of the dipole moments [ZrO_6]-[ZrO_6], [CaO_8]-[CaO_8] or [ZrO_6]-[CaO_8]. At short range the interactions arise through an induction by permanent dipole moment of the neighboring cluster [CaO_8] or [ZrO_6], i.e. polarization of clusters, and at long range a dispersion from the correlation between electrons in the vicinity of clusters [ZrO_6] or [CaO_8] takes place.

These structural changes are related to theoretical results that have shown that the process of breaking of symmetry (order/disorder) in a structure is a necessary condition for the existence of energy levels in the forbidden band gap. Therefore, for the present, it is considered that within the CZO network, structural distortions emerge between the [$ZrO_6{}^{x}_{o}$] [$ZrO_6{}^{x}_{d}$] and/or [$CaO_8{}^{x}_{o}$] [$CaO_8{}^{x}_{d}$] (o-ordered; d-distorted) clusters that allow transfers electronics between them.

3.4.1. *Vibrational analysis*

There are 24 Raman-active modes for the orthorhombic structure of CZO according to Equation (1). However, as noted previously (Section 3.3) not all of these bands can be observed experimentally. It is possible that many of the predicted modes are hidden by other intense bands, which may overlap or involve very low changes in the polarizability.

In Table 2 the theoretical calculated values are presented and compared to experimental data at different temperatures. An analysis of the results shows some discrepancies in a few cases, and to shed light on them a representation of Raman vibration movements above 370 cm ^{1} are depicted in Fig. 7a. The A_g mode (at 370.49 cm ^{1}) corresponds to a Zr-O-Ca bending motion between the clusters, whereas higher values at ~480 cm ^{1} are associated with the O-Zr-O bending. A sum of the B_{1g} and A_g modes is obtained experimentally at ~430 cm ^{1} that corresponds to the theoretical modes at 434.82 and 450.96 cm ^{1}, whereas the theoretical B_{3g} mode at 479.59 cm ^{1} is not seen in the experiments. An asymmetric stretching of Zr O in the [ZrO_6] cluster is observed at ~460 cm ^{1} (B_{1g}), which can be compared to the theoretical mode obtained at 522.21cm ^{1}. This mode has appeared at 515 cm ^{1} experimentally in previous works [77,78]. Another asymmetric stretching of Zr-O in the [ZrO_6] cluster is observed at ~540 cm ^{1} (B_{2g}+ A_g), which is depicted in the lower part of Fig. 7a and can be compared to theoretical modes obtained at 537.44 and 544.99 cm ^{1}. Three theoretical stretching modes above 700 cm ^{1} are also obtained, which are not observed experimentally.

The higher stretching modes up to 480 cm ^{1} are depicted in Fig. 7b for the *t** state, while in Table S1 (of Supporting Information),

Table 2
Raman active modes for s electronic state, compared to experimental data annealing at different temperatures.

Theoretical			Experimental		
Mode,	(cm^{-1})	Corrected[a] (cm^{-1})	Temperature (C)		
			400/600	800	1000
A_g	127.82	120.15		137.90	137.90
B_{1g}	164.69	154.81			
B_{2g}	169.64	159.46	171.44	182.97	183.1
A_g	194.41	182.75			
B_{2g}	203.30	191.10	203.51	205.69	205.69
B_{2g}	225.97	212.41			
B_{2g}	227.59	213.93			
B_{1g}	246.54	231.75		225.91	227.56
A_g	280.77	263.92	238.50	255.26	255.26
A_g	296.77	278.96		279.32	279.32
B_{3g}	317.44	298.39			
B_{2g}	372.05	349.73			
B_{3g}	387.97	364.69			
A_g	394.14	370.49	324.91	351.49	351.49
B_{3g}	457.78	430.31			
B_{1g}	462.57	434.82	422.29	432.40	432.40
A_g	479.75	450.97			
B_{3g}	510.21	479.60			
B_{1g}	555.54	522.21			
B_{2g}	571.74	537.44		463.02	463.02
A_g	579.78	544.99	522.79	540.29	540.29
B_{2g}	737.33	693.09			
B_{3g}	797.02	749.20			
B_{1g}	808.01	759.53			

[a] 0.94 = scaling factor.

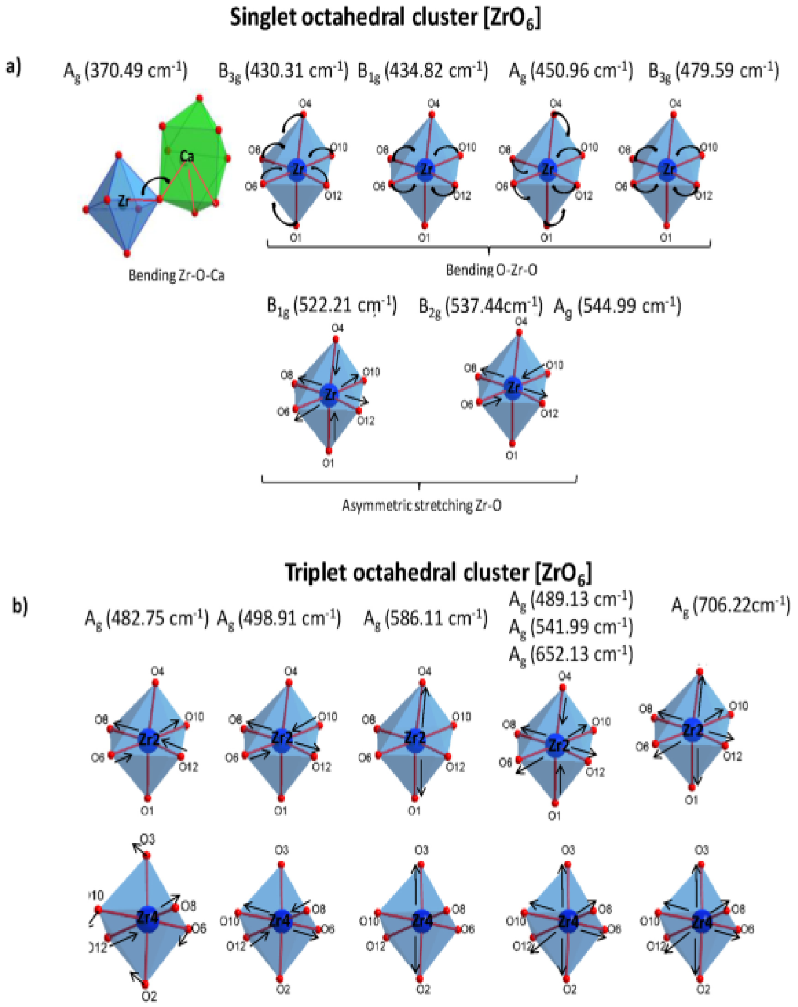

Fig. 7. Theoretical Raman active modes of CZO crystal involving octahderal $[ZrO_6]$ cluster: a) singlet fundamental state, s, and b) triplet excited state, t^*.

the corresponding values for the s^* state is also included for comparison purposes. In both cases, all the modes present A_g symmetry. An analysis of the results shows that the transformation from the fundamental s to s^* is produced by a slight distortion of the $[ZrO_6]$ clusters. The orthorhombic form undergoes a displacive transition to a lower symmetry without bond breaking, which involves the structural order-disorder effect and can be associated to the Zr-O asymmetric stretching mode at 544.99 and 544.28 cm^{-1} for s and s^*, respectively. On the other hand, the transition from s^* to t^* excited electronic states can associated to vibrational movements along 544.28 cm^{-1} and 541,99 cm^{-1} for s^* and t^*, respectively. However, it is important to note that the pathways to reach both s^* and t^* electronic state imply a new spin rearrangement which supports a structural distortion resulting in new electronic configurations.

Optical properties such as PL are strongly dependent upon the structural and morphological features of the crystal system. Structural order–disorder associated effects are a crucial factor in determining the optical behavior of a material [79,80]. During the PL process, a symmetry breaking occurs at short order involving two clusters, i.e., structural distortions associated with the imperfect coordination mainly related to the Zr sites. Then, the under-coordination associated with distorted $[ZrO_6]$ and $[CaO_{6+2}]$ clusters appear. The electron distribution is useful to predict the physical properties and it plays an important role in determining the lattice structure, the DOSs, and the charge density. These structural and electronic changes can be related to the variation of polarization between distorted clusters that are capable of populating stable excited electronic states and hence result in active vibrational Raman modes. The triplet excited state has a higher energy than the excited singlet state; although the s^* state seems to be much more likely to occur, the two states would possibly be reached by irradiation during experimental measurements. Obviously, the decay process involves more than just two electrons, but in our model, two electrons per cell were used. In this study, we associate the experimental results related to characterization methods to theoretical results. On this basis, monitoring the energy and geometry of the singlet and triplet excited states will provide further insight into the PL mechanism. Furthermore, analyzing the relationship of these vibrations and geometries offers the opportunity to interpret the excited states in a new and possibly more intuitive way, linking electronic excitations with the concept of vibrational modes as being mainly responsible for PL behavior.

3.4.2. *Band structure and density of states*

The electron distribution plays an important role in determining the lattice structure, the DOS, and the charge density. The band structures plotted along the path Γ, Y, X, S, Z, T, U, R, and Γ for the *s*, *s**, and *t** electronic states, are depicted in Fig. 8a–c.

The band structure observed in Fig. 8a–c reveals a new configuration from spin alpha to spin beta, with a notable reduction of the energy gap value (from 6.23 eV in s and 6.14 eV in s* to 3.5 eV in t*). In order to understand the electronic structure of the CZO powders, the ground- and excited-density of states (DOS) are calculated. The total DOS and projection on atoms is shown in Fig. 9a–c, where the electronic contributions of the atoms in CZO can be noted in the *s*, *s**, and *t**states, respectively. In addition, the electronic contributions of the atomic orbitals are presented in Fig. 10a–c for the *s*, *s**, and *t** states, respectively.

Analysis of the electronic structure of the *s*, *s**, and *t** states (Figs. 9 and 10) demonstrated that the upper valence band is predominantly formed by the 2p (p_x, p_y, p_z) states of all the O atoms in the cell and the bottom of the conduction band is mainly formed by the 4d (d_{xz}, d_{xy}, d_{yz}, d_{z2}, $d_{x2\text{-}y2}$) states of the Zr atom. (Fig. 10a and b) indicates that the *s* and *s** state presents an orthorhombic structure with the Zr atomic orbitals described as 4d$_z$2, 4d$_{yz}$, and 4d$_{xy}$with a band gap value of 6.23 and 6.14 eV, respectively.

For the *t** state, the displacement of the Zr atom causes a slight distortion of the Zr4-O6, Zr4-O10, and Zr2-O10 bonds (as seen in Table 1), leading to the creation of localized states and a decrease in the gap energy. The calculated gap energy for this model alpha-beta is 3.5 eV.

The DOS in Fig. 10b reveals that these localized states are of 2p character, arising mainly from the 2p states of the oxygen O1 and O2, which are loosely connected to the Zr atom. This can be explained due to the asymmetry generated by the displacement of Zr along the z-axis.

The aforementioned experimental and theoretical results strongly indicate that PL is related to the structural short and long range order in the lattice. X-ray diffraction patterns showed a progressive structural disorganization of the powders milled for different times. The PL intensity increases when the powder is submitted at high temperature and its optical E$_{gap}$ value decreases. This disorder caused in the system is a favorable condition to generate an intense and broad PL band. In this context, the results obtained for the triplet state indicate the existence of energy levels in the gap region, which decrease the value of the band gap and enable PL emissions.

3.5. *Morphology study*

A study of the morphology of CZO in the *s* and *t** states is presented in Fig. 11a and b, respectively. The variation in the equilibrium shapes for these systems using the Wulff construction is a

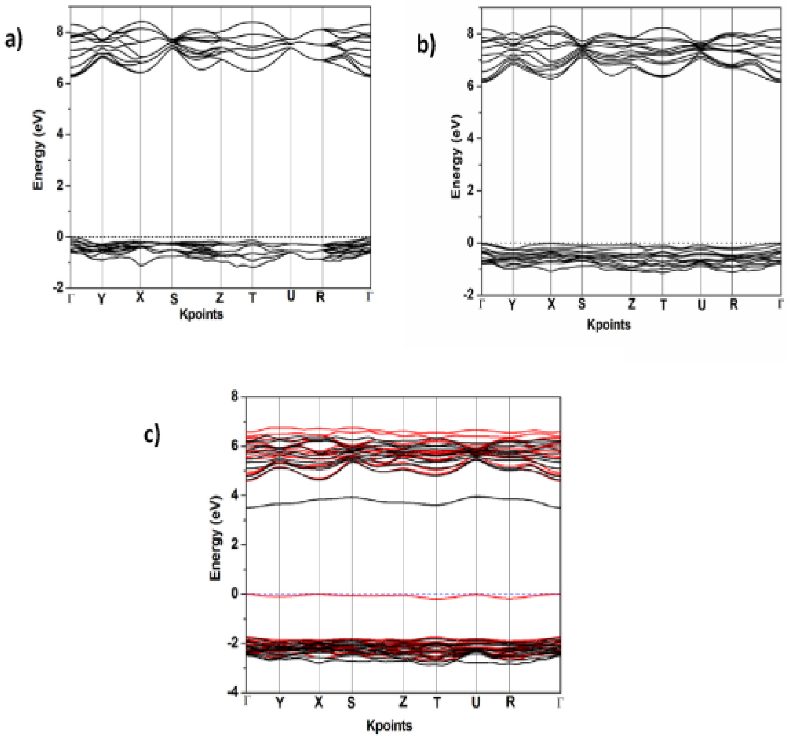

Fig. 8. Band structure of CZO: a) s, b) s* and c) t* electronic states.

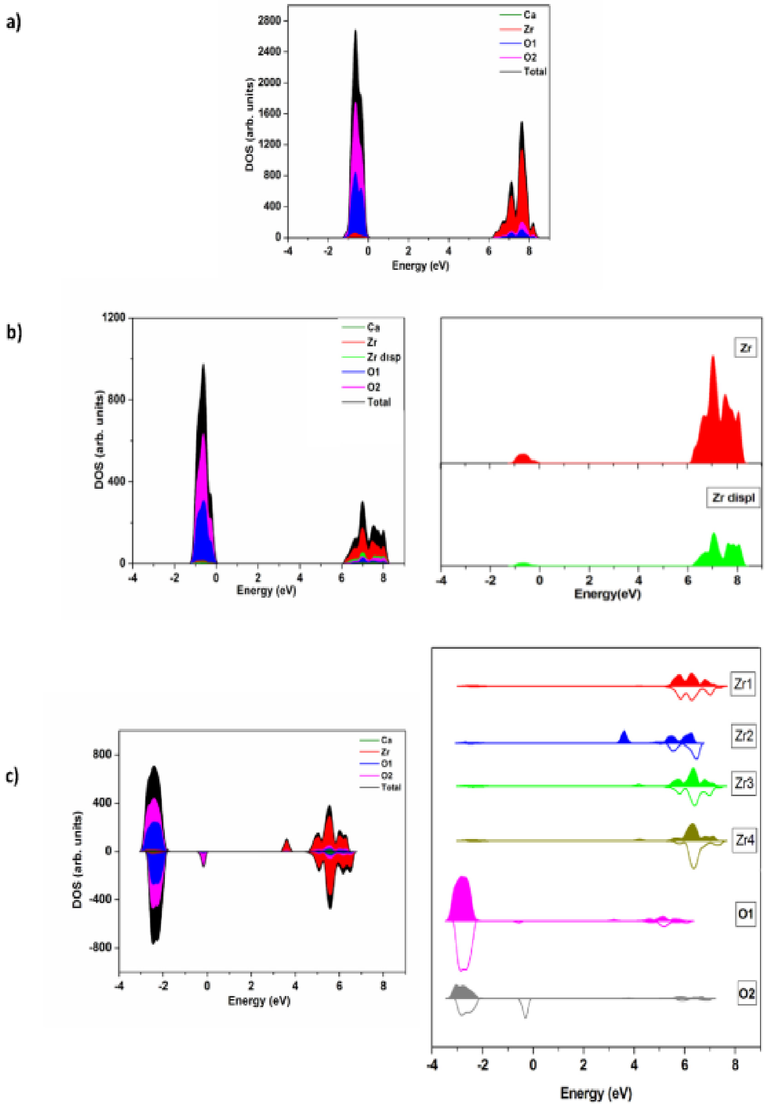

Fig. 9. Total and projected DOS on atoms for CZO: a) s, b) s* and c) t* electronic states.

powerful tool to evaluate the morphology. When the relative stability of the facets changes (increases or decreases), more than one type of facet can appear in the resulting morphology, producing variations. Surface energy values for the studied surfaces of the CZO system in *s* and t^* are listed in Table 3. An analysis of the theoretical results indicates that the most stable surfaces in the singlet state are the (121), (100), (010), (101), (001), (111), and (011) facets, and the ideal morphology of CZO is controlled by the (121), (100), (101), (001), and (010) facets (Fig. 11a). In the case of the triplet state, the thickness of the modeled surfaces have been reduced to the middle due to the computational cost, and the order of stability is (121), (101), (001), (100), (001), (111), and (011) facets, and the ideal morphology is controlled by the (121), (101), (100), and (001) facets (Fig. 11b).

We proposed the hypothesis that the decrease/increase of the surface energy in the triplet state with respect to the singlet state is due to the coordination of the O-Ca and O-Zr atoms, which are more exposed at the surfaces. Fig. 12 shows a comparison of the triplet and singlet surfaces studied in this paper, showing the more exposed metallic clusters for both systems. In addition, the spin density localized in the triplet surfaces is included. All singlet and triplet surfaces are Ca-O terminated and $[CaO_4]$ or $[CaO_5]$ clusters are obtained for the two configurations. The main difference is the change from $[CaO_5]$ to $[CaO_4]$ in passing from *s* to t^* state for the (121) and (101) surfaces. In the case of Zr coordination, $[ZrO_5]$ clusters are obtained in both the configurations, except for (121) in

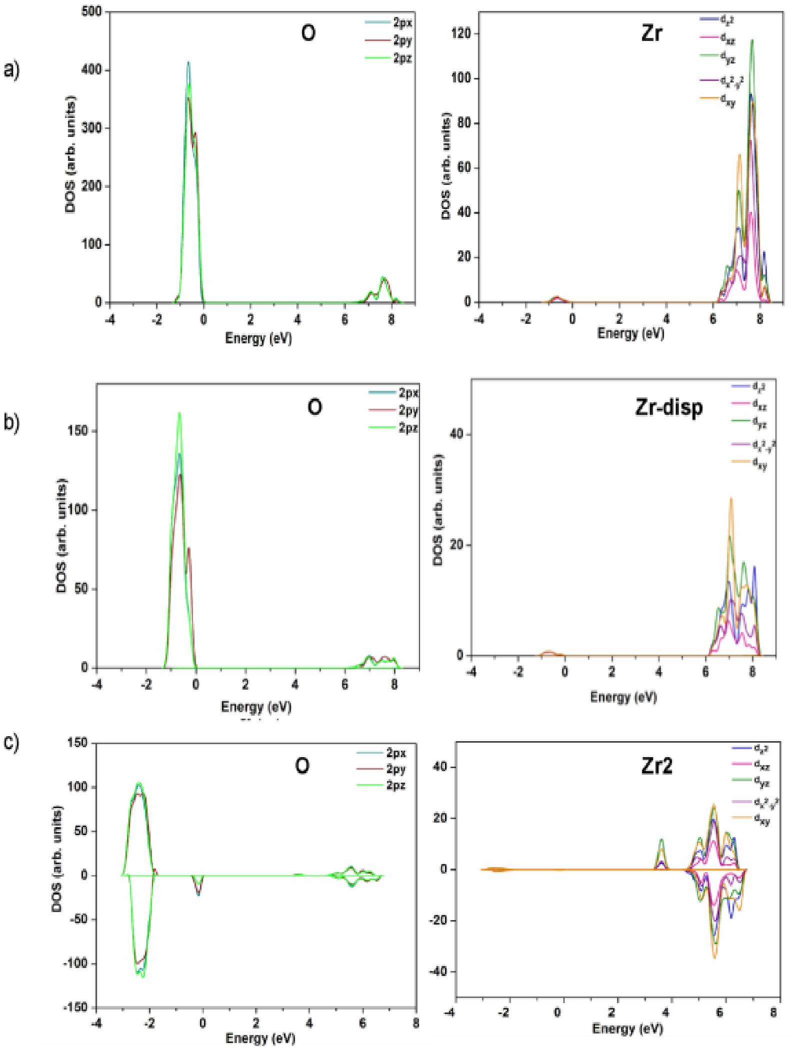

Fig. 10. DOS projected on orbitals CZO: a) s b) $s^*$and c) t^* electronic states.

t^* in which Zr is four-coordinated.

A little modification in the order of stability between the singlet and triplet states occurs due to the contributions of different atoms in each surface of the material. In the triplet state the (121), (101), (100), and (001) surfaces have similar values of E_{surf}, which have strong influence on the triplet morphology. The (010) surface does not appear in the ideal triplet morphology since its E_{surf} value is less stable than in the singlet system. In addition, the E_{surf} values for the (101) and (121) planes are identical, showing a similar percentage of area in the triplet morphology, compared to the singlet.

It is worth noting that the (101) slab cut is produced along the shortest distance between the oxygen and zirconium (1.995 Å) and also along the greater distance of the O-Zr and O-Ca bond distances of 2.294 and 2.998 Å, respectively. The analysis of these results shows that the present equilibrium morphology is consistent with the atomic configurations and the local coordination of atoms for each surface.

The ground-state properties of solid materials are of obvious importance for establishing their structure, stability, and processing. However, the description of processes such as PL emissions requires a detailed characterization of the electronic excited states properties. Elucidating their properties from first principles, on the basis of the constituent atoms and the laws of quantum mechanics, has long been a goal of theoretical and computational materials chemistry [81,82]. A note of caution is mandatory here, on this methodological aspect. While the hybrid methods show good results for ground state properties, their performance for excited states is less satisfactory [83]. Electronic excited-state calculations for periodic systems are challenges in quantum chemistry because it is still very difficult to apply these methods to large/very large systems due to the steep scaling in the number of electrons. In the present work, the excited states have been

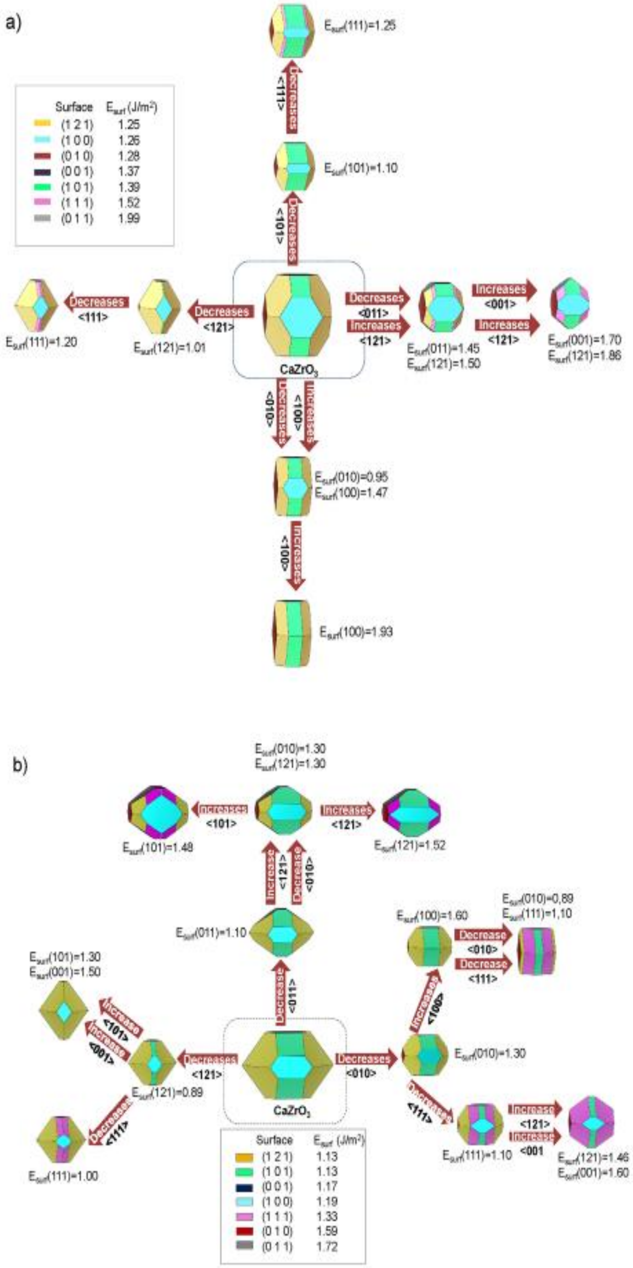

Fig. 11. Morphologies of CZO: a) s and b) t*electronic states.

localized and characterized at the DFT calculation level. This is a strong constraint and from the computational point of view, and represents a technical problem, since to obtain more accurate geometries and electronic properties of the excited states, it is necessary to use more sophisticated and demanding quantum calculations, such as multiconfiguration-based methods or by using the many-body perturbation theory. In this contribution, we do not aim at providing an exact application of DFT calculation, but rather to give a flavor of today possibilities. Methodological developments are mandatory in this context, along with new approaches, to calculate accurately values of band gaps and charge transfer excitations.

Table 3
Surface energy and band gap values for the (121), (100), (010), (101), (001), (111) and (011) surfaces of CZO crystals.

Surface	s			t^*		
	E_{sur} (J/m^2)	Area (Å)	E_{gap} (eV)	E_{sur} (J/m^2)	Area (Å)	E_{gap} (eV)
(121)	1.25	91.13	6.61	1.13	93.28	4.21
(100)	1.26	44.21	6.41	1.19	47.66	4.53
(010)	1.28	32.23	5.62	1.59	33.15	4.66
(101)	1.39	64.41	6.39	1.13	66.00	4.95
(001)	1.37	44.87	6.28	1.17	46.27	4.61
(111)	1.52	72.03	5.64	1.33	73.68	4.75
(011)	1.99	55.25	5.69	1.72	56.73	4.07

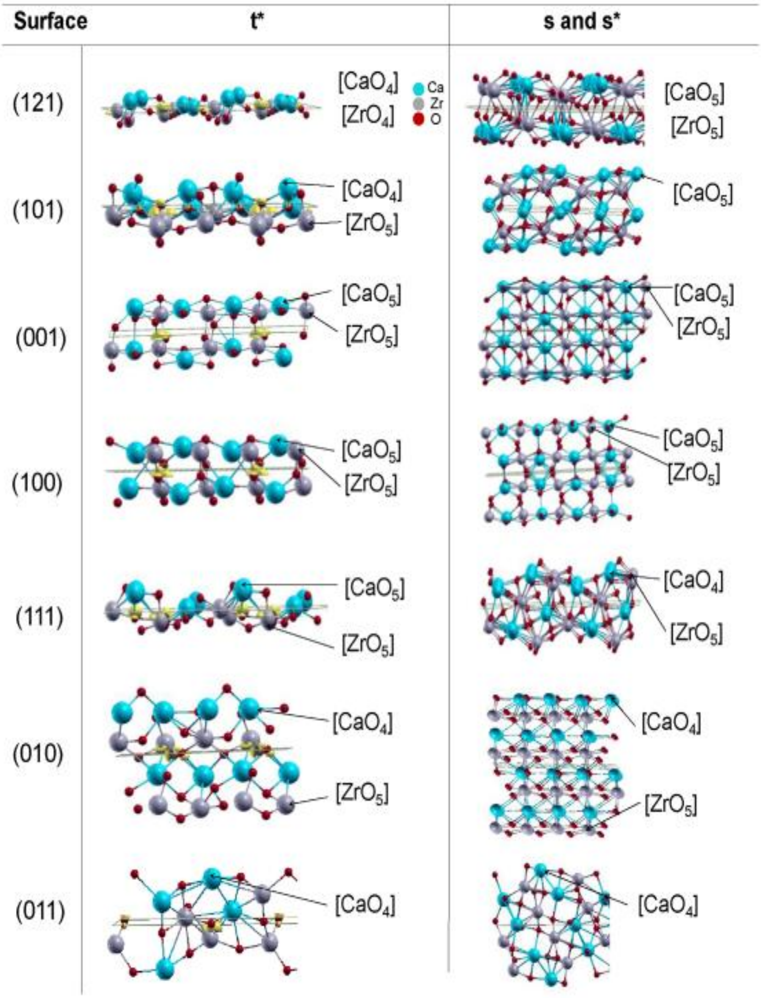

Fig. 12. A schematic representation for the surfaces of t* state of CZO where the spin density (in yellow) is depicted. The most external clusters for t* and s and s* states are indicated. (For interpretation of the references to colour in this figure legend, the reader is referred to the web version of this article.)

4. Conclusions

Modern physics relies heavily on the concepts of classical solid state physics with its emphasis on ideal infinite crystals and perfect symmetries. Real materials are not perfect crystals; they contain a number of defects and lattice imperfections, which are responsible for the properties of the materials. Therefore, in some cases, the reliability of a physical model rather than the precision of mathematical equations should be emphasized if one needs to investigate real materials. In this context, theoretical characterization of the geometrical and electronic structures of ground and excited electronic states can complement experiments inherently limited by equipment accuracy. A theoretical framework to interpret PL emissions, based on the localization and characterization of the nature for the ground, *s*, and excited (singlet, s^*, and triplet, t^*) electronic states, using ideal and distorted periodic supercell models of CZO, has been developed. Their corresponding geometries, electronic structures, and vibrational frequencies were obtained.

In this work, $CaZrO_3$ powders were prepared by the polymeric precursor method. Their structural and electronic properties have been studied previously [75], while the PL properties of crystalline CZO were investigated herein. The techniques of X-ray diffraction (XRD), Raman spectra, and PL spectroscopy at room temperature were used for characterization. XRD patterns indicated a pure orthorhombic perovskite phase of $CaZrO_3$ at annealing temperatures of 400, 600, 800, and 1000 °C. Raman spectra and XRD patterns reported long- and short-range order at 1000 °C.

First principle calculations reveal that the intensity of PL emissions is attributed to structural order-disorder effects related to the polyhedral distortion, i.e. the modification of geometric and electronic structure of both $[ZrO_6]$ and $[CaO_8]$ clusters in the electronically excited states, generating electronic levels located between the valence and conduction bands, which are basically composed of O 2p orbitals (valence band) and Zr 4d orbitals (conduction band). The band structures and the density of states revealed energy gap values of 6.23, 6.14, and 3.50 eV for the s, s^* and t^* electronic states, with the process of breaking of symmetry being a necessary condition for the existence of energy levels in the forbidden region of the band gap. The structural order-disorder effect on the coordination of $[ZrO_6]$ and $[CaO_8]$ clusters is demonstrated by theoretical calculations, as well as the shallow defect states found in the morphologies, where the local coordination of exposed atoms for each surface can be related to the order of surface energy stability. A little modification in the order of stability of surfaces occurs between the singlet and triplet states, generating differences in their corresponding morphologies.

To conclude, in this study, we present a general description of excited electronic states of CZO, thereby shedding light on the complex interplay between structural order-disorder effects and PL emissions, which is a challenging field of study both experimentally and intellectually. This technique can be used to extract chemical shifts for the structural characterization of excited states and to elucidate complex excited states. Finally, we need to recognize that present DFT calculations show limitations inherent in current exchange-correlation functional.

Acknowledgements

The authors acknowledge the financial support of the agencies: Generalitat Valenciana for PrometeoII/2014/022 and ACOMP/2014/270, ACOMP/2015/1202, Ministerio de Economía y Competitividad, project CTQ2015-65207-P, and Programa de Cooperacion Cientifica con Iberoamerica (Brasil) of Ministerio de Educacion (PHBP14-00020). J.A. acknowledges the Ministerio de Economia y Competitividad, "Salvador Madariaga" program, PRX15/00261. M.C.O acknowledges Generalitat Valencia for the Santiago Grisolia program 2015/033.

Appendix A. Supplementary data

Supplementary data related to this article can be found at http://dx.doi.org/10.1016/j.jallcom.2017.06.052.

References

[1] L. Pauling, J. Am. Chem. Soc. 51 (1929) 1010–1026.
[2] M.E. Lines, A.M. Glass, Principles and applications of ferroelectrics and related materials, in: Oxford classic texts in the physical sciences, 1977.
[3] A.E. Souza, G.S. Sasaki, S.A. Camacho, S.R. Teixeira, M.S. Li, E. Longo, J. Lumi. 179 (2016) 132–138.
[4] G. Blasse, Optical electron transfer between metal ions and its consequences, in: Complex Chemistry, Springer Berlin Heidelberg, Berlin, Heidelberg, 1991, pp. 153–187.
[5] E.S. Junior, F.A.L. Porta, M.S. Liu, J. Andres, J.A. Varela, E. Longo, Dalton Trans. 44 (2015) 3159–3175.
[6] F.A.L. Porta, J. Andres, M.V.G. Vismara, C.F.O. Graeff, J.R. Sambrano, M.S. Li, J.A. Varela, E. Longo, J. Mater. Chem. C 2 (2014) 10164.
[7] F.A.L. Porta, J. Andres, M.S. Li, J.R. Sambrano, J.A. Varela, E. Longo, Phys. Chem. Chem. Phys. 16 (2014) 20127–20137.
[8] P.G. Mendes, M.L. Moreira, S.M. Tebcherani, M.O. Orlandi, J. Andres, M.S. Li, N. Diaz-Mora, J.A. Varela, E. Longo, J. Nanopart Res. 14 (2012) 750.
[9] M.R.D. Bomio, L.S. Cavalcante, M.A.P. Almeida, R.L. Tranquilin, N.C. Batista, P.S. Pizani, M.S. Li, J. Andres, E. Longo, Polyhedron 50 (2013) 532–545.
[10] L.S. Cavalcante, E. Moraes, M.A.P. Almeida, C.J. Dalmaschio, N.C. Batista, J.A. Varela, E. Longo, M.S. Li, J. Andres, A. Beltran, Polyhedron 54 (2013) 13–25.
[11] V.D. Araújo, R.L. Tranquilin, F.V. Motta, C.A. Paskocimas, M.I.B. Bernardi, L.S. Cavalcante, J. Andres, E. Longo, M.R.D. Bomio, Mater. Sci. Semicond. Process 26 (2014) 425–430.
[12] F.M.C. Batista, F.A.L. Porta, L. Gracia, E. Cerdeiras, L. Mestres, M.S. Li, N.C. Batista, J. Andres, E. Longo, L.S. Cavalcante, J. Mol. Struct. 1081 (2015) 381–388.
[13] Y.V.B.D. Santana, J.E.C. Gomes, L. Matos, G.H. Cruvinel, A. Perrin, C. Perrin, J. Andres, J.A. Varela, E. Longo, Nanomater. Nanotechnol. 4 (2014) 22.
[14] L.G. Tejuca, J.L.G. Fierro, J.M.D. Tascon, Structure and Reactivity of perovskite-type oxides, in: A. Press (Ed.), Advances in Catalysis, in, 1989. New York.
[15] R. Pazik, R. Tekoriute, S.H. kansson, R. Wiglusz, W. Strek, G.A. Seisenbaeva, Y.K. Gun'ko, V.G. Kessler, Chem. Eur. J. 15 (2009) 6820–6826.
[16] J.A. Enterkin, W. Setthapun, J.W. Elam, S.T. Christensen, F.A. Rabuffetti, L.D. Marks, P.C. Stair, K.R. Poeppelmeier, C.L. Marshall, ACS Catal. 1 (2011) 629–635.
[17] J. Andres, V.M. Longo, L.S. Cavalcante, M.L. Moreira, J.A. Varela, E. Longo, A fresh look at the structural, ferroelectric and photoluminescent properties in perovskites, in: Photoluminescence: Applications, Types and Efficacy, New York - United States, 1 ed., 2012.
[18] M. Misono, Stud. Surf. Sci. Catal. 176 (2013) 67–95.
[19] L. Bia, E. Traversa, J. Mater. Res. 29 (2014) 1–15.
[20] W. Wang, M.O. Tade, Z. Shao, Chem. Soc. Rev. 44 (2015) 5371–5408.
[21] E. Grabowska, Appl. Catal. B 186 (2016) 97–126.
[22] J.F. Nye, in: Physical Properties of Crystals: Their Representation by Tensors and Matrices, Clarendon Press, New York, Oxford, 1985.
[23] A.M. Glazer, Acta Crystallogr. Sect. A Cryst. Phys. Diffr. Theor. Gen. Crystallogr. 31 (1975) 756–762.
[24] A.M. Glazer, Acta Cryst. B28 (1972) 3384–3392.
[25] U. Lüdersa, Q.-R. Lia, R. Feyerhermb, E. Dudzikb, J. Phys. Chem. Solids 75 (2014) 1354–1360.
[26] I. Qasim, P.E.R. Blanchard, S. Liu, C. Tang, B.J. Kennedy, M. Avdeev, J.A. Kimpton, J. Solid State Chem. 206 (2013) 242–250.
[27] V.M. Longo, L.S. Cavalcante, M.G.S. Costa, M.L. Moreira, A.T. de Figueiredo, J. Andres, J.A. Varela, E. Longo, Theor. Chem. Acc. 124 (2009) 385.
[28] S.d. Lazaro, J. Milanez, A.T.d. Figueiredo, V.M. Longo, V.R. Mastelaro, F.S.D. Vicente, A.C. Hernandes, J.A. Varela, E. Longo, Appl. Phys. Lett. 90 (2007) 111904.
[29] M. Anicete-Santos, M.S. Silva, E. Orhan, M.S. Goes, M.A. Zaghete, C.O. Paiva-Santos, P.S. Pizani, M. Cilense, J.A. Varela, E. Longo, J. Lumin. 127 (2007) 689–695.
[30] M. Anicete-Santos, R.C. Lima, E. Orhan, M.A.M.A. Maurera, L.G.P. Simões, G. Souza, P.S. Pizani, E.R. Leite, J.A. Varela, E. Longo, J. Comput. Aided Mater. Des. 12 (2005) 111–119.
[31] L. Gracia, J. Andres, V.M. Longo, J.A. Varela, E. Longo, Chem. Phys. Lett. 493 (2010) 141–146.
[32] L.F. da Silva, J.-C. M'Peko, J. Andres, A. Beltran, L. Gracia, M.I.B. Bernardi, A. Mesquita, E. Antonelli, M.L. Moreira, V.R. Mastelaro, J. Phys. Chem. C 118 (2014) 4930–4940.
[33] V.M. Longo, M.d.G.S. Costa, A.Z. Simões, I.L.V. Rosa, C.O.P. Santos, J. Andres, E. Longo, J.A. Varela, Phys. Chem. Chem. Phys. 12 (2010) 7566–7579.
[34] L. Gracia, V.M. Longo, L.S. Cavalcante, A. Beltran, W. Avansi, M.S. Li, V.R. Mastelaro, J.A. Varela, E. Longo, J. Andres, J. Appl. Phys. 110 (2011) 043501.
[35] M.L. Moreira, P.G.C. Buzolin, V.M. Longo, N.H. Nicoleti, J.R. Sambrano, M.S. Li, J.A. Varela, E. Longo, J. Phys. Chem. A 115 (2011) 4482–4490.
[36] M.L. Moreira, J. Andres, L. Gracia, A. Beltran, L.A. Montoro, J.A. Varela, E. Longo, J. Appl. Phys. 114 (2013) 043714.
[37] R. Uarth Fassbender, T. Strelow Lilge, S. Cava, J. Andres, L. Fernando da Silva, V. Roberto Mastelaro, E. Longo, M. Lucio Moreira, Phys. Chem. Chem. Phys. 17 (2015) 11341–11349.
[38] R.S. Andre, S.M. Zanetti, J.A. Varela, E. Longo, Ceram. Int. 40 (2014) 16627–16634.
[39] X. Liu, J. Zhang, X. Ma, H. Sheng, P. Feng, L. Shi, R. Hu, Y. Wang, J. Alloy. Compd. 550 (2013) 451–458.
[40] Y. Shimizu, S. Sakagami, K. Goto, Y. Nakachi, K. Ueda, Mat. Sci. Eng. B 1611 (2009) 100–103.
[41] H.W. Zhang, X.Y. Fu, S.Y. Niu, Q. Xin, J. Lumi. 128 (2008) 1348–1352.
[42] H. Zhang, X. Fu, S. Niu, Q. Xin, J. Alloy. Compd. 459 (2008) 103–106.
[43] H. Wang, M. Wang, W. Zhang, N. Zhao, W. Wei, Y. Sun, Catal. Today 115 (2006) 107–110.
[44] M. Pollet, S. Marinel, J. Mater. Sci. 39 (2004) 1943–1958.
[45] G. Rog, M. Dudek, A. Kozlowska-Rog, M. Bucko, Electrochim. Acta 47 (2002) 4523–4529.
[46] M.S. Islam, R.A. Davies, J.D. Gale, Chem. Mater. 13 (2001) 2049–2055.
[47] K. Kobayashi, S. Yamaguchi, Y. Iguchi, Solid State Ionics 108 (1998) 355–362.

[48] H. Iwahara, T. Yajima, T. Hibino, K. Ozaki, H. Suzuki, Solid State Ionics 61 (1993) 65–69.

[49] S. Sakaida, Y. Shimokawa, T. Asaka, S. Honda, Y. Iwamoto, Mater. Res. Bull. 67 (2015) 146–151.

[50] H.J.A. Koopmans, G.M.H.V. Velde, P.J. Gellings, Acta Cryst. C39 (1983) 1323–1325.

[51] M. Dudek, E. Drożdż-Ciesla, J. Alloy Compd. 475 (2009) 846–854.

[52] P. Stoch, J. Szczerba, J. Lis, D. Madej, Z. Pędzich, J. Eur. Ceram. Soc. 32 (2012) 665–670.

[53] M.G. Brik, C.-G. Ma, V. Krasnenko, Surf. Sci. 608 (2013) 146–153.

[54] A.L. Ibiapino, L.P. Figueiredo, G.E. Lascalea, R.J. Prado, Quím. Nova 36 (2013) 762–767.

[55] Z.F. Hou, Phys. B-Condens. Matter. 403 (2013) 2624–2628.

[56] S.K. Gupta, P.S. Ghosh, N. Pathak, R. Tewari, RSC Adv. 5 (2015) 56526–56533.

[57] R.A. Gouvêa, E.M. Flores, S.d.S. Cava, M.L. Moreira, J. Lumin. 180 (2016) 73–80.

[58] E. Orhan, F.M. Pontes, C.D. Pinheiro, T.M. Boschi, E.R. Leite, P.S. Pizani, A. Beltran, J. Andres, J.A. Varela, E. Longo, J. Solid State Chem. 177 (2004) 3879–3885.

[59] A.C.V.D. Larson, R. B, in: General Structure Analysis System (GSAS) Program, in, Los Alamos, NM, Rep. N . LAUR 86–748, Los Alamos National Laboratory, University of California., 2004.

[60] W. Finger, D.E. Cox, A.P. Jephcoat, J. Appl. Cryst. 27 (1994) 892–900.

[61] I.L.V. Rosa, M.C. Oliveira, M. Assis, M. Ferrer, R.S. Andre, E. Longo, M.F.C. Gurgel, Ceram. Int. 41 (2015) 3069–3074.

[62] V.R.S.R. Dovesi, C. Roetti, R. Orlando, C.M. Zicovich-Wilson, F. Pascale, B. Civalleri, K. Doll, N.M. Harrison, I.J. Bush, Ph. D'Arco, M. Llunel, M. Causa, Y. Noe, in: U.O. Torino (Ed.), CRYSTAL14, 2014. Torino- Italy.

[63] C.T. Lee, W.T. Yang, R.G. Parr, Phys. Rev. B Condens. Matter. 37 (1988) 785–789.

[64] A.D. Becke, J. Chem. Phys. 98 (1993) 5648–5652.

[65] E. Longo, E. Orhan, F.M. Pontes, C.D. Pinheiro, E.R. Leite, J.A. Varela, P.S. Pizani, T.M. Boschi, J.F. Lanciotti, A. Beltran, J. Andres, Phys. Rev. B 69 (2004) 125115.

[66] L. Valenzano, F.J. Torres, K. Doll, F. Pascale, C.M. Zicovich-Wilson, R. Dovesi, Z. Phys. Chem. 220 (2006) 893–912.

[67] L. Valenzano, B. Civalleri, S. Chavan, S. Bordiga, M. Nilsen, S. Jakobsen, K.P. Lillerud, C. Lamberti, Chem. Mater. 23 (2011) 1700–1718.

[68] F. Cora, Mol. Phys. 103 (2005) 2483–2496.

[69] H.J. Monkhorst, J.D. Pack, Phys. Rev. B 13 (1976) 5188.

[70] K.P. Balashev, Koord. Khim 15 (1989) 116–121.

[71] J.B. Foresman, E. Frisch, Exploring chemistry with electronic structure methods, in: Frequency Calculations, Gaussian, Inc, Pittsburgh. P.A, 1996, pp. 61–90.

[72] M.F.C. Gurgel, M.L. Moreira, E.C. Paris, J.W.M. Espinosa, P.S. Pizani, J.A. Varela, E. Longo, Int. J. Quantum Chem. 111 (2011) 694–701.

[73] V.M. Orera, C. Pecharroman, J.I. Pena, R.I. Merino, C.J. Serna, J. Phys, Condens. Mat. 10 (1998) 7501–7510.

[74] M. Pollet, M. Daturi, S. Marinel, J. Eur. Ceram. Soc. 24 (2004) 1805–1809.

[75] I.L.V. Rosa, M.C. Oliveira, M. Assis, M. Ferrer, R.S. Andre, E. Longo, M.F.C. Gurgel, Ceram. Int. 41 (2015) 3069–3074.

[76] P. McMillan, N. Ross, Phys. Chem. Min. 16 (1988) 21–28.

[77] C.H. Perry, D.J. MacCarthy, G. Ruprecht, Phys. Rev. 138A (1965) 1537–1538.

[78] M. Tarrida, H. Larguem, M. Madon, Phys. Chem. Miner. 36 (2009) 403–413.

[79] R. Borja-Urbya, L.A. Diaz-Torres, P. Salas, M. Vega-Gonzalez, C. Angeles-Chavez, Mat. Sci. Eng. B 174 (2010) 169–173.

[80] Y.V.B.d. Santana, C.W. Raubach, M.M. Ferrer, F.L. Porta, J.R. Sambrano, V.M. Longo, E.R. Leite, E. Longo, J. Appl. Phys. 110 (2011) 123507.

[81] J.-L. Bredas, J.E. Norton, J. Cornil, V. Coropceanu, Acc. Chem. Res. 42 (2009) 1691–1699.

[82] B.M. Savoie, N.E. Jackson, T.J. Marks, M.A. Ratner, Phys. Chem. Chem. Phys. 15 (2013) 4538–4547.

[83] J. Kim, K. Hong, S.-Y. Hwang, S. Ryu, S. Choi, W.Y. Kim, Phys. Chem. Chem. Phys. 19 (2017) 10177–10186.

Study of the energetic, morphological and photoluminescence properties of $CaZrO_3:Eu^{3+}$. An experimental and theoretical investigation

Marisa Carvalho Oliveira[1,2], Renan A. Pontes Ribeiro[3], Lourdes Gracia[4], Sergio R. de Lazaro[3], Marcelo de Assis[2], Ieda L. Viana Rosa[2], Maria Fernanda do C. Gurgel[5], Elson Longo[2], and Juan Andrés*[1]

1 Department of Analytical and Physical Chemistry, Universitat Jaume I, Castelló E-12071, Spain
2 CDMF-UFSCar, Universidade Federal de São Carlos, PO Box 676, 13565-905 São Carlos, SP, Brazil
3 Department of Chemistry, Universidade Estadual de Ponta Grossa, Av. General Carlos Cavalcanti, 4748, 84030-900, Ponta Grossa, PR, Brazil.
4 Department of Physical Chemistry, Universitat de Valencia, Burjassot E-46100, Spain
5 Department of Chemistry, Universidade Federal de Goiás, Regional Catalão, Av.Dr.Lamartine Pinto d eAvelar,75704-020, Catalão, GO, Brazil

Abstract

In this study, we present a combined experimental and theoretical study to investigate the geometry, electronic structure, morphology, photoluminescence properties of $CaZrO_3:Eu^{3+}$ material. The polymeric precursor method has been employed to synthetize these crystals, while density functional theory calculations have been performed to obtain the geometry and electronic properties of $CaZrO_3:Eu^{3+}$ at fundamental and excited electronic states (singlet and triplet). We combine these results with the measurements of X-ray diffraction (XRD) to clarify the local structural changes provoked by the introduction of Eu^{3+} at the crystal lattice. This process induces the creation of intermediary levels in the band-gap region narrowing the E_{gap} value. The PL emissions have been rationalized by characterizing the electronic structure of excited singlet and triplet electronic states, allowing a deep insight into the main fingerprints that can be associated to the structural end electronic features of the $[CaO_8]$, $[EuO_8]$ and $[ZrO_6]$ clusters. Wulff construction, obtained from first principle calculations, allows us to match the experimental morphologies. These results expand the fundamental understanding of atomic processes that underpins the Eu doping.

1. Introduction

Photoluminescence (PL) materials have attracted a large scientific attention due to the technological applications mainly in the electronic industry, such as energy efficient lighting, laser, medical imaging devices, spectroscopy and other. In general, when such materials are excited by photons or ionizing radiation can emit light in visible, ultraviolet (UV) and infrared (IR) regions.[1-3] The fundamental mechanism associated with this process involves the trapping of excited electrons and holes in activators - which are impurities sites that generates intermediate states within band gap - and the electron-hole pair recombination that results in the photo-emission. In this sense, the structural and electronic properties exhibit a new equilibrium showing as order-disorder effects change attractive and repulsive forces inside of solid through chemical bond.[4] In this field, perovskite materials, with ABO_3 formula, are promising candidates due to the structural versatility, stability and are widely used for the electronic industry because of the capability of display a large number of physical and chemical properties depending of metal occupancies in A and B-sites. [5, 6] The ideal perovskite structure has a cubic symmetry (*Pm3m* space group).[7, 8] However, the existence of local structural disorders at the A- and B-site enables a large number of polymorphs, with tetragonal, orthorhombic, rhombohedral symmetry and other. Therefore, the intriguing properties associated with the perovskite materials are commonly reported from distorted [BO_6] clusters through cation displacement, octahedral rotations, doping and tilting.[6, 9]

Calcium zirconate, $CaZrO_3$ (CZO), is a representative member of the perovskite family that has received a lot of attention due to its exceptional dielectric, catalytic and PL properties with applications in diverse areas of science and technology such as hydrogen sensors, luminescence hosts, capacitors, catalysis, and so on.[10-15] At room temperature, CZO crystallizes in the orthorhombic structure (*Pnma* space group), where Ca^{2+} cations occupies the center of 8-fold clusters [CaO_8], while Zr^{4+} exhibits a three dimensional sublattice of corner-connected [ZrO_6] octahedra. In addition, all octahedral sites are slightly tilted with respect to their position in the ideal cubic perovskite structure due to the mismatch of the alkaline earth ions in the A-site cluster of the crystal structure.[13, 16]

In the past years, the inclusion of impurity elements through the doping process has attracted interest due to the possibility to enhance the intensity of the PL emissions as well as to control the photo-generation process. In this context, earth-rare cations show a singular mechanism related to the conversion from low energy near infrared into visible photon with high energy known as up-conversion.[17] Therefore, several earth-rare doped perovskites have been synthesized by various methods, showing superior PL emission and other interesting properties. Especially for CZO, different authors report successful applications of Eu^{3+}, Tm^{3+}, Dy^{3+}, Yb^{3+}, and Er^{3+} cations to increase the PL properties.[12, 16-22] Shimizu *et. al* report the synthesis of Tb-Mg codoped CZO particles with increased luminescence intensity attributed to the local lattice distortion resulting from the doping process.[18] In addition, Shimizu *et. al* reports the synthesis of Tb-Mg codoped CZO particles with increased luminescence intensity attributed to the local lattice distortion resulting from the doping.[23] Maurya *et. al* used solid-state reactions to synthetize Ho-Yb codoped CZO nanoparticles with enhanced up-conversion for green light, showing an interesting potential for optical applications.[21]

Furthermore, many experimental studies reports the synthesis of Eu-doped CZO samples using different techniques. Sheetal *et. al* used sol-gel combustion method to obtain CZO-Eu particles with remarkable red luminescence.[22] Katyayan and Agrawal used conventional solid state reactions to obtain Tb-Eu codoped CZO particles with high-order intensity and variable emissions that confirms the color tenability with the doping.[20] On the other hand, Singh *et. al* have been prepared Er-Yb codoped CZO compounds by the urea combustion route, obtaining strong energy transfer upconversion emission in the green and red spectral regions.[19] Despite the large number of experimental studies for Eu-doped CZO materials, the chemical and physical mechanisms associated with the superior PL emission remains unclear.

From the theoretical viewpoint, the investigation of PL emissions is a challenging topic because requires the understanding of excited states related to the optical phenomena.[1, 24] In our previous work, we present a novel and successful approach, which enables us to explore both ground (singlet) and excited states (excited singlet and triplet) connecting to the experimental PL spectra obtained for CZO nanoparticles.[25] This approach was also successfully applied by our group to investigate the mechanism of PL emissions in $SrTiO_3$, $SrTiO_3$:Sm, $CaWO_4$, $BaZrO_3$, and $BaZr_{1-x}Hf_xO_3$ solid solutions based on the characterization of excited electronic states.[26-31]

In the present work the focus is the PL mechanism and its relationship with the presence of excited electronic states in Eu-doped CZO crystals combining theoretical and experimental efforts. The main novelty of the present work relies on the description of structural and electronic order-disorder effects associated with the Eu doping on the CZO matrix in order to rationalize the PL emissions.

2. Experimental procedures and computational details

2.1. Synthesis and characterization

Pure CZO [32] and europium-doped calcium zirconate (CZO:Eu^{3+}) powders were prepared by the polymeric precursor method (PPM). CZO:Eu^{3+} powder was synthesized using calcium chloride dihydrate ($CaCl_2.2H_2O$) (99%, Synth), zirconium oxychloride (IV) octahydrate ($ZrOCl_2.8H_2O$) (99,5%, Sigma-Aldrich), europium oxide (Eu_2O_3) (99% Sigma-Aldrich), ethylene glycol, ($C_2H_6O_2$) (99.9%, J.T. Baker) and citric acid monohydrate ($C_6H_8O_7.H_2O$) (99.5%, J.T.Baker).

Zirconium citrate was formed by $ZrOCl_2.8H_2O$ dissolution in a citric acid aqueous solution under constant stirring. The citrate solution was stirred at 60°C to obtain a clear homogeneous solution, $CaCl_2.2H_2O$ was added in 1:1 molar of calcium and zirconium and 1:6 molar of citric acid in relation to the sum of molar of the metals used. The doping by the Eu^{3+} ion was fixed in 10% molar of the Eu_2O_3 (prepared though the dissolution of Eu_2O_3 in concentrated HCl) added in a stoichiometric quantity to Ca^{2+} ions and the Zr citrate solution. After solution homogenization, $C_2H_6O_2$ was added to promote a polyesterification reaction using an acid/ethylene glycol ratio fixed at 60/40 in mass. The CZO pure resin was prepared previously and powders were heat treated initially at 400°C for 4h and then were annealed at 900°C for 2h. The crystalline profiles were indexed and matched with JCPDS card No. 35-0790 showing an orthorhombic phase associated to *Pcnm* space group for pure and Eu^{3+} (10 mol%).

Pure and doped CZO powders were characterized by X-ray Diffraction (XRD) technique in a Rigaku Dmax 2500PC diffractometer using Cu Kα (λ= 1.5406 Å) radiation. Data were collected from 10° to 90° in a 2ϑ with a 0.5° divergence slit and a 0.3 mm receiving slit using fixed-time mode with a 0.02º step size and 1s/point. PL spectra were collected with a Thermal Jarrel-Ash Monospec 27 monochromator and a Hamamatsu R446 photomultiplier. The 350.7 nm exciting wavelength from krypton ion laser (Coherent Innova) was used; the nominal output power of the laser was maintained at 200 mW. The microstructural characterization was performed by field emission gun-scanning electron microscopy (FEG-SEM) using Zeiss Supra™ 5 equipment. UV–vis absorption spectra of the annealed samples were taken using total diffuse reflectance mode in a Cary 5G equipment. All measurements were performed at room temperature.

2.2. Computational details

First-principles calculations within the periodic DFT framework and hybrid B3LYP exchange-correlation functional using the CRYSTAL14 program [33], [34], [35] have been performed to characterize the pure CZO and doped CZO:Eu^{3+} systems. The atomic centers were described by all-electron basis sets for the Ca [36], Zr [37] and O [38] and ECP pseudopotential with 11 valence electrons described by (5s5p4d)/[3s3p3d] (VTZ quality) basis sets for trivalent Eu atom [39]. The f-in-core approximation postulates for 4f shell in Eu^{3+} are incorporated into the pseudopotential. Thus, one does not need an explicit treatment of the open 4f shell, which is a computational advantage.

Regarding the density matrix diagonalization, the reciprocal space net was described by a shrinking factor set to 4, corresponding to 36k points in accordance with the Monkhorst–Pack method [40]. The accuracy to evaluate the Coulomb and Exchange series was controlled by 5 thresholds, for which adopted values were 10^{-8}, 10^{-8}, 10^{-8}, 10^{-8} and 10^{-16}. In this work, a orthorhombic supercell of 79 atoms which corresponds to 2x1x2 conventional cell was used to simulate the CZO:Eu^{3+}(12.5%) doping, where two Ca^{2+} ions were replaced by two Eu^{3+} ions summed to the creation of one calcium vacancy ($V_{Ca}^{\bullet\bullet}$), in order to neutralize the unit cell (Eq. 1).

$$CaZrO_3 + Eu(III) \rightarrow Ca_{0.8125}Eu_{0.125}ZrO_3 \ (+ {}_{0.0625}V_{Ca}^{\bullet\bullet}) \qquad (1)$$

In addition, the surface energy (E_{surf}) for (001), (121), (100), (011), (201), (111) and (101) cleavage planes are calculated using Wulff construction[41]. The Visualization for Electronic and Structural Analysis (VESTA) program (version 3.1.8 for Windows) [42] was used for the Wulff construction as well as in the visualization of the morphological mapping of CZO:Eu^{3+} crystals.

In order to understand the PL mechanism associated with CZO:Eu^{3+}(12.5%) material, excited states calculations were carried out considering the existence of both excited singlet (s*) and triplet states (t*) from singlet ground state (s). In this case, the t* model state was reproduced fixing the difference between spin up (α) and spin down (β) (n_α - n_β = 2) along the SCF calculations. The electronic structure was investigated from band structure, density of states (DOS) and spin density isosurfaces.

In this study, it is important to point out that the Eu^{3+} doping in the CZO matrix was computed by single-point calculations for both bulk and slab models, considering the optimized cell for ordered and disordered models of CZO reported in our previous work, [25] enabling the treatment of the main electronic features associated with the doping and the optical properties.

3. Results and discussion

3.1. X-Ray diffraction analysis

Fig. 1a-b show the XRD patterns of pure and Eu^{3+} (10 mol%) doped CZO crystals. The as-synthetized samples show pure single orthorhombic phase (a=5.591Å, b=8.017Å, c=5.761Å) showing the *Pcnm* space group, according with the *Inorganic Crystal Structure Database* number 97464 [43]. Both samples showed definite peaks, presenting a high degree of crystallinity and without any secondary phases.

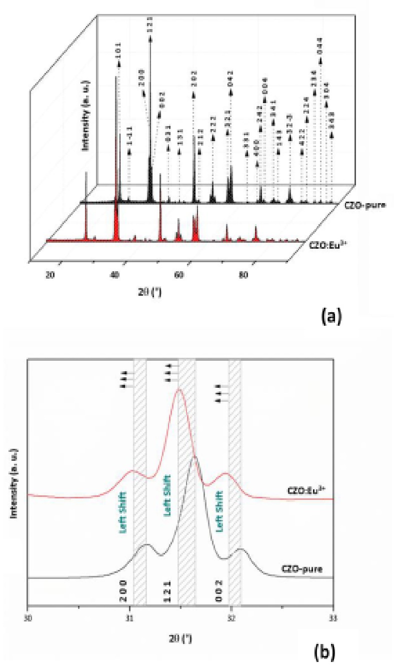

Figure 1. XRD patterns for (a) pure CZO sample with plans indexed and Eu^{3+} doped (10%) samples. (b) Displacement for left shift of the (200), (121) and (002) peaks.

In both crystals, a strongest peak around 2θ=31.60 corresponds to the (121) crystalline plane; however, the doping from Eu^{3+} cations alters the lattice parameters due to the difference in the electronic density in relation to Ca^{2+} ions and the insertion of structural defects, with the formation of clusters of $[EuO_8]$ and $V_{Ca}^{\bullet\bullet}$, which can be seen from the amplification of the strongest diffraction peak (**Fig.1b**) [44]. This statement is a strong indication of the success substitution of Ca^{2+} by Eu^{3+} in the A site ($AZrO_3$) of the CZO [45]. In the syntheses it maintained the load balance, generating vacancies of calcium. In this way, the crystal is structured with vacancies of calcium, which has p-type semiconductor properties and there is a relaxation of the crystalline lattice.

PPM have been carried out on various papers such as $LnMn_{0.5}Fe_{0.5}O_3$ (Ln=La, Pr, Nd, Sm and Gd) [46], $Ca_xBi_{(1-x)}FeO_3$ (x = 0.0, 0.1, 0.2, 0.30) [47], $Ca_{0.98}Er_{0.01}Yb_{0.01}TiO_3$ [48], $SrZrO_3$ and $SrTiO_3$ [49], $SrSn_{1-x}Ti_xO_3$ [50].

3.2 . Optical properties

In molecular systems is well known that optical properties are intrinsically connected with excite electronic states, such as, s* and t* states. However, the solid-state theory is based on electron-hole pair generation to understand as electrical as optical phenomena. Here, we present optical experimental evidences for CZO and $CZO{:}Eu^{3+}$ materials to motivate a new and deeper interpretation for optical effects in solid state.

In previous works we have shown that origin of E_{gap} reduction from defects in crystalline structures is associated to intermediary electronic levels introduced into E_{gap} [51], [52] [53], [54], [55], [56]. Such mechanism has been improved a lot with description from s* and t* states. For us, such electronic-states are the quantum evidence of the electron-hole pair generation of solid state theory. Then, the interpretation of the Fig. 2a and Fig. 2b follow our previous reports.

The addition of the Eu^{3+} doping causes great change in the E_{gap} of the CZO from intermediary electronic levels, which can be investigated more deeply from s* and t* states. Experimental results (Fig. 2) show a decrease from 5.60 eV to 3.82 eV for CZO and $CZO{:}Eu^{3+}$, respectively. This reduction of 1.77 eV on optical property is very emphasized and it is associated with high density of defects introduced by substitution of Ca^{2+} cations by Eu^{3+} cations. [57].

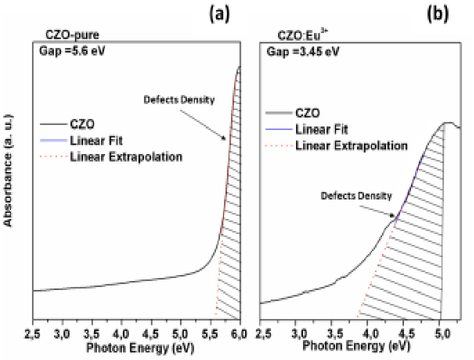

Figure 2. UV–vis absorption spectrum. (a) CZO and (b) $CZO{:}Eu^{3+}$ doped (10%).

PL spectra can be used as signature of how optical property can be change by the doping process of Eu^{3+}. The direct modification of a luminescence profile is a good and fast result to determine changes of the electronic excitations and, consequently, alterations on electronic energy levels. Then, it is important to connect the PL spectra with energy level diagram to identify the nature of the photoemission. PL spectra of pure CZO presents a large band, which represent the density of defects, while in the doped CZO:Eu^{3+} systems, there is $V_{Ca}^{\bullet\bullet}$ and the spectra is dominated by the [EuO$_8$] cluster in the crystalline network. The electronic states involved in the luminescence process were obtained from energy level diagram indicating transition probabilities for Eu^{3+} ions. Electronic transitions associated to $^5D_0 \rightarrow {}^7F_{J(J=0,1,2,3,4,5)}$ emission peaks occur between 570 and 720 nm (**Fig.3**).

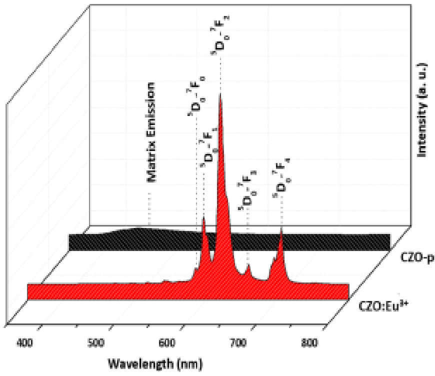

Figure 3. Photoluminescence spectra of CZO pure and CZO:Eu^{3+} (10 mol%).

In particular, the $^5D_0/^7F_2$ transition is allowed; however, the electric dipole mechanism is significantly influenced by crystalline field (hypersensitive transition), while the magnetic dipole mechanism is less altered by crystalline field. Therefore, this transition can be considered as reference for all transitions occurring in the system [58], [59], [60]. Thus, the peak area ratio between $^5D_0/^7F_2$ and $^5D_0/^7F_1$ transitions provides valuable information regarding changes to the surrounding environment occupied by the Eu^{3+} ions and is useful as a tool to show the distortion degree in A site, which provides an asymmetry in the electronic distribution and facilitates the charge transfer process [61], [57], [45]. For the sample of CZO:Eu^{3+}, we obtain the value of the ratio of $^5D_0$-$^7F_2$/$^5D_0$-$^7F_1$ of 5.14. For similar systems such as CaTiO$_3$ doped with Eu^{3+}, the values of the ration between D/F electronic transitions were obtained between 2 and 4 with lower values associated with higher symmetry of the Eu^{3+} site [45] Applying the same analysis for our CZO:Eu^{3+} samples, we obtain the value of the ratio among $^5D_0$-$^7F_2$/$^5D_0$-$^7F_1$ of 5.14. Thus, for CZO:Eu^{3+}, the Ca^{2+} and Eu^{3+} ions were located in a site of low symmetry or more disordered.

3.3. Theoretical study

In this section, we present theoretical results to a new interpretation of optical property in solid state. To reach such goal we connect electron-hole pair generation to excited electronic states, a quantum model never before presented.

The orthorhombic structure for CZO in terms of constituent clusters is displayed in **Fig. 4(a-c)** illustrating the substitution of Eu^{3+} in the [CaO$_8$] cuboctahedral sites while, [ZrO$_6$] sites remain unchanged as octahedral sites. The replacement of Eu^{3+} generates $V_{Ca}^{\bullet\bullet}$ in the host matrix in order to neutralize the unit cell (Eq. 1). Regarding the cation replacement and the vacancy formation mechanism associated to the doping process, the crystalline structure of CZO:Eu^{3+} should exhibit a new equilibrium between attractive and repulsive interactions of solid through chemical bond, resulting in a singular electronic structure compared to pure CZO, which can contribute for interesting electronic properties.

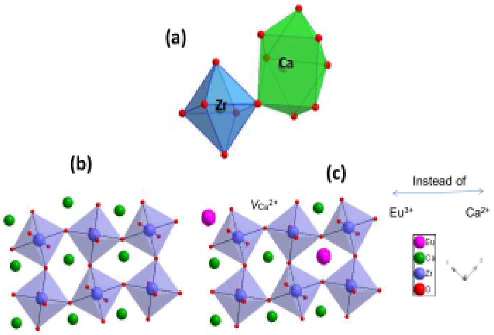

Figure 4. CZO crystalline structure represented by polyhedral clusters. (a) [ZrO$_6$] and [CaO$_8$] clusters in blue and green colors, respectively. (b) Orthorhombic unit cell of the pure CZO and (c) Eu^{3+} doped.

3.3.1. Electronic structure

The precise control of several photo-assisted properties (photoluminescence, photocatalysis, photodegradation and others are often related to electronic structure engineering, where different kinds of mechanisms (doping, vacancies, structural distortions, etc.) are enabled to redistribute the electronic density, mainly close of the E_{gap} region. Charge- and -spin resolved analysis are important tools to rationalize the electronic structure of solid-state materials. Therefore, DOS, band structure profiles area calculated (**Fig. 5a-b**). Considering photo-induced properties are important to take account the existence of excited-states in order to fulfill the nature of electron-hole pair generation, as well as its recombination process. In this study, excited singlet (s*) and triplet-states (*t**) were investigated combining the aforementioned analysis in order to clarify the PL emissions of CZO:Eu^{3+}, in a similar way to our previous work for pure CZO.[25].

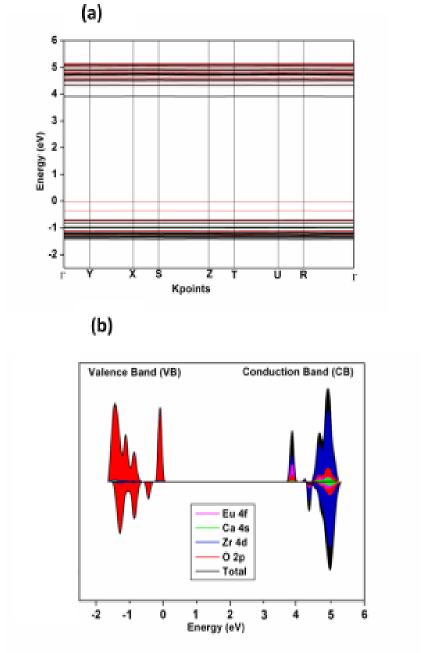

Figure 5. Electronic structure for CZO:Eu (12.5%) in triplet state. (a) Band structures and (b) projected DOS on atomic levels of CZO:Eu^{3+} (12.5%) model.

The experimental values shown in **Fig. 2** for E_{gap} are in the range of 5.60 eV (pure) and 3.82 eV (CZO:Eu^{3+}). Our DFT calculations for pure CZO [25] have indicated an E_{gap} of 6.23 eV in agreement with experimental results. In addition, s, s* (**Figure S1**) and *t** (**Fig. 5**) calculations for CZO:Eu^{3+}(12.5%) show E_{gap} values of 5.09, 4.90 and 3.88 eV, respectively; then, the main electronic structure associated to UV-vis results (Fig. 2) is the *t**. An analysis of the projected DOS for the t* model (**Fig. 5**) presented uppermost levels on valence band (VB) consisting mainly of O atoms, while the conduction band (CB) is formed mainly by Zr and Eu atoms with a small contribution of Ca atoms, as same as s and s* (**Figure S1**). In addition, it was observed that the degenerated band for both valence band maximum (VBM) and conduction band minimum (CBM) is sensitive to the s* and t* electronic states creating an excitation mechanism to clarify from quantum chemistry the electron-hole pair. Indeed, the comparison between the DOS profiles for s and s* (**Figure S1**) indicates that the bands located between in the VBM and CBM for s were displaced to a high-energy region for s*. Further, the transition for the t* perturbs both levels evidencing a band separation in both VB and CB. This fact can be attributed to the existence of non-degenerated energy levels for excited s* and t* states, which are controlled by the spin multiplicity.

The spin-density analyses are helpful to describe the nature and the localization of the electron-hole pair originated from electronic excitation. It is important to point out that such spin density distribution (in electron/bohr^3) was calculated using a regular 3D grid of points, enabling the analysis of the spin-resolved density matrix through the difference between alpha- and beta-spin occupations. Thereby, spin density difference maps provide a pictorial representation of the unpaired electron density. In this case, our spin-density distribution for *t** state was pictured spin density distribution for CZO:Eu^{3+}, as depicted in **Fig. 6**. The spin density distribution indicates a major localization of spin density on the Zr and O atoms with a minor content on the Eu atoms. Furthermore, largest spin populations were found closer to [EuO_8] clusters, suggesting that the doping process induced a local disorder on the electronic density distribution because of oxygen-mediated interaction between Eu- and Zr-centered clusters, [EuO_8] and [ZrO_6], respectively.

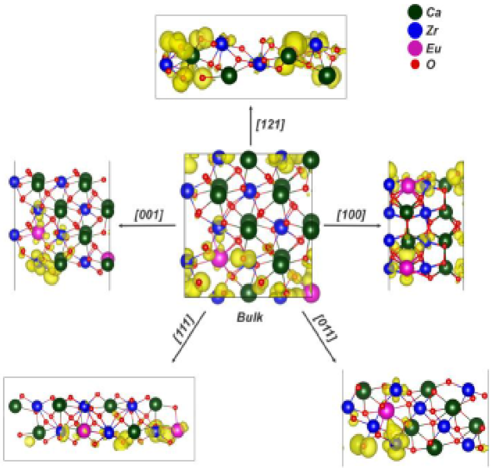

Figure 6. A schematic representation for spin density isosurfaces (in yellow) calculated for bulk and surface models of CZO:Eu^{3+} (12.5%) in triplet state (*t**).

The Eu^{3+} doping mechanism in pure CZO is supported by the presence of $V_{Ca}^{\bullet\bullet}$ in order to counter-balance the charge and neutralize the unit cell (Eq. 1), as previously discussed. Regarding this, [ZrO_6] clusters located near to $V_{Ca}^{\bullet\bullet}$ plays a key role on the stabilization of the *t** state. A possible assumption for this result is the charge/spin density reorganization on the neighboring clusters, increasing the electron density population along the oxygen-mediated interaction $[EuO_8]$-$[ZrO_6]$. In contrast, CZO:Eu^{3+} exhibits the contribution of both $[AO_8]$ (A = Ca, Eu) and $[ZrO_6]$ clusters in the spin population.

From now, the spin distributions calculated for five surfaces of CZO:Eu^{3+} were discussed considering the undercoordinated clusters summed and the presence of impurity centers (Eu^{3+} and $V_{Ca}^{\bullet\bullet}$). At general, a similar pattern of spin density distribution was observed for all investigated surfaces, in agreement with the results obtained for the bulk. The results presented in **Fig. 6** indicate that the exposed surfaces are formed by $[ZrO]_n$ (n = 3-5) clusters exhibiting a largest spin density population, while $[EuO]_n$ (n = 4-6) clusters show a minor contribution for the *t** state stabilization. Therefore, similar to bulk, the perturbation of electronic density is associated to the oxygen-mediated $[EuO_8]$-$[ZrO_6]$ interaction and consequently to electron-hole pair generation on surfaces.

As expected for surface models, the dangling bond effect is strong on the electronic structure of CZO:Eu^{3+} material. The procedure to generate surface models from cutting bulk structure induces spontaneously to generation of oxygen vacancies, resulting in undercoordinated clusters. In this way, the symmetry broken process at the constituent clusters raises a local environment on surface and consequently intermediary energy levels are created in the E_{gap} region. This new intermediary energy levels have high energy because are formed from uncoupling of degenerated orbitals and they act as trapping of excited electrons. Indeed, the unpaired spin density exhibited in **Fig. 6** is majorly localized on undercoordinated clusters of the surface exposed indicating that the electron-hole pair generation is assisted by an electronic migration process from bulk to surface. In this point of view, our results suggest that surfaces of CZO:Eu^{3+} can be actives as a photocatalytic semiconductor, where the excited states has possibility to produce radical species from the adsorption of O_2 and H_2O molecules on the undercoordinated clusters Then, the doping process from Eu^{3+} cations causes a new spin density distribution, which can now be trapped in both empty Zr (4d) and Eu (4f) orbitals, once this spin density is located on the oxygen-mediated $[EuO_8]$-$[ZrO_6]$ interaction.

In order to clarify the effect of Eu^{3+} cations on the PL emissions of CZO, we propose a general scheme combining the results for DOS, Band Structure and spin density for s, s* and *t** states, as presented in **Fig. 7**. Initially, the Eu^{3+} doping process induces the creation of $V_{Ca}^{\bullet\bullet}$ that perturbs the VB energy levels, as well as the insertion of 4f orbitals in CBM, i. e. intermediary energy levels are introduced in the E_{gap} region, narrowing the required energy for electron transfer (**Fig. 7a**). The next step correspond to photo-induction of electron transfer from VB to CB, generating an electron-hole pair inside the CZO:Eu^{3+} electronic structure (**Fig. 7b**). This step is crucial because it shows a new interpretation for optical property in material science. We connect the excited-states theory with electron-hole pair indicating a view more deep for optical effects in solid-state theory. This new approach has been evidenced from previous manuscripts and again verified in the present work [62]. The propose of connection between excite-states and optical property is very proved in molecular quantum approach; however, our quantum evidence for dangling bonds generate trapping levels for electrons localizing spin density is really new. Such quantum modeling level is a great scientific contribution. In particular, the contribution of both empty Zr (4d) and Eu (4f) states in the CBM enables a charge competition between these metallic centers. At last, the photoluminescent effect occurs from electron declining, which is more intense in CZO:Eu than CZO.

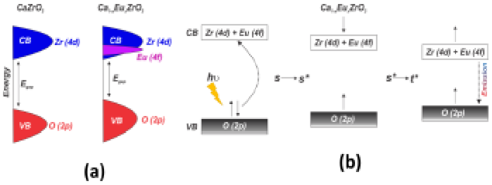

Figure 7. Scheme to represent (a) the electronic structure for both pure and Eu-doped CZO material; (b) photo-induced electron transfer mechanism describing the singlet to triplet state excitation, as well as the electron decaiment related to the light emission.

3.4. Morphology study

The field emission scanning electron microscopy (FE-SEM) technique is very important in our work because analysis of powder surface morphology, since XRD is insufficient to characterize minor structural modifications and to draw meaningful correlations between PL response and structural changes in the sample. Then, the **Fig. 8** reports FE-SEM images of the CZO and CZO:Eu^{3+} powders showing agglomerates with complex morphology and a big number of crystalline faces. This soft-agglomerated powder morphology is a common product of polymeric precursor synthesis, with temperature rising, the release of gas in progressing carbothermal reaction results in the formation of pores with different sizes; then, the same gradually is organized by reducing the density of defects, transformed from amorphous, semicrystalline, to crystalline with low defect density, enabling the construction only of theoretical morphological maps. This fact is proven by its low luminescent broadband of pure CZO. On the other hand, the doped CZO shows well defined spectrum of europium, characteristic of the effect of the crystallinity of the material, i.e. effect of the crystalline field.

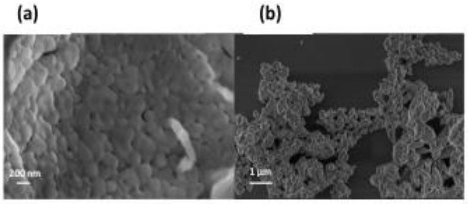

Figure 8. FE-SEM micrographs. (a) pure CZO and (b) CZO:Eu^{3+} (10%).

To clarify the influence of the defects caused by Eu^{3+} dopants on various crystalline facets, we pursued a theoretical model using Wulff construction [63] according to others works obtained by our group [25], [64], [65, 66], [67]. Thus, a Wulff construction for ideal structure of CZO:Eu^{3+} in s* and t* states were investigated. In addition, we show in Fig. 9 from surface thermodynamics and excite-states an approach to predict and assess the morphology transformation of the crystals to get their shape-controlled.

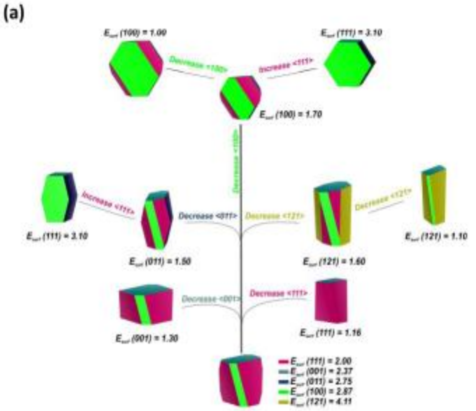

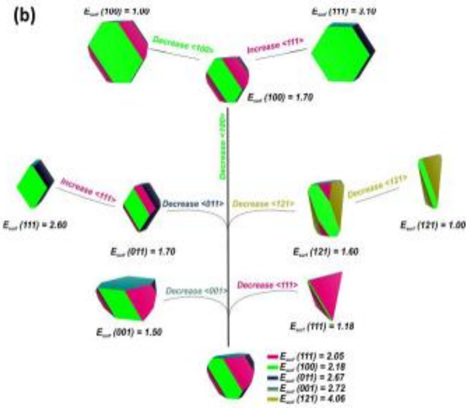

Figure 9. Morphology modulations (a) s and (b) t* for CZO:Eu^{3+} (12.5%) surfaces.

An analysis of **Fig. 9** shows that the ideal morphology for CZO:Eu^{3+} s* and t* states is controlled by (111), (001), (011) and (100) surfaces as presented in **Fig. 9a-b**, respectively. However, ideal morphology for both systems is different, i.e. 61.03% contribution of (111), 29.04% of (001), 8.07% of (100) and 1.86% of (011) surfaces are observed for s* state; while 45.63% of (111), 23.08% of (100), 19.76% of (001) and 11.53% of (011) are found for t* state. Then, we can attribute that change of morphology is associated with an alteration of the stability order between s* and t* states. The E_{surf} values follow the order of stability (111) > (001) > (011) > (100) > (121) in s*; whereas the order of stability (111) > (100) > (011) > (001) > (121) was noted for t*. Moreover, it was noted that the (121) surface correspond to the most unstable surface plane for CZO:Eu^{3+} material, evidencing an inversion of stability order in comparison to the pure CZO, where (121) is the plane with the lowest E_{surf} [25]. This observation in complement to the displacement observed for (121) from X-ray analysis performed for both samples (**Fig. 1**) suggest that the Eu-doping induces disorder in the crystalline structure of CZO, mainly in (121) plane.

Conclusions

CZO:Eu^{3+} material was successfully synthesized using the polymeric precursor method. XRD analysis revealed a good crystallinity and single phase of the samples. Combining as experimental techniques as first-principles calculations was observed a reduction in E_{gap} promoted by the introduction of Eu^{3+} cations and creation of calcium vacancy in the CZO. In addition, theoretical calculations based on excited electronic states were employed to interpret photoluminescent emissions in CZO:Eu^{3+} samples. FEG-SEM images revealed that both pure and Eu-doped CZO_3 materials exhibit similar morphology, indicating less change on shape of CZO particles. From theoretical point of view, faceted morphologies calculated from Wulff construction using (111), (100), (011), (001), (201), (101) and (121) cleavage planes on the CZO:Eu^{3+} crystal was very important to clarify the surface energy on complex morphologies obtained experimentally.

Acknowledgements

The authors acknowledge the financial support of the agencies: Generalitat Valenciana for Prometeo/2016/079 and ACOMP/2014/270, ACOMP/2015/1202, Ministerio de Economia y Competitividad, project CTQ2015-65207-P, Programa de Cooperacion Cientifica con Iberoamerica (Brasil) of Ministerio de Educacion (PHBP14-00020) and, Fundação de Amparo à Pesquisa do Estado de São Paulo (FAPESP) (2013/07296-2). J.Andres acknowledges the Ministerio de Economia y Competitividad, "Salvador Madariaga" program, PRX15/00261. M.C.Oliveira acknowledges Generalitat Valencia for the Santiago Grisolia program 2015/033. R. Ribeiro and S. R. de Lazaro thanks the UEPG, CAPES and Fundação Araucaria for the financial support.

references

[1] S.K. Gupta, P.S. Ghosh, N. Pathak, R. Tewari, Nature of defects in blue light emitting CaZrO$_3$: spectroscopic and theoretical study, RSC Advances 5(70) (2015) 56526-56533.

[2] J. Meyer, F. Tappe, Photoluminescent Materials for Solid-State Lighting: State of the Art and Future Challenges, Advanced Optical Materials 3(4) (2015) 424-430.

[3] A.M. Ibarra-Ruiz, D.C. Rodríguez Burbano, J.A. Capobianco, Photoluminescent nanoplatforms in biomedical applications, Advances in Physics: X 1(2) (2016) 194-225.

[4] S.P. Carlito, Jr., T. Yuxi, S. Villy, G.S. Ivan, Excited state and charge-carrier dynamics in perovskite solar cell materials, Nanotechnology 27(8) (2016) 082001.

[5] S.A. Veldhuis, P.P. Boix, N. Yantara, M. Li, T.C. Sum, N. Mathews, S.G. Mhaisalkar, Perovskite Materials for Light-Emitting Diodes and Lasers, Advanced Materials 28(32) (2016) 6804-6834.

[6] N.A. Benedek, C.J. Fennie, Why Are There So Few Perovskite Ferroelectrics?, Journal of Physical Chemistry C 117(26) (2013) 13339-13349.

[7] A.S. Bhalla, R. Guo, R. Roy, The perovskite structure – a review of its role in ceramic science and technology, Material Research Innovations 4(1) (2000) 3-26.

[8] M. Johnsson, P. Lemmens, Crystallography and Chemistry of Perovskites, Handbook of Magnetism and Advanced Magnetic Materials, John Wiley & Sons, Ltd2007.

[9] A. Cammarata, J.M. Rondinelli, Covalent dependence of octahedral rotations in orthorhombic perovskite oxides, The Journal of Chemical Physics 141(11) (2014) 114704.

[10] R.S. André, S.M. Zanetti, J.A. Varela, E. Longo, Synthesis by a chemical method and characterization of CaZrO3 powders: Potential application as humidity sensors, Ceramics International 40(10, Part B) (2014) 16627-16634.

[11] X. Liu, J. Zhang, X. Ma, H. Sheng, P. Feng, L. Shi, R. Hu, Y. Wang, Violet–blue up conversion photostimulated luminescence properties and first principles calculations of a novel un-doped CaZrO3 phosphor for application in optical storage, Journal of Alloys and Compounds 550 (2013) 451-458.

[12] H. Zhang, X. Fu, S. Niu, Q. Xin, Blue luminescence of nanocrystalline CaZrO3:Tm phosphors synthesized by a modified Pechini sol–gel method, Journal of Luminescence 128(8) (2008) 1348-1352.

[13] G. Róg, M. Dudek, A. Kozłowska-Róg, M. Bućko, Calcium zirconate: preparation, properties and application to the solid oxide galvanic cells, Electrochimica Acta 47(28) (2002) 4523-4529.

[14] K. Kobayashi, S. Yamaguchi, Y. Iguchi, Electrical transport properties of calcium zirconate at high temperature, Solid State Ionics 108(1) (1998) 355-362.

[15] M.S. Islam, R.A. Davies, J.D. Gale, Proton Migration and Defect Interactions in the CaZrO3 Orthorhombic Perovskite: A Quantum Mechanical Study, Chemistry of Materials 13(6) (2001) 2049-2055.

[16] S. Sakaida, Y. Shimokawa, T. Asaka, S. Honda, Y. Iwamoto, Synthesis and characterization of Eu3+-doped CaZrO3-based perovskite-type phosphors. Part I: Determination of the Eu3+ occupied site using the ALCHEMI technique, Materials Research Bulletin 67 (2015) 146-151.

[17] J.-C.G. Bunzli, C. Piguet, Taking advantage of luminescent lanthanide ions, Chemical Society Reviews 34(12) (2005) 1048-1077.

[18] Y. Li, Y. Wang, Photoluminescence properties and energy transfer of Dy3+ and Tm3+ co-activated CaZrO3 phosphor for white LEDs, Journal of Information Display 12(2) (2011) 93-96.

[19] V. Singh, V. Kumar Rai, M. Haase, Intense green and red upconversion emission of Er3+,Yb3+ co-doped CaZrO3 obtained by a solution combustion reaction, Journal of Applied Physics 112(6) (2012) 063105.

[20] S. Katyayan, S. Agrawal, Dynamics of concentration quenching in Eu3+ and Tb3+ doped calcium dioxide-oxo-zirconium perovskite, Journal of Materials Science: Materials in Electronics 29(3) (2018) 2373-2383.

[21] A. Maurya, R.S. Yadav, R.V. Yadav, S.B. Rai, A. Bahadur, Enhanced green upconversion photoluminescence from Ho3+/Yb3+ co-doped CaZrO3 phosphor via Mg2+ doping, RSC Advances 6(114) (2016) 113469-113477.

[22] Sheetal, V.B. Taxak, S. Singh, Mandeep, S.P. Khatkar, Synthesis and optical properties of red emitting Eu doped CaZrO3 phosphor, Optik - International Journal for Light and Electron Optics 125(20) (2014) 6340-6343.

[23] Y. Shimizu, S. Sakagami, K. Goto, Y. Nakachi, K. Ueda, Tricolor luminescence in rare earth doped CaZrO3 perovskite oxides, Materials Science and Engineering: B 161(1) (2009) 100-103.

[24] M.-H. Du, Using DFT Methods to Study Activators in Optical Materials, ECS Journal of Solid State Science and Technology 5(1) (2016) R3007-R3018.

[25] M.C. Oliveira, L. Gracia, M. de Assis, I.L.V. Rosa, M.F. do Carmo Gurgel, E. Longo, J. Andrés, Mechanism of photoluminescence in intrinsically disordered CaZrO$_3$ crystals: First principles modeling of the excited electronic states, Journal of Alloys and Compounds 722 (2017) 981-995.

[26] L. Gracia, J. Andrés, V.M. Longo, J.A. Varela, E. Longo, A theoretical study on the photoluminescence of SrTiO3, Chemical Physics Letters 493(1) (2010) 141-146.

[27] M.L. Moreira, J. Andrés, L. Gracia, A. Beltrán, L.A. Montoro, J.A. Varela, E. Longo, Quantum mechanical modeling of excited electronic states and their relationship to cathodoluminescence of BaZrO3, Journal of Applied Physics 114(4) (2013) 043714.

[28] M.L. Moreira, P.G.C. Buzolin, V.M. Longo, N.H. Nicoleti, J.R. Sambrano, M.S. Li, J.A. Varela, E. Longo, Joint Experimental and Theoretical Analysis of Order−Disorder Effects in Cubic BaZrO3 Assembled Nanoparticles under Decaoctahedral Shape, The Journal of Physical Chemistry A 115(17) (2011) 4482-4490.

[29] L. Gracia, V. M. Longo, L. S. Cavalcante, A. Beltrán, W. Avansi, M. S. Li, V. R. Mastelaro, J. A. Varela, E. Longo, J. Andrés, Presence of excited electronic state in $CaWO_4$ crystals provoked by a tetrahedral distortion: An experimental and theoretical investigation, J. Appl. Phys. 110 (2011) 043501.

[30] L.F. da Silva, J.-C. M'Peko, J. Andrés, A. Beltrán, L. Gracia, M.I.B. Bernardi, A. Mesquita, E. Antonelli, M.L. Moreira, V.R. Mastelaro, Insight into the Effects of Fe Addition on the Local Structure and Electronic Properties of SrTiO3, The Journal of Physical Chemistry C 118(9) (2014) 4930-4940.

[31] V.M. Longo, M. das Graca Sampaio Costa, A. Zirpole Simoes, I.L.V. Rosa, C.O.P. Santos, J. Andres, E. Longo, J.A. Varela, On the photoluminescence behavior of samarium-doped strontium titanate nanostructures under UV light. A structural and electronic understanding, Physical Chemistry Chemical Physics 12(27) (2010) 7566-7579.

[32] I.L.V. Rosa, M.C.Oliveira, M.Assis, M.Ferrer, R.S.André, E.Longo, M.F.C.Gurgel, A theoretical investigation of the structural and electronic properties of orthorhombic $CaZrO_3$, Ceram. Int. 41(2) (2015) 3069–3074.

[33] A.D. Becke, Density-functional thermochemistry. III. The role of exact exchange, J. Chem. Phys 98 (1993) 5648-5652.

[34] C.T. Lee, W.T. Yang, R.G. Parr, Development of the Colle-Salvetti correlation-energy formula into a functional of the electron density, Phys. Rev. B: Condens. Matter 37 (1988) 785-789.

[35] R. Dovesi, R. Orlando, A. Erba, C.M. Zicovich-Wilson, B. Civalleri, S. Casassa, L. Maschio, M. Ferrabone, M. De La Pierre, P. D'Arco, Y. Noël, M. Causà, M. Rérat, B. Kirtman, CRYSTAL14: A program for the ab initio investigation of crystalline solids, International Journal of Quantum Chemistry 114(19) (2014) 1287-1317.

[36] L. Valenzano, F.J. Torres, K. Doll, F. Pascale, C.M. Zicovich-Wilson, R. Dovesi, Ab Initio study of the vibrational spectrum and related properties of crystalline compounds; the case of $CaCO_3$ calcite, Z. Phys. Chem. 220 (2006) 893-912.

[37] V. L, C. B, C. S, B. S, N.M. H, J. S, L.K. P, L. C, Disclosing the Complex Structure of UiO-66 Metal Organic Framework: A Synergic Combination of Experiment and Theory, Chem. Mater. 23 (2011) 1700–1718.

[38] F. Cora, The performance of hybrid density functionals in solid state chemistry: the case of $BaTiO_3$, Mol. Phys. 103 (2005) 2483-2496

[39] http://Www.Crystal.Unito.It/Basis_Sets.Html, Basis Set.

[40] H.J. Monkhorst, J.D. Pack, Special points for Brillouin-zone integrations, Physical review B 13(12) (1976) 5188.

[41] G. Wulff, Xxv. zur frage der geschwindigkeit des wachsthums und der auflösung der krystallflächen, Zeitschrift für Kristallographie-Crystalline Materials 34(1) (1901) 449-530.

[42] K. Momma, F. Izumi, VESTA 3 for three-dimensional visualization of crystal, volumetric and morphology data, J. Appl. Cryst. 44 (2011) 1272-1276.

[43] I. Levin, T.G. Amos, S.M. Bell, L. Farber, T.A. Vanderah, R.S. Roth, B.H. Toby, Phase equilibria, crystal structures, and dielectric anomaly in the $BaZrO_3$–$CaZrO_3$ system, Journal of Solid State Chemistry 175(2) (2003) 170-181.

[44] G. Blasse, A. Bril, A New Phosphor for Flying-Spot Cathode-Ray Tubes for Color Television: Yellow-Emitting $Y_3Al_5O_{12}$-Ce^{3+}, Appl. Phys. Lett., 11(2) (1967) 53-55.

[45] T.M. Mazzo, M.L. Moreira, I.M. Pinatti, F.C. Picon, E.R. Leite, I.L.V. Rosa, J.A. Varela, L.A. Perazolli, E. Longo, $CaTiO_3$:Eu^{3+} obtained by microwave assisted hydrothermal method: A photoluminescent approach, Optical Materials 32(9) (2010) 990-997.

[46] M. Romero, R. Faccio, J. Martínez, H. Pardo, B. Montenegro, C.C. Plá Cid, A.A. Pasa, Á.W. Mombrú, Effect of lanthanide on the microstructure and structure of $LnMn_{0.5}Fe_{0.5}O_3$ nanoparticles with Ln=La, Pr, Nd, Sm and Gd prepared by the polymer precursor method, Journal of Solid State Chemistry 221 (2015) 325-333.

[47] L.F. Goncalves, L.S.R. Rocha, E. Longo, A.Z. Simões, Calcium doped $BiFeO_3$ films: Rietveld analysis and piezoelectric properties, Journal of Materials Science: Materials in Electronics 29(1) (2018) 784-793.

[48] A.C. Eduardo, A.T. de Figueiredo, M. Siu Li, E. Longo, Structural disorder-dependent upconversion in Er^{3+}/Yb3^{+}-doped calcium titanate, Ceramics International 40(10, Part A) (2014) 15981-15984.

[49] V.M. Longo, L.S. Cavalcante, M.G.S. Costa, M.L. Moreira, A.T. de Figueiredo, J. Andrés, J.A. Varela, E. Longo, First principles calculations on the origin of violet-blue and green light photoluminescence emission in $SrZrO_3$ and $SrTiO_3$ perovskites, Theoretical Chemistry Accounts 124(5) (2009) 385.

[50] A.L.M. de Oliveira, M.R.S. Silva, H. Sales, E. Longo, A.S. Maia, A.G. Souza, I.M.G. Santos, Effect of the composition on the thermal behaviour of the $SrSn_{1-x}Ti_xO_3$ precursor prepared by the polymeric precursor method, Journal of Thermal Analysis and Calorimetry 114(2) (2013) 565-572.

[51] A.A.G. Santiago, C.R.R. Almeida, R.L. Tranquilin, R.M. Nascimento, C.A. Paskocimas, E. Longo, F.V. Motta, M.R.D. Bomio, Photoluminescent properties of the $Ba_{1-x}Zn_xMoO_4$ heterostructure obtained by ultrasonic spray pyrolysis, Ceramics International 44(4) (2018) 3775-3786.

[52] L.X. Lovisa, M.C. Oliveira, J. Andrés, L. Gracia, M.S. Li, E. Longo, R.L. Tranquilin, C.A. Paskocimas, M.R.D. Bomio, F.V. Motta, Structure, morphology and photoluminescence emissions of $ZnMoO_4$: RE^{3+}=Tb^{3+} - Tm^{3+} - X Eu^{3+} (x = 1, 1.5, 2, 2.5 and 3 mol%) particles obtained by the sonochemical method, Journal of Alloys and Compounds 750 (2018) 55-70.

[53] G.M. Gurgel, L.X. Lovisa, L.M. Pereira, F.V. Motta, M.S. Li, E. Longo, C.A. Paskocimas, M.R.D. Bomio, Photoluminescence properties of (Eu, Tb, Tm) co-doped $PbMoO_4$ obtained by sonochemical synthesis, Journal of Alloys and Compounds 700 (2017) 130-137.

[54] S.C.S. Lemos, F.C. Romeiro, L.F. de Paula, R.F. Gonçalves, A.P. de Moura, M.M. Ferrer, E. Longo, A.O.T. Patrocinio, R.C. Lima, Effect of Er^{3+} ions on the phase formation and properties of In_2O_3 nanostructures crystallized upon microwave heating, Journal of Solid State Chemistry 249 (2017) 58-63.

[55] L.X. Lovisa, J. Andrés, L. Gracia, M.S. Li, C.A. Paskocimas, M.R.D. Bomio, V.D. Araujo, E. Longo, F.V. Motta, Photoluminescent properties of ZrO_2: Tm^{3+}, Tb^{3+}, Eu^{3+} powders—A combined experimental and theoretical study, Journal of Alloys and Compounds 695 (2017) 3094-3103.

[56] C.R.R. Almeida, L.X. Lovisa, A.A.G. Santiago, M.S. Li, E. Longo, C.A. Paskocimas, F.V. Motta, M.R.D. Bomio, One-step synthesis of CaMoO4: Eu^{3+} nanospheres by ultrasonic spray pyrolysis, Journal of Materials Science: Materials in Electronics 28(22) (2017) 16867-16879.

[57] J. Huang, L. Zhou, Y. Lan, F. Gong, Q. L, J. Sun, Synthesis and luminescence properties of the red phosphor $CaZrO_3$:Eu^{3+} for white light-emitting diode application, Cent. Eur. J. Phys. 9 (4) (2011) 975-979.

8. Apêndice - Resumo em Português

Título: Morfologia e propriedades estruturais de óxidos metálicos complexos: Um enfoque teórico e experimental.

Esta tese doutoral pôde ser realizada devido a concessão de uma bolsa do Programa Santiago Grisolía da Generalitat Valenciana de 01/09/2015 a 01/09/2018 e por poder ter acesso aos computadores de cálculo científico do Serviço de Informática da Universitat Jaume I (UJI), onde a maioria dos cálculos foram realizados.

A pesquisa apresentada aqui abrange uma linha de pesquisa que vem sendo realizada em colaboração entre o grupo de Química Teórica e Computacional da UJI e o centro de desenvolvimento de materiais funcionais (CDMF) da Universidade Federal de São Carlos (UFSCar) há quase 30 anos. Esta colaboração baseia-se no seguinte pilar "Os avanços na modelagem e simulação computacional, baseados na aplicação dos métodos e técnicas da química teórica e computacional, que são estabelecidos como um componente fundamental em pesquisas orientadas e aplicadas em áreas como: desenho racional de sólidos e nano(materiais) com propriedades químicas e físicas inovadoras".

Esta tese doutoral é um trabalho teórico e experimental sobre óxidos inorgânicos complexos da família dos molibdatos ($BaMoO_4$, $CaMoO_4$ e $ZnMoO_4$), tungstatos ($BaWO_4$) e perovisquitas ($CaZrO_3$). A síntese e caracterização dos materiais $BaMoO_4$, $BaWO_4$, soluções sólidas $BaW_{1-x}Mo_xO_4$ (x=0.25, 0.5, 0.75), $CaZrO_3$ e $CaZrO_3:Eu^{3+}$ se realizaram no CDMF da UFSCar e os materiais $CaMoO_4$, $ZnMoO_4$ e $ZnMoO_4:Eu^{3+}$ no laboratório de síntese química e de materiais (LSQM) da Universidade Federal do Rio Grande do Norte (UFRN), enquanto o estudo teórico se realizou no laboratório de química teórica e computacional (LQTC) da UJI. Em particular, o aspecto fundamental tratado é a morfologia, por uma parte temos desenvolvido uma metodologia teórica que nos permite utilizar a construção de Wulff e obter todas as morfologias acessíveis de um determinado material e poder comparar-las com as imagens experimentais que se obtém mediante a microscopia eletrônica.

A continuação se estruturará no presente resumo seguindo as seções refletidas no acordo de cotutela:

- Finalidade e os objetivos da pesquisa
- Abordagem e metodologia utilizada
- Contribuições originais
- Conclusões e futuras linhas obtidas para pesquisa

Finalidade e os objetivos da pesquisa

Este trabalho se baseia em uma caracterização da geometria, morfologia, propriedades eletrônicas e ópticas ("band gap" e de emissão de fotoluminescência), e tem sido demonstrado como os métodos e as técnicas da química teórica e computacional podem ser utilizados para compreender as propriedades físicas e químicas destes materiais. Esta tese é uma investigação interdisciplinar que busca um design racional dos materiais analisando as suas propriedades para poder gerar novas e inovadoras aplicações tecnológicas.

Os objetivos gerais desta tese podem ser divididos em:

- Fornecer um guia científico para o controle morfológico da síntese de (nano) materiais;

- Desenvolver um modelo termodinâmico universal para prever a morfologia acessível de um determinado (nano)material. A modulação morfológica de cristais tridimensionais é demonstrada usando a teoria do funcional da densidade para realizar cálculos de primeiros princípios;

- Obter através do uso de modelo e alterando os valores relativos das energias superficiais, tanto a morfologia desejada como o caminho que liga a morfologia ideal (mais estável) à morfologia que é encontrada experimentalmente, que depende do método e das condições de síntese. Essa estratégia nos permite controlar as morfologias cristalinas, bem como racionalizar os diferentes canais que partem da morfologia ideal;

- Esta análise combinada resulta em um mapa completo de morfologias acessíveis em uma ampla gama de (nano)materiais, e pode servir como um guia para os pesquisadores, ao analisar imagens de microscopia eletrônica, para obter uma melhor compreensão de como controlar a forma de cristal ajustando sinteticamente a química da superfície e controlando os valores relativos das energias superficiais;

- Utilizar métodos teóricos e modelos computacionais baseados na mecânica quântica, para localizar e descrever estados excitados, a fim de determinar sua geometria e estrutura eletrônica e, portanto, prever e explicar as emissões fotoluminescentes dos (nano)materiais.

Os objetivos específicos desta tese podem ser divididos em:

A morfologia de alguns materiais scheelitas, wolframitas e perovisquitas se obtém em várias condições de preparação. Tais como bário molibdato ($BaMoO_4$), tungstato de bário ($BaWoO_4$), soluções sólidas $BaW_{1-x}Mo_xO_4$ (x = 0.25, 0.5, 0.75), molibdato de cálcio ($CaMoO_4$), molibdato de zinco ($ZnMoO_4$), e o zirconato de cálcio ($CaZrO_3$). Estes são os materiais que investigaremos nesta tese, na qual os seguintes objetivos específicos podem ser resumidos da seguinte forma:

• estudar a influência da substituição de cátions de W^{6+} por Mo^{6+} na solução sólida completa $BaW_{1-x}Mo_xO_4$ (x = 0, 0.25, 0.5, 0.75, 1), em função das propriedades estruturais, eletrônicas, ópticas, frequências vibracionais e estruturais morfológicas calculadas. Comparando tudo isso com a parte experimental feita por meio de microscopia eletrônica.

• Analisar a estrutura e propriedades eletrônicas de $CaMoO_4$, a estabilidade das superfícies correspondentes e suas transformações morfológicas.

• Investigar a influência do dopante Eu^{3+} na matriz $ZnMoO_4$, tanto na geometria, estrutura eletrônica e morfologia em função da análise comparativa de cálculos teóricos com microscopia eletrônica.

• Compreender os espectros de fotoluminescência com base na localização e caracterização dos estados eletrônicos fundamental (singlete, s) e excitados (singlete, s* e triplete, t*), utilizando as estruturas ideais e distorcida de $CaZrO_3$ puro e dopado com Eu^{3+}. Além disso, correlacionar suas geometrias, morfologias, estruturas eletrônicas e freqüências vibracionais correspondentes.

Abordagem e metodologia utilizada

Nesta tese foi utilizado o método DFT e funcional hibrido B3LYP que foram de grande utilidade para racionalizar a geometria, estrutura eletrônica, freqüências vibracionais, propriedades ópticas e principalmente a morfologia dos cristais $BaWO_4$, $BaMoO_4$, $BaW_{1-x}Mo_xO_4$,(x = 0.25, 0.5, 0.75), $CaMoO_4$, $ZnMoO_4$ e $CaZrO_3$. Esta metodologia está implementada no programa de cálculo CRYSTAL 2014, que permite realizar cálculos periódicos desde 0, 1, 2 (“slabs” bidimensionais) e 3 a dimensões (cristais). Para descrever os átomos, os orbitais cristalinos são expressos como uma combinação linear de produtos de funções Gaussianas com diferentes expoentes, que dependem do número e tipo de átomos contidos na célula unitária. O conjunto de bases pode abranger todos os elétrons ou pode ser representado por pseudopotenciais, onde partes dos elétrons são englobados no "core" do átomo e não são tratados como elétrons de valência.

Usando o programa J-ICE permitiu a visualização e classificação dos modos normais de vibração dos nano(cristais).Os mapas de densidade de spin usados foram para caracterizar e localizar elétrons desemparelhados em $CaZrO_3$ e $CaZrO_3:Eu^{3+}$ foram obtido sutilizando o programa XCrySDen. Os diagramas da densidade de estados (DOS) e estrutura de bandas calculados para analisar as contribuições eletrônicas dos átomos e seus orbitais atômicos nos materiais $BaWO_4$, $BaMoO_4$, $BaW_{1-x}Mo_xO_4$, $CaMoO_4$, $ZnMoO_4$ e $CaZrO_3$. Foram obtidas com o programa ORIGINLab. Os mapas de morfologia construídos se basearam em cálculos de energia de superfície e o teorema de Wulff com a ajuda do programa VESTA. Este programa permite uma forma de criar morfologia nano(cristais) por meio das distâncias dos planos ao centro do cristal. Essa distância é diretamente proporcional à modulação de energia

Para obter a morfologia usando a construção de Wulff, é necessário calcular as energias superficiais (γ) de um dado material, γ se pode representar como $E_{surf,}$ e também denominar energia superficial. E pode ser calculado a partir do corte em um plano cristalográfico do cristal e corresponde à energia de clivagem. Estes planos cristalográficos dependem do grupo pontual de simetria do material e as superfícies são obtidas cortando o cristal por uma seção perpendicular do “bulk” em relação aos vetores da direção desejada, obtendo-se assim uma estrutura periódica em duas dimensões (“slab”), mas com espessura finita (eixo z).

Desta forma, a energia superficial ou "clivagem" (γ) é definida como a energia por unidade de área necessária para formar a superfície 2-D em relação ao volume e é calculada pela seguinte expressão em T = 0ºK:

$$\boldsymbol{\gamma} = \frac{\mathbf{E_{slab} - N \cdot E_{bulk}}}{\mathbf{2A}}$$

onde E_{slab} é a energia total do “slab” 2D, E_{bulk} é a energia total do volume, respectivamente, enquanto N e A representam o número de unidades de fórmula mínima e a área A, respectivamente. O fator 2 no denominador vem da existência das superfícies superior e inferior do ‘slab”, que possui uma composição simétrica.Após o processo de otimização é verificado e comprovado se o valor de γ atingiu um valor constante e não depende da espessura do "slab", obtém-se o valor de γ.

Contribuições originais

A presente tese doutoral tem sido o resultado de diferentes colaborações entre o LQTC e o CDMF da UFSCar e do LSQM da UFRN. Isso levou à publicação de sete artigos e um capítulo de livro, onde minha contribuição e dos co-autores são indicadas:

I. Título: Synthesis and morphological transformation of $BaWO_4$ crystals: Experimental and theoretical insights
Autores: Marisa Carvalho Oliveira, Lourdes Gracia, Içamira Costa Nogueira, Maria Fernanda do Carmo Gurgel, Jose Manuel Rivas Mercury, Elson Longo, Juan Andrés.
Revista: *Ceramics International* **2016**, 42, 10913-10921. (Material Science, Ceramics, Q1)

II. Título: On the morphology of $BaMoO_4$ crystals: A theoretical and experimental approach.
Autores: Marisa Carvalho Oliveira, Lourdes Gracia, Içamira Costa Nogueira, Maria Fernanda do Carmo Gurgel, Jose Manuel Rivas Mercury, Elson Longo, Juan Andrés.
Revista: *Crystal Research and Technology* **2016**, 51, 634-644. (Crystallography, Q4)

III. Título: Geometry, electronic structure, morphology and photoluminescence emissions of $BaW_{1-x}Mo_xO_4$ (x=0, 0.25, 0.50, 0.75, and 1) solid solutions: theory and experiment in concert.
Autores: Marisa Carvalho Oliveira, Juan Andrés, Lourdes Gracia, Michelle Suzane M. P. de Oliveira, Jose Manuel R. Mercury, Elson Longo, Içamira Costa Nogueira.
Revista: Enviado para su publicación a la revista *Applied Surface Science* (Materials Science, Coatings & Films, Q1).

IV. Título: Crystal Growth: Concepts, Mechanisms and Applications: Analysis for the Morphology Prediction of Materials from First Principles Calculations

Autores: Marisa Carvalho Oliveira, Thiago Martins Duarte, Lourdes Gracia, Elson Longo, Juan Andrés.
Livro*:* *Nova Science Publishers* (**2017**).ISBN**:** 978-1-53612-226-8.

As sínteses e caracterizações experimentais descritas nestes quatro estudos foram realizadas no CDMF pela Dra. I. C. Nogueira e supervisão do Prof. E. Longo. O Dr. J. M. Rivas Mercury, do Instituto Federal do Maranhão, auxiliou na apresentação e discussão dos resultados experimentais dos artigos I, II e III. A Dra. M. F. C. Gurgel, da Universidade Federal de Goiás (UFG), auxiliou na apresentação e discussão dos resultados experimentais dos artigos I e II. O estudante de doutorado T.M. Duarte, que fez uma estância de um ano no LQTC, participou no capítulo do livro (contribuição IV), particularmente no estudo do sistema $BaSnO_3$. Prof. Dr. J. Andrés e Dra. Lourdes Gracia propuseram, planejaram e ajudaram na realização dos cálculos e, juntamente com o Prof. Dr. Elson Longo, na redação final desses quatro trabalhos. Minha participação concentrou-se na realização dos cálculos no LQTC, análise e discussão dos resultados teóricos, elaboração das figuras e tabelas, revisão bibliográfica e redação dos quatro manuscritos.

V. Título: Experimental and theoretical study to explain the morphology of $CaMoO_4$ crystal.

Autores: Fernanda Karine Fonseca de Oliveira, Marisa Carvalho Oliveira, Lourdes Gracia, Ricardo Luis Tranquilin, Carlos Alberto Paskocimas, Fabiana Villela da Motta, Elson Longo, Juan Andrés, Mauricio Roberto Bomio Delmonte.

Revista: *Journal of Physics and Chemistry of Solids* **2018**, 114, 141-152. (Chemistry, Multidisciplinary, Q2).

VI. Título: Structure, morphology and photoluminescence emissions of $ZnMoO_4$: RE^{3+}= Tb^{3+} - Tm^{3+} - x Eu^{3+} (x = 1, 1.5, 2, 2.5 and 3 mol %) particles obtained by the sonochemical method.
Autores: Laura Ximena Lovisa, Marisa Carvalho Oliveira, Juan Andrés, Lourdes Gracia, Maximo Siu Li, Elson Longo, Ricardo Luis Tranquilin, Carlos Alberto Paskocimas, Fabiana Villela da Motta, Mauricio Roberto Bomio Delmonte.
Revista: *Journal of Alloys and Compounds.* **2018**, 750, 55-70. (Materials Science, Multidisciplinary, Q1).

As sínteses e caracterizações experimentais descritos nestes estudos se realizaram no LSQM, pela estudante F.K.F. Oliveira em CaMoO4 e pela estudante de doutorado L.X. Lovisa em $ZnMoO_4$:RE^{3+}= Tb^{3+}-Tm^{3+}-xEu^{3+} (x = 1 , 1.5, 2, 2.5 e 3) e supervisão do Dr. M.R. Bomio, Dra. F.V. Motta, Dr. C.A. Paskocimas da UFRN nos artigos V e VI. O Prof. Dr. M. S. Li, da Universidade de São Paulo, em São Carlos, realizou medidas de espectroscopia de fotoluminescência no artigo VI. O Dr. R. L. Tranquilin, da UFSCar obteve as imagens da microscopia eletrônica de varredura com emissão de campo nos artigos V e VI. Prof. Dr. J. Andres e Dra. Lourdes Gracia proposto, planejado e ajudou a realizar os cálculos e, juntamente com o Prof. Dr. Elson Longo na redacção final destes dois empregos. Meu envolvimento centrou-se na realização de cálculos na LQTC, análise e discussão dos resultados teóricos, elaboração de figuras e tabelas, a revisão da literatura, e a elaboração dos dois manuscritos.

VII. Título: Mechanism of photoluminescence in intrinsically disordered $CaZrO_3$ crystals: First principles modeling of the excited electronic states.
Autores: Marisa Carvalho Oliveira, Lourdes Gracia, Marcelo Assis, Ieda Lúcia Viana Rosa, Maria Fernanda do Carmo Gurgel, Elson Longo, Juan Andrés.
Revista: *Journal of Alloys and Compounds* **2017**, 722, 981-995. (Materials Science, Multidisciplinary, Q1)

VIII. Título: Study of the energetic, morphological and photoluminescent properties of $CaZrO_3$:Eu^{3+}. An experimental and theoretical insight.
Autores: Marisa Carvalho Oliveira, Lourdes Gracia, Marcelo Assis, Ieda Lúcia Viana Rosa, Maria Fernanda do Carmo Gurgel, Elson Longo, Juan Andres.
Revista: Preparado para enviar a publicação.

As sínteses e caracterizações experimentais descritas nesses trabalhos foram realizadas no CDMF pelo estudante de doutorado M. Assis e supervisão do Prof. Dr. E. Longo. A Dra. I. L. Rosa, da UFSCar e a Dra. M.C. Gurgel, da UFG, auxiliaram na apresentação e discussão dos resultados experimentais dos artigos VII e VIII. Prof. Dr. J. Andrés e Dra. Lourdes Gracia propuseram, planejaram e ajudaram na realização dos cálculos e, juntamente com o Prof. Dr. Elson Longo, na redação final desses quatro trabalhos. Minha participação concentrou-se na realização dos cálculos no LQTC, análise e discussão dos resultados teóricos, elaboração das figuras e tabelas, revisão bibliográfica e redação dos dois manuscritos.

Os resultados mais relevantes foram divididos em quatro seções e serão apresentados e discutidos de forma resumida. A primeira seção engloba os artigos I, II e III e capitulo de livro IV, em um estudo refletido na solução sólida completa, uma vez que, x= 0 e x= 1 nos artigos I e II e IV correspondem e compõe os sistemas $BaW_{1-x}Mo_xO_4$ (x = 0, 0.25, 0.50, 0.75, 1). No estudo da solução sólida, foi analisado a substituição de cátions de W^{6+} por cátions de Mo^{6+} no sistema de $BaWO_4$, observando modificações nas propriedades eletrônicas do “bulk” e das superfícies. A análise vibracional mostrou dois modos Raman ativos em alta freqüência de 927 cm^{-1} e 894 cm^{-1} de simetria A_g correspondente aos clusters $[WO_4]^{2-}$ e $[MoO_4]^{2-}$. Neste estudo diferentes intensidades de emissão fotoluminescentes com comprimentos de onda em 522, 520, 528, 512 e 528 nm foram observados. Os materiais estudados nos artigos I, II e III e capítulo de livro IV, foram obtidos pelo método de co-precipitação.

Segunda seção engloba o artigo V e se discute detalhes de cálculos para “bulk” e superfícies de $CaMoO_4$. A análise das propriedades estruturas do “bulk” de $CaMoO_4$ mostra uma coordenação oito átomos de oxigênio ao átomo de Ca, resultando em um cluster dodecaédrico [CaO8] e átomos de Mo coordenado a quatro átomos de oxigênio, formando cluster tetraédrico $[MoO_4]$. Nas superfícies, diferentes tipos de cortes foram realizados em que se observou uma ruptura de ligações entre metal e oxigênios superficiais (Mo-O e Ba-O) comparadas ao “bulk”. O material estudado no artigo V foi obtido pelo método de co-precipitaçãoe processado por um microondas-hidrotermal doméstico sem e com surfactantes (4-dimetilaminobenzoato de etilo e dianidrido 1,2,4,5-benzeno-tetracarboxílico).

Terceira seção se engloba o artigo VI que se discute teoricamente os efeitos do dopante európio na matriz de $ZnMoO_4$ tanto no “bulk” quanto nas superfície com o surgimento de defeitos através de níveis de energia entre as bandas de valencia e condução e um mais baixo valor de energia “gap”. O material estudado no artigo VI foi obtido pelo método sonoquimico.

Quarta e ultima seção se englobam os artigos VI e VII em que se analisam, caracteriza e localiza as estruturas eletrônicas dos estados fundamental singlete, e excitados singlete e triplete em $CaZrO_3$ e $CaZrO_3$:Eu^{3+} tanto no “bulk” quanto nas superfícies, onde se aplica um mecanismo para interpretar as emissões de fotoluminescência. Os materiais estudados nos artigos VI e VII, foram obtidos pelo método de precursores poliméricos.

Outro importante aspecto avaliado foi a modulação teórica da morfologia dos sistemas $BaWO_4$, $BaMO_4$, solução sólida $BaW_{1-x}Mo_xO_4$ (x= 0.25,0.5,0.75), $CaMoO_4$, $ZnMoO_4$, $ZnMoO_4:Eu^{3+}$, $CaZrO_3$ e $CaZrO_3:Eu^{3+}$. Diversas possibilidades de morfologias foram exploradas para explicar possíveis alterações nas condições experimentais e clarificar o conhecimento das propriedades específicas relacionadas com superfícies. Esta combinação de estudos teóricos e experimentais pôde contribuir para proporcionar uma estratégia de investigação científica de qualidade, para a concepção de novas descobertas das propriedades de superfície e também o estudo do comportamento das propriedades morfológicas de tungstatos, molibdatos e zirconatos. A possibilidade de controle tanto da forma quanto do tamanho dos cristais com base na morfologia, demonstrando as etapas envolvidas, que são dependentes da estrutura interna do material e das condições externas de crescimento.

Conclusões e futuras linhas obtidas para pesquisa

Posso acreditar na modelagem e simulação? É uma pergunta frequente para pesquisadores experimentais e teóricos. Para respondê-la, é necessária uma profunda compreensão dos pontos fortes e das limitações da modelagem computacional e dos métodos de simulação utilizados, bem como das técnicas experimentais e suas faixas de aplicação. É obrigatório realizar um diálogo autocrítico entre a teoria e a experiência, em vez de fazer as duas coisas separadamente e dar confiança incondicional nos resultados de tais estudos isoladamente. A combinação de ambos fornece um campo fértil com oportunidades interessantes e uma enorme variedade de possíveis aplicações. É crucial para a modelagem entender os pontos de interesse para experimentais, a complexidade dos sistemas químicos e como abordá-los de maneira apropriada.

As simulações baseadas na mecânica quântica complementam os experimentos e permitem compreender-los a nível atômico, ou seja, testar hipóteses, interpretar e analisar dados em termos de interações em nível atômico não disponível experimentalmente. O uso conjunto e a comparação dos resultados teóricos e experimentais também podem sugerir experimentos e simulações que possam aumentar ainda mais nosso conhecimento. Portanto, os resultados obtidos a partir da simulação são sinérgicos com aqueles que surgem a partir de novos experimentos, e às vezes abrem caminho para resolver problemas onde experimentos não podem fazê-lo. A mecânica quântica está no centro desse esforço e fornece a estrutura para uma descrição em nível atômico e molecular da estrutura química e reatividade que forma a base para a interpretação de dados experimentais e proporciona orientação e guia para realizar novos experimentos. Portanto, há uma grande oportunidade para uma verdadeira sinergia entre teoria e experimento. No entanto, o ponto comum de convergência deve ser as propriedades observáveis do sistema a ser investigado. Os observáveis incluem morfologia, geometria, estrutura eletrônica, freqüências vibracionais, quando disponíveis, e toda essa informação é muito útil, é o ponto de encontro mais frutífero para a teoria e para experimento em ciência de materiais e nanotecnologia.

Morfologia é uma propriedade chave dos materiais e para o desenvolvimento de materiais funcionais é importante para controlar a morfologia e estrutura, e o objetivo principal é o de compreender a química da superfície, uma vez que muitos processos físicos e químicos têm lugar nas superfícies. Na presente Tese, se utiliza artigos publicados no qual os resultados alcançados são através do uso conjunto de trabalhos experimentais e teóricos.

As principais conclusões podem ser resumidas da seguinte maneira:

(I) Caracterizamos as morfologias acessíveis do bário molibdato ($BaMoO_4$), tungstato de bário ($BaWO_4$), soluções sólidas $BaW_{1-x}Mo_xO_4$ (x = 0,25, 05, 0,75), molibdato de cálcio ($CaMoO_4$), molibdato de zinco ($ZnMoO_4$), e o zirconato de cálcio ($CaZrO_3$), aplicando-se a construção de Wulff e usando a teoria funcional de densidade para cálculos de primeiros princípios com o intuito de obter a energia superficial das diferentes superfícies destes materiais, com o objetivo de fornecer um guia científico para o controle morfológico da síntese destes (nano) materiais.

(II) Os resultados apresentados aqui confirmam uma variedade de morfologias que podem ser obtidas ajustando as estabilidades de superfície, que dependem dos métodos de síntese e das condições de reação. Existe uma correlação entre a energia de superfície e a densidade de ligações rompidas em cada uma das diferentes superfícies. Assim, ao analisar as imagens de microscopia eletrônica, se pode obter uma maior compreensão de como controlar a forma cristalina sinteticamente ajustando a química da superfície e controlando os valores relativos das energias de superfície.

(III) Estudamos a estrutura e as propriedades eletrônicas do $CaMoO_4$, a estabilidade das correspondentes superfícies e suas transformações morfológicas. Esta estratégia permite prever possíveis morfologias de outros materiais inorgânicos controlando os valores relativos das energias superficiais e explicando e racionalizando os resultados experimentais encontrados na literatura. Esta abordagem tem o potencial de ser quantitativa se combinada com medidas de morfologia, por exemplo, aquelas obtidas por TEM. As morfologias experimentais correspondem às morfologias de crescimento calculadas, enquanto as morfologias de equilíbrio calculadas coincidiram com as observadas.

(IV) Investigamos e realizamos uma comparação entre os resultados teóricos e experimentais para compreender a influência de dopante Eu^{3+} na matriz $ZnMoO_4$, tanto na geometria, estrutura eletrônica como na morfologia.

(V) Compreendendo os espectros de fotoluminescência, com base na localização e caracterização dos principais estados eletrônicos fundamental (singlete, s) e excitado (singlete, s* e triplete, t*), utilizando as estruturas ideais e distorcida $CaZrO_3$ puro e dopado Eu^{3+}. Além disso, correlacionar suas correspondentes geometrias, morfologias, estruturas eletrônicas e freqüências vibracionais.

Para concluir, a continuação dos trabalhos aqui apresentados deve abordar pelo menos os três aspectos seguintes:

(I) Discernir se as morfologias observadas experimentalmente são impulsionadas pela termodinâmica (morfologia de equilíbrio), como tem sido feito nesta tese, ou pela cinética (morfologia do crescimento). Simulações dinâmicas serão necessárias para investigar o mecanismo de crescimento.

(II) Incluir e avaliar sucessivamente a influência da água e/ou adsorção das impurezas nas superfícies dos materiais estudados, tanto em equilíbrio como durante o crescimento de materiais durante a síntese. De fato, para avaliar estes efeitos de adsorção na morfologia do cristal, é fundamental uma análise aprofundada da estrutura e da energia de faces do cristal que atuam como substratos. As estruturas otimizadas das superfícies que foram determinadas neste trabalho podem ser usadas para calcular as energias de adsorção liberadas quando as moléculas de água ou impurezas específicas entram em contato com o cristal.

(III) Incluir a densidade de spin nos mapas de morfologia, o que implicaria a consideração não apenas da energia superficial, mas também a magnetização de cada uma das superfícies, nas quais haveria elétrons desemparelhados.

(IV) Melhorar o método de cálculo utilizado para caracterizar os estados eletrônicos excitados; o funcional da densidade dependente do tempo pode ser uma boa opção.